Towards ferrite based rare-earth free permanent magnets: from model systems to new technological applications

Thesis submitted to

Universidad Autonoma de Madrid

for the degree of:

Doctor of Philosophy in

Condensed Matter Physics and Nanotechnology

Departamento de Física de la Materia Condensada

Facultad de Ciencias

Candidate:

Francisco Javier Pedrosa Ruiz

Co-directed by:

Alberto Bollero Real and Julio Camarero de Diego

Contents

Abstract

Permanent magnets are essential in many applications of very relevant technological areas (transport, communications technology, energy) and are present in virtually all smart devices. However, they are not without controversy and have generated in recent years serious economic and political problems, as well as having important repercussions on the environment. In 2012 the global alarm was raised due to the monopoly derived from the strategic geographical situation of the so-called rare earths, fundamental constituent elements of these materials. Advances in nanoscience and nanotechnology are key in the search for alternatives to permanent magnets based on rare earths. In this sense, and in a general way, this thesis work combines fundamental studies in nanomagnetism with energetically efficient technological processes in order to be able to develop permanent magnets free of competitive rare earth of last generation, as well as to implement new technological applications. To this end, the objectives set out in the present study have included:

1) The study of rare earth-free magnetic systems exploiting anisotropy, shape and microstructure in both model systems (epitaxial layers and manganese nanowires) and in isotropic ferrite powders.

2) The search for general relations to improve / enhance the magnetic properties of rare earth-free materials based on nanostructured ferrites by effective, reproducible and scalable methods.

3) Understanding and controlling the microstructural effects on the magnetic properties of treated and refined ferrite isotropic powders.

4) The development of new methodologies to enhance the properties of permanent magnets based on isotropic ferrite powder, and the prototyping of new applications making use of the permanent magnets free of developed rare earths.

From the scientific point of view, it is necessary to highlight the microscopic determination of the magnetization reversal processes in model systems as well as the experimental demonstration of the generic effects induced by engineered microstructure (tensions and grain size) on the magnetic properties in processed isotropic powders. From the technological point of view, to review the development of an efficient, reproducible and scalable methodology to produce isotropic powder with improved magnetic properties (coercivity and / or $(BH)_{\mathrm{max}}$ product) as well as the design and prototyping of new technological applications..

Resumen

Los imanes permanentes son esenciales en múltiples aplicaciones de áreas tecnológicas muy relevantes (transporte, tecnología de las comunicaciones, energía) y además están presentes en prácticamente todos los dispositivos inteligentes. Sin embargo, no están exentos de controversia y han generado en años recientes graves problemas económicos y políticos, además de tener importantes repercusiones sobre el medioambiente. En 2012 saltó la alarma a nivel mundial, debido al monopolio derivado de la situación geográfica estratégica de las denominadas tierras raras, elementos constituyentes fundamentales de estos materiales. Los avances en Nanociencia y Nanotecnología son clave en la búsqueda de alternativas a los imanes permanentes basados en tierras raras. En este sentido, y de forma general, este trabajo de tesis combina estudios fundamentales en nanomagnetismo con procesamientos tecnológicos energéticamente eficientes con el fin de poder desarrollar imanes permanentes libres de tierras raras competitivos de última generación, así como para implementar nuevas aplicaciones tecnológicas. Para ello, de los objetivos planteados en el presente trabajo caben destacar:

1) El estudio de sistemas magnéticos libres de tierras raras explotando la anisotropía, forma y la microestructura tanto en sistemas modelos (capas epitaxiales y nanohilos mangéticos) como en polvos isótropos de ferritas.

2) La búsqueda de relaciones generales para mejorar/potenciar las propiedades magnéticas de materiales libres de tierras raras basadas en ferritas nanoestructuradas mediante métodos efectivos, reproducibles y escalables.

3) La comprension y control de los efectos microestructurales en las propiedades magnéticas de polvos isótropos de ferrita tratados y refinados.

4) El desarrollo de nuevas metodologías para potenciar las propiedades de imanes permanentes basados en polvo de ferrita isótropo, y el prototipado de nuevas aplicaciones haciendo uso de los imanes permanentes libres de tierras raras desarrollados.

Desde el punto de vista científico, hay que reseñar la determinación microscópica de los procesos de inversión de imanación en sistemas modelo así como la demostración experimental de los efectos genéricos de la microestructura inducida (tensiones y tamaño de grano) en las propiedades magnéticas de polvos isótropos procesados. Desde el punto de vista tecnológico, reseñar el desarrollo de una metodología eficiente, reproducible y escalable para producir polvo isótropo con propiedades magnéticas mejoradas (coercitividad y/o producto $(BH)_{\mathrm{max}}$) así como el diseño y prototipado de nuevas aplicaciones tecnológicas.

Introduction

Here, the introduction to the scientific topic of the this thesis is presented, underlining the principles related to nanomagnetism and permanent magnets (PMs) that have been used. First, a brief overview on the history of magnetism and magnetic materials is given, emphasizing both fundamentals and applications of PMs. The keys for enhancing the magnetic performance of PMs are disclosed, i.e., tuning both anisotropy and magnetization reversal at the nanoscale, drawing special attention to serious economic, political, and environmental problems of rare-earth (RE) elements, which are essential in current PMs-based technological applications. The state of the art of the alternative routes that were handled at the beginning of this thesis towards the development of RE-free PMs are also reported. Finally, the structure of the thesis is briefly outlined, according to its three main parts - including anisotropic model systems, isotropic powders, and prototype development - aiming to improve the magnetic performance of RE-free PMs (mainly ferrites), highlighting the scientific and technological advances achieved.

The basic concepts about fundamental properties of matter provide the tools to shape and adapt the nature with the available elements to the evolving needs of human society. The challenge of the science is to ensure that knowledge, which requires more effort after the discovery of new materials. Nowadays, magnetism and magnetic materials are basics in many technological applications (e.g., electrical machines, information technology, and biomedical applications) of different scientific areas (including Chemistry, Physics, Materials Science, and Biomedicine) with high impact in society, that benefit most people on Earth. In brief, magnetic-based technologies exploit the ability of magnetic materials to retain their (magnetic) information without any energy input (non-volatile memories), to produce/transform/use electrical energy in a very effective way (permanent magnets), and/or to modify their electrical properties in a controlled manner (spintronics). One lesson from the study of the history of magnetism is that fundamental understanding of the science may not be a prerequisite for technological progress. Yet fundamental understanding helps.

This thesis is focused in nanomagnetism aiming to address the design and development of magnetically hard materials, referred as permanent magnets (PMs), without rare earth (RE) contents, as well as to develop novel advanced magnetic-based technology. First, the history of magnetism and magnetic materials is briefly introduced. The concepts of magnetic hysteresis and magnetic anisotropy are discussed focusing on the different types of ferromagnetic materials, providing the keys exploited in this thesis in order to control (improve) the magnetic performance of the nanocrystalline RE-free (mainly ferrite-based) PMs investigated here. These could replace bonded RE-PMs in several applications for which standard ferrites were not suitable. In addition, our approach combines performance with low cost and environmentally friendly production at the same time, unmatched when compared with the traditionally used RE-PMs. The structure of the thesis is briefly outlined at the end of the chapter, emphasizing the key advances in the field of materials fabrication, processing, and technological development.

A brief history of magnetic materials

The history of magnetism is coeval with the history of science [1]. Magnetic phenomena have been known and exploited for many centuries (see table 1). The magnet's ability to attract ferrous objects acting at a distance was already familiar millennium ago to people in Sumer, ancient Greece, China and pre-Colomban America. The earliest experiences with the magnetism involved Magnetite, iron oxide Fe_3O_4, the only material that occurs naturally in a magnetic state. This mineral was also known as Lodestone, after its property of aligning itself in certain directions if allowed to rotate freely, thus being able to indicate the positions of North and South, and to some extent also latitude. The other well known property of Lodestone is that two pieces of it can attract or even repel each other. The natural magic of these magnets has captivated countless curious spirits over two past millennial

It was not until the beginning of XVII century when the first steps were taken to understand magnetism and magnetic materials. In 1600, William Gilbert published the first systematic experiments on magnetism in 'De Magnete' [2]. Fundamentals of magnetism dates from the XIX century. Hans-Christian Oersted made the connection between magnetism and electricity discovering (by accident) that a current carrying wire deflected a compass needle in 1819 [3]. At that time, André-Marie Ampére and Dominique-François Arago wound wire into a coil and showed that the current-carrying coil was equivalent to a magnet. Michael Faraday discovered electromagnetic induction (1821) and demonstrated the principle of the electric motor with a steel magnet, a current-carrying wire and a dish of mercury. A few years later W. Sturgeon developed the first electromagnet. [4]. The discovery of a connection between magnetism and light followed with the magneto-optic Faraday effect (1845). The electromagnetic revolution was launched. All this experimental work inspired James Clerk Maxwell to formulate a unified theory of electricity, magnetism and light in 1865 [5], considered the most significant mankind event of the nineteenth century [**feyman1964**]. In 1880, Warburg measured the first hysteresis loop for an iron sample, and in 1895 the Curie law was proposed [6]. The problem of explaining how a solid could possibly be ferromagnetic (i.e., material with spontaneous long range parallel magnetic coupling between neighboring atoms) was still unsolved at that time.

In the beginning of XX century, Paul Langevin was the first who explained the theory of diamagnetism (materials with no magnetic atoms) and paramagnetism (materials with spontaneous no magnetic coupling between neighboring atoms), a year before Weiss proposition of ferromagnetic theory (molecular field theory) [7]. A naif atomic view of the different types of magnetic materials is shown in Fig. 1. Ferromagnetism therefore challenged the foundations

Period	Dates	Icon	Drivers	Materials
Ancient period	-2000 to 1500	Compass	State, geomancers	Iron, lodestone
Early modern age	1500 to 1820	Horseshoe magnet	Navy	Iron, lodestone
Electromagnetic age	1820 to 1900	Electromagnet Industry	Infrastructure	Electrical steel
Age of understanding	1900 to 1935	Spin, Quantum Mechanics	Academic	(Alnico)
High-frequency age	1935 to 1960	Magnetic resonance	Military	Ferrites
Age of applications	1960 to 1995	Electric motors	Consumer market	Sm-Co, Nd-Fe-B
Age of spintronics	1995 to ...	Read head	Consumer market	Multilayers

Table 1: The seven ages of magnetism. Adapted from [1].

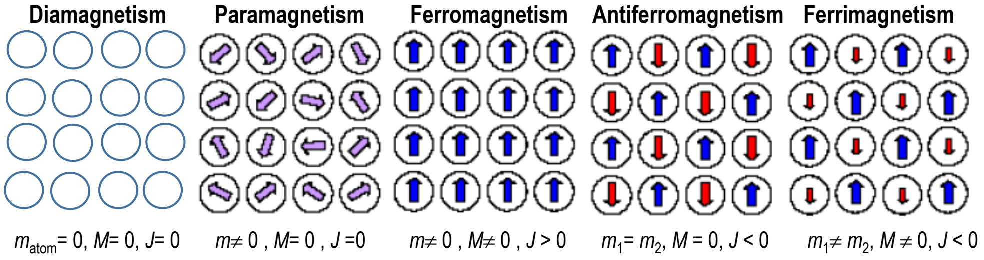

Figure 1: Schematic representation of types of magnetism of matter, on the basis of atomic magnetic moment ($m_{\text{atom}} = m$), total magnetization ($M = \sum m$), and exchange coupling constant between neighbour atoms (J).

of classical physics, and a satisfactory explanation only emerged after quantum mechanics and relativity, the twin pillars on which modern physics rests. The physics of magnetism was developed with theories involving electron spins and exchange interactions in 1920's. When the exchange interaction is negative (antiferromagnetic) rather than positive (ferromagnetic) there is a tendency to align the spins antiparallel rather than parallel. Louis Néel pointed out in 1936 [8] and 1948 [9] that this leads to antiferromagnetism (i.e., material with spontaneous long range antiparallel magnetic coupling between neighboring atoms) or ferrimagnetism (i.e., material with two magnetic sublattices coupled antiparallely), depending on the topology of the crystal lattice. Magnetite, the archetypal natural magnetic material, is a ferrimagnet.

With regard to the discovery and knowledge of important properties associated with magnetic materials, special mention should be made to their transport properties. William Thomson (Lord Kelvin) first discovered magnetoresistance effects in 1856 [10], i.e., the change of a material's resistivity with the application of a magnetic field. In the case of ferromagnetic metals the resistivity is anisotropic, i.e., it depends on the angle between the magnetization vector and the injected current. The anisotropic magnetoresistance (AMR) effect arises from spin-orbit interaction [11] and it was exploited in the recording industry. However, it was not until 1988, with the discovery of the giant magnetoresistance (GMR) by the groups of Albert Fert (University of Paris-Sud, France) [12], and Peter Grünberg (Forschungszentrum Jülich, Germany) [13], that this effect awoke the scientific community interest. Multilayers composed of alternating ferromagnetic (FM) and non-magnetic conductive layers display a giant resistance state when the FM layers are aligned antiparallel. Information storage technology was revolutionized by the application of this technology (mainly applied in magnetic field sensors, e.g., in hard disk drives), since at that moment consisted on bulky matrices with ferrite rings. The size of GMR devices was considerable reduced with an improved capacity. The latest advanced at the end of last century was the observation of room temperature Tunneling MagnetoResistance (TMR) effects in similar multilayered stacks but using thin insulator spacers [14], as predicted twenty years earlier [15]. The term of magneto-electronics or spin-electronic or simply spintronics was then coined grouping magnetoresistive effects (e.g., AMR, GMR, and TMR) exploiting also the use of the spin of the electron [16], in comparison with conventional electronics which ignore it.

The science developed over the last decades of the last century, mostly in Europe, was ripe for exploitation throughout the industrialized world with an immense expansion of magnetic applications. This includes advances in permanent magnetism, high-frequency materials, and magnetic recording. For instance, PMs have come back to replace electromagnets in a billion tiny motors manufactured every year [17, 18]. The third millennium sees us at the threshold of spintronic ages and multifunctional materials. The later refers to system exploiting different functional properties. In all cases, atomic scale engineering of magnetic nanostructures is the key for controlling/enhancing magnetic-based devices. In the case of spintronics, we are learning how to manipulate (spin) currents and to make good use of them in multilayered systems based in (mainly) inorganic [19] but also in organic [20] materials. More recently, we are just beginning to learn how to make use of spin-orbit coupling effects in multilayers with artificially designed interfaces in order to develop more efficient spin(orbit)tronic-based devices [21]. In the case of PMs, engineering of both magnetic anisotropy and magnetization reversal at the nanoscale are at the forefront of present and future of fundamental and applied research [22–25].

Magnetic properties of magnetic materials

The most striking manifestation of magnetism in solids is the spontaneous magnetization of ferromagnetic (FM) materials which is usually associated with magnetic hysteresis trough its magnetization curve, as the one displayed in Fig. 2. This M-H curve corresponds to a polycrystalline ferromagnet in its virgin state, i.e.. initially demagnetized. The system is broken in magnetic domains pointing in different directions averaging total zero magnetization in order to minimize its internal energy, by reducing the magnetostatic energy. During the first magnetization curve from demagnetized state (dashed line), the increasing positive magnetic field H modifies and eventually eliminates the microstructure of magnetic domains, to reveal the spontaneous magnetization $+M_{\mathrm{S}}$. When the applied field is restored to zero, the remanence magnetization M_{R} reflect the magnetic memory effect of FM materials. Sweeping the external field to increasing negative values, the magnetization changes the sign at the coercive field $-H_{\mathrm{C}}$, where the magnetic domain microstructure averages a zero total magnetization, which is uncompensated as the field sweeps to larger negative values, up to reveal $-M_{\mathrm{S}}$. Coming from negative saturation, the remanence is now negative $-M_{\mathrm{S}}$ at zero field. Increasing to positive fields, the magnetization restore to zero at $+H_{\mathrm{C}}$, where the system is broken into magnetic domains with different orientation averaging zero magnetization. increasing up to $+M_{\mathrm{S}}$.

Three important magnetic parameters of magnetic materials have been already introduced:

- Remanence or remanent magnetization or residual magnetism, M_{R}, is the magnetization left behind after the external magnetic field is removed.
- Coercivity or coercive field, H_{C}, is the field required to demagnetize the sample from a saturated state.
- Saturation (spontaneous) magnetization, M_{S}, is the state reached when an increase in applied external magnetic field cannot increase the magnetization of the material further.

In the case of permanent magnets (PMs), the figure of merit is the maximum energy product, $(BH)_{\mathrm{max}}$ which provides a measure to describe their quality. This is extracted from the second

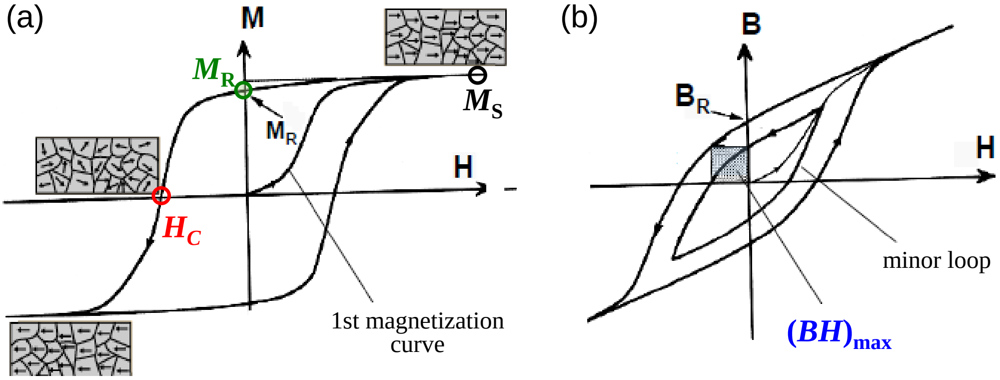

Figure 2: (a) Magnetic hysteresis *M*-*H* curve of a polycrystalline ferromagnetic material initially demagnetized. The system is saturated when the magnetization of all domains pointing along the applied field direction. At the coercive field, $\pm H_C$, the magnetic domain microstructure is compensated, i.e., $M(\pm H_C) = 0$. Removing the applied field (*H* = 0) result in a remaining remanence state which depends on the field sweep direction, $+M_R$ and $-M_R$ coming from positive and negative saturation, respectively (b) Corresponding induction hysteresis *B*-*H* loop. A minor loop arising after the application of fields insufficient for saturation is also shown. The energy product product $(BH)_{max}$, i.e., figure of merit of PMs, is the shaded area in the second quadrant of the *B*-*H* loop.

quadrant of the magnetic flux density $B-H$ loop, where $B = \mu_0(M+H)$ [T] (SI), $\mu_0 = 4\pi \times 10^{-7}$ Vs/Am is the vacuum permeability and the units of M and H are A/m. $(BH)_{max}$ is an energy density and it is equivalent to the area of the largest rectangle that can be inscribed under the normal $B-H$ curve, as shown the inset in Fig. 2. The units of $(BH)_{max}$ are the joule per cubic meter [J/m^3] for SI units and the gauss oersted [GOe] for CGS units, and it shows a benchmark for the maximum amount of magnetic flux taken out from the magnet per unit volume.

So, at a first glance, the hysteresis curve provides relevant information on the characteristic properties of a magnetic material. All theses parameters are intrinsic characteristics of the material and depends basically on magnetic anisotropy and magnetization reversal process

Magnetic Anisotropy

Almost all applications of magnetic materials, in some way or the other, depend on the fact that it is more favorable to magnetize a material in a certain direction than in another one. In general, without an external field, the natural direction of magnetization in a microscopic ferromagnetic domain is usually constrained to lie along one or more specific directions (called easy axes). This is the most relevant property of ferromagnetic materials it makes the material magnetically anisotropic, at least at microscopic scale.

Magnetic anisotropy releases to the non-homogeneity of the magnetic properties when measured in different spatial directions. Magnetic anisotropy is present in magnets of any shape and dimensionality and stabilizes magnetic order in dimensions were the exchange interaction alone would not suffice. The exchange interaction is strong enough (c.a., 0.1 eV/atm in the case of bulk Fe) to stabilize magnetic order against thermal fluctuations (e.g., the Curie tempera-

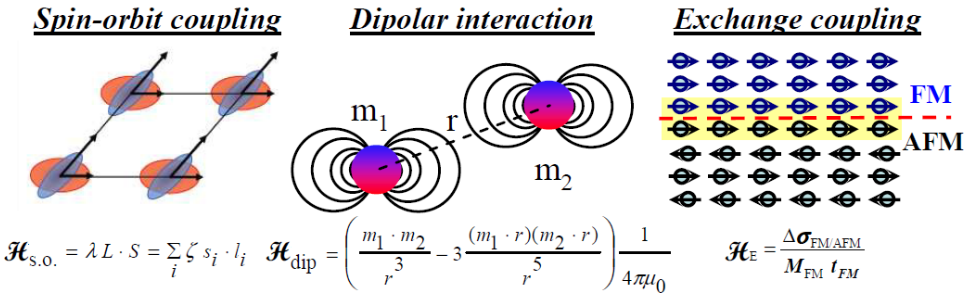

Figure 3: Schematic representation of the fundamental interactions responsible for magnetic anisotropy.

ture (T_C) of bulk Fe is 1043 C), but weakens quickly with imperfections and it is isotropic in nature. Anisotropic effects originate from the spin-orbit coupling, several orders of magnitude smaller (in the μeV/atom range) than exchange, and magnetostatic (shape) effects (of the order of 0.1 meV/atom) are the energy terms contributing to magnetic anisotropy. In addition, interfacial exchange coupling is at the origin of the exchange anisotropy in systems composed of magnetic bilayers with different anisotropy strength (soft/hard ferromagnetic bilayers) or different nature (FM/AFM systems). Fig. 3 show a schematic representation of the fundamental interactions responsible for magnetic anisotropy. The magnetic anisotropy energy is defined as the energy term that describes the dependence of the internal energy on the direction of the magnetization. Usually the magnetic anisotropy energy has the symmetry of the crystal structure (including bulk, interfaces, and strain), the shape of the material, and/or by interfacial exchange. At the origin of magnetic anisotropy one finds crystal lattice symmetry (magnetocrystalline anisotropy), strain (magnetoelastic anisotropy), interfaces (surface anisotropy and exchange anisotropy) and demagnetizing fields (shape anisotropy).

Each magnetic anisotropy contribution can be expressed by anisotropy constants (K) and the effective anisotropy would result from the different competing contributions. For well-oriented magnetic anisotropy systems it can be derived from the anisotropy field (H_K), i.e., the external field required to reverse the magnetization from an e.a. direction to a h.a. direction (see Fig. 4.a). In this case, when the external field is aligned along one e.a. direction the systems with large (small) anisotropy constants should present high (low) coercivity and $M_R = M_S$. As the field becomes missoriented with respect to the anisotropy axis these values decrease. The smallest values are found when the external field is aligned along the h.a. direction, e.g., zero remanence and coercive field are expected in the case of uniaxial magnetic anisotropy systems. This strong anisotropic hysteresis behavior is found in single crystalline magnetic structures and shaped nanostructures. In contrast, systems composed of randomly oriented grains (particles) display an isotropic behavior with reduced both remanence and coercivity values. The expected values can be derived after averaging all over the possible orientations. For instance, coercivity and remanence are c.a. fifty percent reduced for the case of non-interacting randomly oriented uniaxial anisotropic systems (see Fig. 4.b).

For real systems, for both anisotropic and isotropic, although coercivity and remanence still have relationship with the effective magnetic anisotropy, it can not be easily derived from

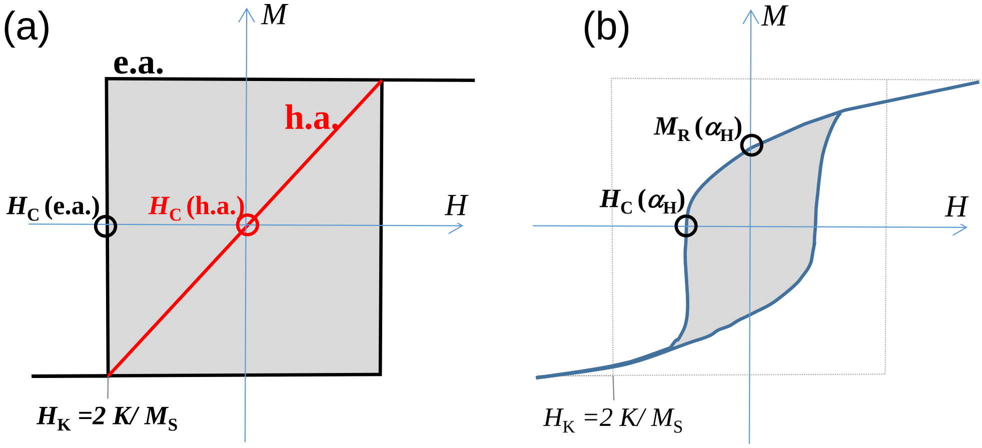

Figure 4: Expected magnetic hysteresis loops of an ideal system composed of non-interacting well-oriented (a) and randomly-oriented (b) single-domain particles with uniaxial magnetic anisotropy. The anisotropy field H_K and coercive field H_C are indicated. Note the large difference between the hysteresis curves of (a), i.e., anisotropic behavior, in contrast with the isotropic behavior of (b), i.e., the hysteresis do not depend on the applied field angle (α_H).

them. This originates from the reversal processes, as discussed below. In any case, and in a generic way, depending on the strength of the magnetic anisotropy the magnetic materials can be classified just by looking the shape of the hysteresis (see Fig. 5). Systems with large (small) anisotropy presents wide (narrow) hysteresis and they are referred as magnetically hard (soft) magnetic materials. Therefore, depending on the strength of the anisotropy and its symmetry it is possible to observe different magnetization features, which can be exploit for different technological applications.

Magnetization reversal

Hysteresis phenomena and magnetization reversal processes are an important issue in Nanomagnetism today [26], both from fundamental and technological points of view. The use of magnetic materials in all applications ranging from compass needles to electrical motors, cellular phones and personal computers has triggered the search for materials with particular properties concerning both their static and dynamic reversal behavior. For instance, magnetization reversal features (i.e., relevant mechanism, reversal times, reversal fields) determine how the magnetization preserves its state in powerful permanent magnet applications, based on nanograin ferromagnetic structures consolidated in bulk systems [23], as well as how the information can be read and written in spintronic devices [19], based on multilayered thin film architectures. Current and future technologies require hence basic understanding and control of hysteresis and magnetization reversal processes [27].

The physical mechanisms responsible for the hysteresis and magnetization reversal in magnetic systems become more complex to interpret as the dimensionality increases [28–31], from zero-dimensional (nanoparticles), two-dimensional (thin films) and three-dimensional (bulky)

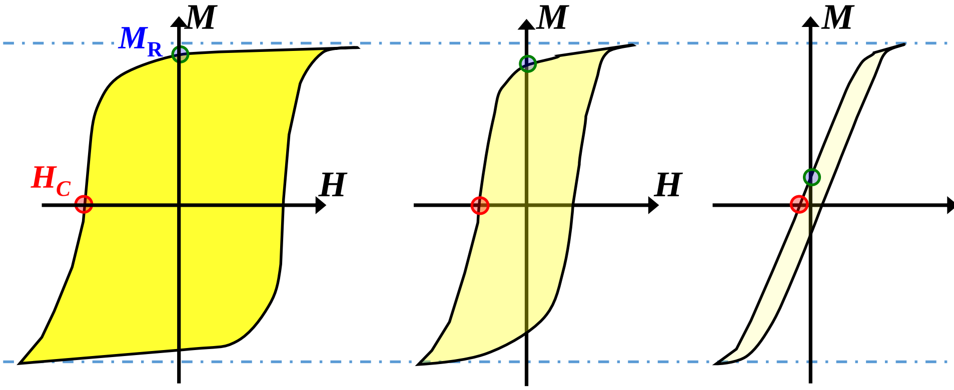

Figure 5: Cartoon of magnetization curves of magnetic materials. From left to right, typical *M*-*H* curves for magnetically hard, medium, and soft systems. Both coercivity and remanent magnetization determine the final application.

magnetic objects. In general, hysteresis include reversible (rotation) and irreversible (switching) magnetic transitions [32]. Magnetization reversal can take place in different ways, depending on object size and physical parameters [33]. The exchange interaction, magnetic anisotropy and magnetostatics are among the most important physical parameters involved. First, exchange interaction favors uniform magnetization configurations. Second, magnetic anisotropy favors the orientation of the magnetization vector along certain preferred directions. And third, magnetostatic interaction favors configurations giving null average magnetic moment, in contrast with anisotropy and exchange. In addition to these intrinsic parameters, the hysteresis depends on extrinsic parameters such as temperature, applied field angle, and applied field sweep rate [34].

Models for collective reversal provide good agreement between experiment and theory in the case of nanoobjects [35], both in uniform reversal modes (Stoner-Wolfhart model [28], macrospin aproximation), as shown for nanoparticles [36], or in non-uniform ones, as in nanowires [37]. What stands out the most is that the SW model predicts identical coercivity and anisotropy field at the e.a. direction (Fig. 4.a). Reduced coercivity values are predicted in non-uniform models depending, on the aspect ratio of the one-dimensional magnetic nanostructure. [38]. For larger magnetic objects, reversible and irreversible magnetization transitions represent different reversal processes, and they are often a manifestation of the magnetic symmetry of the system [32, 34]. Reversible transitions are related to rotation processes, whereas irreversible ones are related to nucleation of reversed magnetic domains (usually created on inhomogeneities or defects) and subsequent propagation of their magnetic domain walls, under the field pressure.

The magnetic properties are hence determined by a combination of nucleation and domain wall propagation behaviors with their associated energy barriers. In the case of oriented anisotropic systems, in addition, the relevance of these processes will depends on the direction of the applied magnetic field with respect to the magnetic anisotropy axes [32, 34], and depends as well on the field rate of change, since they are different in quasi-static and dynamic

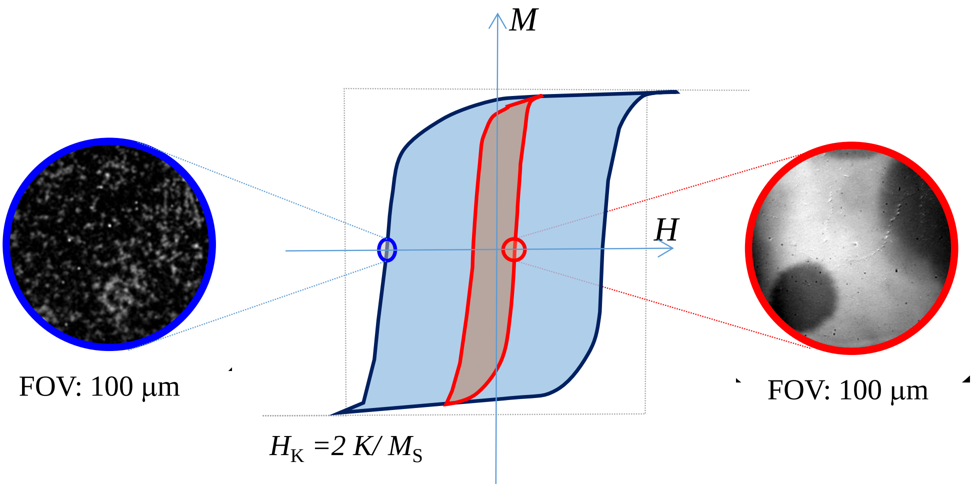

Figure 6: Influence of the relevant reversal mechanism on the hysteresis loop. The images are polar Kerr microscopy images acquired during the reversal of a perpendicular magnetic anisotropy FM system (right) and an exchanged coupled FM/AFM bilayer. The interfacial exchange coupling at the nanoscale of the later result with reversal governed by nucleative processes and much larger coercivities.

regimes [34]. In magnetic thin films with in-plane dimensions considerably larger than the domain wall width, the irreversible processes usually starts at magnetic fields that are significantly lower than expected from SW model, the so-called Brown's paradox [39]. In this case, the dimensions strongly affect the magnetic behavior and the predictions based on the SW model are significantly far from experimental data [40]. In fact, the coercivities found experimentally are usually orders of magnitude lower that the predicted ones.

In general, magnetic systems above a critical size, mostly above a few nanometers, reverse by rotational (reversible) processes and irreversible proceses, such as nucleation of reversed domains and further propagation of domain walls. This takes place in both isotropic (mostly polycristalline and/or randomly oriented systems) and (crystalline and/or shape) anisotropic magnetic systems. The rotational processes are relevant even at any spatial scale for well-oriented anisotropy systems, while this is cancelled out at the macroscale in systems composed of randomly oriented particles after averaging over all arbitrary orientations. The magnetic anisotropy of each single crystal determines the magnetic domain orientation. The irreversible processes are at the origin of the reduced coercivity experimental values found. In general, real magnetic systems are not perfect and contain (structural, chemical, and/or morphological) defects, i.e., low coordination sites, where the effective magnetic anisotropy is weaker and reversal can starts nucleating reversed magnetic domains at much lower magnetic fields than the anisotropy field. Once there are inverted domains, the external field moves the domain wall along the entire sample without having to reach the anisotropy field. The domain wall propagation can be hindered by local pinning centers (defects, grain boundaries), which would allow the nucleation processes to be more relevant during reversal, and get coercive field values closer to anisotropy field. The difficulty for moving domian walls will make it easier to nucleate more domains that need larger magnetic fields, which results with higher coercivities. In fact, recently it has been shown that in systems where nucleation of reversed domains is the dominant mechanism (nucleative regime) the magnetic properties become closer to the ones predicted by the macrospin aproximation [34].

Fig. 6 illustrates the effects on the hysteresis phenomena of magnetic systems where the irreversible process is governed by propagation of domain walls or nucleation of magnetic domains. As discussed above, enhanced coercivities are expected in nucleative regime for any magnetic system. Within this scenario, the coercivity of a given magnetic system can be enhanced by hindereing/avoiding domain wall propagation processes increasing the pinning strength, increasing the density of pinning sites, or/and reducing the grain size.

The magnetic properties are hence determined by a combination of nucleation and domain wall propagation behaviors with their associated energy barriers. Nucleative regime results with enhanced coercivities for any system. In addition, in the case of well defined anisotropty systems the relevance of these processes strongly depends on the direction of the applied magnetic field. This understanding will be exploited all along the thesis for the different scientific cases investigated. This is fundamental to control magnetization reversal processes and hysteresis phenomena in any technological application of magnetic materials.

Technological application of magnetic materials

Magnetic materials are used in many different technological applications. Most people would be surprised by the uses of magnets in everyday life. The functionality of the magnetic material is different as a function of the application requirements. Commonly, magnetic materials are referred are "soft" or "hard" magnetic materials. This classification is done based on their coercivity and remanence magnetization, which depend on their magnetic anisotropy, isotropic or anisotropic character, and reversal processes. In brief, soft materials those with low coercivity (low anisotropy) and low remanence magnetization, i.e., easily to demagnetized, and hard materials those with high coercivity (high magnetic anisotropy) and high remanence (anisotropic), meaning that they are hard to demagnetize.

Soft materials posses low magnetic anisotropy, because of the low fields required to reorient the material magnetization. Ideal soft material posses a high magnetic susceptibility χ (where $\chi = M/H$) in addition to a lineal response. The small energy required to turn the direction of magnetization is the property that takes advantage to make these devices. Furthermore, soft materials with different magnetic relative permeabilities μ (where $\mu = B/H$) greater than the air are used as cores of electromagnets coils to multiply the strength of the generated magnetic field. In general, soft magnets match application in magnetic cores for transformers, antennas, electromagnets and EMI filters. Electromagnets, because they can be turned off and on, are used in powerful pieces of equipment and vehicles, such as magnetic-levitation (maglev) trains.

The so-called "hard" magnetic materials have high magnetic anisotropy and they are also very versatile and strong components of myriad applications as well. Hard materials are identified by large values of H_C and high $(BH)_{max}$. They are basically used to make permanent magnets (PMs). Permanent magnets are used in the following major groups: acoustic transducers, motors and generators, magneto mechanical devices, and magnetic field and imaging systems. We can find permanent magnets in many products, such as televisions, telephones,

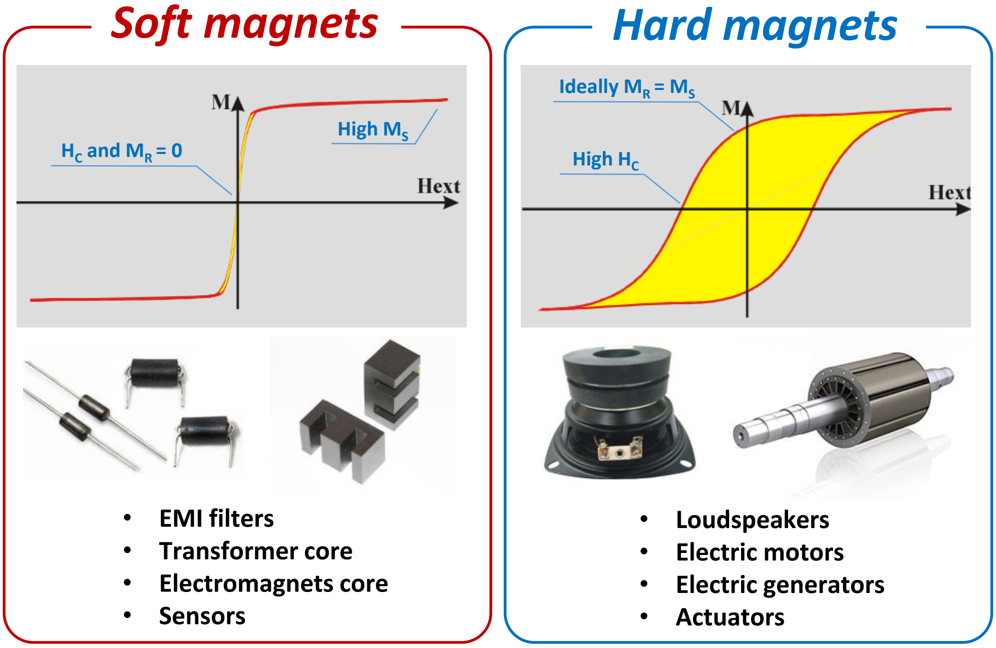

Figure 7: Technological applications of magnetic materials. The graphs are the typical *M*-*H* curves of a soft (left) and a hard (right) magnetic material. This image was obtained from ref [41]

computers, audio systems, and automobiles. In the following it has been described the state of the art of PMs at the beginning og the thesis.

State of the art of PMs

Permanent magnets (PMs) are nowadays essential in the technological development of the moment (see Fig. 8). Emergent applications of permanent magnets in renewable energy have come to the landscape recently, for instance the large-scale applications in electrical vehicles and wind turbines. Permanent magnets are also necessary for the other powder-related novel applications in order to make electric devices smaller, lighter and more energy efficient in the 21st century [22]. Moreover, the application field of these materials not only cover classical electrical machines, but other such as speakers, microphones, actuators and sensors. As an example and to get an idea of the importance of permanent magnets in everyday life: a car has more than 400 permanent magnets, a refrigerator contains approximately 70 magnets, the generator of a medium-power wind turbine contains more than 3 tons of these magnets and also are fundamental part in the hard disks. The rapidly growing market of electric cars and green technologies demands an increased amount of permanent magnets. In fact, the permanent magnet market is currently moving more than $ 9 trillion per year globally and is estimated to reach $ 14 trillion by 2020 through its use in key technological applications.

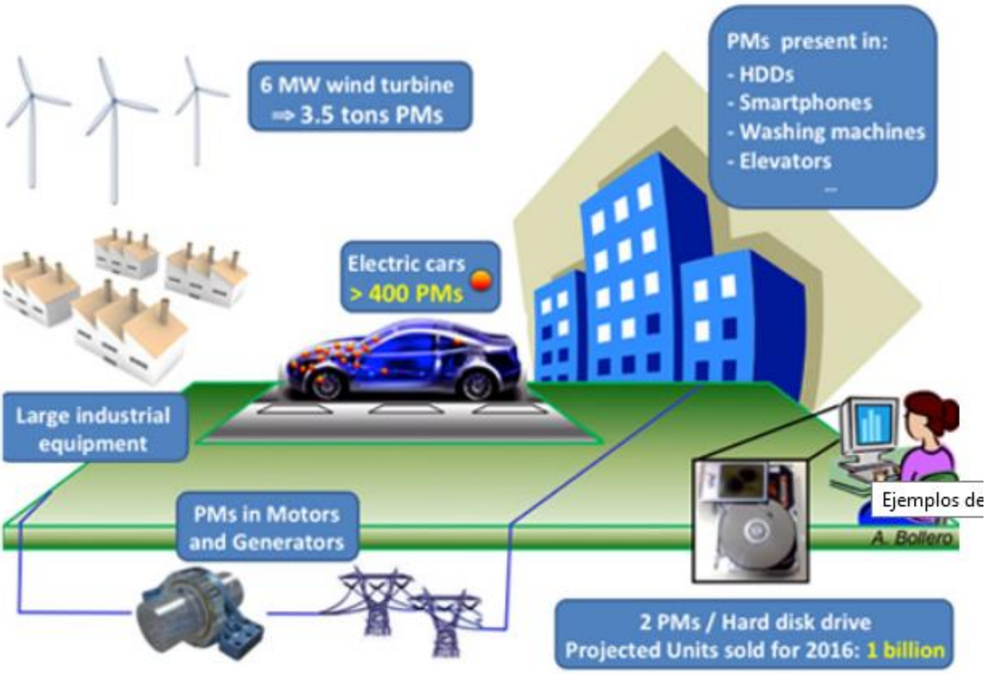

Figure 8: Examples of technological applications of PMs. Courtesy of A. Bollero.

A good permanent magnet should produce a high magnetic field with a low mass, and should be stable against the influences which would demagnetize it. As already mentioned, the figure of merit that determines the performance of a permanent magnet is the maximum energy product $(BH)_{\max}$ which provides an estimation of the magnetic energy density that can be stored in the magnet [42]. Large $(BH)_{\max}$ values require high saturation magnetization (M_S) (with a large remanence value as close as possible to saturation) and coercivity (H_C), i.e., large magnetic anisotropy (besides high Curie temperatures). The first feature (large M_S) is determined by the magnetic moments of the atoms and their exchange interactions. The second (large H_C) relies on high anisotropy of the magnetic structure (i.e., a marked dependence of the energy with the orientation of the magnetic moments) [43]. In practice, remanence is lower than saturation magnetization because of incomplete particle alignment, the presence of magnetic domains, the density being less than the ideal density of the main magnetic phase and existing secondary phases [44]. The materials exhibiting large saturation magnetization (mainly transition metals Fe, Co and Ni and their alloys) show low magnetic anisotropy values [45]. Therefore, the development of high performance permanent magnets represents a challenge for materials science [43–45].

Figure. 9 shows the evolution of the energy products along the last century for the most common type of permanent magnets. The development of PMs has involved firt novel materials and second materials engineering in order to enhance $(BH)_{\max}$ values. Carbon steels were

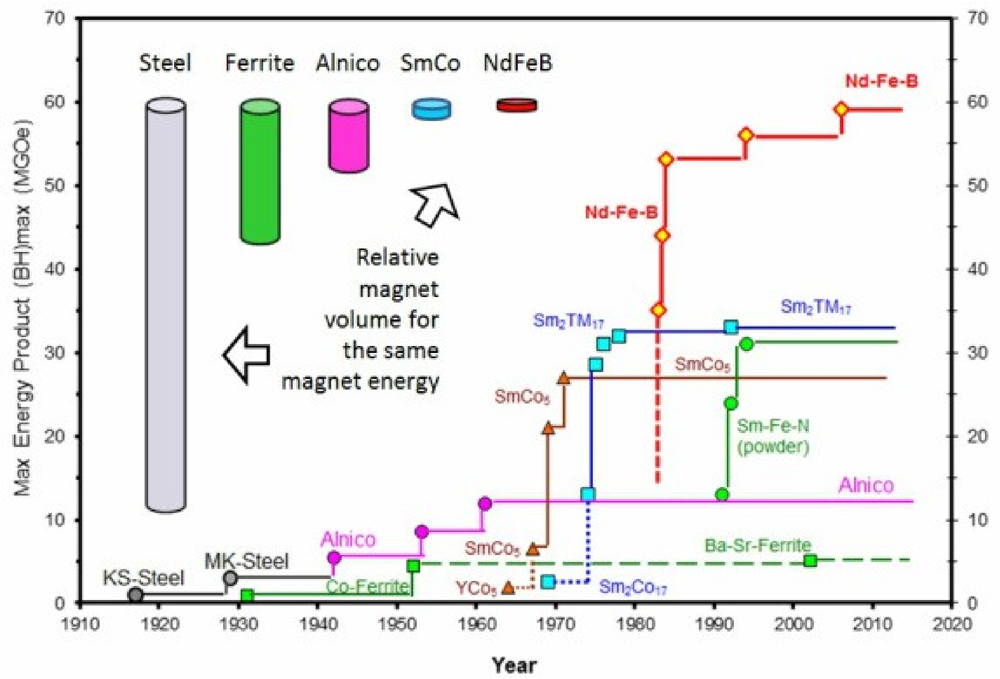

Figure 9: Progress of energy product in the course of the last century. Adapted from...

the first engineered PMs, first developed early the eighteenth century. Although they present high magnetic saturation (far superior to lodestone), they have a tendency to easily demagnetize. In order to avoid it, elongated shapes that minimize demagnetization fields are usually employed. passing to the cheaper and more stable hard ferrites, in the early 30's, In the early 30's, hard ferrites were introduced in the market. They showed similar $(BH)_{\max}$ values, but resulted much cheaper besides more stable against corrosion and oxidation. Ferrites are materials presenting large structural anisotropies due to their particular crystallographic structure (mainly spinels and perovskites), but their $(BH)_{\max}$ products are limited by their low M_S values (note most ferrites are ferrimagnetic with two uncompensated antiparallel spin sublattices) . However, due to their abundancy and low production costs, they are often used in geometrically complex systems. Additionally, their advantages include the fact that they are very resistant to corrosion and easily magnetized. As a result, they remain the most common magnetic material in bulk applications. Their main limitation comes from their low energy product compared to other PM, and their lower Curie temperature, which makes them useless for high-temperature applications.

Alnicos, developed in the 1930s, were the first modern permanent magnets offering considerable improvements in magnetic hardness over the magnetic steels previously available. Their properties rely on the shape anisotropy associated with the two phase nanostructure comprising of ferromagnetic Fe-Co needles in a matrix of non-magnetic Al-Ni. Due to their high

Curie temperature, 850 C, they are still used for certain applications today. An important limitation of Alnicos, besides being more fragile and more expensive than ferrites, is their high electrical conductivity that produces electrical currents in the presence of AC magnetic fields. These currents increase the temperature (reducing the magnetic stability) and result in energy losses. Additionally, they contain large amounts of Co, a strategic metal identified as critical raw material as well [3].

In 1960, the PM market underwent a total revolution with the appearance of Rare Earth (RE) PM. These compounds contain transition metals (with large magnetic moments) as well as rare earths (with high spin-orbit coupling that yields high anisotropy values). Their energy products rise over 240 KJ/$^{-3}$ for SmCo and over 400 JK/$^{-3}$ for NdFeB. The $(BH)_{\max}$ values of RE-PMs were about 5 times larger. Since there was abundance of raw materials for the fabrication of PM that were located in non-developed countries with low production costs, the RE PM rapidly covered most of the market. Most of the world reserves of RE were in third world countries, mainly China and African countries. Thus, RE prices were very competitive and there was no risk of shortage of supplies. Nowadays, about 60% of the PM markets corresponds to REs [46]. As a consequence of their impressive capabilities, rare earth-based permanent magnets (RE-PMs) took over the market and PM made out of ferrites or AlNiCo were mainly restricted to low cost products. As mentioned above, the rapidly growing PMs demands an increased amount of RE-PMs, which combined with supply risks due to mining oligopoly or speculation of REs by China, makes a search for alternatives to these RE-PMs necessary [46–48].

Towards competitive ferrite-based permanent magnets

At the time when this thesis was started (2012), the situation of the PM market had changed dramatically in the last years. With the industrial development of emerging countries (especially China), their requirements of PM has increased substantially, and consequently the prices. More importantly, as holders of 97% of the worldÂ´s rare earth mine production, China controls the supply of such strategic materials. In particular, China produced the vast majority of two particularly important rares, dysprosium (99 percent), required to enhanced coercivity, and neodymium (95 percent).

The EU was aware of this situation and in its report about critical materials [49] stated that RE have capital importance for the EU due to their very high risk of unsupplyment as illustrated in Fig.. 10. Moreover, the main applications for rare earths are magnets. In this context, finding alternatives to RE-PM that would allow replacing them partially or completely would significantly reduce their importation requirements for the EU.

Technological development on ferrites was significantly reduced when RE PM began to thrive, mainly because there was no real need for such developments. Nevertheless, it is worth noting that even though ferrites exhibit energy products 10 times smaller than RE PM, they still constitute 85% of the worldÂ´s PM market in weight due to their extremely low fabrication costs [47]. As stated above, isotropic ferrites exhibit $(BH)_{\max}$ products of the order of 13 KJ/m^3 (35 KJ/m^3 for anisotropic ferrites) and it is scientifically not realistic to think that we can develop ferrites with $(BH)_{\max}$ similar to those of RE-PMs. However, if we are able to increase the $(BH)_{\max}$ product by 10-20 %, some applications that nowadays require RE-PMs could be covered with these advanced ferrites. This would have a double impact on the RE

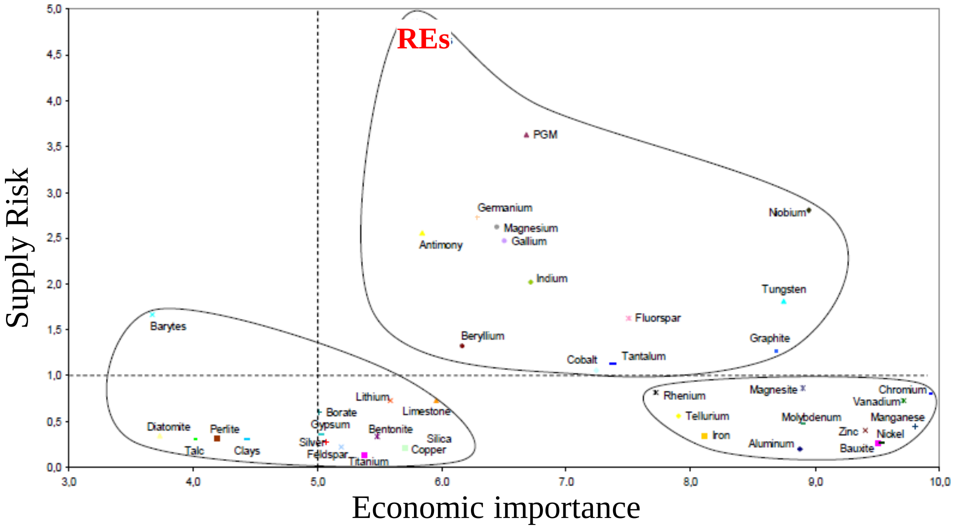

Figure 10: Economic importance and supply risk of the 41 critical raw materials. Adapted from [49].

market: On the one hand we could reduce EU importations of RE. Besides, reducing the RE demand should yield lower prices. This was the main reason why this thesis was focused on the development of RE-free PMs belong the european project NANOPYME [50] (Nanocrystalline Permanent Magnets Based on Hybrid Metal-Ferrites). Taking into account the advantages and limitations of both ferrites and Alnicos stated above, NANOPYME decided to focus the project on the enhancement of the energy product of ferrites. Besides this main goal, two additional significant improvements could potentially take place:

a) The Curie temperature of ferrites could increase, opening the door to higher temperature applications.

b) The fragility of ferrites could improve, allowing easier machining that would decrease production costs.

In order to achieve progress in the performance of ferrites beyond the state-of-the-art, it is crucial to identify the specific physical mechanisms that govern the properties of PM.

The art of permanent magnet design is to prevent demagnetizing fields from demagnetizing the magnet. As discussed previously, magnetic anisotropy is at the heart of the magnetic performance of magnetic systems, but also the isotropic or anisotropic character as well as the relevant mechanism during reversal have also strong influence. The magnetic performance of any magnetic material can be improved through different ways:

- to improve remanence M_R, during the magnet manufacture process, a powerful magnetic field can be used to align the magnetization of the magnet in one specific direction to induce magnetic anisotropy, determining the orientation of the easy axis; the direction where magnetization lies in the absence of an external magnetic applied field.

- H_C and $(BH)_{max}$ can be varied through alterations in the material composition and/or the processing conditions, i.e. by tailoring the microstructure. In order to design magnetic materials for permanent magnets, it might be advantageous to decrease grain size to approach the monodomain regime, that consist of only one existing domain in the particle.
- the creation of defects that act as pinning center, avoiding the domain wall propagation. Both would result with H_C closer to H_K.

Therefore, it is possible to control the magnetic performance of magnetic material to design materials with enhanced magnetic anisotropy and specific magnetization reversal process. In case of permanent magnets, both H_C and M_r, reflect the magnetization reversal process and are related to magnetic anisotropy. Thus to improve the magnetic properties of any given magnet or to synthesize new magnets with better properties, it is essential to understand the relationships between microstructure and magnetic properties, which it will studied throughout the entire thesis, which is schematically described in the following.

Structure of the thesis

The thesis is an experimental scientific-technological work where characterization tasks (microstructural and magnetic), processing of samples (through physical processes), and development of new technology (prototyping) have been combined. The general goal has been to tailor/understand RE-free ferromagnetic materials in order to design/control their final magnetic performance in order to be used as PMs in real technological applications. The thesis has been divided in three parts that contains the following chapters:

Part I contains two chapters, where two different materials are nanostructured to modify its magnetic properties. In Chapter 1, it is shown the possibility of controlling intrinsic properties of $\mathrm{Fe_3O_4}$ thin films grown by PLD. The election of the substrate is crucial in order to promote epitaxial growth, and obtain monocrystalline layers. It has been found anisotropic or isotropic magnetic behavior depending of the substrate orientation. Furthermore, coercivity can be tailored by using different layer thickness, decreasing as the thickness increases. In Chapter 2 shape-induced (magnetostatic) anisotropy has been exploited in order to increase coercivity. The fabrication of nanowires is an interesting approach to obtain materials with a higher magnetic anisotropy through an increase on shape anisotropy. In this case, an array of FeCo nanowires with a high aspect-ratio has been characterized by means of vectorial VSM. In our knowledge, this is the first reported experimental work dealing with angular-dependent vectorial *M-H* VSM measurements of magnetic nanowires. The detailed analysis of the data reveals the direct identification of a complex magnetization reversal process, which it has been reproduced with micromagnetism.

Part II is focused on cobalt ferrite powdres, characterizing the obtained magnetic properties of this material after apply different preparation processes with different parameters to tune the microstrucrture of the powders. In Chapter 3, the effects of heat treatment on the magnetic properties and microstructure of $\mathrm{CoFe_2O_4}$ powders synthesized by the co-precipitation method is discussed. The co-precipitation method is shown to be a scalable method that provides material with repeatable magnetic properties. In Chapter 4, high coercive cobalt ferrite powders are obtained through a high energy ball milling (HEBM) procedure in a record time of few seconds. The influence of the initial material microstructure on the final properties after milling is studied, in both dry (air) and wet (using oleic acid) milling conditions. The oleic acid is a surfactant agent that helps avoiding particles agglomeration after the HEBM process. The increase of coercivity after such short milling times is ascribed to the effectiveness of the HEBM method inducing strain on $CoFe_2O_4$ as well as reducing particle size below the monodomain regime. The milled powder obtained in these experiments is used in Chapter 5, where a post-HEBM heat treatment is carried out. This heat treatment at a moderate temperature allows the recrystallization of cobalt ferrite particles, and a compliance between defects and magnetocrystalline anisotropy, resulting in $CoFe_2O_4$ powders with record energy products up to 18.6 kJ m^3

Part III (Chapter 7) is dedicated to various novel applications (prototypes) combining the CFO-based RE-free PMs investigated in the previous chapters and spintronic-based sensors. First, a device for imaging of magnetic fields with commercial magnetoresistive sensors is described. The prototype device developed is used as a proof of concept to demonstrate the possibility of using it as a magnetic field imaging device for detection of permanent magnets inside electronic devices, for its future extraction an recycling. In addition, the possibility of using magnetovision to study magnetic field distributions, such as interaction between different regions of magnets with different polarities or even different magnets, are also discussed. Finally, the use of permanent magnets to codify metallic boxes such as maritime containers is described as the last proposed application.

The main conclusions, highlights, and perspectives of the data presented in this thesis are summarized in the last chapter. In brief, the results reveal the close relationship between microstructure and magnetic performance in magnetic materials. In addition, new fundamental insights into the technological processes are presented. This knowledge will certainly open additional avenues to develop future advanced RE-free PMs and magnetic-based devices based on microstructure anisotropy tailoring.

References

[1] John MD Coey *Magnetism and magnetic materials* Cambridge University Press, *2010* (cit. on p. iv)

[2] William Gilbert *De magnete* Courier Corporation, *1958* (cit. on p. iv)

[3] Hans Christian Oersted *Electricity and magnetic needles*. in: *Philosophy* ***16***,4 (1820), 273–276 (cit. on p. iv)

[4] Iwan Rhys Morus *Different Experimental Lives: Michael Faraday and William Sturgeon*. in: *History of science* ***30***,1 (1992), 1–28 (cit. on p. iv)

[5] J. Clerk-Maxwell *A Dynamical Theory of the Electromagnetic Field*. in: *Philos. Trans. Roy. Soc.* ***155***, (1865), 459–512 (cit. on p. iv)

[6] Pierre Curie *Propriétés magnétiques des corps a diverses températures* 4 Gauthier-Villars et fils, *1895* (cit. on p. iv)

[7] Pierre Weiss *L'hypothèse du champ moléculaire et la propriété ferromagnétique*. in: *J. phys. theor. appl.* ***6***,1 (1907), 661–690 (cit. on p. iv)

[8] Louis Néel *Propriétés magnétiques de l'état métallique et énergie d'interaction entre atomes magnétiques*. in: *Annales de physique* ***11***, 5 EDP Sciences 1936, 232–279 (cit. on p. v)

[9] M Louis Néel *Propriétés magnétiques des ferrites; ferrimagnétisme et antiferromagnétisme*. in: *Annales de Physique* ***12***, 1948, 137–198 (cit. on p. v)

[10] William Thomson *On the electro-dynamic qualities of metals: effects of magnetization on the electric conductivity of nickel and of iron*. in: *Proceedings of the Royal Society of London* ***8***, (1856), 546–550 (cit. on p. v)

[11] T McGuire and RL Potter *Anisotropic magnetoresistance in ferromagnetic 3d alloys*. in: *IEEE Transactions on Magnetics* ***11***,4 (1975), 1018–1038 (cit. on p. v)

[12] Mario Norberto Baibich, Jean Marc Broto, Albert Fert, F Nguyen Van Dau, Frédéric Petroff, P Etienne, G Creuzet, A Friederich, and J Chazelas *Giant magnetoresistance of (001) Fe/(001) Cr magnetic superlattices*. in: *Physical review letters* ***61***,21 (1988), 2472 (cit. on p. v)

[13] Grünberg Binasch, Peter Grünberg, F Saurenbach, and W Zinn *Enhanced magnetoresistance in layered magnetic structures with antiferromagnetic interlayer exchange*. in: *Physical review B* ***39***,7 (1989), 4828 (cit. on p. v)

[14] Jagadeesh Subbaiah Moodera, Lisa R Kinder, Terrilyn M Wong, and R Meservey *Large magnetoresistance at room temperature in ferromagnetic thin film tunnel junctions*. in: *Physical review letters* ***74***,16 (1995), 3273 (cit. on p. v)

[15] Michel Julliere *Tunneling between ferromagnetic films*. in: *Physics letters A* ***54***,3 (1975), 225–226 (cit. on p. v)

[16] Gary A Prinz *Magnetoelectronics*. in: *Science* ***282***,5394 (1998), 1660–1663 (cit. on p. v)

[17] Jacek F Gieras *Permanent magnet motor technology: design and applications* CRC press, *2002* (cit. on p. vi)

[18] JMD Coey *Topical review: Permanent magnet applications*. in: *Journal of Magnetism and Magnetic Materials* ***248***,3 (2002), 441–456 (cit. on p. vi)

[19] Albert Fert *Nobel lecture: Origin, development, and future of spintronics*. in: *Reviews of Modern Physics* ***80***,4 (2008), 1517 (cit. on pp. vi, ix)

[20] Julio Camarero and Eugenio Coronado *Molecular vs. inorganic spintronics: the role of molecular materials and single molecules*. in: *Journal of Materials Chemistry* ***19***,12 (2009), 1678–1684 (cit. on p. vi)

[21] Anjan Soumyanarayanan, Nicolas Reyren, Albert Fert, and Christos Panagopoulos *Emergent phenomena induced by spin–orbit coupling at surfaces and interfaces*. in: *Nature* ***539***,7630 (2016), 509–517 (cit. on p. vi)

[22] Oliver Gutfleisch, Matthew A Willard, Ekkes Brück, Christina H Chen, SG Sankar, and J Ping Liu *Magnetic materials and devices for the 21st century: stronger, lighter, and more energy efficient*. in: *Advanced materials* ***23***,7 (2011), 821–842 (cit. on pp. vi, xiii)

[23] RW McCallum, Laura H Lewis, R Skomski, MJ Kramer, and IE Anderson *Practical aspects of modern and future permanent magnets*. in: *Annual Review of Materials Research* ***44***, (2014), 451–477 (cit. on pp. vi, ix)

[24] R Skomski *Permanent Magnets: History, Current Research, and Outlook*. in: *Novel Functional Magnetic Materials* Springer, 2016, 359–395 (cit. on p. vi)

[25] Satoshi Hirosawa, Masamichi Nishino, and Seiji Miyashita *Perspectives for high-performance permanent magnets: applications, coercivity, and new materials*. in: *Advances in Natural Sciences: Nanoscience and Nanotechnology* ***8***,1 (2017), 013002 (cit. on p. vi)

[26] Joachim Stöhr and Hans Christoph Siegmann *Magnetism: from fundamentals to nanoscale dynamics 152* Springer Science & Business Media, *2007* (cit. on p. ix)

[27] Giorgio Bertotti *Hysteresis in magnetism: for physicists, materials scientists, and engineers* Academic press, *1998* (cit. on p. ix)

[28] Edmund C Stoner and EP Wohlfarth *A mechanism of magnetic hysteresis in heterogeneous alloys*. in: *Philosophical Transactions of the Royal Society of London. Series A. Mathematical and Physical Sciences* (1948), 599–642 (cit. on pp. ix, x)

[29] EC Stoner and EP Wohlfarth *A mechanism of magnetic hysteresis in heterogeneous alloys*. in: *IEEE Transactions on Magnetics* ***27***,4 (1991), 3475–3518 (cit. on p. ix)

[30] Amikam Aharoni *Theoretical search for domain nucleation*. in: *Reviews of Modern Physics* ***34***,2 (1962), 227 (cit. on p. ix)

[31] Jan Vogel, Jérôme Moritz, and Olivier Fruchart *Nucleation of magnetisation reversal, from nanoparticles to bulk materials*. in: *Comptes Rendus Physique* **7**,9-10 (2006), 977–987 (cit. on p. ix)

[32] Erika Jimenez *Experimental study of angular-dependent magnetic properties of nanostructures: Influence of Magnetic Anisotropy* Thesis, UAM, *2011* (cit. on p. x)

[33] Bernard Dennis Cullity and Chad D Graham *Introduction to magnetic materials* John Wiley & Sons, *2011* (cit. on p. x)

[34] Jose Luis F. Cuñado *Dynamical effects in magnetic nanostructures: a detailed angular-dependent dynamic study of model systems with competing anisotropies, reorentation transitions, or reversal changes.* Thesis, UAM, *2017* (cit. on pp. x–xii)

[35] Wolfgang Wernsdorfer *Classical and quantum magnetization reversal studied in nanometer-sized particles and clusters*. in: *Advances in Chemical Physics* ***118***, (2001), 99–190 (cit. on p. x)

[36] M Jamet, W Wernsdorfer, C Thirion, D Mailly, V Dupuis, P Mélinon, and A Pérez *Magnetic anisotropy of a single cobalt nanocluster*. in: *Physical Review Letters* ***86***,20 (2001), 4676 (cit. on p. x)

[37] W Wernsdorfer, B Doudin, D Mailly, K Hasselbach, A Benoit, J Meier, J-Ph Ansermet, and BPRL Barbara *Nucleation of magnetization reversal in individual nanosized nickel wires*. in: *Physical Review Letters* **77**,9 (1996), 1873 (cit. on p. x)

[38] EH Frei, S Shtrikman, and D_ Treves *Critical size and nucleation field of ideal ferromagnetic particles*. in: *Physical Review* ***106***,3 (1957), 446 (cit. on p. x)

[39] William Fuller Brown *Micromagnetics* 18 Interscience Publishers, *1963* (cit. on p. xi)

[40] U Hartmann *Origin of Brown's coercive paradox in perfect ferromagnetic crystals*. in: *Physical Review B* ***36***,4 (1987), 2331 (cit. on p. xi)

[41] In: () (cit. on p. xiii)

[42] Karl J Strnat *Modern permanent magnets for applications in electro-technology*. in: *Proceedings of the IEEE* ***78***,6 (1990), 923–946 (cit. on p. xiv)

[43] R Skomski and JMD Coey *Magnetic anisotropy - How much is enough for a permanent magnet?* in: *Scripta Materialia* ***112***, (2016), 3–8 (cit. on p. xiv)

[44] Ralph Skomski and JMD Coey *Permanent magnetism* Institute of Physics Pub., *1999* (cit. on p. xiv)

[45] Antonio Hernando, Juan M Rojo, and M Rojo Juan *Física de los materiales magnéticos 2001* (cit. on p. xiv)

[46] Diana Bauer, David Diamond, Jennifer Li, David Sandalow, Paul Telleen, and Brent Wanner *US Department of Energy critical materials strategy*. in: (2010) (cit. on p. xvi)

[47] Marc Humphries *Rare earth elements: the global supply chain*. in: *Congressional Research Service* ***2011***, (2012), 7–5700 (cit. on p. xvi)

[48] S Constantinides *Market Outlook for Ferrite, Rare Earth and Other Permanent Magnets: 2015 to 2025*. in: *The magnetics 2016 meeting was held Jan* 2016, 21–22 (cit. on p. xvi)

[49] European Commission *Critical raw materials for the EU: Report of the Ad-hoc Working Group on defining critical raw materials* http://www.euromines.org/files/what-we-do/sustainable-development-issues/2010-report-critical-raw-materials-eu.pdf, *June 2010* (cit. on pp. xvi, xvii)

[50] European Commission *Nanocrystalline Permanent Magnets Based on Hybrid Metal-Ferrites* FP7-NMP Project ID: 310516, *2012-2016* (cit. on p. xvii)

Chapter 1

Experimental

Several advanced experimental techniques have been used along this thesis, aiming to prepare high quality (tailored) magnetic systems as well as to get a deeper understanding of their underlying physical properties. First, it is given a short introduction to the chemical synthesis (co-precipitaion) method used to prepare cobalt-ferrite powders and the physical deposition method (pulsed laser deposition) to growth epitaxial magnetite thin films. The basics, experimental and analysis procedures of the techniques employed for physical characterization is briefly described. For instance, microstructure analysis have been carried out by x-ray diffraction (XRD), to perform compositional and structural analysis, and scanning electron microscopy (SEM), to obtain the morphology information of powdered samples. Magnetic properties are determined by means of vectorial vibrating sample magnetometry (VSM) and magneto-optic Kerr effect (MOKE) for angular-dependent room temperature measurements, and SQUID (superconducting quantum interference device) measurements for temperature-dependent experiments.

During the last decades, the developing of advanced experimental techniques have led to a deeper understanding of condensed matter and magnetic materials. Experimental techniques and principles are applied in front end research in nanomagnetism. Both type of instrumentations, for preparing complex nanostructured-based systems, by chemical and physical means, as well as for disentangling their fundamental properties under controlled conditions have been used in this thesis. This combination has led to engineer/control the fundamental properties of RE-free magnetic systems, in order to enhance properly their magnetic performance to can be exploited in real applications.

In general, the instrumentations, capabilities, experimental procedures, and the basics of the different techniques used are introduced briefly. The preparation parameters and characterization of the different samples are described in the corresponding chapters, highlighting the critical aspects for reaching the desired purpose. Within the scope of this chapter, the different routes employed to prepare controlled magnetic nanostructures are described in the next section. The techniques used for the detailed microstructural analysis are given in the second section. Next, the different magnetometries employed are described. Finally, a brief introduction to the materials investigated is given in the last section on this chapter.

1.1 Synthesis and growth

1.1.1 $CoFe_2O_4$ synthesized by co-precipitation

Chemicals used are commercial products iron(III) chloride hexahydrate ($\geq$ 98%, Sigma-Aldrich), cobalt(II) chloride hexahydrate ($\geq$ 98%, Sigma-Aldrich) and ammonium hydroxide solution (25% in water, Sigma-Aldrich). All were used as received.

Starting Co-ferrite was synthesized by conventional co-precipitation method. A solution of $CoCl_2 \cdot 6H_2O$ (11.9 g, 0.05 mol) in distilled water (200 ml) was added to another solution of $FeCl_3 \cdot 6H_2O$ (27 g, 0.10 mol) in distilled water (200 ml) as well. The solution was heated to 77 °C under vigorous magnetic stirring. Then, 75 ml of NH_4OH (25% in water) were added and a black precipitate was formed immediately. The mixture was kept at 77 °C for 30 minutes under stirring and then allowed to cool down to room temperature. Once the powder was settled on the bottom of the recipient, the liquid phase was separated from the precipitate with the aid of a water pump, and the remaining black solid was washed three times with distilled water (3 x 500 mL) following the same procedure. Finally, the solid was redispersed in water (500 mL) and the particles were separated by centrifugation at 9000rpm during 5 minutes with water (2 x 250 mL) and acetone (1 x 250 mL). After this process, the sample was heated at 80 °C during 12 hours to allow the evaporation of the liquid phase, resulting in a brown powder.

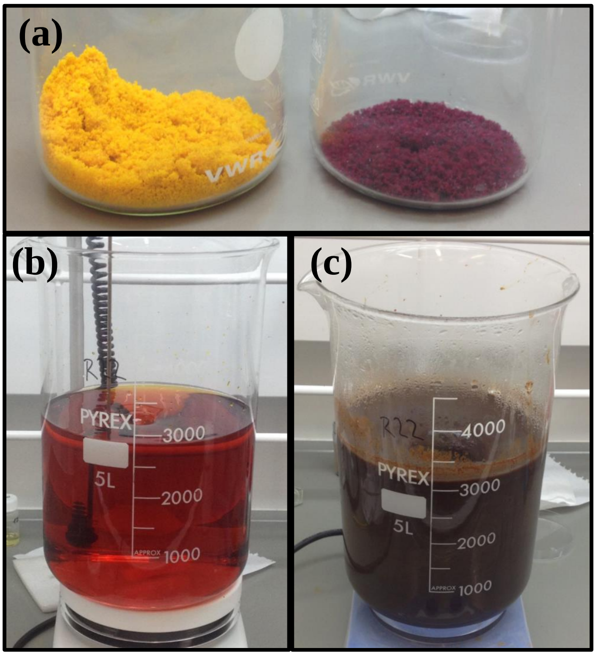

Figure 1.1: On the image (a) are shown precursors used to synthesize $CoFe_2O_4$ through the co-precipitation method; yellow powder is $FeCl_3 \cdot 6H_2O$ and $CoCl_2 \cdot 6H_2O$ is the purple one. It is shown the reaction (b) while both precursors are disolved in water and (c) after the co-precipitation is performed with the addition of NH_4OH

1.1.2 Pulsed Laser Deposition

Pulsed Laser Deposition (PLD) is a physical vapor deposition technique where a bottom-up approximation is employed to obtain thin films of many different materials, specially oxides. A high-power pulsed laser is focused onto a target, heating a determined region at temperatures that allows the evaporation of the target material. The expelled material in plasma phase forms the so-called "plume", in front of which the substrate where the thin film will be grown is placed.

The magnetite thin films studied in this work has been grown in Prof. Juan de la Figuera's laboratory at the Instituto que Química-Física Rocasolano.

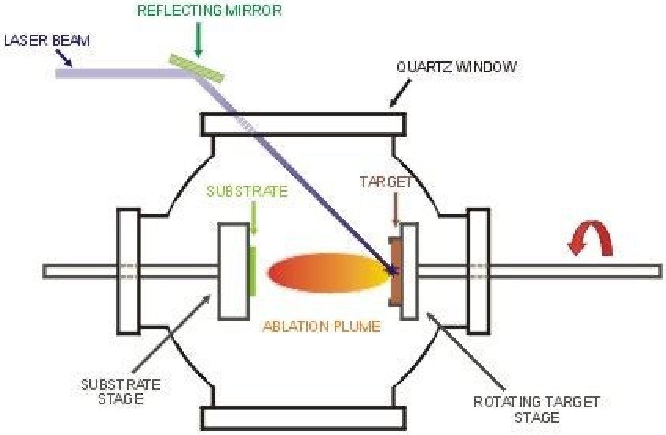

Figure 1.2: Schematic diagram of a PLD system. This image is courtesy of IQFR.

1.2 Microstructural characterization

1.2.1 X-Ray diffraction

X-Ray diffraction technique is probably the most extended experiment used to obtain compositional and structural information. It consist in the irradiation of a sample with an X-Ray beam that is then reflected into an X-Ray photodetector. In particular, θ-2θ scans stand out among other test. This type of experiments allows to perform a phase identification through the obtaining of a diffraction patterns showing peaks at determined 2-θ positions that are later analyzed using Bragg's law (Equation 1.1), by the contrast of the angle in which a particular material, with a determined crystalline lattice, produce coherent or incoherent scattering with the 2θ position of the measured peaks.

$$n\lambda = 2d\sin(\theta) \tag{1.1}$$

where;

θ: angle between the incident X-Ray and the diffraction plane, d: interplane (diffration plane) distance, λ: wavelength of the incident X-ray, n: an integer corresponding to the order of the diffraction plane.

Given a fixed wavelength (λ = 1.5409åfor CuK$_{\alpha 1}$ radiation) of the X-Ray source, the diffraction occur at a certain angle (θ) that corresponds to a concrete d spacing distance of the material. By indexing several sets of diffraction peaks in the XRD spectra, it is possible to perform a phase identification in terms of the unique sets of d-spacing for a particular material. In this work, the COD templates of every material analyzed with XRD is provided on its description. It is important to consider that in case of a multiphase material composed by two crystalline phases, one majority and the other minority, the second might not be registered if its amount is below the 5 per cent of the total amount of sample.

Another interesting information that can be extracted from XRD data once the constituent phase is known, is the calculations of average crystallite size, τ and lattice parameter, d, in order to extrapolate structural information of the crystal lattice. The Scherrer equation [1] relates the diffraction peaks broadening with the crystallite size as shown in Equation 1.2.

$$\tau = \frac{\kappa\lambda}{\beta\cos(\theta)} \tag{1.2}$$

where τ: mean size of the ordered (crystalline) domains, K: dimensionless shape factor. In this work this value is considered as 0.9, λ: X-ray wavelength, β: line broadening at half the maximum, intensity (FWHM) θ: Bragg angle (in degrees).

Multiple crystal lattice defects such as dislocations, stacking faults or grain boundaries, can cause peak broadening apart from crystallite size. Because of this, it is important to consider that Scherrer formula provides a lower bound on the particle size. All these defects of crystalline structure causes variations between some atoms distances, which are known as microstrains, ε, that cause a further broadening of the diffracted peak. The quantitative contribution of microstrains to line broadening is described with equation 1.3

$$\beta_\varepsilon = 4\varepsilon\tan(\theta) \tag{1.3}$$

where β_ε: line broadening due to strain and ε: strain value.

The Williamson-Hall method [2] relies on the principle that the approximate formula for size broadening, β_S, and strain broadening, β_ε, vary quite differently with respect to Braggg angle, θ. Attending to Scherrer equation, it is observed that one contribution varies as $\cos(\theta)$, while in case of strain broadening, that contribution is dependent of $\tan(\theta)$. If both contributions are present then their combined effect might be determined by convolution. The simplification of Williamson and Hall is to assume the convolution is either a simple sum or sum of squares. Using the former of these then we get:

$$\beta_{tot} = \beta_e + \beta_L = 4\varepsilon\tan(\theta) + \frac{\kappa\lambda}{L\cos(\theta)} \tag{1.4}$$

Multiplying Eq. 1.4 by $\cos(\theta)$, equation 1.4 results in a straight line with an intercept point related to the crystallite size and a slope directly related to the strain vale:

$$\beta_{tot}\cos(\theta) = \frac{\kappa\lambda}{L} + 4\varepsilon\sin(\theta) \tag{1.5}$$

These are the operations performed to calculate the mean average crystallite size and microstrain from XRD experiments of materials studied in this thesis. All XRD experiments shown in this thesis work have been performed on SIDI-UAM.

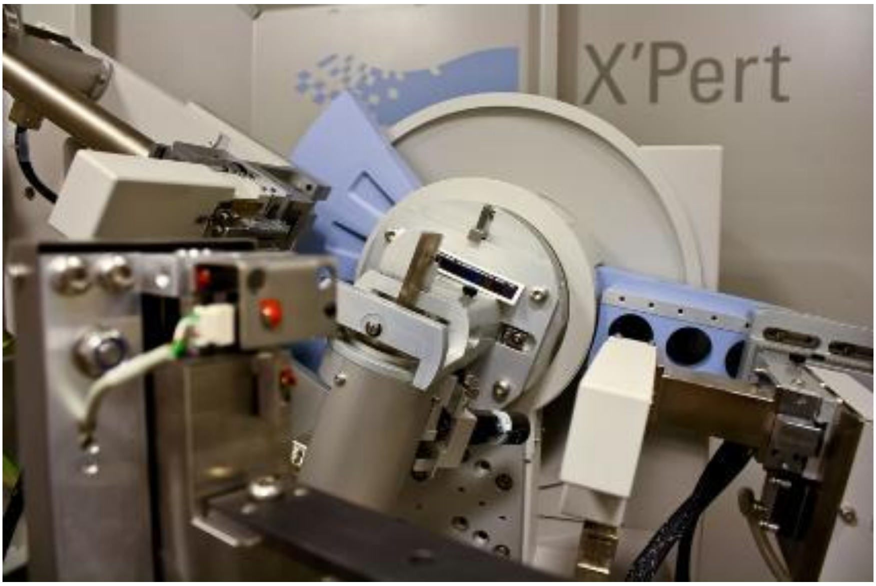

Figure 1.3: Picture of the device used on θ-2θ XRD experiments. This image is courtesy of Sidi-UAM

1.2.2 Scanning Electron Microscopy

Scanning electron microscopy (SEM) is a microscopy technique able to produce high resolution images of a surface by measuring electron-matter interactions. In particular, the interaction of an electron beam that is accelerated and focused into the sample of interest. The result of the interaction of the irradiated electron beam with the atoms at or near the surface of the sample under test are the signals obtained with SEM, including secondary electrons, back-scattered electrons (BSE), characteristic X-rays, photons, specimen current and transmitted electrons that later are extrapolated in images. By the detection of secondary electrons, SEM is able to form images of a sample surface. Moreover, it is possible to obtain information regarding the chemical elements distribution from backscattered electrons as well as X-ray.

Preparation of samples consist in the deposition of a quite small amount of material ($\geq$ 1 mg) onto a conductive carbon double side scotch attached to a metallic sample holder. This sample holder is introduced in the vacuum chamber of the microscope, where a typical pressure in a range of 3 - 5 mbar is generated. When working on SEM with magnetic materials, it is important that the samples have to be always demagnetized prior to SEM microscopy to avoid the interaction of the electron beam with the magnetic field of the sample. In addition, if the sample under test does not present a well electrical conductivity, a charge compensator might be used in order to avoid the sample to get electrically charged, .

Scanning electron microscopy data is presented in this work with the aim of obtaining morphological information of powdered, such as distribution of particle size and particles shape. All SEM images shown in this work has been measured using a Carl-Zeiss Auriga microscope operated by Dr. M.R. Osorio at IMDEA Nanoscience.

Figure 1.4: Image of the SEM microscope employed in this work. Image obtained from Carl-Zeiss webpage.

1.3 Magnetic characterization

1.3.1 Vectorial Vibrating Sample Magnetometer

Vibration Sample Magnetometry (VSM) is an extended technique employed to measure *M*-*H* curves of magnetic materials. It is an open-loop system comprising an electromagnet, able to generate a controlled, homogeneous and spatially localized magnetic field wherein a magnetic sample under test is placed. The sample is attached to a non-magnetic rod connected in turns to a rotatory vibrational head. Typically, two pairs of pick-up cols are on placed on the magnetic poles so that it is measured the magnetic moment of the sample in the direction of the applied field. In case of vectorial VSM, an additional set of pick-up coils are installed in the perpendicular direction, allowing to measure both components contained in the magnetic applied field plane. The methodology consist in vibrate the sample at a certain frequency (82 Hz typically) in such a way that the sample magnetic flux intensity variations will induce a proportional electric current into the pick-up coils. The signal measured on the pick-up coils must present the same frequency than the vibration, and for this purpose, a lock-in amplifier is used to filter the frequency of the signal of interest in addition to avoid electrical noise, as well as to amplify the faint of induced voltage in the pick-up coils. The lower limit of the measurable magnetic moment is in the order of 1 μemu.

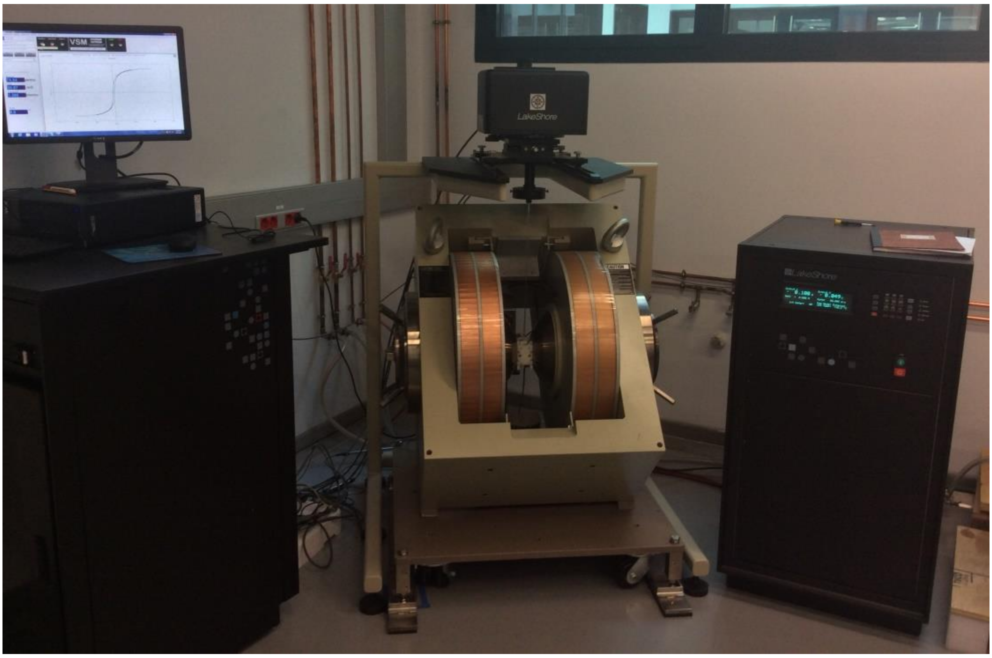

Figure 1.5: Image of the VSM system used in this work.

Before to start a measure, first it is needed to ensure the well-alignment of the sample with the aim of placing it right in the middle between the pick-up coils. The measurement process consists in the application of a fixed magnetic field while recording the magnetic moment of the sample, and this procedure is repeated changing the intensity of the applied field for every collected point. The system used in this work is a Lakeshore 7400 vibrating sample magnetometer, with the peculiarity that the sample is mounted in a rotatory vibration head, allowing to rotate the sample with respect to the magnetic applied field.

All VSM experiments presented in this work starts with the application of a magnetic field of 20 kOe, which is decreased down to -20 kOe, to later be increased again to 20 kOe. The parameters extracted from VSM recorded M-H curves includes magnetization at a maximum applied field of 20 kOe, M_{20kOe}, remanence magnetization, M_R, and coercivity, H_C. When working with powdered materials that might be applied as permanent magnets, $(BH)_{max}$ is evaluated to quantify the performance of the sample as permanent magnets and to assess the suitability of the methodology described in this work.

To measure the magnetization of powdered samples, approximately 20 mg of powder were placed in capsules from Quantum technology. These capsules are attached to a plastic straw which in turns is attached to the equipment rod connected to the vibrational head drive. Once the measure is performed, the obtained magnetic moment is divided by the mass of the sample to obtain the magnetization value. In case of thin films, the samples were carefully attached to the sample holder made out from quartz. Regarding angular measures, two different samples holders were use in dependence of the type of the performed measure; one sample holder is designed to allow the rotation of the sample with the field applied in-plane, and the second sample holder for in-plane/out-of-plane application of the applied field .

1.3.2 Anisotropy estimation by LAS

In real materials, the rotation of magnetization predominates in the high-field region. Therefore, assuming that all irreversible magnetization reversal processes were completed when the major hysteresis loop closed, that further increase of the magnetic moment is due to rotational processes which are connected with the magnetic anisotropy. Moreover, it is experimentally confirmed that ferromagnetic materials follow the law of approach to saturation [3], also known as LAS, which describes the dependence of magnetization $M(H)$ near the saturation magnetization M_S when the applied field $H >> H_C$.

For the LAS approximation it is also assumed that the first order anisotropy constant, K_1, is much larger than the higher order anisotropy constants, i.e. K_2, and thus this later can be neglected [4]. The equation for LAS approach used in this work is expressed as follows [5]:

$$M(H) = M_S \cdot \left(1 - \frac{0.07619{K_1}^2}{H^2 M_S^2} - \frac{0.0384{K_1}^3}{H^3 M_S^3}\right) \tag{1.6}$$

where $M(H)$ is the magnetization, M_S the saturation magnetization, H the applied magnetic field and K_1 the anisotropy constant.

1.3.3 Magneto Optical Kerr Effect (MOKE)

Magneto Optical Kerr Effect (MOKE) is a widely applied technique on thin films magnetic characterization due to its high sensitivity in addition to a relatively simple experimental implementation. This tecnique consist in the observation of the change of intensity and rotation of linearly polarized light after being reflected from a magnetized surface subjected to a variable magnetic field. The Magneto-Optical Kerr effect states that light reflected from a magnetic surface change its polarization as well as its intensity, meaning that if the initial polarization and intensity of the light is known, it is possible to calculate the magnetization state of the system reflecting the beam by the measurement of these changes. This effect is homologous to the Faraday effect where the changes on light occurs when the beam is transmitted through a magnetic material.

The instrumental devices required for a MOKE experiment is described in the following. First, a randomly polarized laser with a 330 nm wavelength is focused to the sample. Between the laser and the sample, there is a polarizer that allows the tuning of a particular light polarization, and then there is a lens to properly focus the spot in the area of the sample that will be studied. Next, the beam goes directly to the sample that is placed in the gap of an electromagnet with which an homogeneous AC magnetic field is applied. More details about the sample holder are given later. Light is reflected from the sample's surface to a diode photodetector, but before the light reach the sensors, the beam goes through a lens, again to allow to focus the light and Wollaston prism where the beam is split in two components; one is A and the other is B. This two components finally reach a sensor each, and three signals are obtained: the difference (A - B), the AC Sum (A+B) and the DC sum (A+B). The first correspond to the projection of the sample magnetization vector in the direction of the applied field, the second is the transversal component if the experiment is done with p-polarized light, and the last is the reflectivity.

Attending to the sample holder, a stepper motor is installed with a 6-DOF goniometer that allows the alignment of the sample, and where the sample holder is placed. The sample is located in the gap of an electromagnet that apply a magnetic field in a direction parallel to laser-sensors plane. The magnetic field is an AC sinusoid signal with a frequency of 3.14 Hz. In the system used in this work, the maximum accessible magnetic field was 250mT.

1.4 Materials used in this work

1.4.1 Magnetite

Magnetite (Fe_3O_4) is a mineral and one of the main iron ores. Magnetite is the most magnetic of all the naturally-occurring minerals on Earth [6]. Naturally-magnetized pieces of magnetite, called lodestone, will attract small pieces of iron, which is how ancient peoples first discovered the property of magnetism. Magnetite is ferrimagnetic, down to nanometer thickness, it has high Curie temperature (858 K), good electrical conductivity and presumed half-metal character [7, 8], which make it a promising candidate for room temperature spintronic devices and applications [9–11].

Magnetite takes an inverse spinel (cubic) crystalline structure at room temperature. which posses the general formula of AB_2O_4 where A and B are cation and O is an anion. Fe_3O_4 has a third of Fe atoms occupying the A-sites and the rest of Fe^{2+} and Fe^{3+} on B-sites (see Figure 1.6). It that changes its structure at a temperature around 125 K, the so called Verwey transition, (T_V) [12, 13], where it transforms from semi-metal to an insulator. At T_V the crystalline structure changes from cubic to monoclinic. An open question is to what extent the preparation of Fe_3O_4 films can affect their detailed magnetic properties, such as the magnetic anisotropy axis.

An important issue for technological applications is hence to control the magnetic behavior of artificially grown magnetite films. Overall, the magnetic properties can be influenced by the film stoichiometric and growth microstructure, including interfacial strain, crystal orientation and thickness. However, there are at present no general consensus regarding the detailed magnetic behavior of magnetite films obtained from different synthesis routes. The magnetization bulk easy-axis directions of Fe_3O_4 at room temperature (RT) are the cubic $\langle 111 \rangle$ ones. Thus, in the (001) surface of bulk samples, the magnetization is expected to lie along the in-plane

$\langle 110 \rangle$ directions, i.e., the projection of the bulk $\langle 111 \rangle$ on the (001) surface, i.e., the in-plane $\langle 111 \rangle$ directions, as confirmed recently by magnetic microscopy observations [14]. Overall, the magnetic properties can be influenced by the film growth microstructure, including interfacial strain, crystal orientation and thickness, as dicussed in Chapter 2.

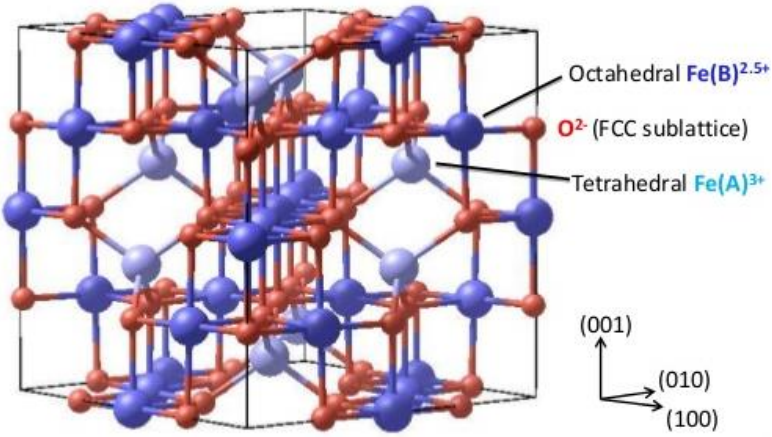

Figure 1.6: Unit cell structure of Fe_3O_4. Spinel structural group, iron(II,III) oxide, $Fe^{2+}Fe^{3+}{}_2O_4$. Lattice parameter a=0.8397 nm). Adapted from [15].

.

1.4.2 Cobalt ferrite

Among ferrites, $CoFe_2O_4$ is an interesting material because of its high magnetic anisotropy. Magnetocrystalline anisotropy constant, K_1, of cobalt ferrite increases with decreasing temperature, with $1.9 \cdot 10^6$ J/m^3 at room temperature [16]. Furthermore, the magnetic performance of cobalt ferrite can be enhanced by controlling the particle size distribution through chemical methods during synthesis [17]. For instance, at room temperature (RT), the superparamagnetic behavior is observed for nanoparticles (NP) sizes below 20nm [18] whereas the optimum single domain behavior where thermally driven demagnetization effects are avoided, i.e. maximum coercivity (H_c) of $CoFe_2O_4$, accounts for 40nm [19].

$CoFe_2O_4$ is classified within the group of spinels, which posses the general formula of AB_2O_4 where A and B are cation and O is an anion. Specific, $CoFe_2O_4$ belongs to the space group Fd3m (227) and it takes an inverse spinel ferrite, with Co^{2+} ions occupying octahedral sites (B sites) and the Fe^{3+} ions on both tetrahedral (A sites) and octahedral sites. The structure of a cobalt ferrite unit cell is depicted in Figure 1.7. Its lattice parameter a = b = c is 8.3919 A. Density of $CoFe_2O_4$ is 5.29 g/cm^3. The theoretical spontaneous magnetization of cobalt ferrite is 80 emu/g [20], and its Curie temperature, T_C = 520 °C.

.

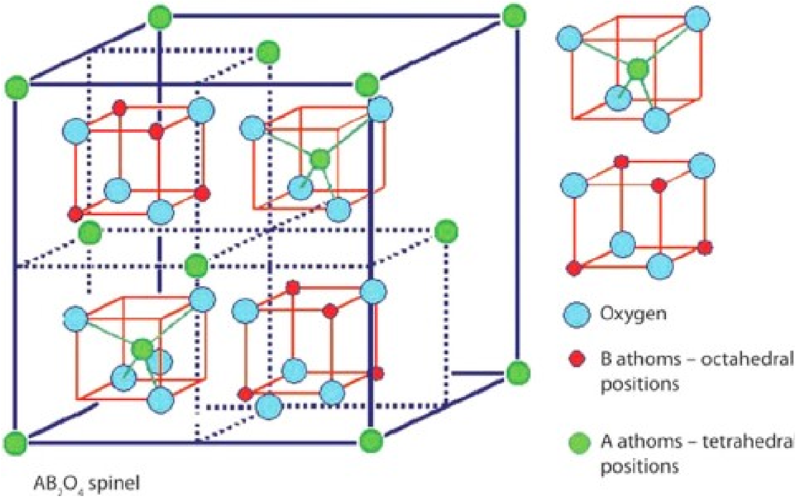

Figure 1.7: Unit cell structure of $CoFe_2O_4$. This image was taken from ref [**Houshiar14**].

References

[1] AL Patterson *The Scherrer formula for X-ray particle size determination*. in: *Physical review* ***56***,10 (1939), 978 (cit. on p. 4)

[2] GK Williamson and WH Hall *X-ray line broadening from filed aluminium and wolfram*. in: *Acta metallurgica* ***1***,1 (1953), 22–31 (cit. on p. 4)

[3] Hui Zhang, Dechang Zeng, and Zhongwu Liu *The law of approach to saturation in ferromagnets originating from the magnetocrystalline anisotropy*. in: *Journal of Magnetism and Magnetic Materials* ***322***,16 (2010), 2375–2380 (cit. on p. 8)

[4] R Grössinger *A critical examination of the law of approach to saturation. I. Fit procedure*. in: *physica status solidi (a)* ***66***,2 (1981), 665–674 (cit. on p. 8)

[5] Bing Hai Liu, J Ding, ZL Dong, CB Boothroyd, JH Yin, and JB Yi *Microstructural evolution and its influence on the magnetic properties of $CoFe_2O_4$ powders during mechanical milling*. in: *Physical Review B* ***74***,18 (2006), 184427 (cit. on p. 8)

[6] John MD Coey *Magnetism and magnetic materials* Cambridge University Press, *2010* (cit. on p. 9)

[7] Allan A Mills *The lodestone: History, physics, and formation*. in: *Annals of science* ***61***,3 (2004), 273–319 (cit. on p. 9)

[8] Mikhail Fonin, Yu S Dedkov, Rossitza Pentcheva, Ulrich Rüdiger, and Gernot Güntherodt *Magnetite: a search for the half-metallic state*. in: *Journal of Physics: Condensed Matter* ***19***,31 (2007), 315217 (cit. on p. 9)

[9] PJ Van der Zaag, PJH Bloemen, JM Gaines, RM Wolf, PAA Van Der Heijden, RJM Van de Veerdonk, and WJM De Jonge *On the construction of an Fe 3 O 4-based all-oxide spin valve*. in: *Journal of magnetism and magnetic materials* ***211***,1 (2000), 301–308 (cit. on p. 9)

[10] Michael Ziese *Extrinsic magnetotransport phenomena in ferromagnetic oxides*. in: *Reports on Progress in Physics* ***65***,2 (2002), 143 (cit. on p. 9)

[11] E Wada, K Watanabe, Y Shirahata, M Itoh, M Yamaguchi, and T Taniyama *Efficient spin injection into GaAs quantum well across Fe 3 O 4 spin filter*. in: *Applied Physics Letters* ***96***,10 (2010), 102510 (cit. on p. 9)

[12] Friedrich Walz *The Verwey transition-a topical review*. in: *Journal of Physics: Condensed Matter* ***14***,12 (2002), R285 (cit. on p. 9)

[13] Joaquín García and Gloria Subías *The Verwey transition - a new perspective*. in: *Journal of Physics: Condensed Matter* ***16***,7 (2004), R145 (cit. on p. 9)

[14] Matteo Monti, Mikel Sanz, Mohamed Oujja, Esther Rebollar, Marta Castillejo, **Pedrosa, Francisco J**, Alberto Bollero, Julio Camarero, Jose Luis F Cunado, Norbert M Nemes, et al. *Room temperature in-plane< 100> magnetic easy axis for Fe3O4/SrTiO3 (001): Nb grown by infrared pulsed laser deposition*. in: *Journal of Applied Physics* ***114***,22 (2013), 223902 (cit. on p. 10)

[15] John W Anthony, Richard A Bideaux, Kenneth W Bladh, and Monte C Nichols *Handbook of mineralogy, mineralogical society of America, Chantilly, VA 20151-1110, USA 2011* (cit. on p. 10)

[16] Henry Shenker *Magnetic anisotropy of cobalt ferrite (Co 1.01 Fe 2.00 O 3.62) and nickel cobalt ferrite (Ni 0.72 Fe 0.20 Co 0.08 Fe 2 O 4)*. in: *Physical Review* ***107***,5 (1957), 1246 (cit. on p. 10)

[17] Alberto López-Ortega, Elisabetta Lottini, Cesar de Julian Fernandez, and Claudio Sangregorio *Exploring the magnetic properties of cobalt-ferrite nanoparticles for the development of a rare-earth-free permanent magnet*. in: *Chemistry of Materials* ***27***,11 (2015), 4048–4056 (cit. on p. 10)

[18] M Rajendran, RC Pullar, AK Bhattacharya, D Das, SN Chintalapudi, and CK Majumdar *Magnetic properties of nanocrystalline* $CoFe_2O_4$ *powders prepared at room temperature: variation with crystallite size*. in: *Journal of Magnetism and Magnetic Materials* ***232***,1 (2001), 71–83 (cit. on p. 10)

[19] CN Chinnasamy, B Jeyadevan, K Shinoda, K Tohji, DJ Djayaprawira, M Takahashi, R Justin Joseyphus, and A Narayanasamy *Unusually high coercivity and critical single-domain size of nearly monodispersed* $CoFe_2O_4$ *nanoparticles*. in: *Applied physics letters* ***83***,14 (2003), 2862–2864 (cit. on p. 10)

[20] J Ding, PG McCormick, and R Street *Magnetic properties of mechanically alloyed* $CoFe_2O_4$. in: *Solid state communications* ***95***,1 (1995), 31–33 (cit. on p. 10)

Part I

Magnetization reversal studies on model systems; epitaxial thin films and nanowires

Introduction

The effect of the magnetic anisotropy symmetry in model nanostructures is investigated by angular-dependent magnetometry measurements. In particular Fe_3O_4(001) thin films and FeCo nanowires with well-defined four-fold and two-fold magnetic symmetry, respectively. In magnetite films this originates from the choice of crystal symmetry of the substrate used (substrate-induced), whereas the large aspect ratio promotes the two-fold symmetry in the magnetic nanowires (shape-induced). The experimental data reveal that the magnetic properties, including coercivity, remanence, and magnetization reversal processes, are strongly influenced by the magnetic symmetry. This understanding opens additional avenues to tailor the magnetic properties of future nanostructures.

No matter what application one is interested in, a key property of a magnetic system is the preferred direction of its magnetization. Magnetic symmetry is a key parameter in the design of all magnetic materials. In permanent magnets, this direction should be fixed rigidly to ensure proper functioning of the magnet.

In the next two chapters, detailed angle-dependent magnetic investigations on model nanostructures with well-defined magnetic symmetry are presented (see Fig. 1.8). The studies have been performed by using vectorial-resolved magnetometry techniques (v-MOKE and v-VSM), described in Chapter 1. The study reveals that although the magnetic symmetry is found in different magnetic parameters, i.e., remanence and coercivity, the detailed angular analysis shows complex mechanisms to be responsible for the reversal process, following micromagnetic modes distinct from those pure classically established.

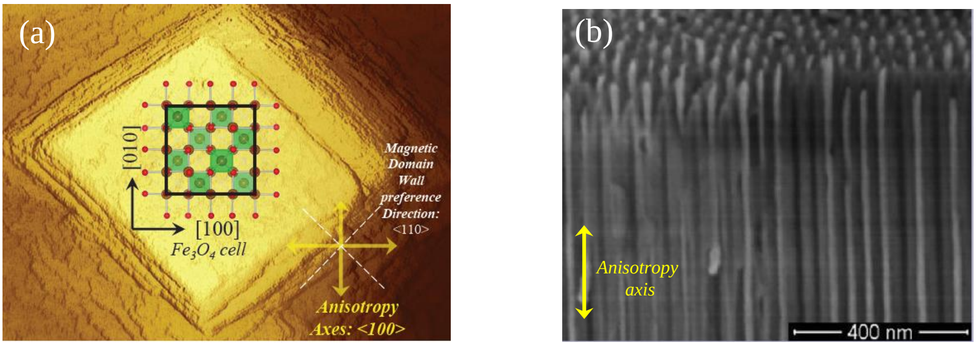

Figure 1.8: Model systems investigated in Part I, with well-defined (substrate-induced) four-fold (a) and (shape-induced) two-fold (b) magnetic symmetry, indicated with yellow arrows. (a) STM image of a Fe_3O_4(001) grown on $SrTiO_3$(001). (250×200 nm^2). The unit cell of magnetite is set. Notice that the magnetic symmetry is aligned along in-plane $< 100 >$ film directions. Adpated from [0]. (b) SEM image of an array of Co-base nanowires [0]

Chapter 2

Epitaxial Fe$_3$O$_4$ thin films

High quality stoichiometric magnetite (Fe$_3$O$_4$) films grown by infrared pulsed laser deposition (IR-PLD) on different surfaces have been investigated in order to study the influence of the substrate, orientation, and thickness on their magnetic behavior. Different single crystal (001)-oriented substrates, i.e., SrTiO$_3$(100), MgAl$_2$O$_4$(100)and MgO(100), have been used for the preparation of epitaxial Fe$_3$O$_4$(001) films. By comparison, polycrystalline magnetite films were obtained on both single crystal Al$_2$O$_3$(0001) and amorphous Si/SiO$_2$ substrates. The thickness has been varied between 50 - 350 nm. All films consist of nanocrystalline stochiometric magnetite with very small strain ($< 1\%$) and present the Verwey transition (T_V) between 110-120 K, i.e., close to bulk magnetite (125 K). In general, T_V depends on both microstructure and thickness, increasing mainly as the thickness increases. Room temperature angular-dependent measurements reveal an in-plane fourfold symmetry magnetic behavior for all films grown on (001)-oriented surfaces, and with the easy axes lying along the Fe$_3$O$_4$[010] and [100] directions. Remarkably, the fourfold magnetic symmetry is shown up above 400 nm thick films. In turn, the films grown on single crystal Al$_2$O$_3$(0001) and on amorphous Si/SiO$_2$ surfaces display an isotropic magnetic behavior. In general, the coercive field (H_C) depends on microstructure and film thickness. The largest (lowest) H_C value has been found for the thinner film grown on a single crystal SrTiO$_3$(001) (amorphous Si/SiO$_2$) surface, which present the largest (lowest) strain (crystallinity). Moreover, the coercivity follows an inverse law with film thickness. Our results demonstrate that we can artificially control the magnetic behavior of stoichiometric IR-PLD grown Fe$_3$O$_4$ films by exploiting substrate-induced anisotropy and thickness-controlled coercivity, that might be relevant to incorporate magnetite in future spintronic devices.

2.1 Introduction

Magnetite (Fe$_3$O$_4$) is attracting much interest in the last years due to its robust ferrimagnetism down to nanometer thickness, high Curie temperature (858 K), good electrical conductivity and presumed half-metal character [1, 2], which make it a promising candidate for room temperature spintronic devices and applications [3–5]. Fe$_3$O$_4$ takes an inverse spinel crystalline structure at room temperature, with a third of Fe atoms occupying the A-sites and the rest of Fe^{2+} and Fe^{3+} on B-sites. It presents a low-temperature metal-insulator transition below 120K known as the Verwey transition (T$_V$) [6, 7], where the crystalline structure changes from cubic to monoclinic. An open question is to what extent the preparation of Fe$_3$O$_4$ films can affect their detailed magnetic properties, such as the magnetic anisotropy axis. This information is required to efficiently use Fe_3O_4 films in spintronic applications.

An important issue for application in new devices is to control the magnetic behavior of artificially grown magnetite films. Overall, the magnetic properties can be influenced by the film stoichiometric and growth microstructure, including interfacial strain, crystal orientation and thickness. However, there are at present no general consensus regarding the detailed magnetic behavior of magnetite films obtained from different synthesis routes such as molecular beam epitaxy (MBE) [8–12], sputtering [13–16] and pulsed laser deposition (PLD) [17–21], and also related to different substrates such as MgO, Al2O3, MgAl2O4, BaTiO3 and SrTiO3 [7, 9–15], despite some results indicates that the magnetism and magneto-transport phenomena in this kind of film are controlled by the domain boundaries and the anti-ferromagnetic couple strength in the boundary [9].

The magnetization bulk easy-axis directions of Fe_3O_4 at room temeperature (RT) are the cubic $\langle 111 \rangle$ ones. Thus, in the (001) surface of bulk samples, the magnetization is expected to lie along the in-plane $\langle 110 \rangle$ directions, i.e., the projection of the bulk $\langle 111 \rangle$ on the (001) surface, i.e., the in-plane $\langle 11 \rangle$ directions, as confirmed recently by magnetic microscopy observations [20]

Overall, the magnetic properties can be influenced by the film growth microstructure, including interfacial strain, crystal orientation and thickness.

The structure these films depends strongly from the synthesis method and growth conditions, as well as from the substrate and thickness. In this way, the magnetic and transport properties are strongly influenced by the synthesis method and growth conditions.

From the above discussion it is clear that precise control over the microstructure and phase purity is necessary firstly to control the magnetic behavior and secondly to disentangle the underlying transport mechanisms.

The domain size or the APB density seems to be dependent of the thickness [16] and of the misfit with the structure of the substrate [14].

In this study high quality stoichiometric Fe_3O_4 thin films have been grown by ablation from a sintered hematite target using a nanosecond infrared (IR) laser at 1064 nm [22]. It has been previously reported the observation on Fe_3O_4 film grown on $SrTiO_3$:Nb of individual domains with magnetization that lies mostly along the in-plane directions $<100>$, while the domain walls are aligned with the $<110>$ directions. [23], i.e., the easy-axis orientation differs from bulk magnetite and films prepared by other techniques. Furthermore, and despite of magnetite being a material extensively studied in the shape of bulk and films, a rigorous study of the angular evolution of the magnetic properties for magnetite films grown by PLD on different substrates is still due.

In this work we extend previous knowledge on the magnetic properties of pure magnetite films that can be achieved under different experimental conditions, namely substrate, orientation, and thickness. The morphology, microstructure, stoichiometry, Verwey transition, and angular-dependent magnetic behavior of all films prepared have been correlated in order to identify the key parameters controlling the magnetic properties of high quality nanostructured magnetite films grown by IR-PLD. The paper is organized as follows. The growth and experimental details are described in Section I. The influence of the substrate is discussed in Sect. II, showing that all (100)-oriented substrates used induce fourfold magnetic symmetry. Section III shows that this magnetic symmetry is preserved for thicknesses as large as 450 nm, and that the coercivity follows an inverse law with the film thickness. The summary is presented in Sec.

VI, concluding that the magnetic properties of high quality magnetite films can be tailored by using specific substrates and thicknesses.

2.2 Experimental

We employed the best growth conditions, i.e., infrared pulsed laser deposition (IR-PLD) and deposition at 780K, for the fabrication of pure nanostructured magnetite thin films [22]. High quality stoichiometric Fe_3O_4 thin films have been grown by ablation from a sintered hematite target using a nanosecond infrared (IR) laser at 1064 nm. The Q-switched Nd:YAG laser had a full width at half-maximum of 15 ns with a 10 Hz repetition rate at a typical fluence of 4 J/cm2. The substrates were heated to 780K during deposition. We have previously reported that Fe_3O_4 films grown by IR-PLD show less particulates on the films, compared to the extensively used UV wavelengths [24].

Magnetite films of different thickness, ranging from 30 to 450 nm, have been prepared on different single-crystal surfaces, i.e., MgO(001), $SrTiO_3$(001), $MnAl_2O_3$(001) and Al_2O_3(0001), and on an amorphous surface, i.e., silicon with a native SiO_2 layer.

MgO and Fe3O4 has a small lattice mismatch between them of 0.3

The substrate temperature were kept at 780K during deposition to enhance the quality of the resulting magnetite films [22].

The (001)-oriented cubic substrates have different mismatch

Different substrates have been used in order to study both the substrate-induced crystal structure and

The morphology, microstructure, and stoichiometry of the films were characterized by atomic force microscopy (AFM), X-ray diffraction (XRD) and Mössbauer spectroscopy, respectively. Magnetic characterization was carried out by superconducting quantum interference device magnetometry (SQUID) and vectorial magneto-optical Kerr effect (v-MOKE).

Magnetite thin films were grown by PLD technique in a system consisting on a stainless-steel vacuum deposition chamber at a base pressure of 2 x 10^{-4} Pa by a turbo-molecular pump. The self-made hematite targets were prepared from a >99% iron (III) oxide powder (Sigma Aldrich, particle size $<$ 5 um) that was pelletized into disks of 10 mm diameter and about 2 mm thickness using a hydrostatic press at 8 ton cm^{-2}, followed by sintering at 1173 K in air for 8 h. The target was placed on a rotating sample holder and ablated with a Q-switched Nd-YAG laser (FWHM 15 ns, 10 Hz), focused at 45° to target's normal vector with a spot area of 0.14 mm^2, at the excitation wavelengths of 1064 nm using at a fluence of 4 J cm^{-2}. Deposits were grown by delivering 144000 pulses to the target. The substrates were ultrasonically degreased in acetone and methanol for 10 minutes before being placed in front of the target at a distance of 40 mm.

Layer thicknesses were determined ex situ either by X-ray fluorescence with and/or by X-ray reflectometry.

Magnetic characterization was performed by SQUID magnetometry (Quantum Design MPMS5S) or by angular dependent magneto-optical Kerr effect (MOKE) studies. The former has been used to ide

The angular dependence MOKE study allows to identify the magnetic symmetry and the magnetization reversal processes of the films as well as to extract relevant magnetic parameters, i.e., coercivity and remanence. The measurements have been performed at room temperature every...

The latter has the advantage of allowing a local measurement of the hysteresis curve of a sample,

In order to study the magnetic behavior of magnetite when it is grown on different substrate conditions, substrates with cubic structure has been choose in terms of their lattice compatibility with Fe_3O_4 (lattice parameter of 8.395), where $SrTiO_3$:Nb and $MgAl_2O_4$ present lattices parameters of 3.905 and 8.03 respectively. This directly influence the magnetic behaviour of magnetite since stress (i.e. compressive strain) and relaxation (i.e. tensile strain) of Fe_3O_4 plays an important role on magnetic anisotropy as it will be shown later. Substrates of Si(100)/SiO_2 - which can be considered amorphous - and Al_2O_3(0001) with hexagonal crystalline structure are used as cases of non-cubic substrates.

The angular dependence of Fe_3O_4 films magnetization was measured at room temperature (RT) by high-resolution vectorial-Kerr magneto-optical measurements in a longitudinal configuration [25, 26]. MOKE hysteresis loops were recorded by changing the in-plane angular rotation of the sample (α_H) and keeping fixed the external magnetic field direction, which is applied parallel to the film plane. The angular rotation, ranging from 0 - 360°, was probed at intervals of 4.5°, applying a maximum magnetic field of 250 mT. In addition to MOKE, Superconducting Quantum Interference Device (SQUID) magnetometry is employed to measure the evolution of magnetization with temperature, used to determine the Verwey transition of magnetite thin films.

Structural characterization is performed.....

2.3 Results and Discussion

2.3.1 Comparison of Fe_3O_4 layers grown on different substrates

Figure 1 depicts XRD spectra recorded for Fe_3O_4 deposits grown on non-cubic substrates, amorphous SiO_2 and Al_2O_3(0001) (Figures 1.a and b respectively), and on cubic substrates, $SrTiO_3$:Nb(100) and $MgAl_2O_4$(100) (Figures 1.c and d respectively). Fe_3O_4 films deposited on SiO_2 and Al_2O_3 are polycrystalline, displaying peaks located at 2-Theta positions 30.2°, 35.5°, 43.3°, 53.6°, 57.2° and 62.7°, which are assigned to Fe_3O_4 reflections (220), (311), (400), (422), (511) and (440) planes respectively. An additional peak at 44.67° is observed due to the presence of metallic iron on film grown on Al_2O_3 substrate. When the substrates are that ones with cubic structures ($SrTiO_3$:Nb and $MgAl_2O_4$), magnetite presented a preferential orientation related to the target crystalline structure, as can be observed by the predominance of (400) reflection peaks (Figures 1.c and d). In this case, the films exhibit a small contribution of Westite ($Fe_{0.8}O_{0.2}$) that can be observed at 2-Theta angle 41.8°. Furthermore, by comparing the intensity of reflection peaks obtained for both type of substrates it can be rapidly noticed the high crystallinity of Fe_3O_4 films obtained when a cubic substrate was employed. We assume that the crystallographic structure of the substrate is the reason why, using a systematic method of growth, in some cases Fe_3O_4 layers are monocrystalline and in other case polycrystalline.

Crystallite average sizes have been calculated for all samples using Scherrer formula ($d = n\times\lambda/2\times\sin(2\Theta)$) calculating size values of 28.35, 23.31, 31.14 and 50.4 nm for Fe_3O_4 layers grown on $SrTiO_3$:Nb, $MgAl_2O_4$, Al_2O_3 and SiO_2 substrates respectively. XRD spectra has been used as well to calculate the c-axis parameter based on Bragg's law, obtaining values of 8.357, 8.361, 8.364 and 8.333 for SiO_2, Al_2O_3, $MgAl_2O_4$ and $SrTiO_3$:Nb substrates respectively. These values are quite close to bulk ones, and in all cases there is a small strain with positive sign ($< 1\%$), indicative of compressive strain.

We investigated the Verwey transition using measurements of the magnetization as a function of temperature.

Magnetite presents a phase transition at 120K (for bulk material) known as "Verwey transition" (T_v). Below this temperature, the crystalline structure changes from cubic to monoclinic, and conductivity is decreased two orders of magnitude, which is related as well to a decrease in magnetization. This transition is defined as the point with maximum rate of change in magnetization against temperature. Warming curves measured for non-cubic and cubic substrates are plot on Figures 2.a and 2.b respectively. To ease the identification of this point, derivatives of magnetization against temperature are plot for both cases in Figures 2.c and 2.d. Verwey transition temperatures of 115.4 and 116.0 K were measured on layers grown on SiO_2 and Al_2O_3 respectively, while for $SrTiO_3$:Nb and $MgAl_2O_4$ these transition are found at 110.6 and 111.6 K respectively. The difference of temperatures for Verwey transition is related to strain induced by the substrate during first stages of growth, as well as to crystalline average size. [27]. On the other hand, those obtained polycrystalline layers of magnetite have similar Verwey transition temperatures, very close to the value obtained for bulk magnetite (120 K). By comparing Fe_3O_4 layer grown on Al2O4 (polycrystalline) and the one grown on $MgAl_2O_4$ (monocrystalline), both with similar thickness (115 and 100 nm respectively) and similar crystallite sizes (31.14 and 27.31 nm respectively), a difference on T_v of 5.4K lower for $MgAl_2O_4$ can be observed, which might related with the strain induced on the first layers due to the lattice

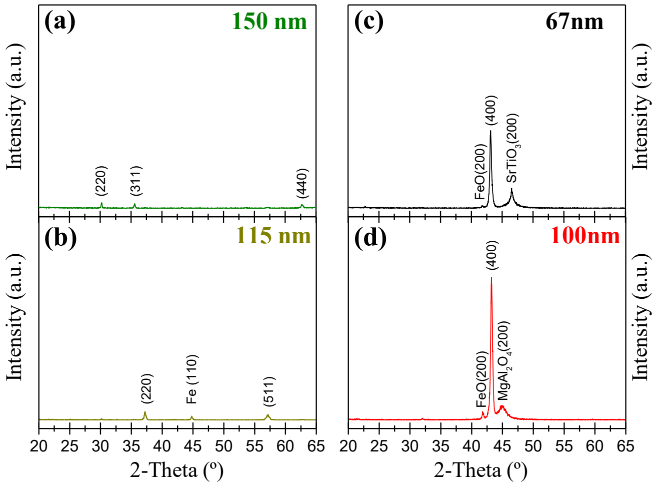

Figure 2.1: XRD spectras of Fe_3O_4 thin films deposited on (a) Si with a native SiO_2 layer, (b) Al_2O_3, (c) $SrTiO_3$:Nb and (d) $MgAl_2O_4$.

mismatch between the substrate and Fe_3O_4.

In-plane hysteresis loop measured at RT for Fe_3O_4 films deposited on different substrates are shown on Figure 3. Two loops are plot for each sample, one with an applied magnetic field in the substrate <100> direction (α_H = 0°), and a second one measured in the substrate in-plane <110> direction (α_H = 45°). First observation is that for samples grown on SiO_2 and Al_2O_3 substrates, both hysteresis loops are identical, indicating an isotropic magnetic behavior, while for $SrTiO_3$:Nb and $MgAl_2O_4$ substrates (Figures 3.c and d) this two hysteresis loops exhibit different coercivity (Hc) values; one corresponding to the easy axis (field applied at α_H = 0°) and a second one to the hard axis (field applied at α_H = 45°). This is confirmed through the angular analysis of coercivity (H_c) and M_R/M_S ratio (Figure 4), where the four-fold simmetry of both parameters indicate a well defined biaxial anisotropy present on monocrystalline layers. The easy axes are observed at 0°, 90°, 180° and 270° (directions <100> and <010> of the substrate). The squareness of easy axis hysteresis loops of films grown on $SrTiO_3$:Nb and $MgAl_2O_4$, both $M_R/M_S > 0.9$, are indicative of a high quality epitaxial growth with a well defined texture. On the other hand, the angular evolution observed for SiO_2 and Al_2O_3 samples confirms its magnetic isotropic nature, with lower H_c and M_R/M_S than that measured in monocrystalline layers.

2.3.2 Comparison of Fe_3O_4 layers with different thicknesses

Figure 5. displays spectra of different thickness Fe_3O_4 deposits grown on $SrTiO_3$:Nb and $MgAl_2O_4$. At a first glance, the increase of Fe_3O_4 (400) reflection peak intensity is related with the increased thickness of magnetite. In both cases, peaks corresponding to substrate are observed; $SrTiO_3$:Nb (Figs. 5.a and b) and $MgAl_2O_4$ (Figs 5.c and d). Note than even with sizes of 330 and 350 nm, Fe_3O_4 still being a monocrystalline layer, indicating the suitability

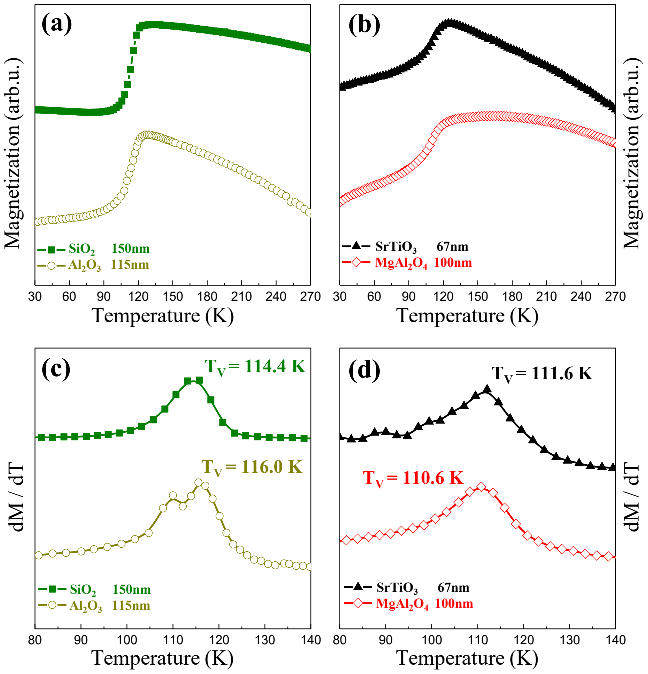

Figure 2.2: Warming curves measured with an in-plane applied field of 2 kOe of Fe_3O_4 thin films deposited on (a) Si/SiO_2 (full squares, green) and Al_2O_3 (open circles, dark yellow); (b) $SrTiO_3$:Nb (full triangles, black) and $MgAl_2O_4$ (open diamonds, red). The derivative of magnetization against temperature variation indicates Verwey transition temperature; (c) Si/SiO_2 (full squres, green) and Al_2O_3 (open circles, dark yellow); (d) $SrTiO_3$:Nb (full triangles, black) and $MgAl_2O_4$ (open diamonds, red).

of PLD technique employed to obtain high crystalline thick layers of magnetite. Lattice parameter of Fe_3O_4 is 8.395 , and $SrTiO_3$:Nb and $MgAl_2O_4$ posses a lattice parameter of 3.905 and 8.030 respectively. This mean that in case of an epitaxial growth, the misfit of the first layers between Fe_3O_4 and the substrate is 6.3% and 3.8% for $SrTiO_3$:Nb and $MgAl_2O_4$ respectively. However, this samples are well above the thickness where pseudomorphic growth occurs [28]. The calculated strain of these magnetite films are 0.8% and 0.37% for thinnest layers grown on $SrTiO_3$:Nb (67 nm) and $MgAl_2O_4$ (100 nm) substrates respectively, and this strain is maintained on thickest films (330 and 350 nm). Crystalline size calculated using the Scherrer equation generates values of 28.35 and 69.96 nm on $SrTiO_3$:Nb films with thickness of 67 and 330 nm respectively, and 27.31 and 49.78 nm when the films grown on $MgAl_2O_4$ are 100 and 350 nm thick.

Warming curves of different thickness Fe_3O_4 layers plotted on Figures 6.a and 6.b with its respective calculated Verwey temperature in Figures 6.c and 6.d . As it was previously mentioned, there is a shift on Verwey transition to lower temperatures as the thickness decreases due to a reduced crystallite size. It can bee seen on Figure 6.d that T_v of Fe_3O_4 grown on $MgAl_2O_4$, with a crystallite size 69.9 nm is very close to that of bulk magnetite. However, the

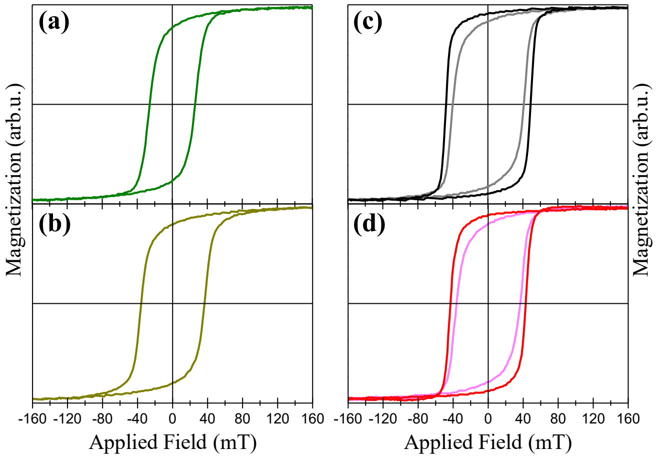

Figure 2.3: In-plane hysteresis loops of Fe_3O_4 thin films deposited on (a) Si with a native SiO_2 layer, (b) Al_2O_3, (c) $SrTiO_3$:Nb and (d) $MgAl_2O_4$. Graphs (c) and (d) contains easy and hard axis hysteresis loops.

deposits with comparable thickness grown on $SrTiO_3$:Nb (330nm), but with a smaller crystallite size is 115.8 K. Growth defect of magnetite are known as antiphase boundaries (APB's), and it appears due to the lattice missmatch between Fe_3O_4 and the substrate. It is well known that exchange interaction of these APB's is antiferromagnetic [29]. As Figures 5.a and 5.b reveals, increased thickness of Fe_3O_4 films causes a more sharp decrease on magnetization which might be the result of a better crystalline structure achieved on thickest samples, since the duration of fabrication (where the sample is being heated) request longer time, providing finally a lower density of antiphase boundaries.

Hysteresis loops comparing Fe_3O_4 films grown on the same substrates but with different thickness are plot on Figure 7. All cases shows single loop behaviour. The lattice mismatch between Fe_3O_4 and the substrate ease the appearance of APB's, which may act as pinning centers increasing coercivity. This can be the reason why Fe_3O_4 layers grown on $SrTiO_3$:Nb present higher coercivity than those ones deposited on $MgAl_2O_4$. In both system it is observed the thinnest magnetite layer, the highest coercivity measured. This effect might be related again to a lower density of APB's in thicker samples than in the thinnest ones, since the longer time this samples were heated during the growing process is known to be beneficial to the extinction of this type of defects due to the fact that heating allows the recrystallization and reconstruction of Fe_3O_4 films, resulting in a diminished density of APB's. Differences on Hc due to different film thickness can be clearly observed on Figure 8. Unlike other studies, where a lower Hc is found for Fe_3O_4 layers with lower lattice parameter than bulk, we obtained the opposite results, with coercivities up to 50 mT in the case of magnetite film grown on $SrTiO_3$:Nb. [30] Thinnest samples shows a close to unity M_R/M_S, and this values decreases as the thickness is increased.

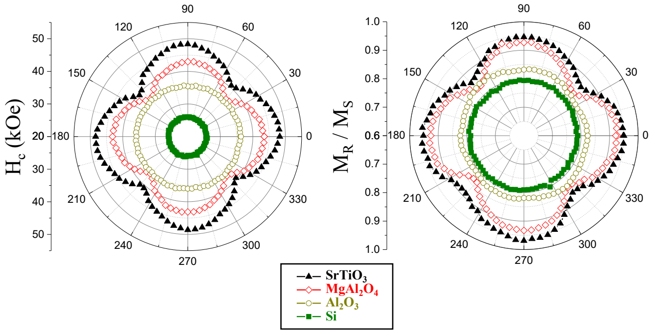

Figure 2.4: Angular evolution of in-plane H_C and M_R/M_S of Fe$_3$O$_4$ thin films deposited on SrTiO$_3$:Nb (full triangles, black), MgAl$_2$O$_4$ (open diamonds, red), Al$_2$O$_3$ (open circles, dark yellow) and Si with a native SiO$_2$ layer (full squares, green) in dependance of the angle of the applied field.

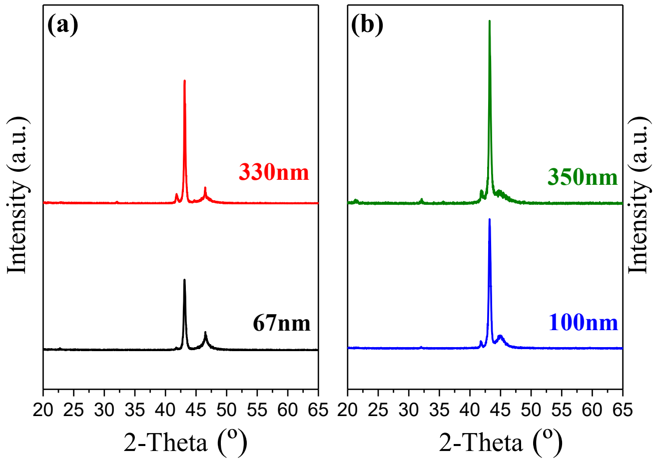

Figure 2.5: XRD spectras of different thickness Fe$_3$O$_4$ thin films deposited on (a,b) SrTiO$_3$:Nb and (c,d) MgAl$_2$O$_4$.

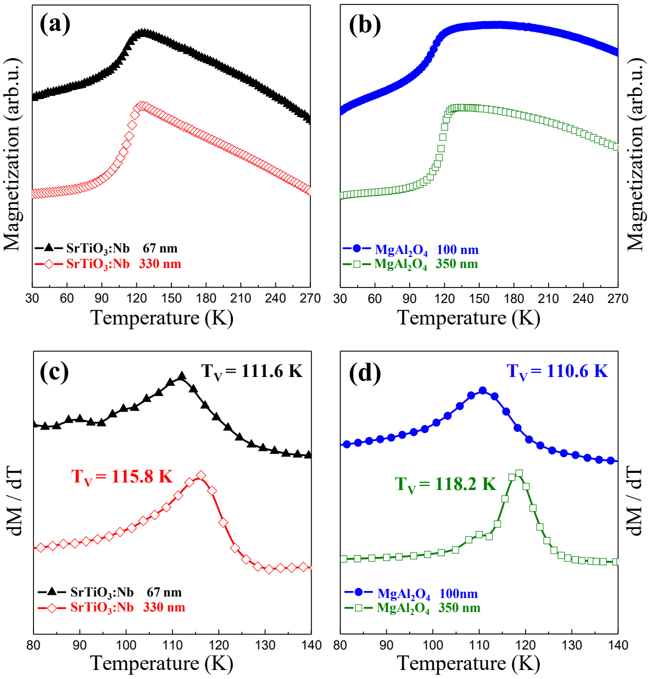

Figure 2.6: Warming curves measured with an in-plane applied field of 2 kOe of Fe_3O_4 thin films deposited on (a) $SrTiO_3$:Nb substrates with thickness of 67 nm (full triangles, black) and 330 nm (open diamonds, red), and (b) $MgAl_2O_4$ substrates with thicknesses of 100 nm (full circles, blue) and 350 nm (open squares, green). The derivative of magnetization against temperature variation indicates Verwey transition temperature; (c) $SrTiO_3$:Nb and (d) $MgAl_2O_4$ substrates.

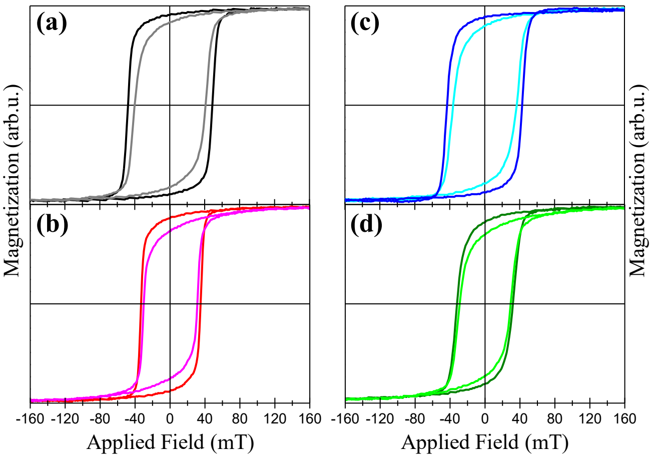

Figure 2.7: In-plane hysteresis loops (easy and hard axis) of anisotropic Fe$_3$O$_4$ thin films: (a) 67 nm and (b) 330 nm deposited on SrTiO$_3$:Nb, and (c) 100 nm and (d) 350 nm deposited on MgAl$_2$O$_4$.

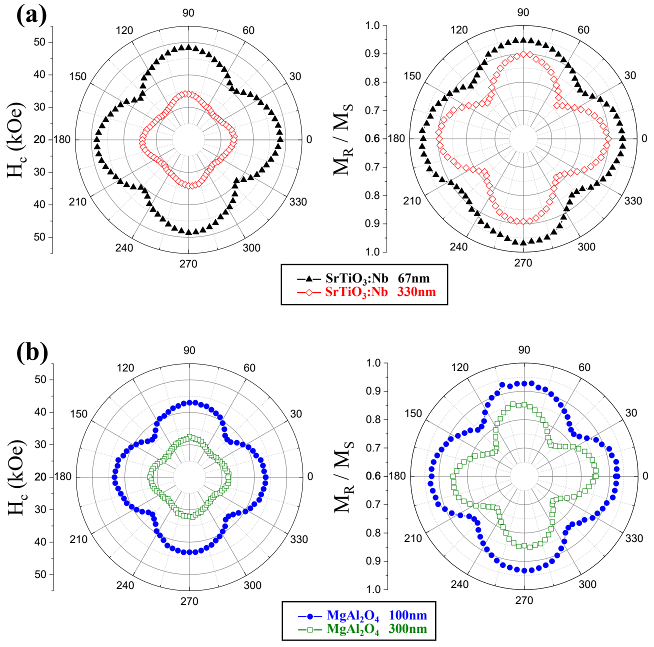

Figure 2.8: Angular evolution of in-plane H_C and M_R/M_S of Fe$_3$O$_4$ thin films deposited on SrTiO$_3$:Nb substrates with thickness of 67 nm (full triangles, black) and 330 nm (open diamonds, red), and MgAl$_2$O$_4$ substrates with thickness of 100 nm (full circles, blue) and 350 nm (open squares, green).

2.4 Conclusions

We have shown is this letter the possibility to obtain epitaxial monocrystalline Fe_3O_4 films by using infrared PLD. The use of a substrate with a cubic structure results in Fe_3O_4 layers with a well-defined four-fold symmetry on H_C and M_R/M_S, indicative of biaxial magnetic anisotropy, in contrast with those films grown in non-cubic substrates where polycrystalline Fe_3O_4 with an isotropic magnetic behavior was obtained, using in all cases the same deposition conditions. All samples present Verwey transition at temperature in the range 110 - 120K. A comparison of samples grown on identical substrates but with different thickness show that this biaxial magnetic anisotropy can be achieved even in samples with thickness greater than 300 nm. Easy axis are found at <100> and <010> directions of the substrate, while the hard axis are in <110> directions.

References

[1] Allan A Mills *The lodestone: History, physics, and formation*. in: *Annals of science* ***61***,3 (2004), 273–319 (cit. on p. 15)

[2] Mikhail Fonin, Yu S Dedkov, Rossitza Pentcheva, Ulrich Rüdiger, and Gernot Güntherodt *Magnetite: a search for the half-metallic state*. in: *Journal of Physics: Condensed Matter* ***19***,31 (2007), 315217 (cit. on p. 15)

[3] PJ Van der Zaag, PJH Bloemen, JM Gaines, RM Wolf, PAA Van Der Heijden, RJM Van de Veerdonk, and WJM De Jonge *On the construction of an Fe 3 O 4-based all-oxide spin valve*. in: *Journal of magnetism and magnetic materials* ***211***,1 (2000), 301–308 (cit. on p. 15)

[4] Michael Ziese *Extrinsic magnetotransport phenomena in ferromagnetic oxides*. in: *Reports on Progress in Physics* ***65***,2 (2002), 143 (cit. on p. 15)

[5] E Wada, K Watanabe, Y Shirahata, M Itoh, M Yamaguchi, and T Taniyama *Efficient spin injection into GaAs quantum well across Fe 3 O 4 spin filter*. in: *Applied Physics Letters* ***96***,10 (2010), 102510 (cit. on p. 15)

[6] Friedrich Walz *The Verwey transition-a topical review*. in: *Journal of Physics: Condensed Matter* ***14***,12 (2002), R285 (cit. on p. 15)

[7] Joaquín García and Gloria Subías *The Verwey transition - a new perspective*. in: *Journal of Physics: Condensed Matter* ***16***,7 (2004), R145 (cit. on pp. 15, 16)

[8] PAA Van der Heijden, MG Van Opstal, CHW Swüste, PHJ Bloemen, JM Gaines, and WJM De Jonge *A ferromagnetic resonance study on ultra-thin Fe3O4 layers grown on (0 0 1) MgO*. in: *Journal of magnetism and magnetic materials* ***182***,1-2 (1998), 71–80 (cit. on p. 16)

[9] S Celotto, W Eerenstein, and T Hibma *Characterization of anti-phase boundaries in epitaxial magnetite films*. in: *The European Physical Journal B-Condensed Matter and Complex Systems* ***36***,2 (2003), 271–279 (cit. on p. 16)

[10] Jean-Baptiste Moussy *From epitaxial growth of ferrite thin films to spin-polarized tunnelling*. in: *Journal of Physics D: Applied Physics* ***46***,14 (2013), 143001 (cit. on p. 16)

[11] XH Liu, AD Rata, CF Chang, AC Komarek, and LH Tjeng *Verwey transition in Fe 3 O 4 thin films: Influence of oxygen stoichiometry and substrate-induced microstructure*. in: *Physical Review B* ***90***,12 (2014), 125142 (cit. on p. 16)

[12] Tobias Schemme, Nico Pathé, Gang Niu, Florian Bertram, Timo Kuschel, Karsten Kuepper, and Joachim Wollschläger *Magnetic anisotropy related to strain and thickness of ultrathin iron oxide films on MgO (001)*. in: *Materials Research Express* ***2***,1 (2014), 016101 (cit. on p. 16)

[13] H Yanagihara, M Myoka, D Isaka, T Niizeki, K Mibu, and Eiji Kita *Selective growth of Fe3O4 and γ-Fe2O3 films with reactive magnetron sputtering*. in: *Journal of Physics D: Applied Physics* ***46***,17 (2013), 175004 (cit. on p. 16)

[14] Pilar Prieto, José Emilio Prieto, Raquel Gargallo-Caballero, José Francisco Marco, and Juan de la Figuera *Role of the substrate on the magnetic anisotropy of magnetite thin films grown by ion-assisted deposition*. in: *Applied Surface Science* ***359***, (2015), 742–748 (cit. on p. 16)

[15] Hua Xiang, Fengyuan Shi, Mark S Rzchowski, Paul M Voyles, and Y Austin Chang *Epitaxial growth and magnetic properties of Fe 3 O 4 films on TiN buffered Si (001), Si (110), and Si (111) substrates*. in: *Applied Physics Letters* ***97***,9 (2010), 092508 (cit. on p. 16)

[16] Pilar Prieto, Juan de la Figuera, Laura Martín-García, José Emilio Prieto, and José F Marco *Fourfold in-plane magnetic anisotropy of magnetite thin films grown on TiN buffered Si (001) by ion-assisted sputtering*. in: *Journal of Materials Chemistry C* ***4***,32 (2016), 7632–7639 (cit. on p. 16)

[17] Elke Arenholz, Gerrit van der Laan, Rajesh V Chopdekar, and Yuri Suzuki *Anisotropic X-ray magnetic linear dichroism at the Fe L 2, 3 edges in Fe 3 O 4*. in: *Physical Review B* ***74***,9 (2006), 094407 (cit. on p. 16)

[18] A Hamie, Y Dumont, E Popova, A Fouchet, B Warot-Fonrose, C Gatel, E Chikoidze, J Scola, B Berini, and N Keller *Investigation of high quality magnetite thin films grown on SrTiO 3 (001) substrates by pulsed laser deposition*. in: *Thin Solid Films* ***525***, (2012), 115–120 (cit. on p. 16)

[19] Mikel Sanz, Mohamed Oujja, Esther Rebollar, José F Marco, Juan de la Figuera, Matteo Monti, Alberto Bollero, Julio Camarero, **Pedrosa, Francisco J**, Mar García-Hernández, et al. *Stoichiometric magnetite grown by infrared nanosecond pulsed laser deposition*. in: *Applied Surface Science* ***282***, (2013), 642–651 (cit. on p. 16)

[20] Matteo Monti, Mikel Sanz, Mohamed Oujja, Esther Rebollar, Marta Castillejo, **Pedrosa, Francisco J**, Alberto Bollero, Julio Camarero, Jose Luis F Cunado, Norbert M Nemes, et al. *Room temperature in-plane< 100> magnetic easy axis for Fe3O4/SrTiO3 (001): Nb grown by infrared pulsed laser deposition*. in: *Journal of Applied Physics* ***114***,22 (2013), 223902 (cit. on p. 16)

[21] Joonghoe Dho, Byeonggeon Kim, and Sanghoon Ki *Substrate Effects on In-Plane Magnetic Anisotropy and Verwey Transition Temperatures of (100) Magnetite (Fe 3 O 4) Films*. in: *IEEE Transactions on Magnetics* ***52***,7 (2016), 1–4 (cit. on p. 16)

[22] Mikel Sanz, Mohamed Oujja, Esther Rebollar, José F Marco, Juan de la Figuera, Matteo Monti, Alberto Bollero, Julio Camarero, Francisco J Pedrosa, Mar García-Hernández, et al. *Stoichiometric magnetite grown by infrared nanosecond pulsed laser deposition*. in: *Applied Surface Science* ***282***, (2013), 642–651 (cit. on pp. 16, 17)

[23] Matteo Monti, Mikel Sanz, Mohamed Oujja, Esther Rebollar, Marta Castillejo, Francisco J Pedrosa, Alberto Bollero, Julio Camarero, Jose Luis F Cunado, Norbert M Nemes, et al. *Room temperature in-plane< 100> magnetic easy axis for Fe3O4/SrTiO3 (001): Nb grown by infrared pulsed laser deposition*. in: *Journal of Applied Physics* ***114***,22 (2013), 223902 (cit. on p. 16)

[24] A Bollero, M Ziese, R Höhne, HC Semmelhack, U Köhler, A Setzer, and P Esquinazi *Influence of thickness on microstructural and magnetic properties in Fe 3 O 4 thin films produced by PLD*. in: *Journal of Magnetism and Magnetic Materials* ***285***,1 (2005), 279–289 (cit. on p. 17)

[25] E Jiménez, N Mikuszeit, JLF Cuñado, P Perna, J Pedrosa, D Maccariello, C Rodrigo, MA Niño, A Bollero, J Camarero, et al. *Vectorial Kerr magnetometer for simultaneous and quantitative measurements of the in-plane magnetization components*. in: *Review of Scientific Instruments* ***85***,5 (2014), 053904 (cit. on p. 18)

[26] Jose Luis F Cuñado, Javier Pedrosa, Fernando Ajejas, Alberto Bollero, Paolo Perna, Francisco J Teran, Rodolfo Miranda, and Julio Camarero *Note: Vectorial-magneto optical Kerr effect technique combined with variable temperature and full angular range all in a single setup*. in: *Review of Scientific Instruments* ***86***,4 (2015), 046109 (cit. on p. 18)

[27] XH Liu, AD Rata, CF Chang, AC Komarek, and LH Tjeng *Verwey transition in Fe 3 O 4 thin films: Influence of oxygen stoichiometry and substrate-induced microstructure*. in: *Physical Review B* ***90***,12 (2014), 125142 (cit. on p. 19)

[28] Sangeeta Kale, SM Bhagat, SE Lofland, T Scabarozi, SB Ogale, A Orozco, SR Shinde, T Venkatesan, B Hannoyer, B Mercey, et al. *Film thickness and temperature dependence of the magnetic properties of pulsed-laser-deposited Fe 3 O 4 films on different substrates*. in: *Physical Review B* ***64***,20 (2001), 205413 (cit. on p. 21)

[29] SK Arora, RGS Sofin, and IV Shvets *Magnetoresistance enhancement in epitaxial magnetite films grown on vicinal substrates*. in: *Physical Review B* ***72***,13 (2005), 134404 (cit. on p. 22)

[30] Pilar Prieto, Juan de la Figuera, Laura Martín-García, José Emilio Prieto, and José F Marco *Fourfold in-plane magnetic anisotropy of magnetite thin films grown on TiN buffered Si (001) by ion-assisted sputtering*. in: *Journal of Materials Chemistry C* **4**,32 (2016), 7632–7639 (cit. on p. 22)

Chapter 3

FeCo nanowires

Nanowires fabricated with magnetic material are of interest nowadays because of its potential application in high-density magnetic recording [1], high-frequency devices [2], sensors [3, 4], spintronics [5] and biomedical applications. From a scientific point of view, these systems are ideal to study the dimensionality effects on a given material. For instance, the high aspect-ratio of a nanowire produces magnetic materials with an effective magnetic anisotropy governed by shape and magnetocrystalline anisotropy. Specific, the high aspect ratio of these structures will determine the shape magnetic anisotropy of the material that competes with magnetocrystalline anosotropy resulting in a higher or lower effective anisotropy. However, their increased complexity requires specific physical characterization methods, due to their particular features such as high anisotropy, small magnetic volume, dipolar interaction field between them, and interesting electronic properties.

This work presents the experimental identification of magnetic reversal processes of an array of $Fe_{32}Co_{68}$ nanowires, in addition to the determination of intrinsic switching fields distributions of the system. *M-h* curves measured at room temperature with the magnetic field applied at different orientations are compared. In particular, the system under study presents a high shape anisotropy value in the direction of the nanowires c-axis caused by the high aspect ratio length/diameter in comparison with magnetocrystalline anisotropy value of Fe_32Co_68

The aim of this chapter was to offer an ample overview of the magnetic, electric, and physical characterization techniques that are suitable for cylindrical magnetic nanowire investigation, of what is the specific care that one needs to take into account and which information will be extracted, with typical and varied examples.

3.1 System description

Iron-cobalt alloys, also known as Permender, present a cubical BCC structure. This material present a low magnetic anisotropy, close to zero in the ordered phase. Its main characteristic is a very high magnetic saturation (Js = 2.4T). FeCo alloys are employed in electrical transformer as well in magnetic nucleus where high magnetic flux density is required.

Magnetic properties of FeCo alloys nanowires can be tuned by adjusting the alloy composition or adding other elements 8,10 or by suitable thermal treatments 11

From the large variety of magnetic systems, FeCo nanowires exhibit the necessary capability to be employed in novel generation of rare-earth-free permanent magnets.

3.2 Structural and morphological characterization

Every nanowire is 40 nm in diameter, and the interdistance between nanowires 120 nm. FeCo alloys nanowires crystallize into cubic phases with a (STRONG/WEAK) magnetocrystalline anisotropy and magnetostatic interaction mostly determined by their overall magnetic response.

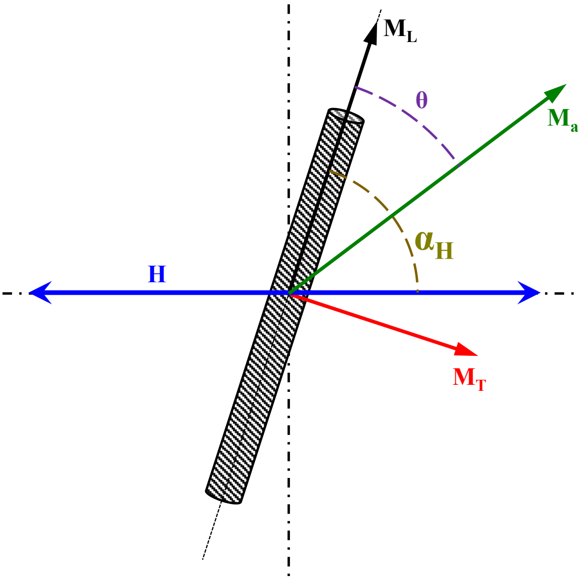

Figure 3.1: Structural and Morphological characterization of FeCo nanowires

3.3 Description of the model

Isolated nanowires present an intrinsic uniaxial anisotropy as a consequence of its length-to-diameter ratio, that in addition, the intrinsic properties of the material such as magnetocrystalline, magnetoelastic and surface anisotropy constants play an important role on the final "effective" anisotropy. In particular, FeCo alloys posses reduced magnetocrystalline anisotropy in contrast to shape anisotropy.

It is considered three magnetization reversal modes for individual nanowires [**Escrig**, **aharoni**]; coherent rotation, transverse domain wall and vortex domain wall.

Coherent rotation is an assumption in which all spins of a system are considered parallel, and magnetization reversal consist in the homogeneous rotation of those spins to the angle of the applied field. This implies that the net value of magnetization vector is constant in all cases. For instance, the Stoner-Wolfhart model [6] is employed to estimate demagnetization curves of a single domain nanoparticle when a magnetic field is applied at a certain angle.

When the system is not on coherent rotation regime, two complex phenomenas occurs during the magnetization reversal process of a nanowire; vortex nucleation/anihilation and domain wall propagation. Guslienko et al. [7] described the evolution of vortices on dots, defining the nucleation field, H_N, and the anihilation field, H_A as the critical fields where vortices appears and are expeled respectively. In nanowires there is an additional process during the magnetization reversal which is the propagation. Vortices are mainly localized on the top and bottom ends of nanowires, and under certain conditions it can be propagated from one end to the other switching the direction of the magnetic moment of the nanowires cores. Vortex are magnetic structures contained in a plane where the net magnetization is null in that plane direction, but with a magnetic moment in the perpendicular direction. This vortex is propagated along the nanowire during the magnetization reversal process.

It is considered an array of FeCo nanowires arranged in a hexagonal closed-package distribution. All nanowires are simetric with cylindrical shape and an overall uniaxial magnetic anisotropy. Simulations shows that the reversal modes of NWs with single crystalline cubic anisotropy correspond to single DW (TDW or VDW) propagation (field applied parallel to NW axis) or quasi-coherent rotation (field applied perpendicularly to NW axis). [8] When the model is extended to an array of nanowire, magnetostatic energy is need to be into account.

The wire was discretized intro approximately 2600 uniformly magnetized cubic cells with a N nm cell side (less tha the exchange length for FeCo with is about X nm [Citar la referencia]). The effective magnetic field inside each cell is taken as the sum if the magnetostatic field created by all the cells, the anisotropy field, the applied field and the exchange length [9]

$$\vec{H} = \vec{H}_m + \vec{H}_k + \vec{H}_{app} + \vec{H}_{ex} \tag{3.1}$$

In the analysis here presented, the magnetization vector included in the plane of the applied film plane is decomposed in two components; one component called "Longitudinal" and an orthogonal one denoted as "Transversal". The longitudinal component is parallel to the high simmetry axis and the transversal is perpendicular to the later. Domain wall propagation occurs mainly along the high anisotropy axis, so changes of this component might be asociated mainly to it. On the other hand, Vortex are contained in a section of such a nanowire.

3.4 VSM-Referenced loops

A vectorial Lakeshore 7400 vibrating sample magnetometer was employed to measure magnetization M-H curves at room temperature of the FeCo nanowires array previously described with a maximum applied field os 20 kOe in an angular range of 0 - 360 ° with an angular step of 9 °. The magnetometer measures the sample magnetic moment in de direction of the applied field (m_x) and additionaly in the orthogonal one (m_y). The array of nanowires are rotated along ....

Figure 3.2 depicts M-H curves measured on the FeCo array of nanowires for different α_H. At a first glance, it can be noticed the angular dependence of hysteresis curves shape with α_H, indicating that the system present a well defined uniaxial anisotropy in the direction of the nanowire c-axis, with a magnetic easy axis at $\alpha_H = 0$ ° and a hard axis localized at $\alpha_H = 90$ °. This is expected due to high shape anisotropy of the system, with a shape ratio of R=L/d of 50, in addition to a reduced magnetocrystalline anisotropy.

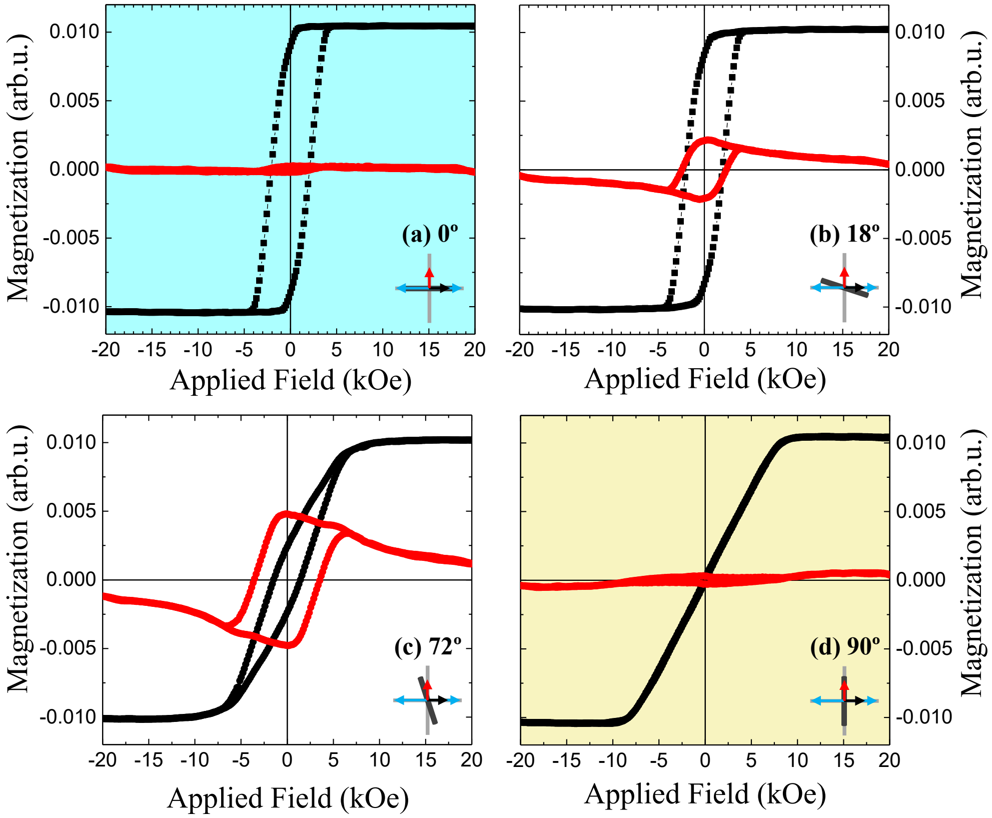

Figure 3.2: Hysteresis loops in the direction of the applied field (black) and in the orthogonal one (red) measured on a FeCo array of nanowires, with the field applied at (a) 0Â°, (b) 18Â°, (c) 72Â° and (d) 90Â° with respecto to the nanowires c-axis.

Figure 3.3 shows the measured value of remanence magnetization for both components (Figure 3.3.(a)) as well as coercivity (Figure 3.3.(b)).

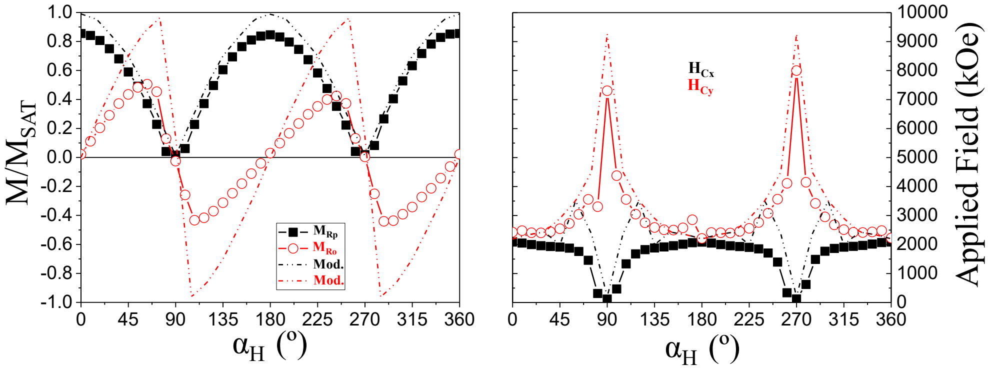

Figure 3.3: Hysteresis loops in the direction of the applied field (black) and in the orthogonal one (red) measured on a FeCo array of nanowires, with the field applied at (a) 0Â°, (b) 18Â°, (c) 72Â° and (d) 90Â° with respecto to the nanowires c-axis.

On the easy axis, the magnetization component in the direction of the applied field, M_X, and the orthogonal component M_Y is negligible, indicating that magnetization lies on the direction of the applied field. The inversion event occurs at a field of Maximum value of M_X is reached with applied fields of ±10 kOe.

3.4.1 Experimental FeCo 40nm

A vectorial Lakeshore 7400 vibrating sample magnetometer was employed to measure magnetization *M-H* curves at room temperature of the FeCo nanowires array previously described with a maximum applied field os 20 kOe in an angular range of 0 - 360 ° using an angular step of 9 °. The magnetometer measures the sample magnetic moment m_x in de direction of the applied field (m_x) and, in the orthogonal direction of the applied field (m_y). The array of nanowires are rotated along the z-axis. Figure 3.4 illustrate the spatial resolution of parameters involved in this analysis. First, it is defined α_H as the angle between the direction of the applied magnetic field and the nanowires c-axis.

Both magnetic moment components are used to calculate M_{abs} using equation 3.2. For a better understanding of the obtained data, this magnetic components are referenced to the array of nanowires; M_L, which is parallel to the nanowires c-axis, and the transversal component, M_T. This is performed with a rotational matrix as described in equation 3.3. Moreover, this matrix is divided by M_{20kOe} so that $M_L(H)$ and $M_T(H)$ are normalized.

$$M_{abs} = \sqrt{M_x^2 + M_y^2} \tag{3.2}$$

$$R = \begin{pmatrix} \cos(\alpha_H) & \sin(\alpha_H) \\ -\sin(\alpha_H) & \cos(\alpha_H) \end{pmatrix}$$

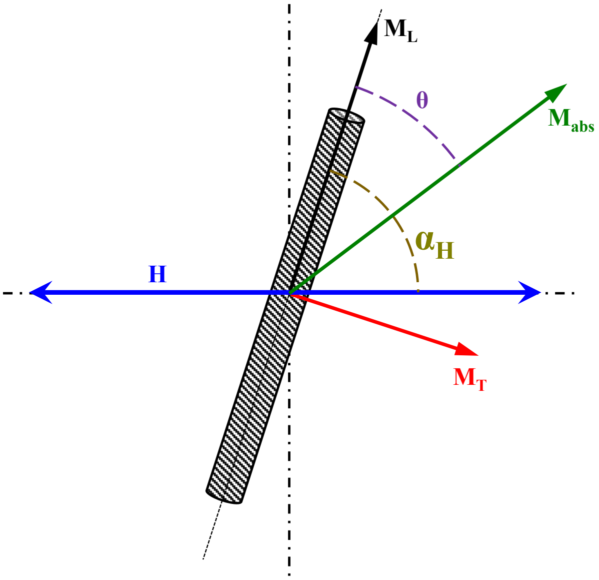

Figure 3.4

$$\begin{pmatrix} M_L(H) & M_T(H) \end{pmatrix} = \frac{1}{M_{abs}} \cdot \cdot \begin{pmatrix} \cos(\alpha_H) & \sin(\alpha_H) \\ -\sin(\alpha_H) & \cos(\alpha_H) \end{pmatrix} \cdot \begin{pmatrix} M_x(H) & M_y(H) \end{pmatrix} \tag{3.3}$$

The hysteresis loops of longitudinal and transversal curves measured at different angles of the applied field are displayed on figure 3.5 when the magnetic field is applied at α_H = 0, 27, 72 and 90 °.

With a magnetic field applied in the easy axis (Figure 3.5.(a)), M_L curve present values similar to M_{abs}, indicative that the magnetization vector mostly lies on this direction. In the contrary, M_t follows a linear tendency, from a negative value at high fields to negative values at negative fields. M_t might be zero in case of a perfect alignment of the sample and the magnetic field. However, this negative value at high fields is indicative that there is a slight missmatch in α_H. Increasing the angle of the applied field to 27 and 72 ° (Figures 3.5.(b-c)) provides curves where M_l is decreased at M_{20kOe} but with a positive increase approaching to zero field, and M_t increases up to reach the M_{abs} when the applied field is in the hard axis (α_H = 90 °, see Figure 3.5.d)). The change of sign of $\vec{M}_x$ in the range α_H > 180 ° and M_y in the range α_H > 180 ° is a consequence of the established axial reference.

The magnetization reversal in cylindrical nanowires with uniaxial anisotropy parallel to the c-axis are caused by the propagation of a vortex-like domain wall from one of the ends. **??**. On Figure **??** it is seen that $M_{\text{abs}}(H)$ is constant when the applied field is higher than 10 kOe.

Considering a macrospin coherent rotation model where it is assumed that M_{abs} is constant, it is possible to determine the coherent rotation regime. Using equation 3.4, the field in which the system change its reversal behavior from or to coherent rotation. Initially, the intensity of the applied field is reduced from 20 kOe

$$M_{abs}(H) > 0.95 \cdot M_{20kOe} \tag{3.4}$$

This event is considered as the nucleation field H_N. When the field is further reduced, the M_{abs} value decreases. The angle θ of the magnetization vector follows a linear decrease to θ = 0Â° when the magnetic applied field is reduced.

The VDW propagation is observed on the θ angle. There is a well localized transition from α_H to α_H+180 .

Once the core of the nanowires are switched vortices are anihilated.

Due to the phenomenology involved in the magnetization reversal process, it is convenient to start analyzing the easy and the hard axis first. On the easy axis (see Figure **??** first row), magnetization reversal is mainly affected by coherent rotation and propagation. The magnetization vector of the system lies on the c-axis direction (α_H = 0Â°) which is the direction of the applied field. H_N presents a positive value of x kOe and M_L decreases.

In the hard axis by curling. In between, there is a coexistence of both phenomenas. Differences on M_L can be associated to TDVW while the M_T component gives an idea of the density of vortex. The coercive field, H_c, is defined as the field at which the magnetization is equal zero. In the case of this study it is considered more appropiated to define the propagation field, H_p as the applied field at which the TDW starts to propagate, and the anihilation field, H_A which is the field where the vortex are expeled

.

For instante, FIGURA A displays the evolution of θ with de angle of the applied field. When the applied field H = 20 kOe, there is a small angle between the magnetization vector of the system and the magnetic applied field direction.

It is interesting from a scientific point of view, the observation of a microscopic phenomena. In turns, it is described the magnetization reversal mechanism observed with VSM measurements.

On the other hand, the hard axis (Figure **??**.(c)).

The easy axis shows a longitudinal component with a sharp transition, while in the hard axis it is observed linear dependency with the applied field in addition to a peak with a maximum when no field is applied.

The transversal component is associated to vortex formation. However, it is observed a peak as-well, coincident with the transition. The linear dependency of this component with the applied field on the easy axis is typical of coherent rotation.

aturation magnetization when the applied field is higher than 10 kOe. might be due to the interaction of nanowires to minimize the energy of the system. By contrast, on the hard axis it is seen how this component is null when no magnetic field is applied. In both cases, the transverse component presents a linear behavior in dependence of the applied field.

3.4.2 reversal mechanism

On Figure X, it is compared the obtained data and the predictions of simulations. Red curves correspond to vortex nucleation (VN) point. This event occur at a positive applied fields. On the easy axis, VN is almost 4-fold higher experimentally than in simulations, probably due to the reduced number of nanowires simulated. At this field, the magnetization of the system ends to rotate coherently with the field and vortex start to be created.

A negative field is accompannied by a further increase of vortex when the field is applied at 0Â°.

However, when the field is applied perpendicular at 90Â°, the VN increase un to 8kOe.

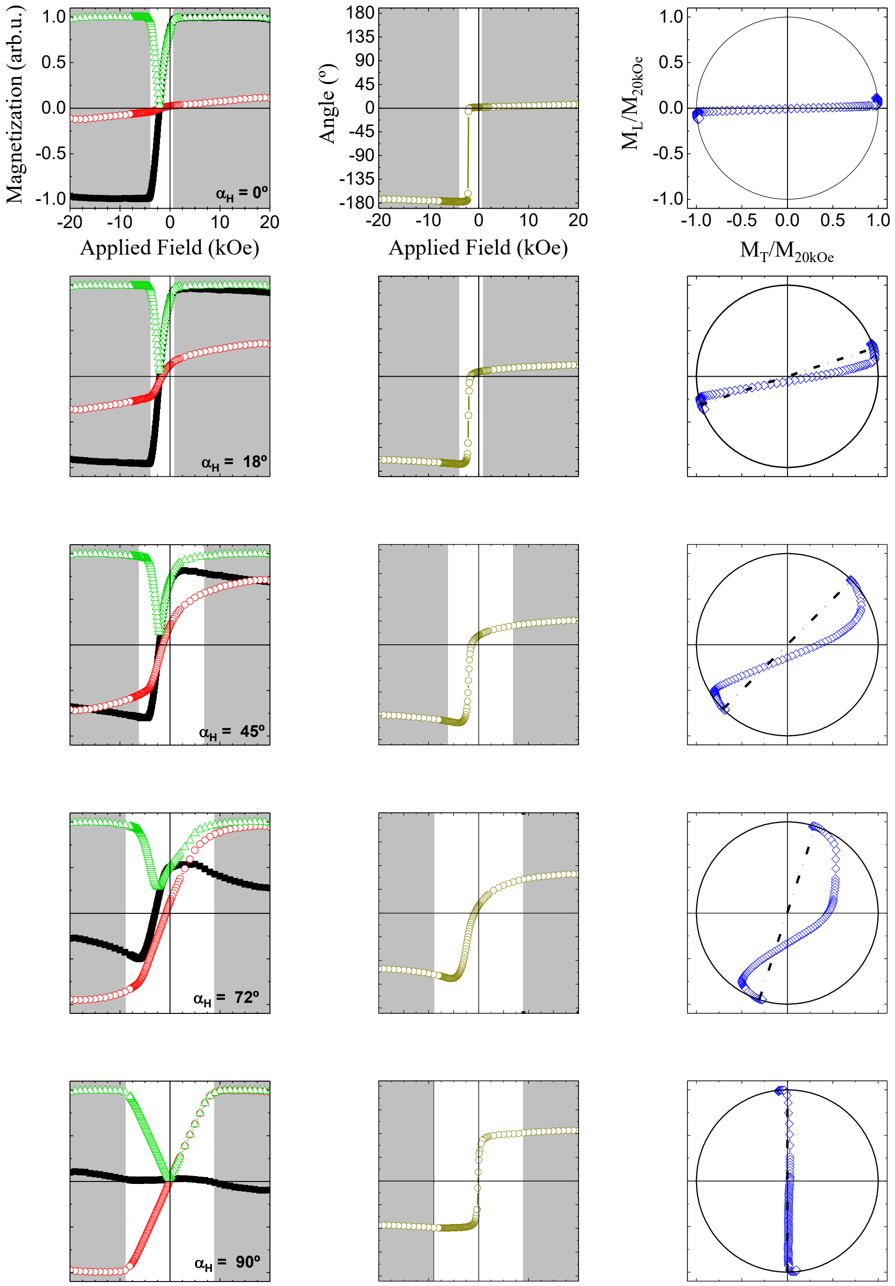

Figure 3.5: *M-H* curves containing longitudinal (black) and transversal (red) components of the nanowire magnetic moment, as well as the resultant saturation maGnetization (green) when a magnetic field is applied at an angle of (a) 0 °, (b) 27 °, (c) 72 ° and (d) 90 ° with respect to the nanowires c-axis.

References

[1] Caroline A Ross *Patterned magnetic recording media*. in: *Annual Review of Materials Research* ***31***,1 (2001), 203–235 (cit. on p. 29)

[2] Aimad Saib, Michaël Darques, Luc Piraux, Danielle Vanhoenacker-Janvier, and Isabelle Huynen *An unbiased integrated microstrip circulator based on magnetic nanowired substrate*. in: *IEEE transactions on microwave theory and techniques* ***53***,6 (2005), 2043–2049 (cit. on p. 29)

[3] A Fert and L Piraux *Magnetic nanowires*. in: *Journal of Magnetism and Magnetic Materials* ***200***,1 (1999), 338–358 (cit. on p. 29)

[4] H Zheng, J Wang, SE Lofland, Z Ma, L Mohaddes-Ardabili, T Zhao, L Salamanca-Riba, SR Shinde, SB Ogale, Feiming Bai, et al. *Multiferroic BaTiO3-$CoFe_2O_4$ nanostructures*. in: *Science* ***303***,5658 (2004), 661–663 (cit. on p. 29)

[5] A Mourachkine, OV Yazyev, C Ducati, and J-Ph Ansermet *Template nanowires for spintronics applications: nanomagnet microwave resonators functioning in zero applied magnetic field*. in: *Nano letters* ***8***,11 (2008), 3683–3687 (cit. on p. 29)

[6] EC Stoner and EP Wohlfarth *A mechanism of magnetic hysteresis in heterogeneous alloys*. in: *IEEE Transactions on Magnetics* ***27***,4 (1991), 3475–3518 (cit. on p. 31)

[7] K Yu Guslienko, V Novosad, Y Otani, H Shima, and K Fukamichi *Magnetization reversal due to vortex nucleation, displacement, and annihilation in submicron ferromagnetic dot arrays*. in: *Physical Review B* ***65***,2 (2001), 024414 (cit. on p. 31)

[8] Yu P Ivanov, M Vázquez, and O Chubykalo-Fesenko *Magnetic reversal modes in cylindrical nanowires*. in: *Journal of Physics D: Applied Physics* ***46***,48 (2013), 485001 (cit. on p. 31)

[9] Andrei Diaconu, Ioan Dumitru, Alexandru Stancu, and Leonard Spinu *The temperature dependence of magnetostatic interactions in nanowire systems*. in: *Development and Application Systems (DAS), 2014 International Conference on* IEEE 2014, 132–136 (cit. on p. 31)

Part II

Cobalt ferrite powder as an alternative on rare-earth free permanent magnets

Introduction

In this part, the design and development of rare-earth free permanent magnets based on cobalt ferrite oxides are addressed. A comprehensive correlation between morphology, microstructure and magnetic properties of isotropic cobalt ferrite oxide ($CoFe_2O_4$) powders after using different post-synthesis processes is provided. The study has been carried out for isotropic CFO powders synthesized by different chemical routes (co-precipitation and sol-gel methods) with different post-synthesis processes, including annealing, high energy ball milling (HEBM) in different medias (dry and surfactant assisted (wet) milling), and post-milling annealing processes. Reproducibility and scalability issues are also investigated. In general, the data provides the technological keys to manage the production of $CoFe_2O_4$ powders with high magnetic performance in record processing times of only a few minutes. Remarkably, several-fold increase in coercivity (up to 4.7 kOe) of isotropic cobalt ferrite powders after only 180 seconds of HEBM and a record $(BH)_{\max}$ value of 18.6 kJ m^{-3} after post-processing annealing at moderate temperatures are reported. The data shows how to tailor the magnetic performance via altering microstructure, combining induced-strain and grain size controls. This magnetic performance combined with the required short processing times, reproducibility and easy scalability makes this $CoFe_2O_4$ powder a good candidate for permanent magnet applications.

Nowadays, rare earth-based permanent magnets, RE-PMs, are used in a large number of technological applications, as described in Introduction . The rapidly growing market of green technologies demands an increased amount of this type of magnets, which combined with the geographical distribution of rare-earths, makes a search for alternatives to these RE-PMs necessary. During the last years, substitution of materials and innovative processing technologies in the permanent magnet industry are focused to avoid the supply risks due to mining oligopoly or speculation as well as to find efficient technological processes [1, 2].

In order to achieve this goal -the substitution of traditional rare earth based magnetic materials- the employment of ferrite nanostructures has been proposed as a promising approach for high coercivity permanent magnet applications. Coercivity is the ability to resist demagnetization, including field demagnetization from the electric or magnetic circuit and thermal demagnetization from the operating temperature.

Nevertheless, it is not realistic to aspire to the complete substitution of this kind of magnets due to the unique combination of magnetic properties of Nd_2Fe_14B. A strong scientific and technological effort is focused in the improvement of the magnetic performance of rare-earth free magnetic materials to match RE low-grade permanent magnets in specific applications, allowing the replacement of this type of magnets. In this direction, nanostructured ferrites have been pointed out as a feasible alternative to rare-earth bonded magnets in technological applications.

Among ferrites, $CoFe_2O_4$ is an interesting material because of its high magnetic anisotropy. It takes an inverse spinel structure with Co^{2+} ions occupying octahedral sites (B sites) and the Fe^{3+} ions on both tetrahedral (A sites) and octahedral ones. Many synthesis techniques have been successfully applied to obtain the spinel phase of $CoFe_2O_4$, such as the hydrothermal method [3, 4], microwave calcination [5], sol-gel process [6, 7], thermal decomposition [8, 9], and co-precipitation technique [10]. The magnetic performance of cobalt ferrite can be enhanced by controlling the particle size distribution through chemical methods during synthesis [11]. For instance, at room temperature (RT), the superparamagnetic behavior is observed for nanoparticles (NPs) sizes below 20nm [12] whereas the optimum single domain behavior where thermally driven demagnetization effects are avoided, i.e. maximum coercivity (H_c) of $CoFe_2O_4$, accounts for 40nm [13], where thermally driven demagnetization effects are avoided. An energy product of 18 kJ m^{-3} is the highest $(BH)_{\max}$ -figure of merit of a PM quality- reported value for randomly oriented non-strained cobalt ferrite nanoparticles at room temperature with a maximum coercivity of about 3.0 kOe [11]

On other hand, post-synthesis processes have been used in order to enhance the magnetic performance of PMs. In this sense, mechanical milling during several hours is a well-known technique that has been applied in permanent magnets fabrication at both laboratory and industrial scales. For instance, Liu et al. [14] obtained $CoFe_2O_4$ powders after milling for 1.5 hours with record values of coercivity of about 5.1 kOe. This enhancement is probably due to the stress anisotropy and defects created during processing, which might act as pinning centers during magnetization reversal.

Although these results are already promising for the use of isotropic cobalt ferrite powders for low and medium grade RE-PMs applications, at the date when these studies started, there were both scientific and industrial cornerstones to be solved:

- The optimization of $CoFe_2O_4$ initial isotropic free-standing powders for its application as permanent magnets, as well as the characterization of the powder after different processing steps.
- A detailed and systematic study that might allow for discrimination of the different parameters involved in the mechanism for increased coercivity was still missed in the literature.
- The scale up possibility is mandatory in order of $CoFe_2O_4$ industrial implementation, and at the moment the amount of material obtained for traditional methods was insufficient to match large-scale production. Furthermore, reproducibility studies still missed.

Here, this part will provide a comprehensive correlation between morphology, microstructure and magnetic properties of isotropic cobalt ferrite powders after using different post-synthesis processes, providing the technological keys to manage the production of powders in record processing times. First, Chapter 4 describes the properties of $CoFe_2O_4$ powders synthesized by the co-precipitation method as a function of a post-synthesis annealing treatment temperature, necessary to crystallize the inverse spinel phase of cobalt ferrite, as well as the exploration of reproducibility and scalability issues. The possibility of coercivity development by high-energy ball milling, HEBM, in record times of few minutes is demonstrated in Chapter 5. The use of different milling medias (air and oleic acid) are also compared. The effect of post-milling annealing processes enhancing $(BH)_{\max}$ values is shown in Chapter 6. Finally, Chapter 7 discuss the magnetic properties of some of the most representative cobalt ferrite powders over a wide temperature range, from 5 K to 400 K. The determination of the correlations between the microstructural properties (grain size and strain) and the magnetic properties (anisotropy, coercivity, energy product) shows that the origin of the improvement of the magnetic properties is associated to the intrinsic properties of the material. In particular, the nanometer size and the effective anisotropy -enhanced by the induced strain- control (tailor) the magnetic properties useful for RE-PMs applications.

References

[1] Oliver Gutfleisch, Matthew A Willard, Ekkes Brück, Christina H Chen, SG Sankar, and J Ping Liu *Magnetic materials and devices for the 21st century: stronger, lighter, and more energy efficient*. in: *Advanced materials* ***23***,7 (2011), 821–842 (cit. on p. 42)

[2] Laura H Lewis and Félix Jiménez-Villacorta *Perspectives on permanent magnetic materials for energy conversion and power generation*. in: *Metallurgical and Materials Transactions A* ***44***,1 (2013), 2–20 (cit. on p. 42)

[3] Zhan Jie Wang, Yan Na Chen, Fan Zhang, Yang Liu, Rui Liang Su, and Li Zhi Shi *Hydrothermal Synthesis of $CoFe_2O_4$ Nanoparticles and their Magnetic Properties*. in: *Advances in Textile Engineering and Materials III* ***821***, Advanced Materials Research Trans Tech Publications, Dec. 2013, 1358–1361 (cit. on p. 43)

[4] Henrik L Andersen and Mogens Christensen *In situ powder X-ray diffraction study of magnetic $CoFe_2O_4$ nanocrystallite synthesis*. in: *Nanoscale* **7**,8 (2015), 3481–3490 (cit. on p. 43)

[5] Amal M. Ibrahim, M.M. Abd El-Latif, and Morsi M. Mahmoud *Synthesis and characterization of nano-sized cobalt ferrite prepared via polyol method using conventional and microwave heating techniques*. in: *Journal of Alloys and Compounds* ***506***,1 (2010), 201–204 (cit. on p. 43)

[6] A Hunyek, Chitnarong Sirisathitkul, and P Harding *Synthesis and Characterization of $CoFe_2O_4$ particle by PVA sol-gel method*. in: *Advanced Materials Research* ***93***, Trans Tech Publ 2010, 659–663 (cit. on p. 43)

[7] Adrian Quesada, Cecilia Granados-Miralles, Alberto López-Ortega, Sergey Erokhin, Elisabetta Lottini, Javier Pedrosa, Alberto Bollero, Ana M Aragón, Fernando Rubio-Marcos, Marian Stingaciu, et al. *Energy Product Enhancement in Imperfectly Exchange-Coupled Nanocomposite Magnets*. in: *Advanced Electronic Materials* (2016) (cit. on p. 43)

[8] S. Prasad, A. Vijayalakshmi, and N. S. Gajbhiye *Synthesis of Ultrafine Cobalt Ferrite by Thermal Decomposition of Citrate Precursor*. in: *Journal of Thermal Analysis and Calorimetry* ***52***,2 (1998), 595–607 (cit. on p. 43)

[9] Le T Lu, Ngo T Dung, Le D Tung, Cao T Thanh, Ong K Quy, Nguyen V Chuc, Shinya Maenosono, and Nguyen TK Thanh *Synthesis of magnetic cobalt ferrite nanoparticles with controlled morphology, monodispersity and composition: the influence of solvent, surfactant, reductant and synthetic conditions*. in: *Nanoscale* **7**,46 (2015), 19596–19610 (cit. on p. 43)

[10] Yue Zhang, Zhi Yang, Di Yin, Yong Liu, ChunLong Fei, Rui Xiong, Jing Shi, and GaoLin Yan *Composition and magnetic properties of cobalt ferrite nano-particles prepared by the co-precipitation method*. in: *Journal of Magnetism and Magnetic Materials* ***322***,21 (2010), 3470–3475 (cit. on p. 43)

[11] Alberto López-Ortega, Elisabetta Lottini, Cesar de Julian Fernandez, and Claudio Sangregorio *Exploring the magnetic properties of cobalt-ferrite nanoparticles for the development of a rare-earth-free permanent magnet*. in: *Chemistry of Materials* ***27***,11 (2015), 4048–4056 (cit. on p. 43)

[12] M Rajendran, RC Pullar, AK Bhattacharya, D Das, SN Chintalapudi, and CK Majumdar *Magnetic properties of nanocrystalline* $CoFe_2O_4$ *powders prepared at room temperature: variation with crystallite size*. in: *Journal of Magnetism and Magnetic Materials* ***232***,1 (2001), 71–83 (cit. on p. 43)

[13] CN Chinnasamy, B Jeyadevan, K Shinoda, K Tohji, DJ Djayaprawira, M Takahashi, R Justin Joseyphus, and A Narayanasamy *Unusually high coercivity and critical single-domain size of nearly monodispersed* $CoFe_2O_4$ *nanoparticles*. in: *Applied physics letters* ***83***,14 (2003), 2862–2864 (cit. on p. 43)

[14] Bing Hai Liu, J Ding, ZL Dong, CB Boothroyd, JH Yin, and JB Yi *Microstructural evolution and its influence on the magnetic properties of* $CoFe_2O_4$ *powders during mechanical milling*. in: *Physical Review B* ***74***,18 (2006), 184427 (cit. on p. 43)

Chapter 4

Tuning $CoFe_2O_4$ synthesized by co-precipitation

The synthesis of nanocrystalline cobalt ferrite powders by the co-precipitation method, followed by a post-synthesis annealing treatment are described in this chapter. This study is performed in search of the optimum preparation parameters that provide $CoFe_2O_4$ isotropic powder with the best magnetic performance, in view of its application as permanent magnets. Furthermore, it is discussed a comparison of properties obtained in different batches synthesized following the same route, shedding some light in relation with repeatability and sacalabilty of the production process.

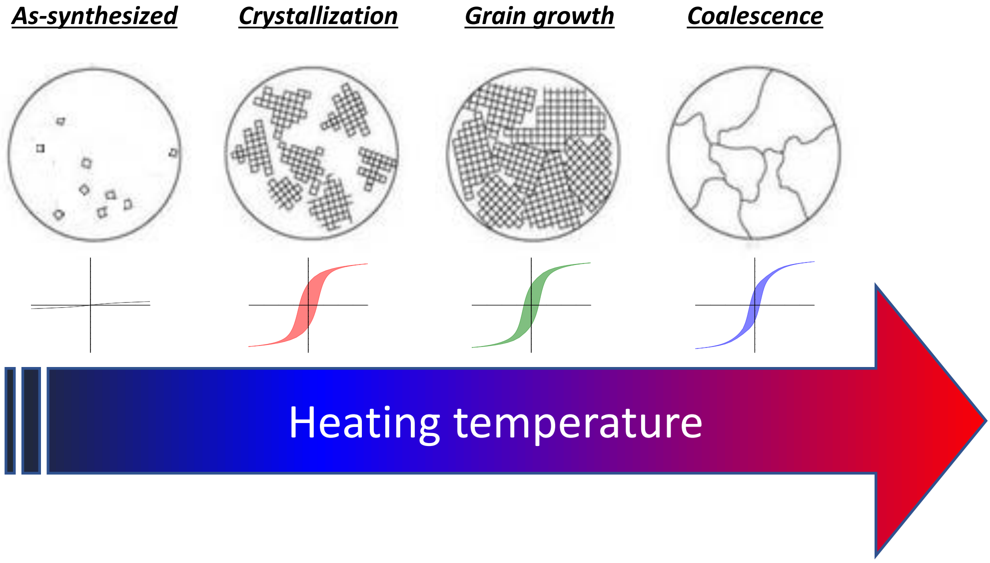

Figure 4.1: Sketch of chapter 4: Magnetic properties optimization of $CoFe_2O_4$ powders synthesized by the co-precipitation method.

4.1 Fabrication of CoFe$_2$O$_4$ for permanent magnets

Many synthesis techniques have been successfully applied to obtain the spinel phase of CoFe$_2$O$_4$, such as the hydrothermal method [1, 2], microwave calcination [3], sol-gel process [4, 5], thermal decomposition [6, 7], and co-precipitation technique [8]. For industrial applications, it is mandatory to demonstrate the scale up possibility. In this sense, the co-precipitation route is a technique that can be performed in a short time interval (less than a day) and offers the possibility of scaling up the production of cobalt ferrite to an industrial level by increasing the volume of the processing steps. The synthesis reaction procedure of CoFe$_2$O$_4$ by the co-precipitation method is described in section 1.1.1.

Last step to obtain CoFe$_2$O$_4$ by the co-precipitation method consist in a heat treatment of the powder resulting from the synthesis reaction, in order to crystallize the inverse spinel phase of cobalt ferrite, as the synthesis of well defined CoFe$_2$O$_4$ crystals usually requires higher temperatures in accordance to previous reports [9–11]. It is important to take into consideration how the temperature of the post-synthesis heat treatment influences the microstructure, even though it will influence the powder magnetic performance. Therefore, a systematic study that can lead to proper optimization of the preparation parameters is necessary

4.1.1 Experiment description

Microstructural and magnetic properties of as-synthesized CoFe$_2$O$_4$ powder, and after being annealed to different temperatures are analyzed and discussed, with the aim to determine the post-synthesis annealing temperature that provides CoFe$_2$O$_4$ powder with optimum magnetic properties for its application as isotropic permanent magnets.

Powder synthesized by the co-precipitation method in a reaction volume of 1 L (see section 1.1.1), was separated in batches with a mass of 100 mg and annealed to a different temperature each, ranging from 650 to 1000 °C. With this treatment, the crystallization of the inverse spinel structure of CoFe$_2$O$_4$ is achieved. The heat treatment was performed with a Carbolite tubular oven model STF 15/450 using air atmosphere, consisting of an increasing temperature ramp of 10K/min from RT to the goal temperature, which was maintained for 3 hours before cooling down to room temperature.

XRD spectra were measured with a Highscore X'pert θ-2θ diffractometer, using Cu-K_α radiation source. Mean crystallite size was calculated by applying the Equation 1.2 to the four most intense peaks, and the mean average strain was obtained using Equation 1.3. These parameters extracted from XRD data are analyzed as a function of the heating temperature.

SEM images were obtained with a Carl-Zeiss Auriga microscope at a filament voltage of 3 kV. These images provide morphological information of CoFe$_2$O$_4$ powder in every stage of the experiment.

A Lakeshore 7400 VSM was employed to measure magnetization M-H curves at RT. Parameters extracted from the hysteresis loops include magnetization at maximum applied field of 20 kOe, ($M_{20\mathrm{kOe}}$), remanence magnetization (M_r), and coercivity (H_c). Energy product, $(BH)_\mathrm{max}$, was evaluated, in order to quantify the performance as permanent magnets and to assess the suitability of this methodology.

4.1.2 Structural and compositional analysis

Representative XRD spectra of as-synthesized CoFe$_2$O$_4$ powder and after being annealed to different temperatures are shown in Figure 4.2. The as-synthesized powder spectra shows broad and unresolved peaks while the annealed ones display reflection peaks corresponding to CoFe$_2$O$_4$ inverse spinel phase, as it was expected since crystallization temperature of cobalt ferrite is 214 °C [12]. Only CoFe$_2$O$_4$ reflection peaks are observed, indicating the absence of any other phase or possible contamination during the synthesis nor heating process. All annealed samples displays the same diffraction peaks. Different intensities of concrete diffraction peaks among heated samples might be ascribed to the enhanced crystallinity of those powders heated to higher temperatures. Specifically, increased heating temperatures lead to narrower peaks with stronger intensities, which is indicative of the progressive grain growth.

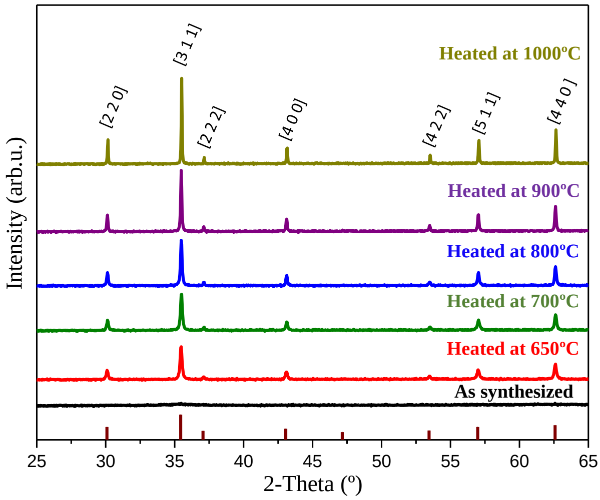

Figure 4.2: XRD spectra of CoFe$_2$O$_4$ powders heated to different temperatures. From bottom to top: as-synthesized powder and after heating to 650, 700, 800, 900 and 1000 °C. Brown lines in the bottom are reference of CoFe$_2$O$_4$ diffraction peaks (ref: 00-022-1086).

Mean crystallite size, $<D_v>$, as well as strain, ε, are calculated by applying the Equation 1.2 and Equation 1.3 to the four most intense peaks of the XRD spectra. Assessed values of $<D_v>$ as a function of heating temperature are represented in Figure 4.3. $<D_v>$ is gradually increased with increasing temperatures. A heating temperature of 650 °C already provides CoFe$_2$O$_4$ with a $<D_v>$ = 55 nm, slightly above the monodomain critical size (40 nm [13]). Maximum $<D_v>$ was observed in the sample heated to 1000 °C with an calculated average size $<D_v>$ = 115 nm.

Mean strain follows a decline with increased heating temperature, with the lowest value measured in the sample annealed to the highest temperature. A decreased density of dislocations is expected in samples heated to higher temperatures as a consequence of the better defined crystallinity, resulting in lower ε values (see Figure 4.2). Strain varies from the maximum $\varepsilon = 1.8 \cdot 10^{-3}$ calculated in powder heated to 650 °C to $\varepsilon = 0.7 \cdot 10^{-3}$ of powder heated to 1000 °C.

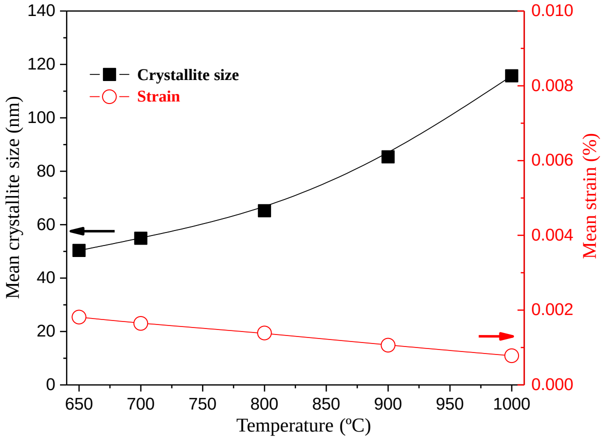

Figure 4.3: Evolution of mean crystallite size, <D$_v$>, and residual strain, ε of CoFe$_2$O$_4$ powders as a function of annealing temperature. Lines and guides for the eyes.

From the discussion above, it can be concluded that the annealing process above 650 °C have produced the crystallization of CoFe$_2$O$_4$ as-synthesized powder, emphasizing that the highest temperature of the annealing process, the lowest mean strain and biggest mean crystallite size.

4.1.3 Morphological analysis

SEM images of as-synthesized powder, and after being heated to 700 °C, 900 °C and 1000 °C are shown in Figure 4.4. These images confirms the temperature dependence of CoFe$_2$O$_4$ particle size with temperature.

While it was not clearly observed any preferential shape on as-synthesized powder further than ellipsoids, which are an unidentified amorphous phase. Heating the as-synthesized powder to a temperature above 650 °C caused CoFe$_2$O$_4$ spinel phase crystallization, providing cobalt ferrite NPs with an irregular polyhedral shape. The biggest particle size was observed in the powder heated to the highest temperature i.e. 1000 °C, in agreement with the structural data discussed before (see 4.3). Except for powder heated to 1000 °C, in the rest of samples the observed particle size is very similar to its previously calculated from XRD mean crystallite size (the yellow circles of each image represent the crystallite size previously calculated, to allow the visual comparison with the particle size), indicating that these CoFe$_2$O$_4$ nanoparticles might be monocrystals.

A drastic difference in the morphology of that sample heated to 1000 °C is noticed by it comparison with those samples heated to lower temperatures, i.e. in the range from 700 °C to 900 °C. Powder annealed to 1000°C exhibit a particle size greater than a micron formed due to particles coalescence during the heating process, as it has been reported previously for sintered CoFe$_2$O$_4$ material [14]. In Figure 4.4.(d), one can see that these particles are much more bigger than that of Figures 4.4.(b-c). In this case, the observed particle size in SEM images is well above the assessed $< D_V >$ discussed above, confirming that in this situation the CoFe$_2$O$_4$ powder is constituted by polycrystalline particles resulting from the coalescence of cobalt ferrite. This can be clearly seen in Figure 4.4.(d) zoom, where different crystals orientations can be appreciated. Nevertheless, it has to be noticed that in addition to these micron-sized particles created due to the melting of smaller particles, there are isolated nanocrystalline particles that were not melted yet (see Figure 4.4.(d)).

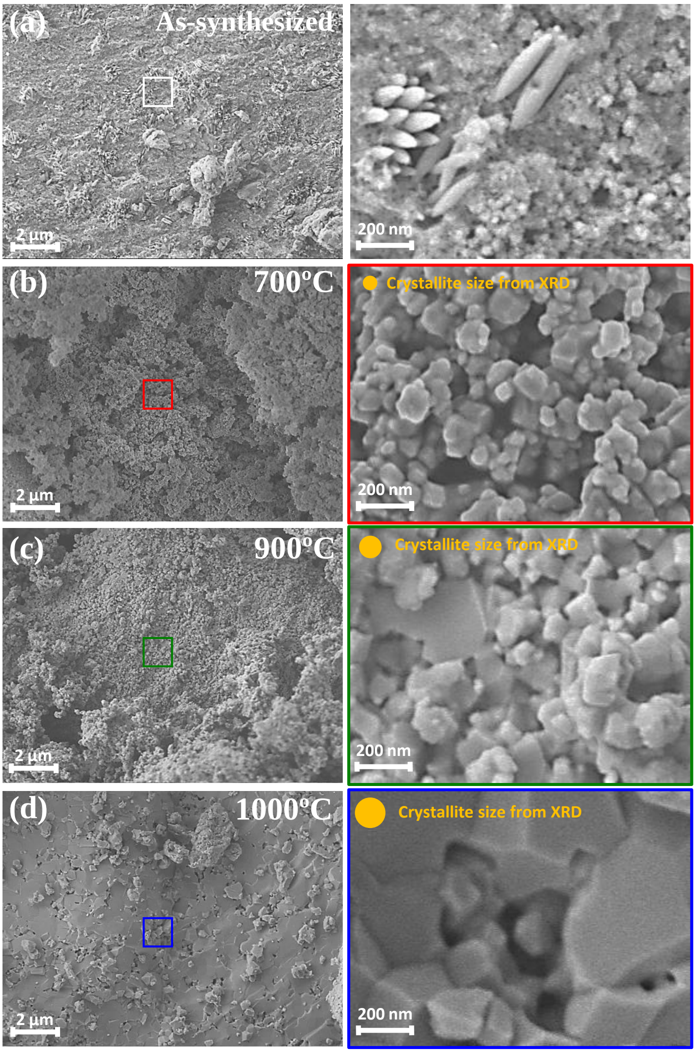

Figure 4.4: SEM images of (a) powder resulting from the co-precipitation synthesis method and (b-d) after heating to 700, 900 and 1000 °C respectively. Right images are zooms, and the yellow circle diameter size is proportional to crystallite size previously calculated from XRD, in order to ease the comparison with particle size.

4.1.4 Magnetic properties analysis

Magnetization curves at RT of as-synthesized cobalt ferrite powder, and after heating to 700 °C, 900 °C and 1000 °C are displayed in Figure 4.5. *M*-*H* curve of as-synthesized powder indicates that the percentage in weight of cobalt ferrite or any other ferromagnetic phase in this powder is relatively low in comparison with other amorphous phases. The *M*-*H* curve of this sample looks like a superparamagnetic hysteresis loop with a $M_{20\mathrm{kOe}}$ = 15 emu/g, far away from the 80 emu/g expected for bulk cobalt ferrite [15]. A heating temperature in a range from 650 °C to 900 °C provides *M*-*H* curves were a single-loop behavior is observed. However, when the powder was heated to 1000 °C, its *M*-*H* curve exhibited a double-loop shape, possibly due to a very dissimilar particle size as it was previously shown in Figure 4.4.(d).

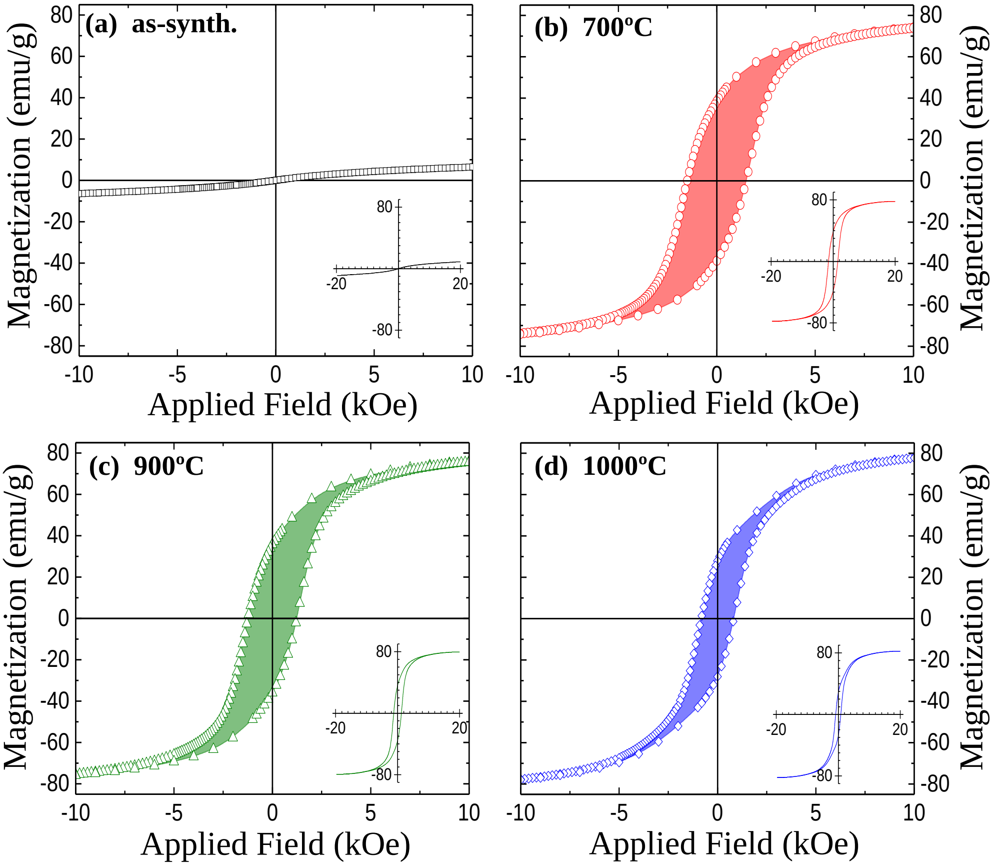

Figure 4.5: *M*-*H* curves measured with VSM at RT, of (a) as-synthesized powder, and after heating at (b) 700 °C, (c) 900 °C and (d) 1000 °C. Inset allows to see how *M* approximates the M_S value.

Parameters extracted from the *M*-*H* curves above are plot in Figure 4.6 as a function of the post-synthesis heating temperature. According the previous XRD and SEM observations, three regions are distinguished; first, the $CoFe_2O_4$ crystallization that occurs when the as-synthesized powder is heated above 214 °C [12], second, a temperature range where grain growth was observed (shadowed with light blue in the figure), and third, where coalescence between previously crystallized nanoparticles occurs (shadowed with light yellow).

All heated samples shows $M_{20\text{kOe}}$ quite close to bulk value of cobalt ferrite saturation magnetization (see Figure 4.6.(a)). Powder heated to 650 °C posses a $M_{20\text{kOe}}$ = 77.0 emu/g, which is linearly increased up to 82.0 emu/g for powder heated to 1000 °C. These results agrees well with data found on literature [16]. Regarding M_r, shown in 4.6.(b), the maximum value was obtained when a heating temperature of 650 °C was used, and it diminished with increased temperature. This might be ascribed to the bigger particle size, leading to a magnetic mul-

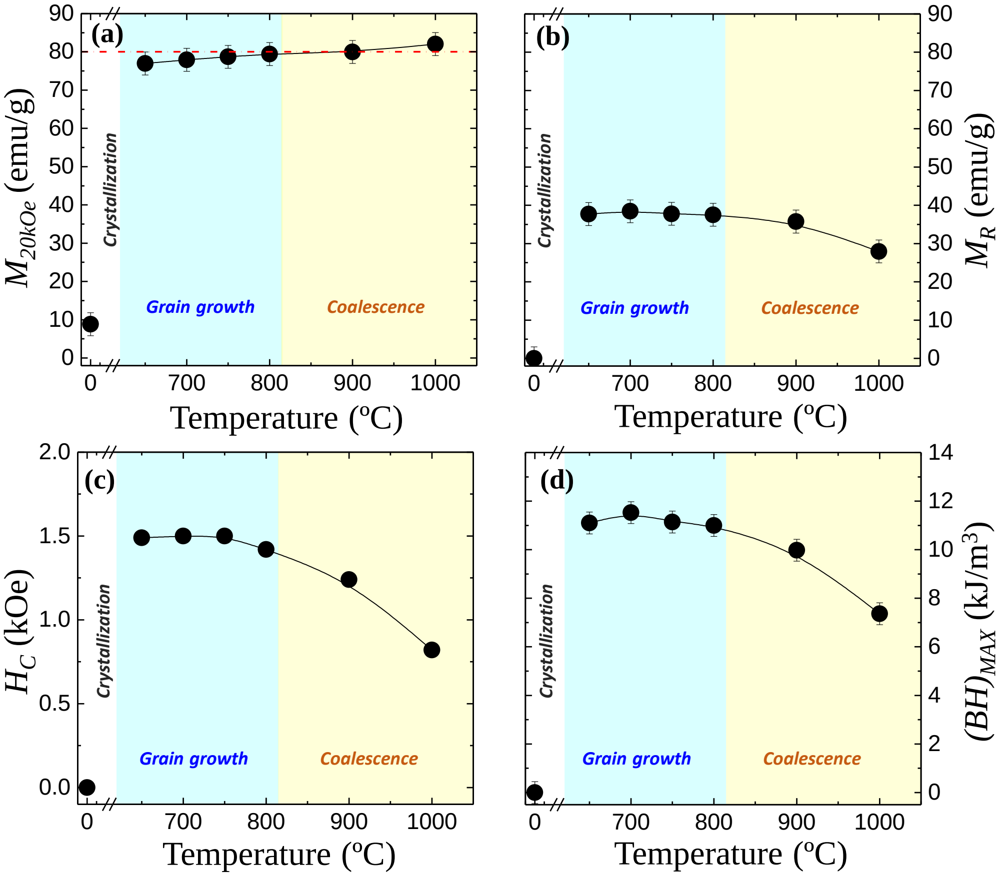

Figure 4.6: Evolution of $CoFe_2O_4$ (a) $M_{20\text{kOe}}$, (b) M_r, (c) H_c and (d) *(BH)max*, as a function of heating temperature. These parameters were extracted from the *M-H* curves measured with VSM at RT previously shown. Blue and yellow shadowed regions indicates where crystallization and coalescence was observed in SEM. Red dash line in (a) is a reference of $CoFe_2O_4$ M_S bulk value.

tidomain state that minimize the magnetostatic energy, and thus a reduced M_r. Furthermore, the ratio M_r/M_{20kOe} is decreased at higher heating temperatures, pointing to the existence of a multidomain magnetic state [17].

Coercivity is represented in Figure 4.6.(c). A larger H_c, is obtained in the early stages of cobalt ferrite inverse spinel phase formation. An H_c = 1.5 kOe is the maximum coercivity of the serie of samples, measured in the powder heated to 650 °C. Coercivity was $H_C \approx$ 1.4 kOe when the heating temperature was in a range from 650 to 750 °C. Notwithstanding, heating above 750 °C provided a diminished H_C value, which was linearly decreased to a minimum of 0.9 kOe obtained after heating to 1000 °C. That might be explained as a consequence of the increased $< D_V >$, well above the magnetic monodomain critical-size (Se Figure 4.3), in addition to the enhanced crystallinity of particles and thus a less density of defects, favoring the domain wall propagation.

Regarding energy product plot in Figure 4.6.(d), the highest $(BH)_{max}$ = 10.5 kJ m^{-3}, resulting from a combination of H_c = 1.5 kOe and M_r = 37.5 emu/g, was measured in the powder heated to 700 °C while the minimum $(BH)_{max}$ = 8 kJ m^{-3} was calculated in the sample heated to 1000 °C, with H_c = 0.8 kOe and M_r = 30 emu/g. Energy product obtained for powder heated to 700 °C (10.5 kJ m^{-3}) is considered a high-quality raw material within the actual state of the art among commercial ferrites.

The possibility to synthesize CoFe$_2$O$_4$ isotropic powders with controlled magnetic properties through the proper election of the annealing temperature of the as-synthesized powder have been demonstrated with this experiment. Optimum magnetic properties for the application of cobalt ferrite as permanent magnet are found in the temperature range 650 °C to 750 °C, resulting in CoFe$_2$O$_4$ isotropic powder with energy products above 10 kJ m^{-3}.

4.2 Repeatability and scalability

Repeatability studies are mandatory to ensure that differences observed in magnetic properties of powders synthesized following the same procedure are not relevant. In this sense, a vast number of reactions were performed during the realization of this thesis, and in this section, different batches are compared in order to validate the process.

Furthermore and in view of a possible implementation of CoFe$_2$O$_4$ powder production in an industrial scale, it is important the optimization of the resources employed on its fabrication in order to reduce the cost of the produced material. An efficient production method of magnetic materials for it use on technological applications involves a compliance between invested resources and the material quality in terms of magnetic properties. The production cost of cobalt ferrite involves the precursors cost and the total energy consumed in the production processes. One of the highest energy consumption processes is the annealing process. In particular, it is relevant to examine the effect of annealing time since the reduction of it might be translated into a cheapest production cost of CoFe$_2$O$_4$ and enhanced quality-to-cost ratio.

Additionally, an increase in the synthesis reaction volume from 1 L to 3 L is performed, and magnetic properties of the obtained CoFe$_2$O$_4$ powders are compared to validate the scalability of the production process. The co-precipitation technique is not only an efficient technique to obtain cobalt ferrite powder, but also a scalable technique since the total amount of the obtained material can be scaled just by increasing the reaction volume.

4.2.1 Experiment description

In this section, different $CoFe_2O_4$ powders are compared. All $CoFe_2O_4$ powders used in this experiment are from different syntheses reactions that were performed following the same fabrication route, which is the co-precipitation method described in section 1.1.1. However, there are some differences in some preparation conditions. The materials used in this comparison are described below:

- **Powder A** is the cobalt ferrite powder previously described in section 4.1.
- **Powder B** is $CoFe_2O_4$ powder synthesized in a 1 L reaction. As-synthesized powder was then heated to 750 °C using air atmosphere in a Carbolite tubular oven model STF 15/450. The heating procedure consisted of an increasing temperature ramp of 10K/min from room temperature to the goal temperature, which was maintained a determined time (1 or 3 hours) before cooling down to room temperature. The rest of preparation conditions of Powder B are identical to those of powder A.
- **Powder C** is $CoFe_2O_4$ powder obtained from two different syntheses reactions done in a volume of 3 L each. The resulting powders, when dried, were mixed, and separated in four batches with a mass of 50 g. Each batch was heated using air atmosphere in a Naberthem muffle oven model L1 1/11/R6. The heating procedure consisted of an increasing temperature ramp of 10K/min from room temperature to the set temperature, which was maintained for 1 hour before cooling down to room temperature. A different temperature was used for each batch, ranging from 700 °C to 1000 °C with 100 °C steps. It has to be remarked that this particular oven might present some overdamping in the temperature ramp control due to its different PID parameters, meaning that it is possible to overpass the set temperature (only for a while) when the oven is reaching this set temperature.

XRD spectra were measured with a Highscore X'pert θ-2θ diffractometer, using a Cu-K_α radiation source. Mean crystallite size was calculated by applying the Equation 1.2 to the four most intense peaks, and the mean average strain was obtained using Equation 1.3.

A Lakeshore 7400 VSM was employed to measure magnetization M-H curves at RT. Parameters extracted from the hysteresis loops include magnetization at maximum applied field of 20 kOe, ($M_{20\mathrm{kOe}}$), remanence (M_r), and coercivity (H_c). Energy product, $(BH)_\mathrm{max}$, has been evaluated in order to quantify the performance as permanent magnets and to assess the suitability of this methodology.

4.2.2 Results and discussion

In section 4.1, the optimum heat treatment temperature to achieve the best magnetic properties combination of $CoFe_2O_4$ powder was found to be in the temperature range 650-750 °C. As-synthesized Powder A was annealed to 700 °C (a microstructural and morphological analysis of this powder was done previously in section 4.1, and as-synthesized Powder B, synthesized in a different reaction, was heated to a temperature of 750 °C. Both batches were heated during 3 hours. In order to validate the repeatability, both powders are compared after being subjected to similar treatments.

Figure 4.7 contains the comparison of XRD and VSM measurements of Powder A and Powder B. First, in Figure 4.7.(a) is observed that both spectra show diffraction peaks originated by CoFe$_2$O$_4$ nanocrystals with comparable intensities. Moreover it is important to note the existence of a small peak corresponding to hematite, α-Fe$_2$O$_3$, observed at the position $2\theta = 33.1$ ° position in powder B spectra. The origin an effect of α-Fe$_2$O$_3$ in the overall magnetic properties will be discussed later. Calculated crystallite size, <D$_v$> of Powders A and B is 57.9 and 63.8 nm respectively, thus a difference of only 8.9 nm in size between both syntheses.

Hysteresis loops depicted in Figure 4.7.(b) are quite similar. Both samples display comparable ($M_{20\mathrm{kOe}}$); Powder A possessed $M_{20\mathrm{kOe}}$ = 77.9 emu/g, which was slightly below $M_{20\mathrm{kOe}}$ = 80.5 emu/g measured on Powder B. The reason of the highest $M_{20\mathrm{kOe}}$ observed in Powder B might be its bigger crystallite size. In addition, this powder contains a small fraction of α-Fe$_2$O$_3$, which is known to be a weak ferromagnetic soft phase above the Morin transition, with a close to zero M_r [18], and in consequence, this will explain why Powder B presented a lower M_r = 36.1 emu/g than Powder A, where exclusively cobalt ferrite was detected and M_r = 38.4 emu/g. H_C = 1.5 kOe was measured for both batches.

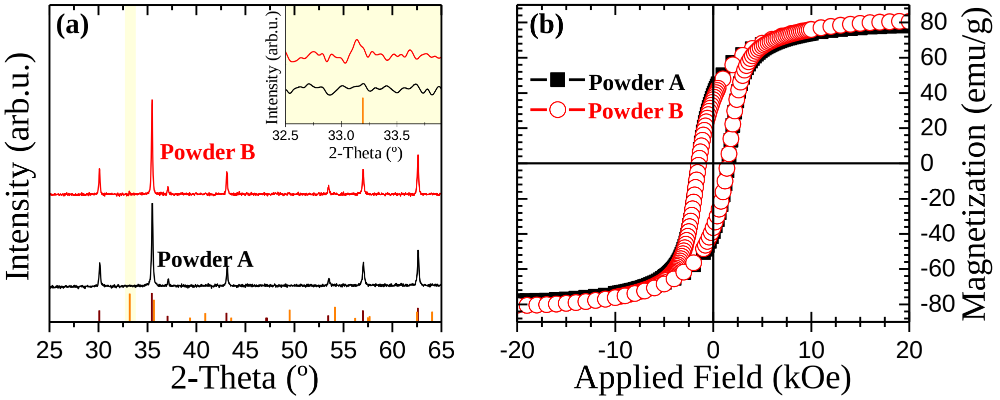

Figure 4.7: Comparison of (a) XRD spectra and, (b) *M-H* curves, of CoFe$_2$O$_4$ powders from different batches; Powder A (black) and Powder B (red). In XRD plot, the inset allows to appreciate α-Fe$_2$O$_3$ difracction peak. Brown lines in the bottom are references of CoFe$_2$O$_4$ diffraction peaks (ref: 00-022-1086), and orange lines correspond to α-Fe$_2$O$_3$ (ref: 01-089-0599)

In order to analyze the effect of the annealing process duration, two batches from the same reaction synthesis (Powder B) were heated to the same temperature (750 °C) during 1 and 3 hours, and the structural and magnetic properties of both were compared. This reduction in annealing time means two thirds of the oven energy consumption, and in consequence the reduced cost of CoFe$_2$O$_4$ production. Figure 4.8 shows a comparison of two samples of powder B heated during 1 and 3 hours.

XRD spectra of both samples are depicted in Figure 4.8.(a). As it was previously noted, it is observed a diffraction peak of hematite indicating that the powder contains a certain amount of α-Fe$_2$O$_3$ in the sample heated during 3 hours, and in the one heated for 1 hour it is observed too. Calculated <D$_v$> = 58.5 nm for the sample annealed during 1 h is a few nanometers smaller than <D_v> = 63.8 nm assessed in the sample annealed during 3 h. ε for both powder is quite similar also, with values of $\varepsilon = 1.5 \cdot 10^{-3}$ and $\varepsilon = 1.4 \cdot 10^{-3}$ for annealing times of 1 h and 3 h respectively. Therefore, in terms of microstructural parameters there is not a great difference when heated to the same temperature for 1 h and 3 h.

Regarding magnetic properties, *M-H* curves of both samples are compared in Figure 4.8.(b). $M_{20\mathrm{kOe}}$ = 80.5 emu/g of sample heated for 1 h is practically identical than $M_{20\mathrm{kOe}}$ = 80.4 emu/g when the treatment was during 3 h. Nevertheless, M_r values measured are 38.7 and 36.1 emu/g for powder heated during 1 and 3 hours respectively. The different content of α-Fe_2O_3, in addition to structural differences such as the smaller crystallite size of powder heated for 1 hour, might be the reason behind this differences in M_r. Coercivity of the sample heated for 1 h is H_C = 1.6 kOe, only 0.1 kOe above H_C = 1.5 kOe measured for sample heated during 3 h. Apart from small quantitative differences found in values of specific parameters, in light of the data it can be concluded that it is more efficient to perform the post synthesis annealing process during 1 hour, since an extended heating time of 3 hours makes not relevant differences on the obtained magnetic properties.

The average amount of powder obtained from a co-precipitation synthesis using a reaction volume of 1 L is 14 grams before the heat treatment. However, after the annealing process, the mass is reduced down to 10 grams. This is due to the evaporation of water or any other organic solvent present in the powder from the synthesis reaction process [19].

The effect of the material production scalability in the magnetic properties of the obtained $CoFe_2O_4$ powder is studied by the contrast of properties measured in Powder A (discussed in section 4.1.4) and Powder C. The "as-synthesized" Powder C presents differences in the preparation route with respect that of Powder A; first, the synthesis reaction was done in several times and using a greater reaction volume (the reaction was scaled to 3 L), second, Powder C was heated during 1 hour instead of 3 hours used for Powder A (as it has been previously

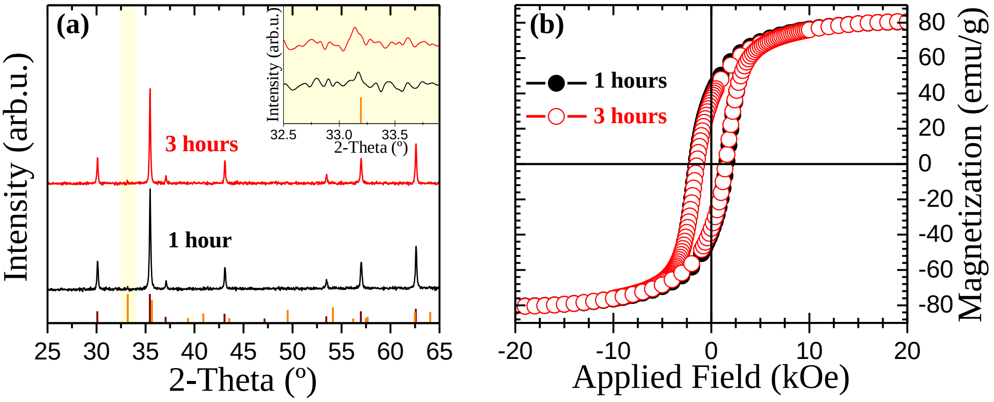

Figure 4.8: Comparison of (a) XRD spectra, and (b) its corresponding *M-H* curves, of $CoFe_2O_4$ powders from Powder B, heated to 750 °C during 1 (black) and 3 hours (red). In XRD plot, the inset allows to appreciate α-Fe_2O_3 diffraction peak. Brown lines in the bottom are references of $CoFe_2O_4$ diffraction peaks (ref: 00-022-1086), and orange lines correspond to α-Fe_2O_3 (ref: 01-089-0599)

shown, there is no relevant difference between both heating times), and third, the amount of mass annealed every time during Powder C heat treatments was significantly higher (50 g) than that used in the heat treatment of Powder A (150 mg) . Finally, the oven used for Powder C heat treatments was a muffle oven, more similar to that employed on industrial plants.

Figure 4.9 contains XRD spectra of Powder C after different temperatures heat treatment of 1 hour. $CoFe_2O_4$ diffraction peaks are observed in all cases, with stronger diffraction peaks in the samples heated to higher temperatures. In Figure 4.9.(b) inset correspond to a zoom where peaks coming from α-Fe_2O_3 are highlighted. Samples heated with temperature in a range 700 to 900 °C displays a small contribution of α-Fe_2O_3. Interestingly, this peak was not observed when the powder was heated to 1000 °C, indicating that α-Fe_2O_3 might be a transitory phase before obtaining pure cobalt ferrite. For instance, one synthesis method of $CoFe_2O_4$ consist in the calcination of α-Fe_2O_3 with Co_3O_4 [20].

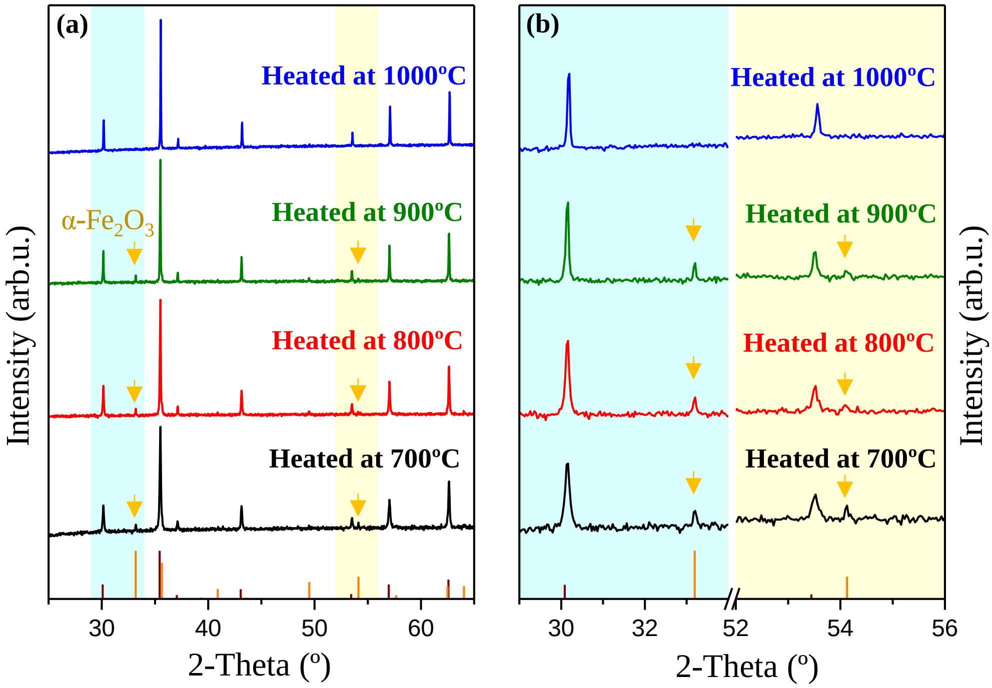

Figure 4.9: Comparison of (a) XRD spectra of Powder C after heating to different temperatures, and (b) a zoom in the regions 29 ° < 2θ < 34 ° and 52 ° < 2θ< 56 °, to allow the appreciation of α-Fe_2O_3 diffraction peaks. From bottom to top: Powder C after a heat treatment to 700, 800, 900 and 1000 °C. Brown lines in the bottom are references of $CoFe_2O_4$ diffraction peaks (ref: 00-022-1086), and orange lines correspond to α-Fe_2O_3 (ref: 01-089-0599).

Calculated values of <D$_v$> and ε as a function of the heating temperature are depicted in Figure 4.10, in addition to a comparison with the evolution of the same parameters of Powder A, previously discussed. By comparing <D$_v$> of powders heated to the same temperature (see Figure 4.9.(a)), one can see that crystallite size of Powder C is bigger than that of Powder

A heated to the same temperature. Furthermore, the same deviation is observed in ε values. This might be due to the different ovens used for the heat treatment since it is normal to have a mismatch in temperatures, as well as the different heating and cooling rates. In addition, the increased amount of as-synthesized powder mass heated on each Powder C heat treatment might be playing a role. In any case, the evolution of both, crystallite size and strain with heating temperature of both batches displays a similar trend, with monotonic increase with increased temperature observed in <D$_v$>, and a decline tendency of ε at higher heating temperatures.

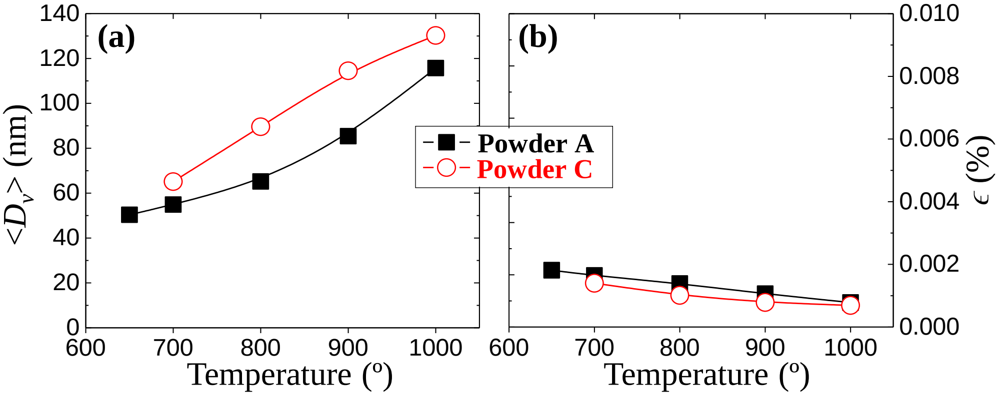

Figure 4.10: Mean crystallite size, <D$_v$>, and mean average strain, ε, as a function of annealing temperature, calculated from XRD spectra. Powder A (black) synthesized at a laboratory scale, is compare with Powder C (red), synthesized in a 6-fold increased volume reaction.

Figure 4.11 depicts a comparison of hysteresis loops measured in Powders A and C when heated to the same temperature. It is observed comparable demagnetization curves consisting in a single-loop behavior, in exception to the M-H curves measured in samples heated to 1000 °C, where a double-loop in both samples can be appreciated (see Figure 4.11.(d)). As it was proposed before in section 4.1.3, this might be a consequence of particles coalescence during growth, since this type of hysteresis loops is characteristic of materials with a dissimilar particle size distribution. In this case, both powders are constituted by nanoparticles that seems to be monocrystals, and polycrystalline microparticles formed by melted nanoparticles (see Figure 4.4.(d)).

Parameters extracted from M-H curves of both batches are represented in Figure 4.12 as a function of the heating temperature. At a first glance, the same tendency of magnetic properties with heating temperature is observed but with some quantitative differences. First, Powder A magnetization values $M_{20\mathrm{kOe}}$ and M_r are above that observed in Powder C. The existence of α-Fe$_2$O$_3$ in Powder C might be the reason of the reduced, since it means a lower percentage of cobalt ferrite. H_C in Powder C is several hundreds oesterds lower than Powder A as well, probably due to its bigger $<D_V>$ (see Figure 4.10). These slight differences in M_r and H_C results in a greater energy product in Powder A, which possess a maximum $(BH)_\mathrm{max}$ = 11.5 kJm^{-3} was measured in the sample heated to 700 °C, resulting from the combination of M_r = 38.4 emu/g and H_C = 1.5 kOe. In case of Powder C, after heating to 700 °C, a M_r = 34.0 emu/g and H_C = 1.3 kOe was measured providing an energy product $(BH)_\mathrm{max}$ = 9.0 kJm^{-3}.

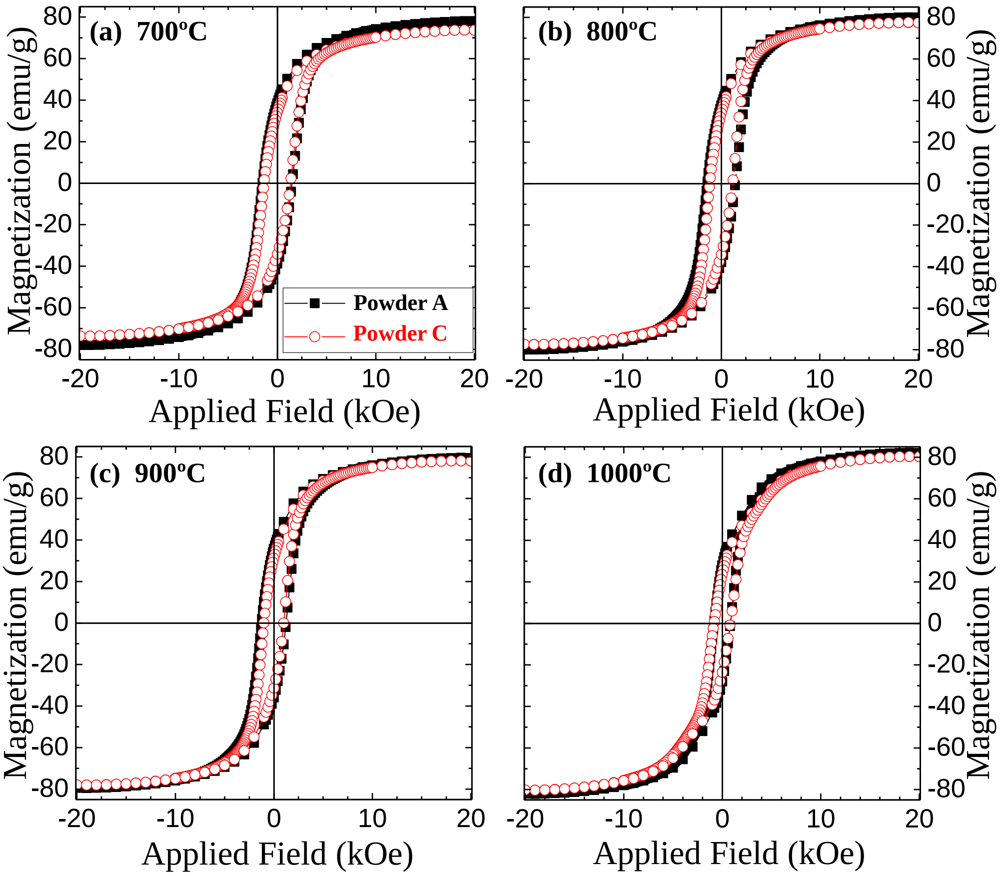

Figure 4.11: *M-H* curves measured with VSM at RT of Powder A and Powder C after heating at different temperatures. Comparison of curves obtained after heating to (a) 700 °C, (b) 800 °C, (c) 900 °C and (d) 1000 °C.

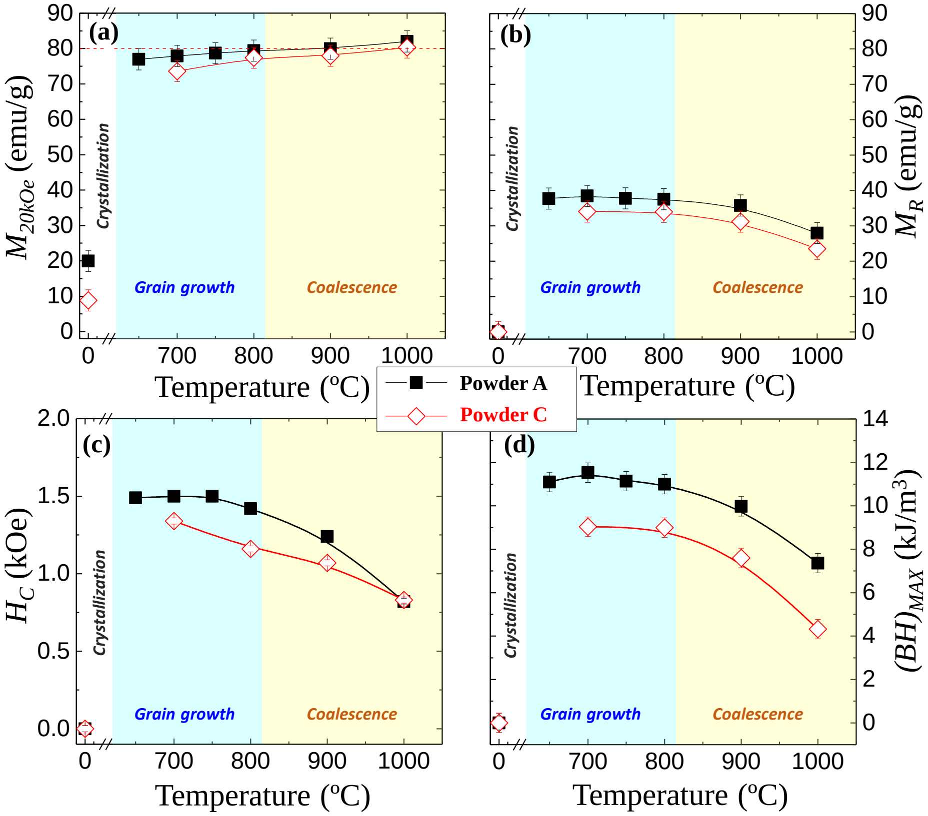

Figure 4.12: Comparison of the evolution of magnetic properties at RT with the heating temperature of $CoFe_2O_4$ Powder A (black full squares) and Powder C (red empty circles). Parameters extracted from M-H are: (a) $M_{20\mathrm{kOe}}$, (b) M_r, (c) H_c and (d) $(BH)_{max}$. Blue and yellow shadowed regions indicates where crystallization and coalescence was observed in SEM. Red dash line in (a) is a reference of $CoFe_2O_4$ M_S bulk value.

4.3 Conclusions

A systematic study of the magnetic properties obtained in $CoFe_2O_4$ powder, synthesized by the co-precipitation method, as a function of a post-synthesis heat treatment temperature have been presented in this section, demonstrating the possibility to synthesize $CoFe_2O_4$ isotropic powders with controlled magnetic properties through the proper election of the post-synthesis annealing temperature. The microstructural characterization reveals that the higher heating temperature, the bigger $< D_V >$ and lower ε. An annealing temperature of 650 °C is sufficient to achieve the crystallization of $CoFe_2O_4$ as-synthesized powder, emphasizing that the highest temperature of the annealing process, the lowest mean strain and biggest mean crystallite size. The correlation between morphology and microstructure allows to understand the behavior of this material. Three processes were observed as a function of the heating temperature; crystallization, grain growth and coalescence. Cobalt ferrite crystallization occurs at 214 °C, and heating temperatures in the range from 650 °C to 800 °C caused grain growth. Higher temperatures caused coalescence between $CoFe_2O_4$ particles; only SEM images of powder heated to 1000 °C shows clearly sintered polycrystalline powder, however, from the magnetic characterization it can bee deduced that the coalescence stage is initiated when the heating temperature is above 800 °C. Furthermore, XRD reveals that crystallite size increases with higher temperature. The second process observed at heating temperatures above 800 °C is coalescence, consisting in the melting of grains forming polycrystalline particles with sizes in the micron size regime. Optimum magnetic properties for the application of cobalt ferrite as permanent magnet are found in the temperature range 650 °C to 750 °C. Specific, the best magnetic properties were found in the powder heated to 700 °C, which posses an $(BH)_{max}$ = 10.5 kJ m^{-3}, resulting from a combination of H_c = 1.5 kOe and M_r = 37.5 emu/g.

Repeatability experiments have been discussed as well. Powders synthesized with the same method but in different moments were compared, finding that magnetic properties obtained are very similar between batches. Although some of them might present a reduced percentage α-Fe_2O_3, it is not relevant in the magnetic performance. The post-synthesis heat treatment was optimized, demonstrating that a heat treatment during 1 hour is sufficient to achieve $CoFe_2O_4$ NPs formation. Furthermore, scalability have been demonstrated to be feasible; a 21-fold increase in the amount of as-synthesized powder was achieved by simply increasing the volume of the synthesis reaction (14 g from a 1 L synthesis reaction, 300 g from two 3 L syntheses reactions)

References

[1] Zhan Jie Wang, Yan Na Chen, Fan Zhang, Yang Liu, Rui Liang Su, and Li Zhi Shi *Hydrothermal Synthesis of $CoFe_2O_4$ Nanoparticles and their Magnetic Properties*. in: *Advances in Textile Engineering and Materials III* ***821***, Advanced Materials Research Trans Tech Publications, Dec. 2013, 1358–1361 (cit. on p. 47)

[2] Henrik L Andersen and Mogens Christensen *In situ powder X-ray diffraction study of magnetic $CoFe_2O_4$ nanocrystallite synthesis*. in: Nanoscale **7**,8 (2015), 3481–3490 (cit. on p. 47)

[3] Amal M. Ibrahim, M.M. Abd El-Latif, and Morsi M. Mahmoud *Synthesis and characterization of nano-sized cobalt ferrite prepared via polyol method using conventional and microwave heating techniques*. in: Journal of Alloys and Compounds ***506***,1 (2010), 201–204 (cit. on p. 47)

[4] A Hunyek, Chitnarong Sirisathitkul, and P Harding *Synthesis and Characterization of* $CoFe_2O_4$ *particle by PVA sol-gel method*. in: *Advanced Materials Research* ***93***, Trans Tech Publ 2010, 659–663 (cit. on p. 47)

[5] Adrian Quesada, Cecilia Granados-Miralles, Alberto López-Ortega, Sergey Erokhin, Elisabetta Lottini, Javier Pedrosa, Alberto Bollero, Ana M Aragón, Fernando Rubio-Marcos, Marian Stingaciu, et al. *Energy Product Enhancement in Imperfectly Exchange-Coupled Nanocomposite Magnets*. in: Advanced Electronic Materials (2016) (cit. on p. 47)

[6] S. Prasad, A. Vijayalakshmi, and N. S. Gajbhiye *Synthesis of Ultrafine Cobalt Ferrite by Thermal Decomposition of Citrate Precursor*. in: Journal of Thermal Analysis and Calorimetry ***52***,2 (1998), 595–607 (cit. on p. 47)

[7] Le T Lu, Ngo T Dung, Le D Tung, Cao T Thanh, Ong K Quy, Nguyen V Chuc, Shinya Maenosono, and Nguyen TK Thanh *Synthesis of magnetic cobalt ferrite nanoparticles with controlled morphology, monodispersity and composition: the influence of solvent, surfactant, reductant and synthetic conditions*. in: Nanoscale **7**,46 (2015), 19596–19610 (cit. on p. 47)

[8] Yue Zhang, Zhi Yang, Di Yin, Yong Liu, ChunLong Fei, Rui Xiong, Jing Shi, and GaoLin Yan *Composition and magnetic properties of cobalt ferrite nano-particles prepared by the co-precipitation method*. in: Journal of Magnetism and Magnetic Materials ***322***,21 (2010), 3470–3475 (cit. on p. 47)

[9] Francisco Augusto Tourinho, Raymonde Franck, and René Massart *Aqueous ferrofluids based on manganese and cobalt ferrites*. in: Journal of Materials Science ***25***,7 (1990), 3249–3254 (cit. on p. 47)

[10] Yeong Il Kim, Don Kim, and Choong Sub Lee *Synthesis and characterization of* $CoFe_2O_4$ *magnetic nanoparticles prepared by temperature-controlled coprecipitation method*. in: Physica B: Condensed Matter ***337***,1 (2003), 42–51 (cit. on p. 47)

[11] Debabrata Moitra, Subhenjit Hazra, Barun Kumar Ghosh, RK Jani, MK Patra, Sampat Raj Vadera, and Narendra Nath Ghosh *A facile low temperature method for the synthesis of* $CoFe_2O_4$ *nanoparticles possessing excellent microwave absorption properties*. in: RSC Advances ***5***,63 (2015), 51130–51134 (cit. on p. 47)

[12] TR Tatarchuk, EV Boyko, IP Yaremiy, BI Rachiy, and SV Fedorchenko *Synthesis, Crystal Chemistry and Antistructure Modelling of* $CoFe_2O_4$ *Nanoparticles Prepare by Citrat Sol-Gel Method*. in: Physics and Chemistry of Solid State ***15***,4 (2014), 792–797 (cit. on pp. 48, 52)

[13] CN Chinnasamy, B Jeyadevan, K Shinoda, K Tohji, DJ Djayaprawira, M Takahashi, R Justin Joseyphus, and A Narayanasamy *Unusually high coercivity and critical single-domain size of nearly monodispersed* $CoFe_2O_4$ *nanoparticles*. in: Applied physics letters ***83***,14 (2003), 2862–2864 (cit. on p. 48)

[14] WS Chiu, Shahidan Radiman, R Abd-Shukor, MH Abdullah, and PS Khiew *Tunable coercivity of $CoFe_2O_4$ nanoparticles via thermal annealing treatment*. in: *Journal of Alloys and Compounds* ***459***,1 (2008), 291–297 (cit. on p. 49)

[15] J Ding, T Reynolds, WF Miao, PG McCormick, and R Street *High magnetic performance in mechanically alloyed Co-substituted Fe3O4*. in: *Applied physics letters* ***65***,24 (1994), 3135–3136 (cit. on p. 51)

[16] J Ding, PG McCormick, and R Street *Magnetic properties of mechanically alloyed $CoFe_2O_4$*. in: *Solid state communications* ***95***,1 (1995), 31–33 (cit. on p. 52)

[17] M Chithra, CN Anumol, Baidyanath Sahu, and Subasa C Sahoo *Exchange spring like magnetic behavior in cobalt ferrite nanoparticles*. in: *Journal of Magnetism and Magnetic Materials* ***401***, (2016), 1–8 (cit. on p. 53)

[18] Franz Bødker, Mikkel F Hansen, Christian Bender Koch, Kim Lefmann, and Steen Mørup *Magnetic properties of hematite nanoparticles*. in: *Physical Review B* ***61***,10 (2000), 6826 (cit. on p. 55)

[19] GA El-Shobaky, AM Turky, NY Mostafa, and SK Mohamed *Effect of preparation conditions on physicochemical, surface and catalytic properties of cobalt ferrite prepared by coprecipitation*. in: *Journal of Alloys and Compounds* ***493***,1 (2010), 415–422 (cit. on p. 56)

[20] Karen S Martirosyan, Long Chang, James Rantschler, Sakhrat Khizroev, Dan Luss, and Dmitri Litvinov *Carbon combustion synthesis and magnetic properties of cobalt ferrite nanoparticles*. in: *IEEE transactions on magnetics* ***43***,6 (2007), 3118–3120 (cit. on p. 57)

Chapter 5

High coercive $CoFe_2O_4$ obtained with HEBM

The possibility of developing high coercive $CoFe_2O_4$ isotropic powder by a novel flash-milling route is demonstrated in this chapter. Milling times as short as three minutes are reported for the first time to be sufficient to refine microstructure and to induce microstrain, which act efficiently providing $CoFe_2O_4$ powder with an increased coercivity. This is achieved exclusively through microstructural modification. Milling times as short as 180 seconds have resulted in a 5-fold increase in H_C, with a maximum achieved value of 4.7 kOe. Moreover, cobalt ferrite with $(BH)_{\max}$ = 14.8 kJm^{-3}, a 76% higher with respect that of the initial powder, was achieved after 30 seconds milling.In addition, $CoFe_2O_4$ powders with different initial microstructure subjected to the same milling process are analyzed, allowing the right choice of processing parameters for $CoFe_2O_4$ as a function of the magnetic property to be enhanced.

Finally, isotropic cobalt ferrite powder processed by dry and surfactant assisted (wet) ball milling is compared, where the use of surfactant is shown to be advantageous in the formation of a more homogeneous structure constituted by non-agglomerated and strained nanoparticles. The main advantage of the method here proposed is the possibility of producing large amounts of cobalt ferrite with enhanced magnetic properties in extremely short processing times.

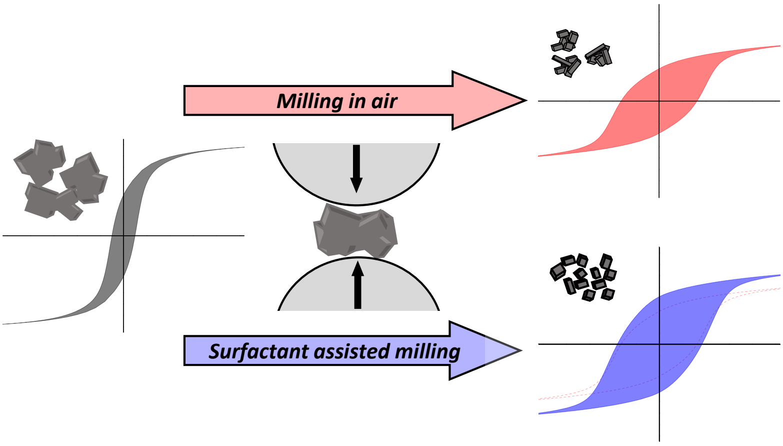

Figure 5.1: Sketch of chapter 5: High coercive $CoFe_2O_4$ powders are obtained by dry and surfactant assisted high energy ball milling in record times.

5.1 HEBM of CoFe$_2$O$_4$ in air

Coercivity in cobalt ferrite can be enhanced by controlling the particle size distribution and by inducing high-level residual strain through mechanical milling. For instance, CoFe$_2$O$_4$ powders after milling for 1.5 hours have shown record values of coercivity of about 5.1 kOe and an energy product $(BH)_{\mathrm{max}}$ = 15.9 kJm^{-3} at RT [1, 2]. A milling time of 1.5 hours is a significant advance in comparison with typical durations of dozens of hours, but still excessively long when considering its implementation in permanent magnet manufacturing plants.

A detailed and systematic study of the influence of an ultra-fast ball-milling process on the magnetic properties of co-ferrite powder is presented in this section. In particular, structural, morphology, and magnetic properties are discussed as a function of milling time, providing a comprehensive correlation between them. High coercive isotropic co-ferrites, with energy products up to 12.5 kJ m^{-3} and $H_c = 4.7$ kOe at room temperature were obtained by this milling method in times as short as 180 seconds. This efficient methodology provides a technological key to manage the production of isotropic powders in processing times of only a few minutes.

5.1.1 Experiment description

Following the co-precipitation method, two syntheses reactions with a volume of 3 L each were preformed. Powders of both reactions were mixed when dried, obtaining a total amount of 300 g of as-synthesized powder. A mass of 50 g of the total as-synthesized powder was heated to 1000 °C. The heating procedure was carried out with a Naberthem muffle oven model L1 1/11/R6, using a temperature ramp of 10K/min, from room temperature to 1000 °C, which was maintained for 1 hour before cooling down to room temperature. Properties of this powder were previously discussed in section 4.2, named 'Powder C'.

HEBM experiments at different milling times with a total duration of 30, 60, 90, 120 and 180 seconds were performed on 4 grams of the aforementioned CoFe$_2$O$_4$ powder, using a high-energy ball milling equipment Pulverizete 7 premium line from Fritsch at a speed of 900 rpm and a ball-to-powder ratio of 40:1. The powder was milled in air atmosphere, using tungsten carbide milling media (balls and vessel) to enhance the impact energy, i.e. accelerate an efficient milling process, due to the larger density of tungsten carbide (14.95 g/cm^3) by comparison with that of steel (7.8 g/cm^3).

XRD spectra were measured with a Highscore X'pert θ-2θ diffractometer, using Cu-K_α radiation source. Mean crystallite size was calculated by applying the Equation 1.2 to the four most intense peaks and averaging the value, as well as the mean average strain that was obtained with the same method using Equation 1.3. These parameters extracted from XRD data are analyzed as a function of milling time.

SEM images were collected with a Carl-Zeiss Auriga microscope at a filament voltage of 3 kV, and used to obtain morphological information of CoFe$_2$O$_4$ powder before and after milling.

A Lakeshore 7400 VSM was employed to measure magnetization M-H curves at room temperature. The parameters extracted from the hysteresis loops include magnetization at maximum applied field of 20 kOe ($M_{20\mathrm{kOe}}$), remanence (M_r), and coercivity (H_c). Energy product, $(BH)_{\mathrm{max}}$, has been evaluated, in order to quantify the performance as permanent magnets and to assess the suitability of this methodology.

5.1.2 Structural analysis

Representative XRD patterns of initial powder spectra and after milling during 30, 90 and 180 seconds are compared in Figure 5.2. Only CoFe$_2$O$_4$ reflection peaks are observed, indicating the absence of any other phase or possible contamination during the milling process. Milling for 30 and 180 s results in a progressive broadening of the reflection peaks due to refinement of the microstructure. It is observed a broadening of Bragg's peaks in addition to a decrease of its intensity, which is indicative of the CoFe$_2$O$_4$ crystallite size reduction and induced strain as a consequence of high energy impacts that occurs during the milling process. Figure 5.2.(b) allows to see how the intensity of diffraction peaks is decreased, as well as its displacement in 2θ position due to induced strains.

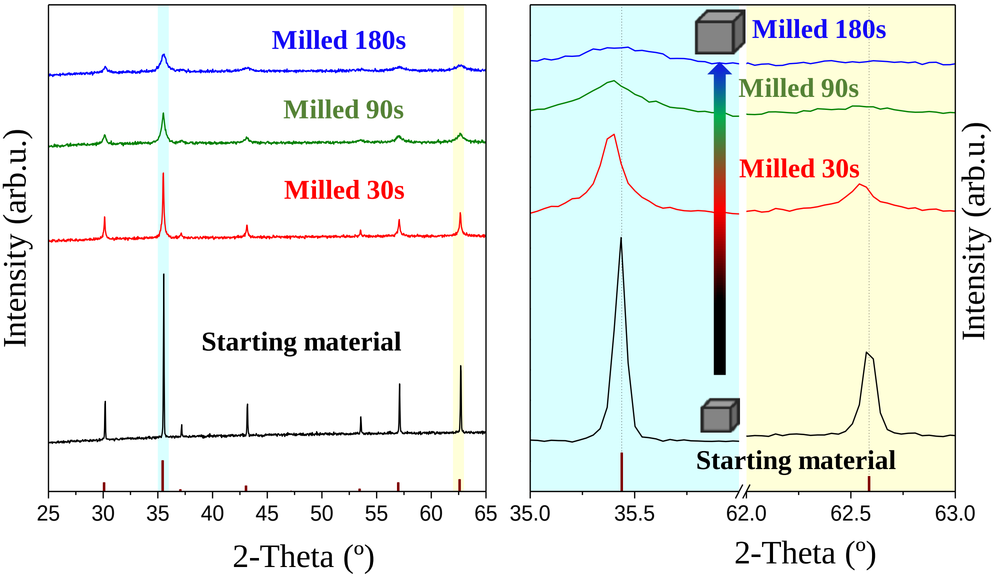

Figure 5.2: The (a) XRD spectra of initial material (black) and after HEBM in air. From bottom to top: as-synthesized powder and after milling during 30, 90 and 180s. Additionally, (b) a zoom of the shadowed areas ease the observation of diffraction peaks displacement in 2θ position as well as peak broadening. Brown lines in the bottom are references of CoFe$_2$O$_4$ diffraction peaks (ref: 00-022-1086).

Figure 5.3 display the evolution of the mean crystallite size, $<D_V>$, and microstrain, ε, of the starting and the as-milled materials. The estimated average crystallite size of the starting powder is $<D_V> = 117.6$ nm, which is reduced down one order of magnitude to $<D_V> = 15.9$ nm after only 90 seconds of milling, well below the CoFe$_2$O$_4$ monodomain regime (40 nm). [3] Further milling to 180 seconds provides CoFe$_2$O$_4$ powder with a crystallite size value of 9.1 nm. Regarding ε, the positive sign of calculated strains indicates a tensile strain which is induced during mechanical milling. ε values follows a monotonic increase as a function of milling time, from $\varepsilon = 0.5 \cdot 10^{-3}$ for the starting material prior to milling to $\varepsilon = 9 \cdot 10^{-3}$ after milling for 180 seconds. This mean that with this method, it is possible to introduce strain in CoFe$_2$O$_4$ nanocrystals at a rate of $47 \cdot 10^{-6}$ of mean strain per second. Longer milling times might cause the amorphization of CoFe$_2$O$_4$ that could promote low M [1, 2, 4].

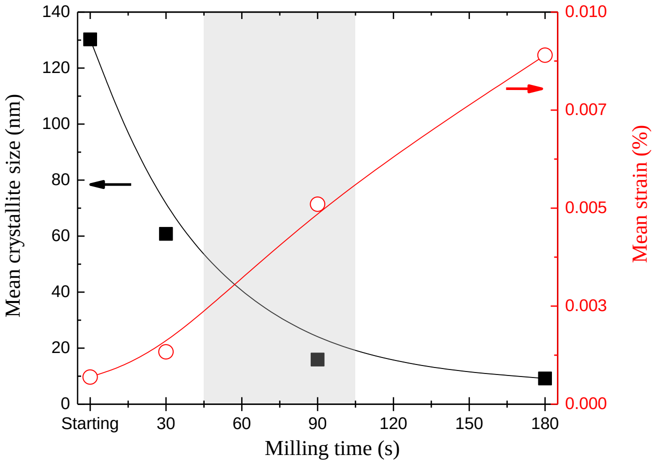

Figure 5.3: Evolution with milling time of mean crystallite size $< D_v >$ (black full squares), and mean strain ε (red empty circles). The shadowed region correspond to the area with maximum energy product (see Figure 5.6)

5.1.3 Morphological analysis

The morphology of the starting powder and after different milling times can be visualized in SEM images depicted in Figure 5.4. It is clearly observed in Figure 5.4.(a) that the starting powder is constituted by polycrystalline micron-size particles with well-defined crystalline grains, formed due to particles coalescence during the heating process, as it has been reported previously for sintered CoFe$_2$O$_4$ material [5].

SEM images obtained of powders milled for 30 seconds (Figure 5.4.(b)) reveals the coexistence of two different particles size distributions; there are newly created particles in the submicrometer regime and initial micron-size particles not milled yet, since such a short milling time is not sufficient to refine the powder microstructure and resulting in a mixture of both type of particles. Homogenization of the material is guaranteed through extended milling time of 180 s (Figure 5.4.(e)).

The efficiency of this ultrafast milling method in obtaining a refined and homogeneous powder in a short milling time is evidenced when comparing particle size of the starting material (Figure 5.4.(a)) with that obtained after 30 and 180 seconds of milling (Figs 5.4.(c) and (e), respectively).

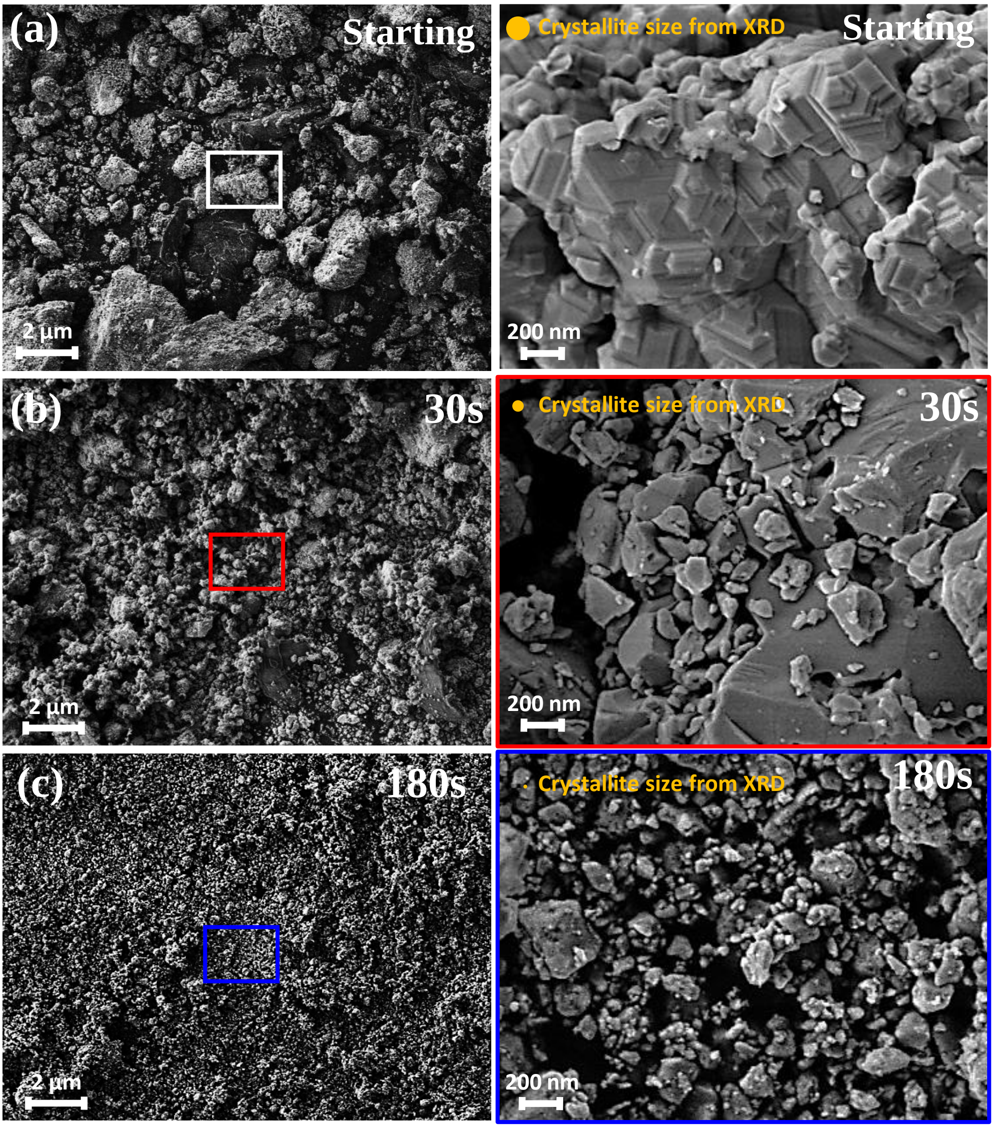

Figure 5.4: SEM images of (a) starting CoFe$_2$O$_4$ powders, and after HEBM for (b) 30 seconds and (c) 180 seconds. Scale bar: 2 μm. Right column: Magnified images (scale bar: 200 nm). Yellow circle in the left top corner is a visual indication of the previously calculated $< D_v >$.

5.1.4 Magnetic properties analysis

Room-temperature magnetization curves of the starting CoFe$_2$O$_4$ powder and after different milling times are represented in Figure 5.5. At a first glance, there is a strong increase in H$_C$ with increasing the milling time, accompanied by a change in the shape of the *M*-*H* curve. The two-steps hysteresis loop measured after milling for 30 seconds (Figure 5.5.(b)) is characteristic of a magnetic material with an inhomogeneous microstructure, consisting in particles with a broad particle size distribution. This is in good agreement with SEM observations (Figure 5.4.(b)) where large (up to 1μm) and small (nanometric) particles are observed. Milling for 90 s leads to a single hysteresis loop (Figure 5.5(c)) while 180 s is sufficient to homogenize the microstructure (Figure 5.4.(c)) resulting in a single hysteresis loop (Figure 5.5(b)).

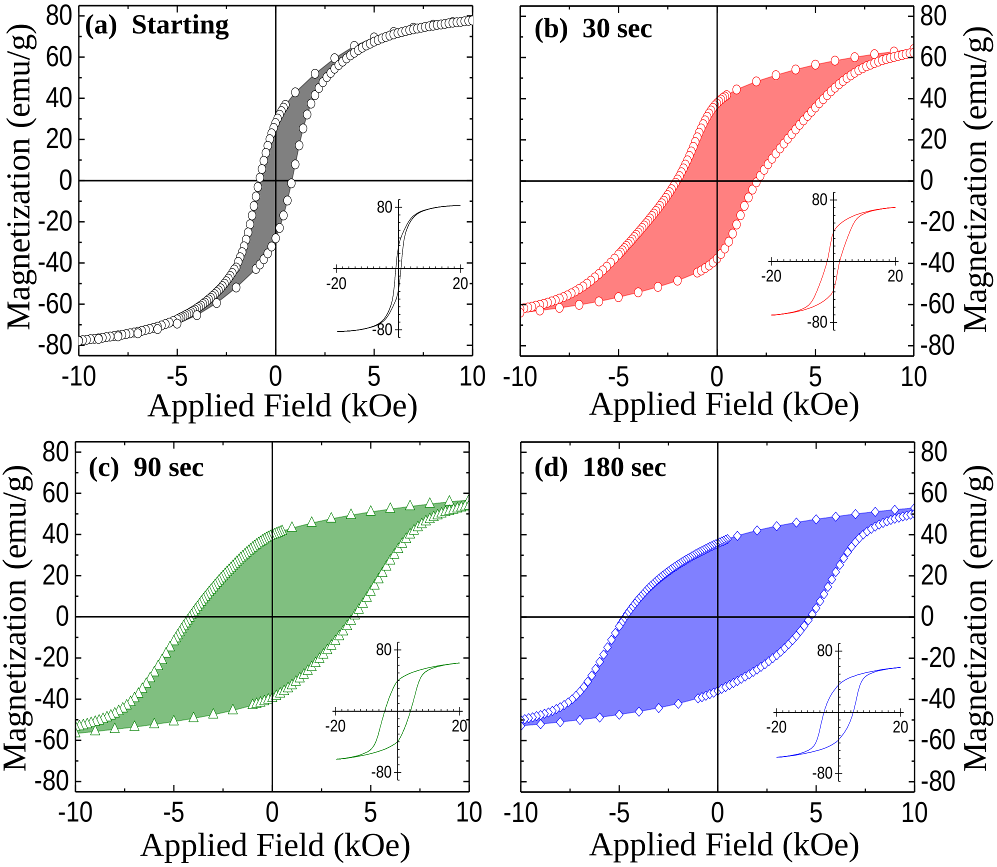

Figure 5.5: *M*-*H* curves measured at room temperature with VSM of: (a) starting CoFe$_2$O$_4$, and after milling for (b) 30 seconds, (c) 90 seconds, and (d) 180 seconds. Inset allows to see how *M* approximates the M_S value.

The evolution of the CoFe$_2$O$_4$ powder magnetic properties as a function of milling time, extracted from the measured M-H curves, are illustrated in Figure 5.6. M_{20kOe} decrease monotonically with extended milling times, from M_{20kOe} = 80.4 emu/g for the initial powder to M_{20kOe} = 58.6 emu/g after milling for 180 seconds. This observation can be explained as an effect of surface-to-volume ratio modification due the size reduction undergone on initial micron-size particles, as well as its partial amorphization during extended milling. An increased surface-to-volume ratio will evidence the effect of the "dead layer" (due to spin disorder in a surface shell region contributing less to the magnetization than the core due to spin fluctuations at the surface) originating the decrease in M_{20kOe} and M_r [6–8]. Interestingly, and contrary to the trend followed by M_{20kOe}, remanence magnetization increased from M_r = 23.5 emu/g for the starting material to 37.7 and 39.9 emu/g after milling for 30 and 60 s, respectively, prior to a parallel to M_{20kOe} decrease for longer milling times.

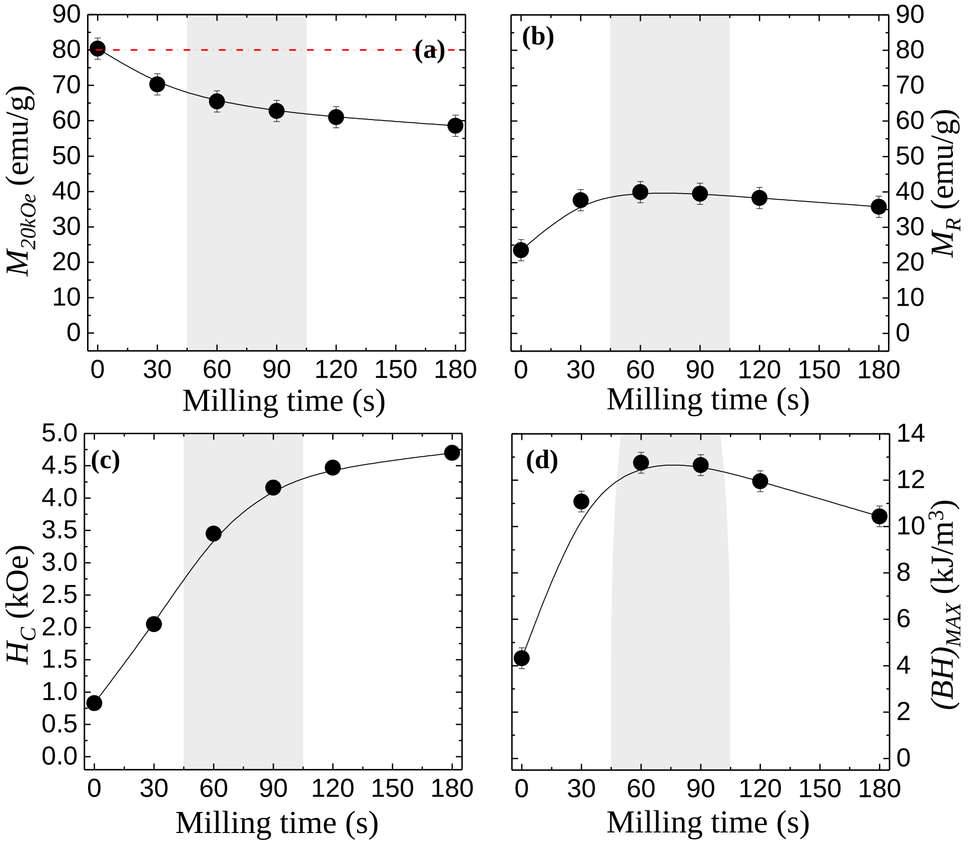

Figure 5.6: Evolution with HEBM time of CoFe$_2$O$_4$ powder magnetic properties, (a) Magnetizations M_{20kOe}, (b) M_r, (c) coercivity H_c, and (d) energy product $(BH)_{max}$. Red dashed line indicates the M$_S$ = 80 emu/g of bulk CoFe$_2$O$_4$. Shadowed area indicates the interval where higher $(BH)_{max}$ was obtained.

Milling for 90 s is sufficient to achieve a coercivity well above 4 kOe while extending this milling time to 180 s results in a 5.5 times increase in H_c from 0.83 kOe for the starting material to H_c = 4.7 kOe for the as-milled powder. This large increase in coercivity is the combined result of a reduced mean crystallite size and the induced strain during milling (Figure 5.3) that results in the creation of defects acting as pinning centers during magnetization reversal. [2] The correlation between magnetic anisotropy and coercivity will be further studied in Chapter 7.

A maximum $(BH)_{\mathrm{max}}$ = 12.8 $\mathrm{kJm^{-3}}$ was attained after milling for 60 s. Milling time up to 180 s kept increasing coercivity, but the progressive decrease in magnetization resulted in reduced $(BH)_{\mathrm{max}}$. As it is reported in other experiments, longer milling times produce as well a coercivity reduction [2], therefore resulting detrimental for $(BH)_{\mathrm{max}}$. Furthermore, and by using this extremely short processing time, a combination of magnetic properties for high coercive Co-ferrite powders with H_c = 4.7 kOe, M_r = 35.8 emu/g was been obtained in only 180 seconds milling.

For the aim of this study, it is important to highlight that while other studies present same trend of increasing coercivity with increasing milling time [1, 4], here is shown the possibility of reducing the timescale of the process from several hours to a few minutes by using HEBM.

5.2 Influence of starting material microstructure

A comparative study of HEBM on $CoFe_2O_4$ powders with different initial microstructure is discussed in this section. By using a determined temperature in the post-synthesis heat treatments, it is possible to control the microstructure of the obtained cobalt ferrite powder (see Chapter 4). The fact that all batches comes from the same as-synthesized powder, in addition to the use of identical milling parameters allows the discrimination of the effect of structural modifications of $CoFe_2O_4$ such as crystallite size and induced strain on its magnetic properties.

5.2.1 Experiment description

Following the co-precipitation method, two syntheses reactions with a volume of 3 L each were preformed. Powders of both reactions were mixed when dried, obtaining a total amount of 300 g of as-synthesized powder. The as-synthesized powder was divided in for batches with a mass of 50 g each, and it were heated to a different temperature each, ranging from 700 to 1000 °C. The characterization and properties of these materials were previously discussed, named 'Powder C' in section 4.2. Batches used in this experiment will be referred as:

- **Powder A**, for the batch heated to 700 °C.
- **Powder B**, for the batch heated to 800 °C.
- **Powder C**, for the batch heated to 900 °C.
- **Powder D**, for the batch heated to 1000 °C, and previously discussed in section 5.1.

The heating procedure was performed in a Naberthem muffle oven model L1 1/11/R6. In this case, the heating procedure consisted of an increasing temperature ramp of 10K/min from room temperature to the goal temperature which was maintained for 1 hour before cooling down to room temperature. This treatment allows to crystallize the inverse spinel structure of $CoFe_2O_4$ with different crystallite sizes and strains for every batch as a function of the temperature used in the heat treatment (see chapter 4, Figures 4.3 and 4.4).

HEBM experiments at different milling times with a total duration of 30, 60, 90, 120 and 180 seconds were performed on 4 grams of each $CoFe_2O_4$ powder batch, using a high-energy ball milling equipment Pulverizete 7 premium line from Fritsch at a speed of 900 rpm and a ball-to-powder ratio of 40:1. The powders were milled in air atmosphere, using tungsten carbide milling media (balls and vessel) to enhance the impact energy, i.e. accelerate an efficient milling process, due to the larger density of tungsten carbide (14.95 g/cm^3) by comparison with that of steel (7.8 g/cm^3).

XRD spectra were measured with a Highscore X'pert θ-2θ diffractometer, with Cu-K_α radiation source. Mean crystallite size was calculated by applying the Equation 1.2 to the four most intense peaks and averaging the value, as well as the mean average strain that was obtained with the same method using Equation 1.3. These parameters extracted from XRD data are analyzed as a function of milling time.

SEM images were collected with a Carl-Zeiss Auriga microscope at a filament voltage of 3 kV, and used to obtain morphological information of $CoFe_2O_4$ powder before and after milling.

A Lakeshore 7400 VSM was employed to measure magnetization M-H curves at room temperature. The parameters extracted from the hysteresis loops include magnetization at maximum applied field of 20 kOe ($M_{20\mathrm{kOe}}$), remanence (M_r), and coercivity (H_c). Energy product, $(BH)_\mathrm{max}$, has been evaluated, in order to quantify the performance as permanent magnets and to assess the suitability of this methodology.

5.2.2 Structural and compositional analysis

The XRD spectra of every batch, with the initial powder pattern and its evolution after different milling times, are represented in Figure 5.7. As it was previously shown in section 4.1.2, the higher heating temperature applied to as-synthesized powder, the stronger diffraction peaks of $CoFe_2O_4$ observed. Importantly, even if all batches comes from the same synthesis reaction, batches heated in a temperature range from 700 °C to 900 °C present diffraction peaks at 2θ = 33.1 °C identified as $\alpha - Fe_2O_3$ (discussed in section 4.2), emphasized with yellow arrows in Figure 5.7. The intensity of these $\alpha - Fe_2O_3$ peaks seems to be independent of milling time. The batch heated to 1000 °C do not exhibit the existence of $\alpha - Fe_2O_3$ either in the starting material or after HEBM. Notwithstanding, it has to be considered that XRD technique do not have enough resolution for the analysis α-Fe_2O_4, since only phases involving more than 5% of the total mass of the sample will be seen in the spectra.

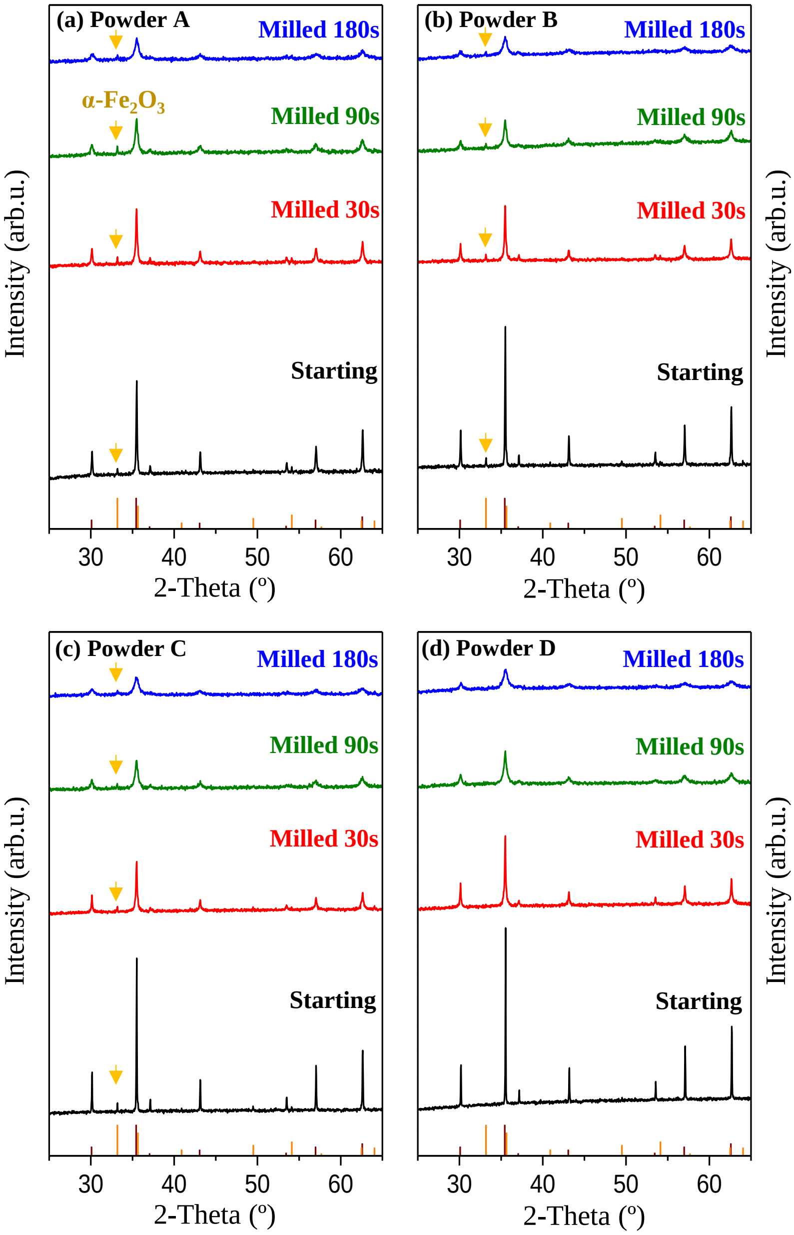

Figure 5.7: XRD spectra of $CoFe_2O_4$ powders with different initial microstructure, before and after HEBM. All graphs display: the spectra of initial material (black) and after HEBM during 30 s (red), 90 s (blue) and 180 s (green). Yellow arrows emphasize the observed α-Fe_2O_3 diffraction peaks. Red lines in the bottom are references of $CoFe_2O_4$ diffraction peaks (ref: 00-002-1086), and black lines correspond to α-Fe_2O_3 (ref: 01-089-0599)

After only 30 seconds milling, Powder D displays stronger reflection peaks than powders A, B and C, all with similar spectra. It has to be noticed that while these latter batches present a particle size distribution in the nanoscale regime (see Figure 4.4), Powder D is constituted by polycrystalline particles with sizes greater than a micron, and therefore it is needed more time to homogenize the microstructure. Extended milling of 90 s already show spectra with similar height of $CoFe_2O_4$ Bragg's peaks in all batches, and after 180 seconds milling, it can not be observed any difference between spectra. The evolution of diffraction peaks in dependence of milling time indicates that HEBM is an efficient technique to achieve a refined powder with a reduced crystallite size in short milling times, independently of the initial powder crystallinity. Longer milling time might cause particles amorphization due to the reiterative impact of milling balls with cobalt ferrite particles, and consequently the disappearance of $CoFe_2O_4$ magnetic properties.[2, 4]

Calculated mean average crystallite size, <D_V>, and microstrain induced during milling, ε, are plot in Figure 5.8.(a) and (b) respectively. In accordance with chapter 4, the higher heating temperature of as-synthesized powder, the highest <D_V> and lowest ε of the obtained cobalt ferrite powder. Powder A, heated to 700 °C posses a <D_V> = 65.1 nm, close to a half lower than that of Powder D heated to 1000 °C, with <D_V> = 117.6 nm. These are the starting powders with the lowest and highest crystallite sizes respectively.

Interestingly, after 90 seconds milling, all batches present grain sizes below 40 nm, which is the $CoFe_2O_4$ threshold of magnetic monodomain critical size [3]. The effectiveness of this HEBM process might be conditioned to the probability of impact between the particles of cobalt ferrite and the milling balls, thus the bigger particle size pf starting powder, the higher probability to impact with milling balls creating milled NPs. All batches display a similar <D_V> after only 180 seconds milling, with values in the range $< D_V >$ = 13.7 nm obtained in Powder A, and $< D_V >$ = 9.2 nm measured in Powder D, demonstrating the high efficiency of this HEBM technique in crystallite size reduction, independently of the initial $< D_V >$.

In case of strain, the starting Powder A is the sample with the highest ε among the initial powder of the four batches, with $\varepsilon = 1.4 \cdot 10^{-3}$, almost three times higher than $\varepsilon = 0.5 \cdot 10^{-3}$ assessed in Powder D. A monotonic increase of ε as a function of milling time with a different slope each is observed. Only 90 seconds milling are necessary to increase the strain of Powder D up to $\varepsilon = 5.1 \cdot 10^{-3}$, while for Powder A it only rose up to $\varepsilon = 3.7 \cdot 10^{-3}$. The highest ε values were attained after milling during 180 s; the highest $\varepsilon = 9 \cdot 10^{-3}$ in case of Powder D, that is a 30% greater than $\varepsilon = 6.9 \cdot 10^{-3}$ measured in Powder A, the lower value after 180 seconds milling. The evolution of ε in Powders B and C is very similar, and after 180 seconds milling, $CoFe_2O_4$ powders with $\varepsilon = 4.4 \cdot 10^{-3}$ (Powder B) and $\varepsilon = 4.7 \cdot 10^{-3}$ (Powder C) was obtained respectively.

In accordance with structural and morphological data from Figure 4.1.3, the XRD data discussed above shows that HEBM process is more effective in both, crystallite size reduction and induction of strain, when the $CoFe_2O_4$ powder to be milled is constituted by big particles.

5.2.3 Magnetic properties analysis

Figure 5.9 displays a comparative of the four batches hysteresis loops before and after milling for 30, 90 and 180 seconds. These *M-H* curves were measured with VSM at RT using a maximum magnetic applied field of 20 kOe.

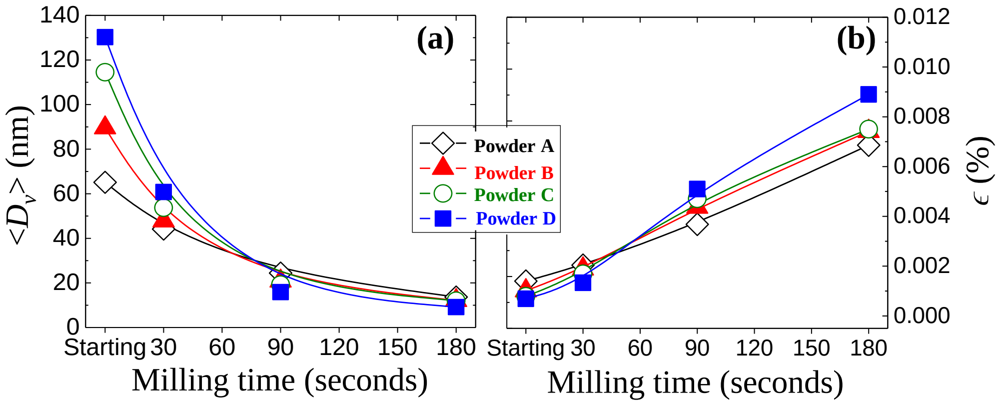

Figure 5.8: Evolution of crystallite size and strain wit milling time, calculated for powder A (black), powder B (red), powder C (green) and powder D (blue)

First, a double-loop shape of the hysteresis loops during the early time of milling (i.e. 30 seconds, see Figure 5.9.(b)) is observed in all batches, probably due to the combination of the two different particles sizes distributions (see Figure 5.4.(b)); after milling for 30 seconds, the resultant powder is constituted by nanoparticles that are created during the milling process, when milling balls impact with initial CoFe$_2$O$_4$ particles, in addition to particles that have not been milled yet. Contributions from both type of particles are the reason of that double loop behavior observed after milling for 30 seconds, since milled NPs posses higher H_C than initial particles due to reduction in size and induced strain. Extended milling causes the increase of hysteresis loops squareness (see 5.9.(c)), followed by the rounding of the curves, with an evident decrease in $M_{20\text{kOe}}$ and M_r.

These curves have been employed to determine coercivity, H_c, remanence magnetization M_r and saturation magnetization $M_{20\text{kOe}}$, as well as to asses the energy product $(BH)_\text{max}$. All these parameters are represented in Figure 5.10 and discussed in the following.

It is known that for cobalt ferrite, the smaller particle size, the lower saturation magnetization [9–12]. The efficiency of this ultra-fast HEBM reducing cobalt ferrite crystallite size might explain the behavior of saturation magnetization $M_{20\text{kOe}}$ with milling time, by comparing Figure 5.10.(a) with Figure 5.8.(a). Magnetization $M_{20\text{kOe}}$ of initial powders vary from $M_{20\text{kOe}}$ = 72.6 measured in powders A to $M_{20\text{kOe}}$ = 80.4 emu/g recorded for Powder D (which are the batches with the highest and lowest $M_{20\text{kOe}}$ of the serie respectively). After 180 seconds milling, these $M_{20\text{kOe}}$ were in the range 57.6 - 58.6 emu/g for Powders A and D respectively, both values very similar as a consequence of the achieved powder crystallite size reduction. Similar values of $M_{20\text{kOe}}$ were observed in both, Powders B and C.

Regarding M_r, relative maximal values are observed in every batch; after 30 seconds milling for Powders A, B and C, and after 60 seconds milling for Powder D. Once this maximal is achieved, quite similar M_r values were measured in powders B, C and D. Powder A follows the same tendency but with a lower remanence magnetization; for instance, after 180 seconds, Powder A attained a M_r = 31.1 emu/g while for Powders B and C this value was M_r = 34.6 emu/g and M_r = 35.8 emu/g for Powder D. The quantitative differences of M_r among the different batches might be explained as a result of the the different α-Fe_2O_3 content of each batch (see Figure4.9), since this material is antiferromagnetic at RT and thus, it is expected to contribute to a lower magnetization per unit of mass. Therefore, the batch with a higher concentration of hematite is the one with lower remanence magnetization values.

Attending to coercivity, an exponential increase of this parameter as a function of milling time is observed. Note that longer milling times results in the detriment of H_C due to particle amorphization. In general, the maximum coercivity of all batches was obtained after 180 seconds milling (Figure 5.10.(c)). Powder A is the batch with the lowest attained H_C = 3.8 kOe, while the maximum was found in Powder D with H_C = 4.7 kOe. H_C values of 4.2 kOe and 4.6 kOe were measured in Powders B and C respectively. Considering the ε values previously discussed of Figure, it seems that since crystallite size is similar in all batches and are below the monodomain critical size, the highest level of induced strain leads to cobalt ferrite powders with the greatest coercivity.

Calculated energy products, $(BH)_{max}$, are plotted in Figure 5.10.(d). In general, it is ob-

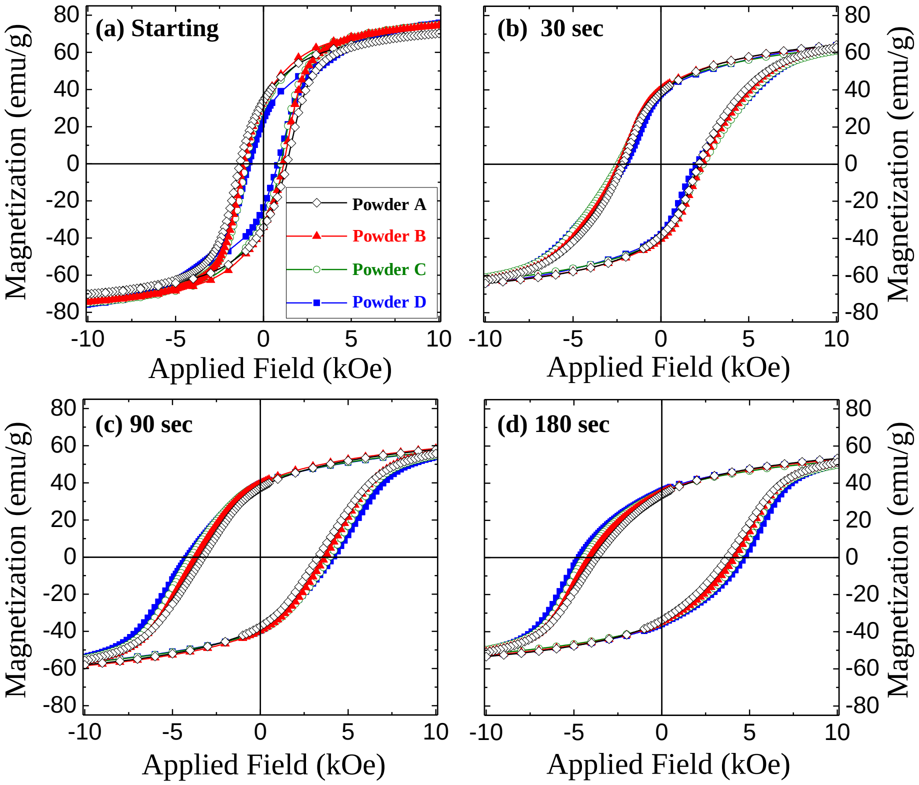

Figure 5.9: *M-H* curves of (a) initial $CoFe_2O_4$ and after (b) 30 s, (c) 90 s and (d) 180 s milling. The curves correspond to powder A (black), powder B (red), powder C (green) and powder D (blue)

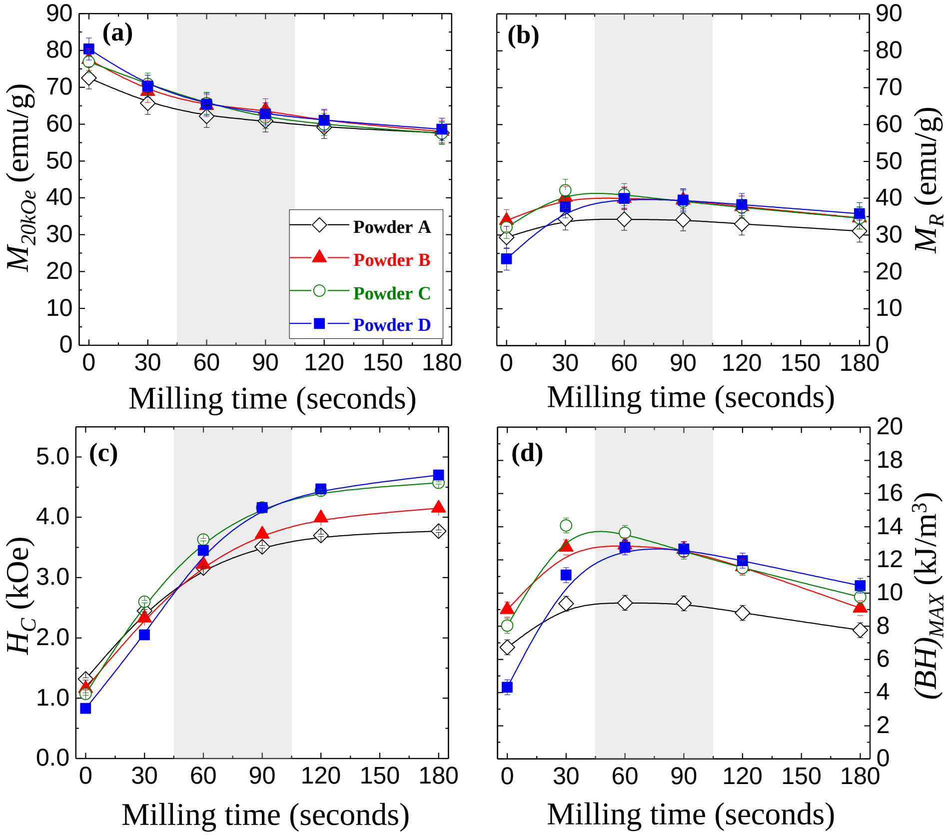

Figure 5.10: Evolution of (a) saturation magnetization, $M_{20\mathrm{kOe}}$, (b) remanence magnetization, M_r, (c) coercivity, H_c, and (d) Energy product, $(BH)_\mathrm{max}$, with HEBM time of powder A (black), powder B (red), powder C (green) and powder D (blue). These parameters are extracted from M-H curves.

served a maximum of energy product in Powders A, B and C after 30 seconds milling, and in powder D after 60 seconds milling. Longer milling causes this value to diminish. The highest $(BH)_\mathrm{max}$ among the four batches was measured in Powder C, the batch heated to 900 °C, that rose up from $(BH)_\mathrm{max}$ = 8 kJm^{-3} of the starting powder to $(BH)_\mathrm{max}$ = 14.1 kJm^{-3}) after 30 seconds milling, supposing a 76% increase. On the other side, the lowest enhancement of $(BH)_\mathrm{max}$ was observed in Powder D, where energy product was increased only a 40%, from $(BH)_\mathrm{max}$ = 6.7 kJm^{-3} of the starting powder to $(BH)_\mathrm{max}$ = 9.4 kJm^{-3} after milling for 30 seconds

From the data discussed above, one can see that while all batches follows a similar behavior in dependence of milling time, the microstructure of the initial powder to be milled plays an important role in the enhancement obtained in magnetic properties. If the desired parameter to be enhanced is H_C, the highest coercivity was obtained in the batch with the bigger initial particle size, i.e. Powder D. But if the achievement of CoFe$_2$O$_4$ with an enhanced $(BH)_\mathrm{max}$

is the goal, the best option is to mill during 30 seconds cobalt ferrite powder constituted by not-sintered NPs with as best crystallinity as possible, for instance like the case of Powder C. A 76% increase in the energy product with respect that of the initial powder was obtained in Powder C after 30 seconds of HEBM, with a $(BH)_{\text{max}}$ = 14.1 kJm^{-3}) resulting from a combination of H_C = 2.6 kOe and M_{r} = 42.1 emu/g.

5.3 Surfactant assisted HEBM of CoFe$_2$O$_4$

Dry milling has been demonstrated to be an efficient method for nanostructuring cobalt ferrite powder, as well as the possibility of improving its magnetic performance in different time windows depending on the milling procedure under optimized processing conditions, i.e. hours for standard milling [1, 2] and a few minutes for ultrafast ball milling. However, one of the most important challenges is the preservation of an enhanced magnetic performance without particles agglomeration and avoiding amorphization of the crystalline grains during the manufacturing process. Mechanochemical techniques assisted with surfactant are widely used for the preparation of ferrite nanoparticles [13, 14]. In particular, the use of oleic acid during milling has been proven to result in a well dispersed powder with regular crystallite size and an improved magnetic performance for ferrites and RE-based materials, [15–17]. Investigations of surfactant assisted (wet) milling on CoFe$_2$O$_4$ are however missed in literature.

In this section, the possibility of coercivity development after very short milling times (a few minutes) in isotropic CoFe$_2$O$_4$ powder using surfactant assisted milling, is demonstrated to be advantageous because of the possibility to avoid particles agglomeration and amorphization. Using the method here described, a combination of magnetic properties with H_{c} = 4.5 kOe and M_{r} = 41.8 emu/g after 12 minutes milling that results in isotropic CoFe$_2$O$_4$ powder with $(BH)_{\text{max}}$ = 14.8 kJm^{-3} was obtained.

5.3.1 Experiment description

CoFe$_2$O$_4$ powder was synthesized following a sol-gel route using Fe and Co nitrates. The nitrates were dissolved in 1:2 ratios in deionized water. Citric acid was subsequently added to the solution, which was then constantly stirred at 60 °C for 1 h. The gel formed was dried in a hot air oven for 24 h. The precursor obtained was calcined for 1 h at 400 °C. The resulting powder was subsequently annealed at 900 °C to crystallize the inverse spinel structure of CoFe$_2$O$_4$.

HEBM of CoFe$_2$O$_4$ powder with 2wt.% of oleic acid added as surfactant prior to milling (wet milling) has been carried out up to 6 minutes, with 1.5 min increment. Additionally, in the wet series 12 minutes milling was conducted. The milling was performed in 4 grams of CoFe$_2$O$_4$ powder. A rotational speed of 900 rpm and a ball-to-powder ratio of 40:1 were used in the milling experiments. Oleic acid was removed after the milling process by washing the powder with hexane. Finally, a subsequent heat treatment in air at 200 °C allowed for the complete evaporation of any residual organic components.

Synchrotron powder X-ray diffraction (SR-PXD) measurements were performed at the Swiss-Norwegian beam line (SNBL) at ESRF (Grenoble, France), at the BM01B station (λ = 0.68138 Å). The 2D diffraction data were collected with a Pilatus2M detector, at a sample-detector distance of 143 mm. Data integration was carried out using the SNBL Tool Box [18] and Fit2D [19] programs. In all SR-PXD experiments powders were sealed in a boron-glass capillary (d = 0.3 mm). An average crystallite size and an isotropic lattice strain were extracted from diffraction line broadening by conventional Rietveld analysis (program package Fullprof [20]). The diffraction profiles were modeled using a Thomson-Cox-Hastings pseudo-Voigt function [21] to simulate the peak shapes of $CoFe_2O_4$. The instrumental resolution function (IRF) was obtained from the refinement of LaB6. The deconvolution process by Fullprof allowed for an extraction of the intrinsic line profile from the observed one based on IRF. Any increase of FWHM in the observed diffraction profiles, with respect to the instrumental FWHM, was considered to be intrinsic to the sample. The variation of the averaged crystallite size $< D_v >$ and the degree of microstrain formation in the crystal lattice ε have been determined from SR-PXD. Quantitative analysis of the SR-PXD data was undertaken with a full pattern fitting procedure based on the Rietveld method. The isotropic average crystallite size and strain effects were then separated and refined due to the distinct angular dependences of the Lorentzian and Gaussian components of the intrinsic line broadening.

Morphological analysis is done using Scanning electron microscopy (SEM) images obtained from the samples using a Carl-Zeiss Auriga microscope at a filament voltage of 3 kV.

Magnetic properties obtained from *M-H* curves have been measured at room temperature with a Lakeshore 7400 VSM, with a maximum applied field of 20 kOe. Magnetization obtained with this maximum field, $M_{20\mathrm{kOe}}$, remanence magnetization, M_r, and coercivity, H_c, have been determined from the recorded hysteresis loops. $(BH)_\mathrm{max}$ has been evaluated, in order to quantify the performance as permanent magnets and to assess the suitability of this methodology.

5.3.2 Structural and compositional analysis

Figure 5.11 depicts representative powder diffraction patterns recorded before and after the (a) dry, and (b) wet high-energy ball milling processes for different milling times. Only $CoFe_2O_4$ reflection peaks are observed, indicating the absence of any other phase or possible contamination during the milling process. In addition, no impurities are observed in wet sample series due to a possible decomposition of an organic surfactant (oleic acid) during milling. Wet milled SR-PXD data show stronger $CoFe_2O_4$ Bragg peaks than dry milled ones, indicating that the initial powder crystallinity is more effectively preserved during the HEBM process. This contrasts with the standard milling procedures extended during hours, where the obtained $CoFe_2O_4$ crystals are surrounded by an amorphous matrix generated during milling. [1] A decreased intensity in the reflection peaks of dry milled powder can be ascribed to early amorphization by comparison with the surfactant assisted process (Figure 5.11). This is later supported by SEM microscopy images (see Figure 5.13).

The comparison of diffraction profile lines shows reflections broadening with increased milling time for both dry and wet milling processes. This broadening is related to the reduction of particles size and the lattice strain induced during milling. Figure 5.12 summarizes the quantitative analysis of the recorded diffraction patterns showing the evolution of the (a) crystallite size, and (b) the strain of the starting and as-milled $CoFe_2O_4$ powder. In general, a similar trend is found for both dry and wet milling processes, $< D_v >$ decreases and ε increases with longer milling time, but at a slower rate for the wet than for the dry milling method. In the dry series, the average crystallite size value is dramatically reduced from 254 nm in the starting

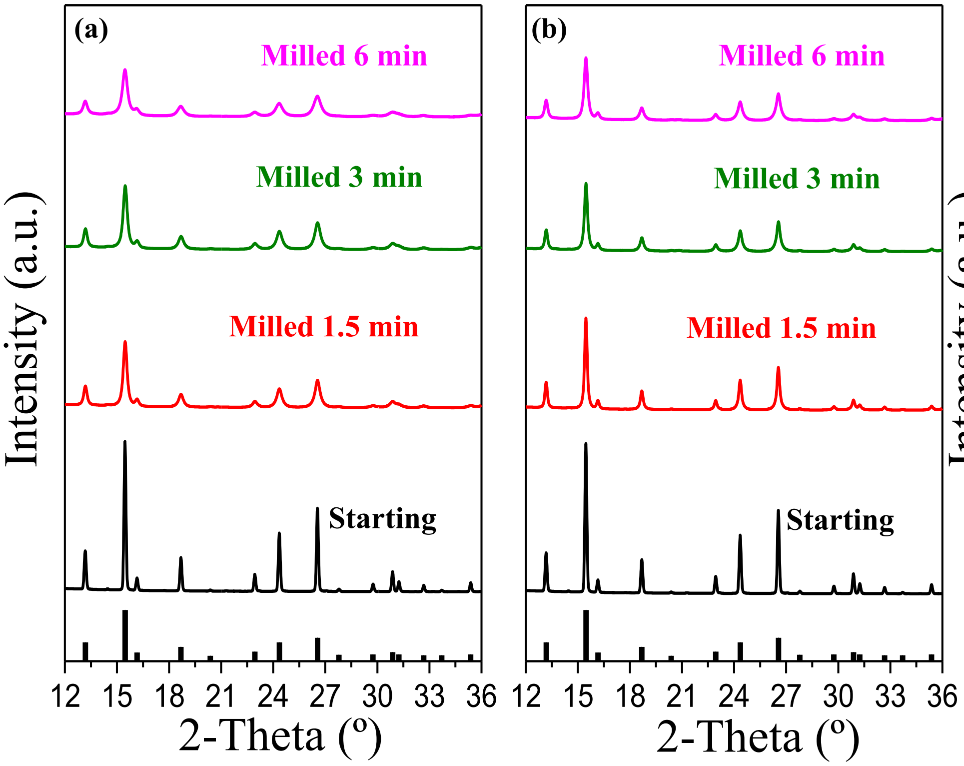

Figure 5.11: SR-PXD diffraction patterns of CoFe$_2$O$_4$ powder processed by (a) dry and (b) wet milling methods. From bottom to top: starting CoFe$_2$O$_4$, milled during 1.5, 3 and 6 min. References lines correspond to CoFe$_2$O$_4$ (ref. 00-022-1086).

state (non-milled powder) to about 30 nm after milling for only 1.5 min. The average crystallite size remains almost unchanged for powder processed longer than 1.5 min in the studied range (1.5-6 min milling time). This contrasts with the wet milled series where $< D_v >$ is reduced to 88 and 29 nm after 1.5 and 4.5 min of milling respectively.

The effect of lattice strain, barely present in the starting Co-ferrite powder, rises gradually with milling time for both sample series (Figure 5.12.(b)). Nevertheless, ε value is significantly larger in the dry series than in the wet one, even if samples are milled with the same time intervals. Such a behavior results from the presence of oleic acid in wet series, which reduces the impact energy. The surfactant seems to decrease the level of milling induced microstructural deformations, since the maximum strain ε is still smaller for the sample ball milled for 12 min with oleic acid than for the sample milled just for 1.5 min without the organic dispersant. The presence of oleic acid is likely to homogenize the fracturing process, while reducing the induced strain and amorphization.

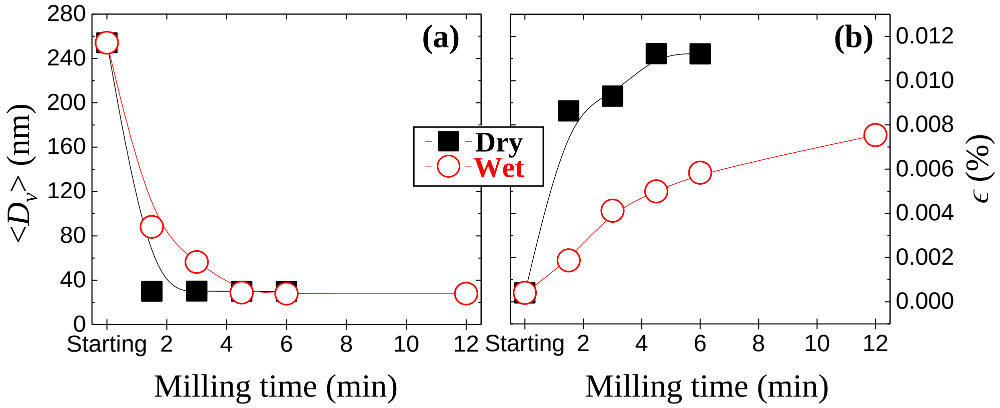

Figure 5.12: Evolution of (a) the average crystallite size $< D_v >$ and (b) the average maximum lattice strain ε with milling time for dry (black full squares) and wet (red open circles) processed powder. Lines are guides for the eye.

5.3.3 Morphological analysis

SEM images depicted in Figure 5.13 reveal significant differences in the morphology of the dry and wet milled powders. The starting material contains particles with sharp edges and a broad particle size distribution (Fig. 5.13.(a)). Dry milling for 1.5 min reduces the particle size below 1 μm but results in the formation of large agglomerates containing irregular shaped particles (Fig. 5.13.(b)). Extended milling for 6 min refines further the microstructure but cannot avoid the continued formation of agglomerates (Fig. 5.13.(c)).

By comparison, milling for 1.5 min with oleic acid leads to a more homogeneous microstructure comprising submicron particles with a well-defined polyhedral shape and a significantly reduced number of agglomerates (Figs. 5.13.(d)) These observations apply even after milling for 6 min (Fig. 5.13.(e)). This is due to the polar nature of the solvent that eases the creation of a protective layer around the particles during milling. This indicates that the attachment of the molecules of the surfactant to the Co-ferrite particles acts as a protective layer, avoiding their agglomeration and cold welding [17], and thus resulting in a more homogeneous powder with a narrowest distribution of particle size as can be seen in Figure 5.13.(f).

Therefore, wet milling is shown to be a more efficient procedure to develop a homogeneous nanocrystalline powder, since the surfactant layer diminishes the friction between the particles and the milling balls, and importantly, prevents agglomeration during the milling process [22, 23].

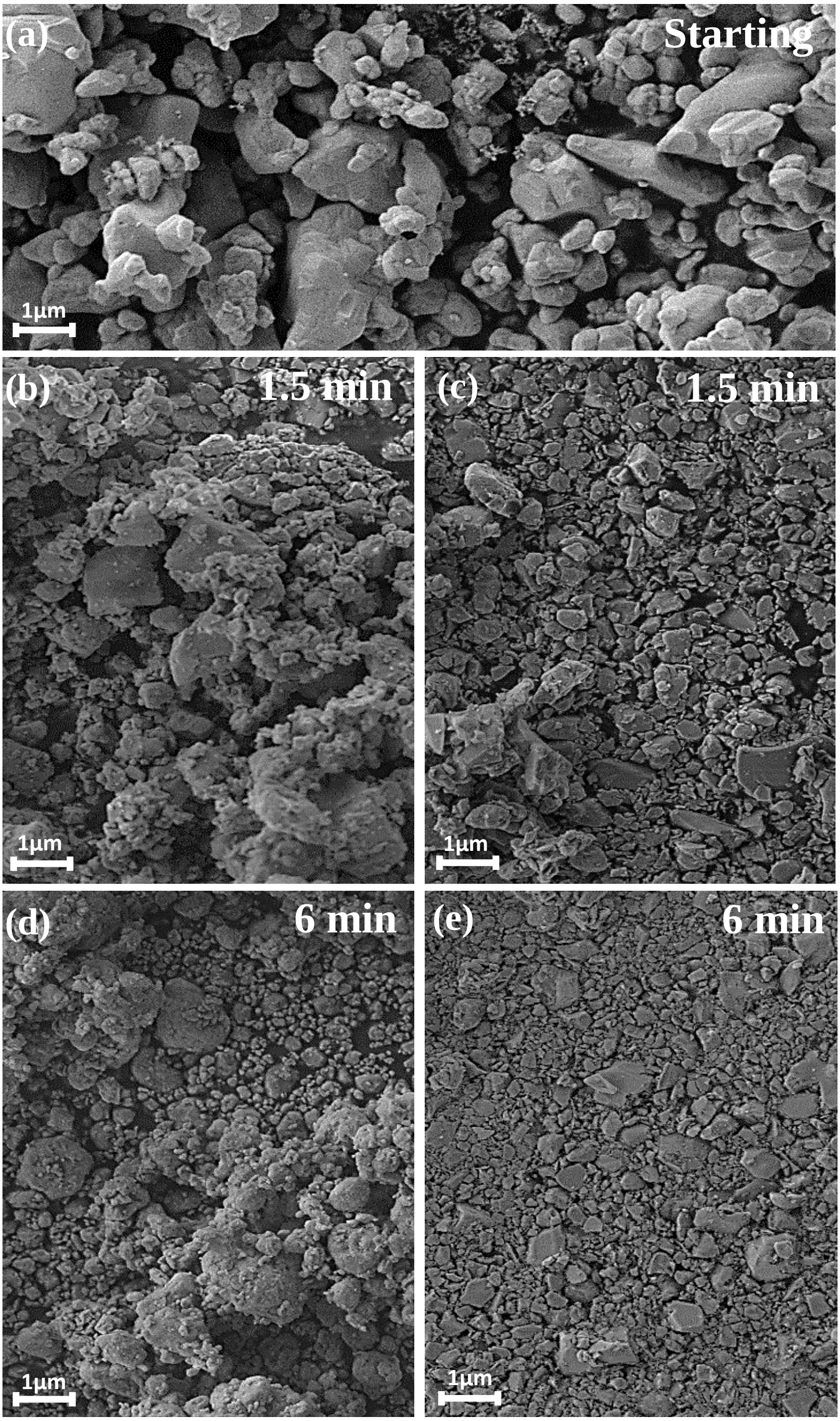

Figure 5.13: SEM images of (a) initial CoFe$_2$O$_4$ isotropic powder (a), and after 1.5 and 6 minutes of dry and wet milling (b,d and c,e respectively).

5.3.4 Magnetic properties analysis

Representative magnetization curves at room temperature of the starting CoFe$_2$O$_4$ isotropic powder, and after different milling times for dry and wet milling are shown in Figure 5.14. All hysteresis curves show magnetically single-loop behavior. Independently of the milling procedure, widening of the hysteresis loop, i.e. coercivity development, is observed by comparison with the starting material. This agrees well with the strain induced and the crystallite size refinement with increasing milling time shown in Fig. 5.12, which leads to a mean size below the critical single-domain value right after very short times (1.5 and 4.5 min for dry and wet milling, respectively). The correlation between magnetic properties and microstrucure is detailed in the following.

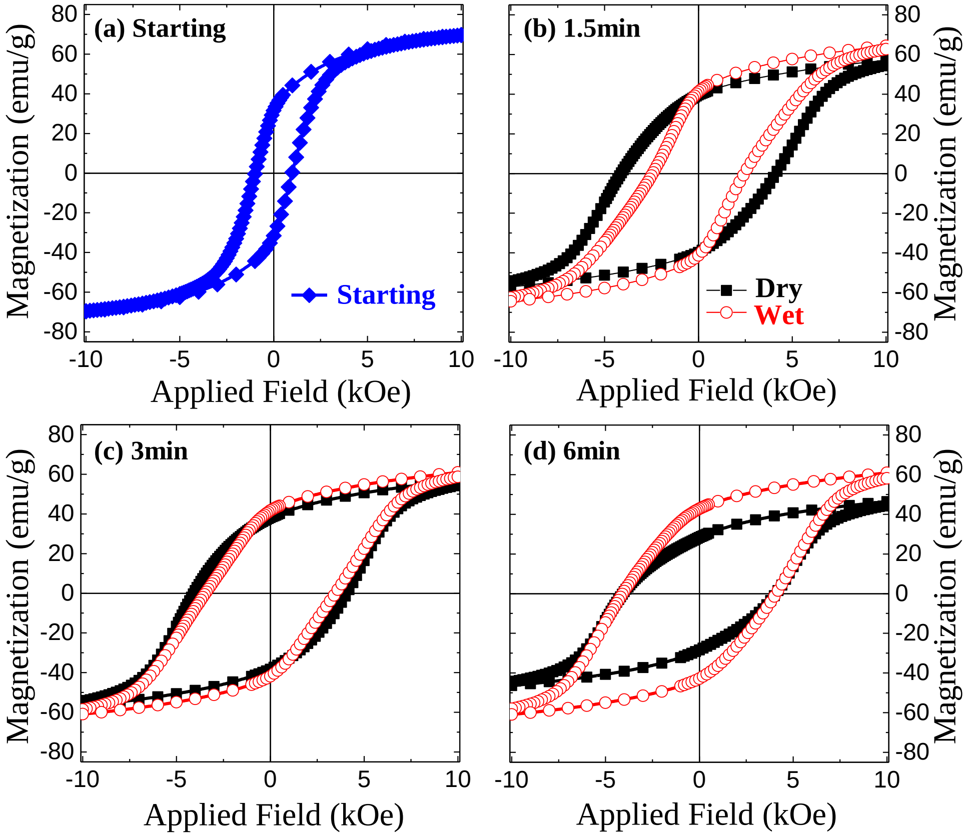

Figure 5.14: Hysteresis loops of starting CoFe$_2$O$_4$ (full circles) isotropic powder (a) milled in air for 3 min (open squares) and 6 min (full triangles), and (b) milled with 2 wt.% of oleic acid for 3 min (open squares) and 12 min (full triangles).

Magnetic properties resulting from both milling methods as a function of milling time are compared in Figure 5.15. The starting CoFe$_2$O$_4$ presents a saturation magnetization ($M_{20\text{kOe}}$) of 77.8 emu/g and a remanence magnetization M_r = 31.5 emu/g. Evolution of magnetization ($M_{20\text{kOe}}$ and M_r) shows a non-monotonous decrease with milling time, slowed in the wet milling method. Reduction of particle size leads to an increased surface-to-volume ratio, evidencing the effect of the "dead layer" (originated from spin disorder in a surface shell region contributing less to the magnetization than the core due to spin fluctuations at the surface) and resulting in the loss of magnetization during milling. [7, 11] It is noteworthy the differences observed on the evolution of remanence magnetization with milling by comparing powders milled with the dry and wet method. In case of dry milling, M_r decreases parallel to $M_{20\text{kOe}}$ after 1.5 minutes milling, but in case of wet milling, these values are practically constant along the milling process. For instance, after 12 minutes milling it is obtained CoFe$_2$O$_4$ with a M_r value of 41.8 emu/g, which is above the 39.6 emu/g obtained as maximum M_r of dry milled powder. The reduced density of agglomerated particles and the amorphization avoidance might be the reasons for the larger magnetization found for wet milled powders.

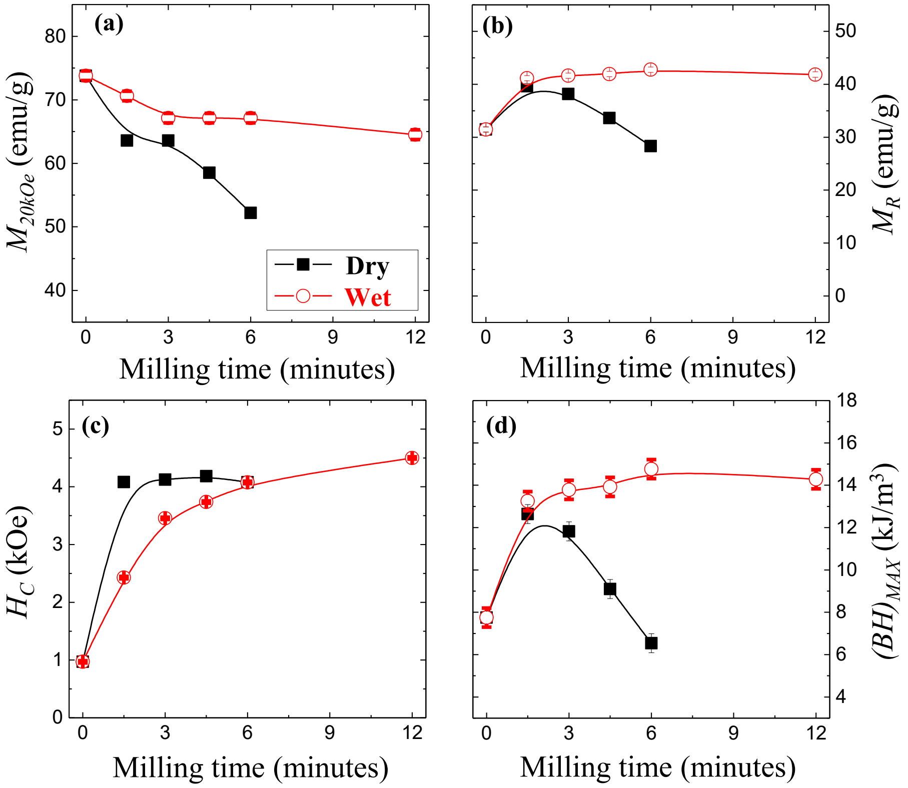

Figure 5.15: Evolution of magnetic properties of isotropic CoFe$_2$O$_4$ powder with milling time for dry (full squares) and wet (open circles) milling. Lines are guides for the eye.

Regarding coercivity, a 4-fold increase with respect to the starting powder can be achieved with both methods, but in different milling time windows. Only 1.5 min of dry milling provides an increase in H_c from 1.0 kOe to 4.1 kOe, and it remains approximately constant for extended milling times. The wet milling method requires longer times to achieve similar increment in H_c (4.0 kOe after 6 min) than by the dry milling method. This increased coercivity is caused by the particle size reduction undergone in the starting powder, in addition to the strain induced during milling (Figure 5.12). In case of wet milling, where critical single-domain size is achieved after only 4.5 min accompanied by an induced strain of $5{\cdot}10^{-3}$ (see Fig. 5.12), a coercivity value of 3.7 kOe is obtained. This value increases to 4.5 kOe after 12 min of milling due to an increased induced strain of $7.5{\cdot}10^{-3}$, while maintaining similar crystallite size (Fig. 5.12).

Maximum values of $(BH)_{\mathrm{max}}$ = 12.6 and 14.8 kJ m^{-3} were obtained after 1.5 min of dry and 6 min of wet milling, respectively. The energy product obtained by the wet milling is not rapidly reduced as in the case of dry milling, probably due to the avoidance of agglomerates as well as to the crystallinity preservation. A M_r = 42.8 emu/g, in addition to a coercivity of 4.0 kOe provide the highest energy product obtained for the as-milled powders under study after 6 min of wet milling. Extended milling for 12 minutes, which is double the time required to obtain the maximum $(BH)_{\mathrm{max}}$, provides powder with 14.3 kJ m^{-3}, which is slightly lower. Consequently, this fact demonstrate that Co-ferrite microstructure can be controlled through an adequate choice of the milling parameters.

5.4 Conclusions

In this section have been demonstrated the possibility of achieving a 5-fold increase in coercivity of CoFe$_2$O$_4$ powders, with a maximum value of 4.7 kOe obtained after a HEBM process during only 180 seconds. For the aim of this study, it is important to highlight that while other studies present same trend of increasing coercivity with increasing milling time [1, 4], here is shown the possibility of reducing the timescale of the process from several hours to a few minutes by using HEBM. A reduction in the milling time needed to achieve maximum coercivity has important implications (energy saving, i.e., reduced production costs) in the possible implementation of this process for large-scale production.

Reduction in crystallite size below the critical single-domain size, in combination with the strain induced during milling, are the two factors behind this large increase in coercivity. The fundamental role played by microstrain induced during milling in increasing the coercivity has been discriminated from the grain size effects with the analysis of cobalt ferrite powders with different initial microstructures after being subjected to the same milling procedure. This has allowed the right choice of processing parameters for CoFe$_2$O$_4$ synthesis in order to obtain a high $(BH)_{\mathrm{max}}$ - 14.1 kJm^{-3} after 30 seconds milling a CoFe$_2$O$_4$ powder synthesized with an annealing to 900 °C - or high coercive cobalt ferrite - H_C = 4.7 kOe obtained after milling for 180 s CoFe$_2$O$_4$ powder synthesized with an annealing to 1000 °C - after a HEBM process. Furthermore, the efficiency of this ultrafast milling method in obtaining a refined and homogeneous powder in a short milling time is confirmed by XRD and SEM data, as well as by the similarities of M-H curves measured in powders with initially different microstructure after being milled during 180 seconds.

Moreover, this section have show that in addition to dry milling, surfactant-assisted milling of $CoFe_2O_4$ powder is not only an efficient methods to develop coercivities above 4.0 kOe (which means a four times increase by comparison with that of the starting material) but also that the use of surfactant in the milling process was proven advantageous to deliver a homogeneous powder while avoiding particles agglomeration, and achieving smaller crystallite sizes. Using the method here described, a combination of magnetic properties with H_c = 4.5 kOe and M_r = 41.8 emu/g after 12 minutes milling that provides isotropic $CoFe_2O_4$ powder with $(BH)_{max}$ = 14.8 kJm^{-3} was obtained. This combination of magnetic properties obtained for isotropic $CoFe_2O_4$ powders with effective processing times and feasible scalable synthesis methods (co-precipitation and ultrafast milling), makes them good candidates for permanent magnet applications.

References

[1] BH Liu and J Ding *Strain-induced high coercivity in $CoFe_2O_4$ powders*. in: *Applied physics letters* ***88***,4 (2006), 2506 (cit. on pp. 65, 67, 71, 78, 79, 85)

[2] Bing Hai Liu, J Ding, ZL Dong, CB Boothroyd, JH Yin, and JB Yi *Microstructural evolution and its influence on the magnetic properties of $CoFe_2O_4$ powders during mechanical milling*. in: *Physical Review B* ***74***,18 (2006), 184427 (cit. on pp. 65, 67, 71, 74, 78)

[3] CN Chinnasamy, B Jeyadevan, K Shinoda, K Tohji, DJ Djayaprawira, M Takahashi, R Justin Joseyphus, and A Narayanasamy *Unusually high coercivity and critical single-domain size of nearly monodispersed $CoFe_2O_4$ nanoparticles*. in: *Applied physics letters* ***83***,14 (2003), 2862–2864 (cit. on pp. 66, 74)

[4] AS Ponce, EF Chagas, RJ Prado, CHM Fernandes, AJ Terezo, and E Baggio-Saitovitch *High coercivity induced by mechanical milling in cobalt ferrite powders*. in: *Journal of Magnetism and Magnetic Materials* ***344***, (2013), 182–187 (cit. on pp. 67, 71, 74, 85)

[5] WS Chiu, Shahidan Radiman, R Abd-Shukor, MH Abdullah, and PS Khiew *Tunable coercivity of $CoFe_2O_4$ nanoparticles via thermal annealing treatment*. in: *Journal of Alloys and Compounds* ***459***,1 (2008), 291–297 (cit. on p. 67)

[6] Ekaphan Swatsitang, Sumalin Phokha, Sitchai Hunpratub, Brian Usher, Atipong Bootchanont, Santi Maensiri, and Prinya Chindaprasirt *Characterization and magnetic properties of cobalt ferrite nanoparticles*. in: *Journal of Alloys and Compounds* ***664***, (2016), 792–797 (cit. on p. 70)

[7] A Franco Jr, FC e Silva, and Vivien S Zapf *High temperature magnetic properties of Co1-xMgxFe2O4 nanoparticles prepared by forced hydrolysis method*. in: *Journal of Applied Physics* ***111***,7 (2012), 07B530 (cit. on pp. 70, 84)

[8] John Michael David Coey *Noncollinear spin arrangement in ultrafine ferrimagnetic crystallites*. in: *Physical Review Letters* ***27***,17 (1971), 1140 (cit. on p. 70)

[9] M Rajendran, RC Pullar, AK Bhattacharya, D Das, SN Chintalapudi, and CK Majumdar *Magnetic properties of nanocrystalline $CoFe_2O_4$ powders prepared at room temperature: variation with crystallite size*. in: *Journal of Magnetism and Magnetic Materials* ***232***,1 (2001), 71–83 (cit. on p. 75)

[10] Kush Rana, Preeti Thakur, Parul Sharma, M Tomar, V Gupta, and Atul Thakur *Improved structural and magnetic properties of cobalt nanoferrites: influence of sintering temperature*. in: *Ceramics International* ***41***,3 (2015), 4492–4497 (cit. on p. 75)

[11] Ekaphan Swatsitang, Sumalin Phokha, Sitchai Hunpratub, Brian Usher, Atipong Bootchanont, Santi Maensiri, and Prinya Chindaprasirt *Characterization and magnetic properties of cobalt ferrite nanoparticles*. in: *Journal of Alloys and Compounds* ***664***, (2016), 792–797 (cit. on pp. 75, 84)

[12] Alberto López-Ortega, Elisabetta Lottini, Cesar de Julian Fernandez, and Claudio Sangregorio *Exploring the magnetic properties of cobalt-ferrite nanoparticles for the development of a rare-earth-free permanent magnet*. in: *Chemistry of Materials* ***27***,11 (2015), 4048–4056 (cit. on p. 75)

[13] VM Chakka, B Altuncevahir, ZQ Jin, Y Li, and JP Liu *Magnetic nanoparticles produced by surfactant-assisted ball milling*. in: *Journal of applied physics* ***99***,8 (2006), 08E912 (cit. on p. 78)

[14] Mukta V Limaye, Shashi B Singh, Sadgopal K Date, Deepti Kothari, V Raghavendra Reddy, Ajay Gupta, Vasant Sathe, Ram Jane Choudhary, and Sulabha K Kulkarni *High coercivity of oleic acid capped $CoFe_2O_4$ nanoparticles at room temperature*. in: *The Journal of Physical Chemistry B* ***113***,27 (2009), 9070–9076 (cit. on p. 78)

[15] Narayan Poudyal, Chuan-bing Rong, J Ping Liu, et al. *Anisotropic bonded magnets fabricated via surfactant-assisted ball milling and magnetic-field processing*. in: *Journal of Physics D: Applied Physics* ***44***,33 (2011), 335002 (cit. on p. 78)

[16] WA Kaczmarek and BW Ninham *Surfactant-assisted ball milling of BaFe 12 O 19 ferrite dispersion*. in: *Materials chemistry and physics* ***40***,1 (1995), 21–29 (cit. on p. 78)

[17] SK Pal, K Güth, TG Woodcock, L Schultz, and O Gutfleisch *Properties of isolated single crystalline and textured polycrystalline nano/sub-micrometre Nd2Fe14B particles obtained from milling of HDDR powder*. in: *Journal of Physics D: Applied Physics* ***46***,37 (2013), 375004 (cit. on pp. 78, 81)

[18] VA Dyadkin *SNBL tool box swiss norwegian beam lines at ESRF*. in: *Grenoble, France, Release* ***1***, (2012) (cit. on p. 78)

[19] AP Hammersley *Internal Report ESRF97HA02T*. in: *ESRF, Grenoble, France* (1997) (cit. on p. 79)

[20] Juan Rodríguez-Carvajal *Recent advances in magnetic structure determination by neutron powder diffraction*. in: *Physica B: Condensed Matter* ***192***,1 (1993), 55–69 (cit. on p. 79)

[21] P Thompson, DE Cox, and JB Hastings *Rietveld refinement of Debye–Scherrer synchrotron X-ray data from Al2O3*. in: *Journal of Applied Crystallography* ***20***,2 (1987), 79–83 (cit. on p. 79)

[22] B. Z. Cui, A. M. Gabay, W. F. Li, G. C. Hadjipanayis, M. Marinescu, and J. F. Liu *Anisotropic SmCosub 5 nanoflakes by surfactant-assisted high energy ball milling*. in: *Journal of Applied Physics* ***107***,9 (May 2010) (cit. on p. 81)

[23] Santosh K Pal, Ludwig Schultz, and Oliver Gutfleisch *Effect of milling parameters on SmCo5 nanoflakes prepared by surfactant-assisted high energy ball milling*. in: *Journal of Applied Physics* ***113***,1 (2013), 013913 (cit. on p. 81)

Chapter 6

Post-milling $(BH)_{max}$ enhancement

A detailed and systematic study on the influence of a post-milling heat treatment in $CoFe_2O_4$ powder magnetic properties is presented in this chapter. It is possible to reduce defects while maintaining an homogeneous particle size distribution by performing a heat treatment on milled powder at a moderate temperature (400- 600 °C) even though recrystallization and grain growth occur at different heating temperatures. Therefore, $CoFe_2O_4$ powders microstructure might be further controlled after the milling process in order to maximize its $(BH)_{\max}$.

Remarkably, $CoFe_2O_4$ with $(BH)_{\max} = 18.6\ \mathrm{kJ\ m^{-3}}$ was obtained - the highest $(BH)_{\max}$ for cobalt ferrite powder reported up to date - through a post-milling heat treatment to 750 °C that decreased coercivity to H_C = 1.6 kOe, but with an increased M_R= 48.8 emu/g. Furthermore, it is demonstrated the reversibility of $CoFe_2O_4$ magnetic properties; as-milled powder after being heated to 1000 °C have the same magnetic properties than the initial material before milling. This is important regarding the industrial application of this material since it means that $CoFe_2O_4$ can be recycled at the end of it life cycle.

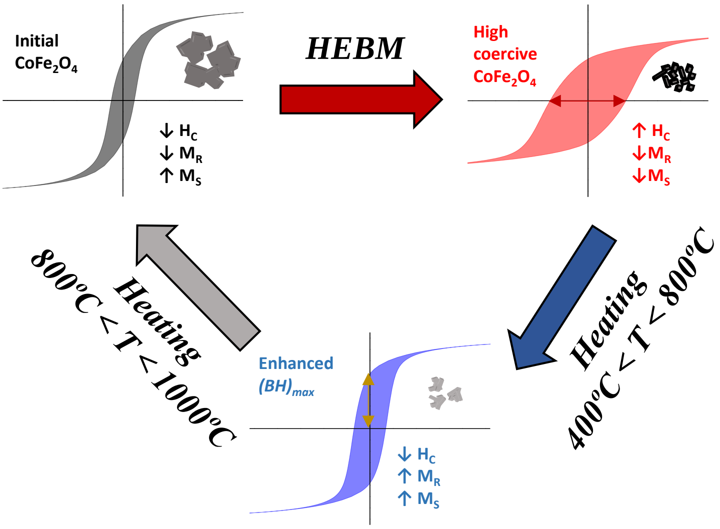

Figure 6.1: Sketch of chapter 6: Heating high coercive $CoFe_2O_4$ powders obtained by HEBM at moderated temperatures allows recrystallization, that is translated into an increased $(BH)_{max}$ at expenses of a diminished H_C. Heating above 800 °C causes coalescence, and minimization of magnetostatic energy originates a decreased M_R.

6.1 Heating of dry milled $CoFe_2O_4$

The evolution of cobalt ferrite powder synthesized by the co-precipitation method as a function of the post-synthesis annealing process temperature was discussed in previous chapters (see chapter 4). On the other hand, in the last chapter was discussed how the increased coercivity, as well as the decreased magnetization of milled $CoFe_2O_4$ particles, strongly depends on microstrain and particle size (see chapter 5). In this section is suggested to go a step forward, and the possibility of further control the microstructure of this milled cobalt ferrite powder with a post-milling heat treatment is demonstrated.

According to results obtained in Chapter 4, this heat treatment will result in the recrystallization of cobalt ferrite particles, i.e. reducing defects and increasing particle size. As a consequence, the high coercivity of HEBM cobalt ferrite powders is decreased but with increased magnetization. The combination of both parameters allows to increase the energy product of milled $CoFe_2O_4$ powders up to $(BH)_{\text{max}}$ = 17.8 kJ m^{-3}.

This efficient methodology provides a technological key to manage the production of isotropic powders, providing a comprehensive correlation between cobalt ferrite microstructure and the preparation parameters that allows us to apply next, for instance to the production of high performance isotropic Co-ferrites. The combination of high performance isotropic Co-ferrite powders with feasible scalable synthesis and processing method in record time make them good candidates for rare-earth free permanent magnet applications.

6.1.1 Experiment description

Following the co-precipitation method, two syntheses reactions with a volume of 3 L each were preformed. Powders of both reactions were mixed when dried, obtaining a total amount of 300 g of as-synthesized powder. A mass of 50 g of the total as-synthesized powder was heated to 1000 °C. The heating procedure was performed in a Naberthem muffle oven model L1 1/11/R6. In this case, the annealing procedure consisted of an increasing temperature ramp of 10K/min from room temperature to the goal temperature which was maintained for 1 hour before cooling down to room temperature. This treatment allows to crystallize the inverse spinel structure of $CoFe_2O_4$ (see chapter 4). Characterization and properties of this powder were previously discussed in section 4.2, named 'Powder C'.

HEBM experiment with a total duration of 180 seconds was performed to 4 grams of the aforementioned $CoFe_2O_4$ powder, using a high-energy ball milling equipment Pulverizete 7 premium line from Fritsch at a speed of 900 rpm and a ball-to-powder ratio of 40:1. The powder was milled in air atmosphere, using tungsten carbide milling media (balls and vessel) to enhance the impact energy, i.e. accelerate an efficient milling process, due to the larger density of tungsten carbide (14.95 g/cm^3) by comparison with that of steel (7.8 g/cm^3). The characterization and properties of these materials was previously discussed in section 5.1.

The as-milled powder was separated in batches of 150 mg and heated in a temperature range from 400 to 1000 °C, with 100 °C intervals, using air atmosphere with a Carbolite tubular oven model STF 15/450. The heating procedure consisted of an increasing temperature ramp of 10K/min from room temperature to the goal temperature which was maintained for 1 hour before cooling down to room temperature.

XRD spectra of as-synthesized powder and after different heat treatments were measured with a Highscore X'pert θ-2θ diffractometer, using Cu-K_α radiation source. Mean crystallite size was calculated by applying the Equation 1.2 to the four most intense peaks and averaging the value, as well as the mean average strain that was obtained with the same method using Equation 1.3. These parameters extracted from XRD data are analyzed as a function of the heating temperature.

SEM images were collected with a Carl-Zeiss Auriga microscope at a filament voltage of 3 kV, and these images were employed to obtain information regarding the evolution of $CoFe_2O_4$ powder morphological evolution as a function of the heating temperature.

A Lakeshore 7400 VSM was employed to measure magnetization M-H curves at room temperature. Parameters extracted from the hysteresis loops include magnetization at maximum applied field of 20 kOe ($M_{20\mathrm{kOe}}$), remanence (M_r), and coercivity (H_c). Energy product, $(BH)_\mathrm{max}$, has been evaluated, in order to quantify the performance as permanent magnets and to assess the suitability of this methodology.

6.1.2 Structural and compositional analysis

In section 4 was discussed how the annealing treatment applied to the powder obtained from the co-precipitation synthesis reaction provides energy to form $CoFe_2O_4$ crystals [1–3], and the obtained crystallite size and strain was analyzed as a function of the heating temperature. In this case, the the powder is already crystallized but with high level of defects, strain and amorphization imparted through the HEBM process.

XRD patterns of as-milled $CoFe_2O_4$ powder and after being heated to different temperatures are shown in Figure 6.2. Spectra of as-milled powder was previously discussed in chapter 5. It displays broad $CoFe_2O_4$ inverse spinel phase diffraction peaks with low intensity. Heating this powder produce the increment of the diffraction peaks intensities as a consequence of cobalt ferrite recrystallization (above 214 °C [4]). Interestingly, Figure 6.2.(b) highlights the appearance of α-Fe_2O_3 diffraction peak detected at $2\theta = 33.2\,^\circ$ when the heating temperature was in the range 500 °C to 900 °C. The $CoFe_2O_4$ powder used in this experiment was synthesized by the co-precipitation method with a heat treatment to 1000 °C, and XRD patterns of as-synthesized and as-milled powders (see Figure 5.2, labeled as 'Starting material' and 'Milled 180 s' respectively) didn't exhibit the existence of hematite. It is reported the crystallization of hematite at a temperature of 445 °C [5]. Moreover, when the as-milled powder was heated to 1000 °C, the XRD did not exhibit the presence of α-Fe_2O_3.

Parameters extracted from XRD spectra were analyzed as a function of the post-milling heat treatment temperature. Figure 6.3 displays the evolution of mean crystallite size, $<D_V>$, as well as residual strain, ε. Calculated average crystallite size of as-milled powder was $<D_V> = 9.1$ nm, which was slightly increased when heated in a temperature range from 400 °C to 600 °C, with $<D_V> = 13.4$ nm and $<D_V> = 20.1$ nm respectively. The latest suppose a 2-fold increment in crystallite size with respect as-milled powder, and still a half lower than critical single-domain size (40 nm [6]). When the heating temperatures was above 600 °C, a notably increment in crystallite size was observed. $<D_V> = 33.5$ nm was calculated for powder heated to 700 °C, which is increased up to $<D_V> = 114.2$ nm when the heating temperature was 1000 °C.

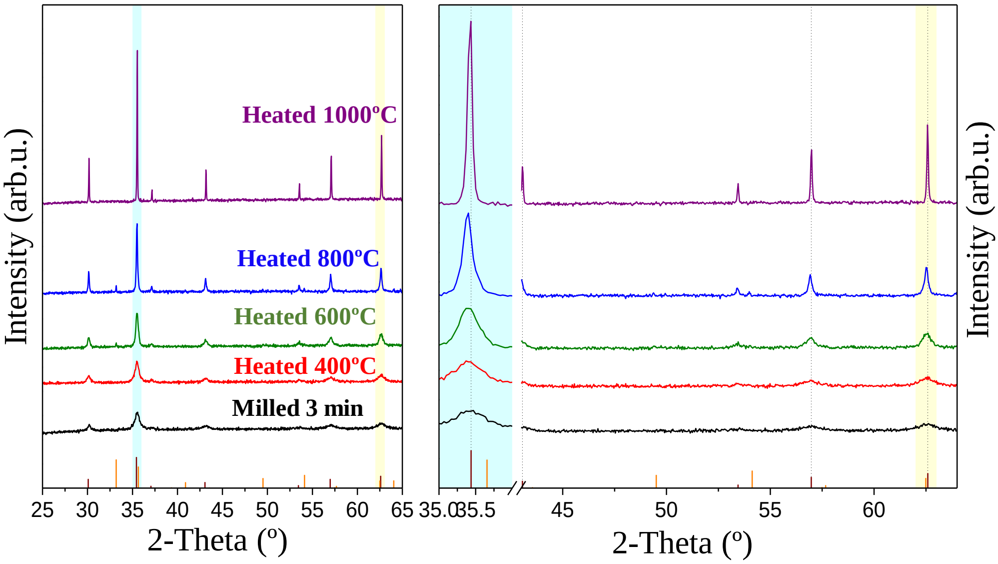

Figure 6.2: XRD spectra of milled CoFe$_2$O$_4$ powder after a heat treatment to different temperatures. From bottom to top: as-milled powders (180 seconds), and heated to 400, 600, 800 and 1000 °C. Brown lines in the bottom are references of CoFe$_2$O$_4$ diffraction peaks (ref: 00-022-1086), and orange lines correspond to α-Fe$_2$O$_3$ (ref: 01-089-0599)

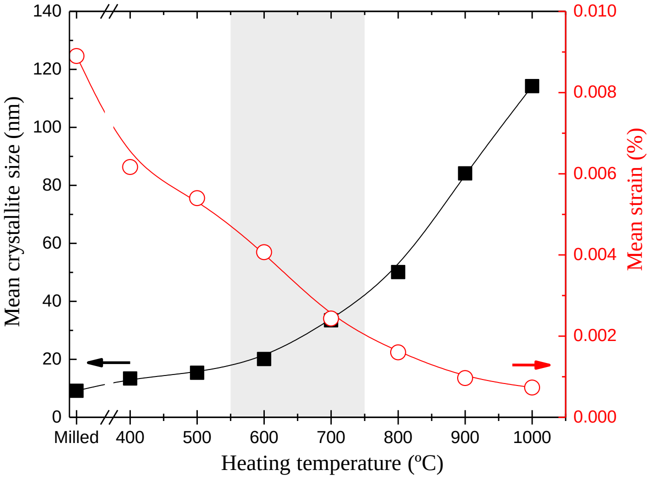

Figure 6.3: Evolution of mean crystallite size (filled symbols) and residual strain (empty circles) of as-milled powders with annealing temperature. Lines and guides for the eyes.

Attending to strain, ε, the as-milled powder possessed $\varepsilon = 9{\cdot}10^{-3}$, which continuously drops with increased heating temperature. The most pronounced decrease of ε is observed in powder heated to 400 °C, with $\varepsilon = 6.1{\cdot}10^{-3}$, a 45% lower than as-synthesized powder. This change might be ascribed to recrystallization of $CoFe_2O_4$ which leads to the disappearance of defects and dislocations. In general, ε evolves with a linear decline as a function of heating temperature. Powder heated to 800 °C and higher temperatures already display strain values comparable to as-synthesized powders previously discussed (see section 4.2.2).

In summary, the crystallization of α-Fe_2O_3 was observed when heating milled cobalt ferrite powder in a temperature range from 500 to 900 °C. If heating temperature is increased up to 1000 °C, exclusively $CoFe_2O_4$ diffraction peaks are observed in XRD. Furthermore, $<D_V>$ monotonically increases with heating temperature, overpassing the critical single domain size when the heating temperature was above 700 °C. In parallel, ε is decreased with increasing temperature down to values comparables to that obtained in as-synthesized powders.

6.1.3 Morphological analysis

SEM images included in Figure 6.4 show the evolution of $CoFe_2O_4$ morphology with the heating temperature. Morphology of as-milled powder was previously discussed in section 5.1.3 (named 'Milled 180 s').

Aggregates of submicrometer particles are observed in more detail in the right side figures. When the as-milled powder was heated to a temperature in a range from 400 to 600 °C (Figures 6.4.(b) and (c), respectively), it was observed a slight increase of particle size, as well as the rounding of particles edges. However, these changes are not significant by comparison with the powder heated to 1000 °C, where enlarged particles with polyhedral shapes, typical of sintered metallic materials, are observed. Moreover, the zoom of Figures 6.4.(d) allows the observation of two spherical particles formed due to coalescence and where different crystal orientations can be seen. This was also observed when heating as-synthesized powder to the same temperature (see Figure 4.4.(d))

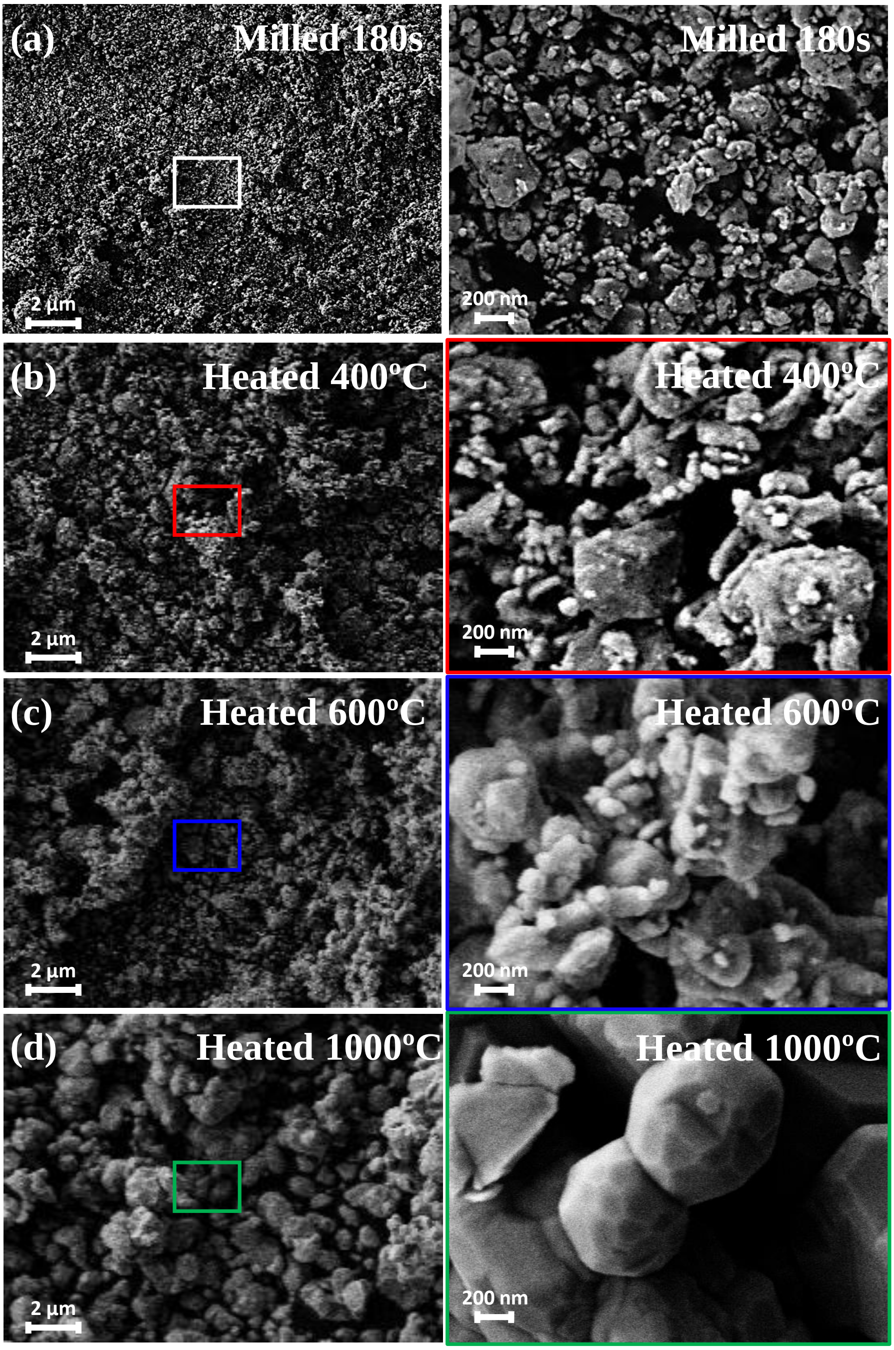

Figure 6.4: SEM images of (a) $CoFe_2O_4$ powders dry milled during 180 seconds and after being heated to (b) 400 °C, (c) 600 °C, and (d) 1000 °C. Scale bar: 2 μm. Right column images are magnified (scale bar: 200 nm).

6.1.4 Magnetic properties analysis

Room-temperature magnetization curves of the as-milled $CoFe_2O_4$ powder and after different post-milling heat treatments are represented in Figure 6.5. In general, it is observed a narrowing of the hysteresis loops accompanied by an increase in magnetization. The *M*-*H* curves evolves from a rounded-like shape of as-milled powder (Figure 6.5.(a)) to a squared-like shape observed in powder heated to 600 °C (Figure 6.5.(c)). Heating to a temperature of 1000 °C causes particles coalescence, in whose early stage might coexist melted polycrystalline particles and particles that did not coalescence yet. This is translated into a double-loop curve due to the contribution of particles types.

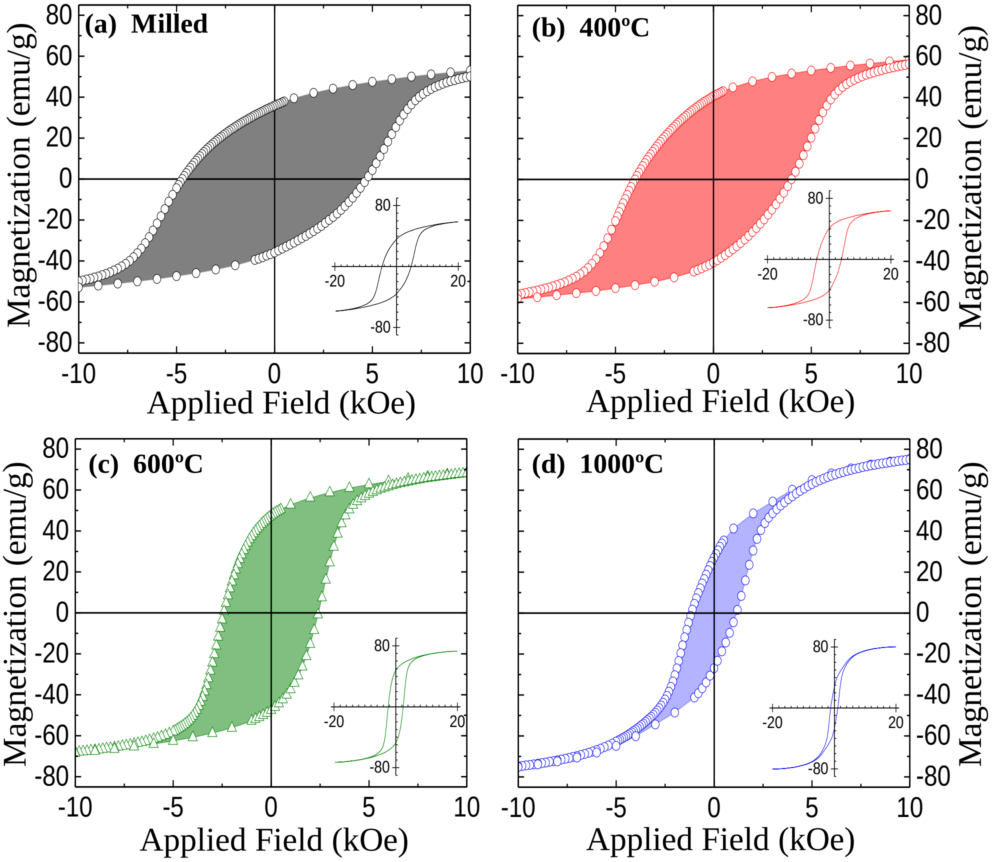

Figure 6.5: *M*-*H* curves of (a) $CoFe_2O_4$ powders after 3 minutes milling, and after a heat treatment to (b) 400 °C, (c) 600 °C and (d) 1000 °C.

Parameters extracted from hysteresis loops at RT are plot in Figure 6.6 as a function of the heat treatment temperature. The influence of the temperature of this heating process in the magnetic properties is discussed in the following.

As a first observation, heating as-milled powders results in an increase of M_{20kOe} due to the recrystallization of the amorphous phase and grain growth effect observed at temperatures above 400 °C [7–9]. This is in good agreement with XRD data previously discussed (see Figure 6.3). By comparison of the stepped increase in coercivity previously obtained in this powder with increasing HEBM milling time (see figure 5.6), the post-heat treatment strongly degrades the attained coercivity (Fig 6.6.(c)). When this milled powder was heated to 400 °C coercivity was already reduced in favor of enhanced M_R and M_{20kOe}. This behavior is due to the combined effect of the increased mean crystallite size - evolving from the monodomain (below 40 nm for T $\leq$700 °C) to the multidomain regime [10] - in combination with the relaxation of the strain induced during milling (Figure 6.3). However, the latter is playing a predominant role as proven by the fact that crystallite size does not vary significantly in the temperature range 400-700 °C while the mean strain drops. Accordingly, the measured coercivity decreases dramatically from 4.7 to 2.1 kOe after heating to 400 and 700 °C, respectively. An increased heating temperature results in a progressive elimination of the defects that were acting as pining centers for magnetization reversal in the as-milled powders, i.e. decreasing coercivity. Heating above 800 °C affects the microstructure due to a considerable particle size growth and early stage of coalescence (Figure 6.4). In this case, H_C only decreases from 1.9 to 1.2 kOe, after heating the milled sample to 800 and 1000 °C, while remanence magnetization drops.

The combination of an optimum remanence magnetization and a still significant coercivity obtained at a temperature of 600 °C results in a maximum $(BH)_{\mathrm{max}}$ = 17.8 kJm^{-3}. This energy product value is well above the $(BH)_{\mathrm{max}}$ determined for the as-milled powders. This value compares to the state-of-the-art value of 18 kJm^{-3}, reported for Co-ferrite nanoparticles synthesized by thermal decomposition of metal-organic precursors [11]. It is interesting to note that heating of the as-milled powder to 1000 °C results in practically complete reversibility in microstructural (Figure 4.4) and magnetic properties (Figure 4.12), i.e. obtaining values comparable to those measured in the starting material prior to milling.

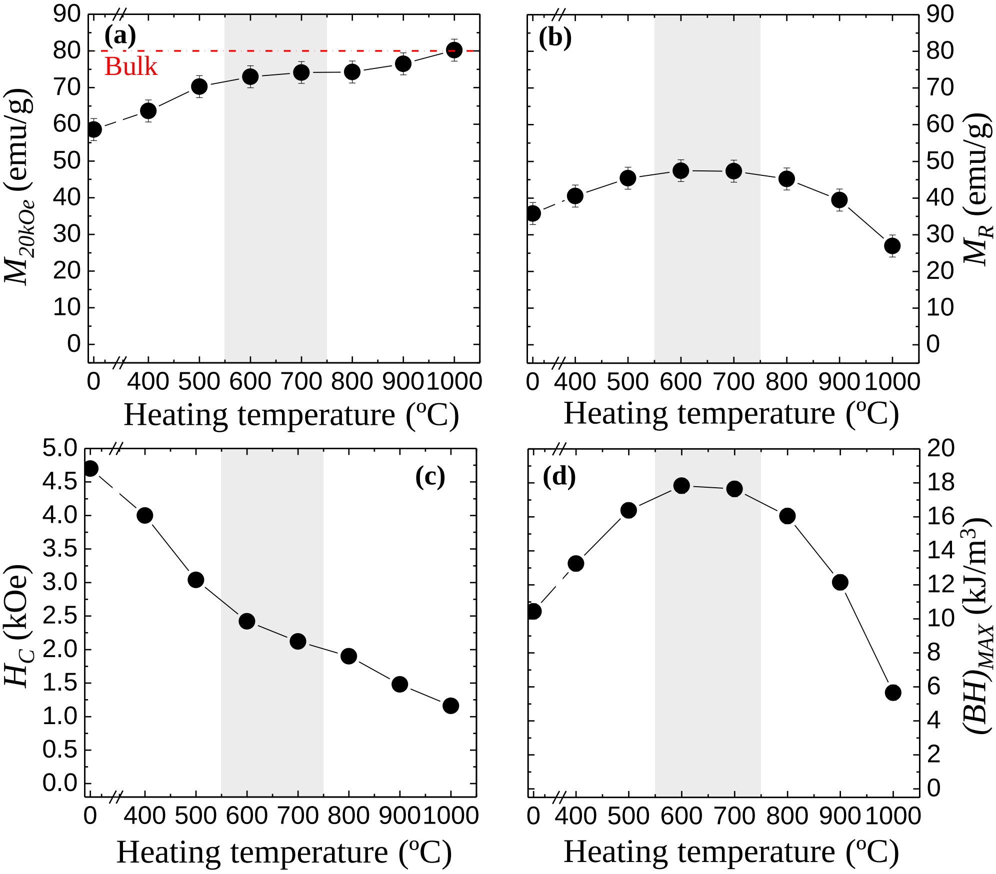

Figure 6.6: Evolution with post-milling heat treatment temperature of (a) saturation magnetization, $M_{20\mathrm{kOe}}$, (b) remanence magnetization, M_r, (c) coercivity , H_c and (d) Energy product, $(BH)_{\max}$, for $CoFe_2O_4$ powders milled during 180 seconds and heated in a temperature range from 400°C to 1000°C.

6.2 Heating of dry milled $CoFe_2O_4$

Once the possibility of further controlling cobalt ferrite microstructure is already demonstrated, the next question to answer is related with how the material properties influences the magnetic properties obtained after the post-synthesis heat treatment. For instance, in the previous chapter 5.2 was shown that the initial particle size of cobalt ferrite influences the effectiveness of the HEBM process, so in order to achieve high coercive cobalt ferrite, the most suitable starting material is that with the biggest particle size.

For the case of milled powder subjected to a post-milling heat treatment, a comparative study regarding the evolution of high coercive $CoFe_2O_4$ powders magnetic properties (obtained by ultra-fast high energy ball milling) of batches with different initial microstructure, with the temperature of a post-milling heat treatment is presented in this section. This study allows the correlation of microstructural modifications with magnetic properties enhancement in order to achieve $CoFe_2O_4$ isotropic powders with an optimum magnetic performance

6.2.1 Experiment description

Following the co-precipitation method, two syntheses reactions with a volume of 3 L each were preformed. Powders of both reactions were mixed when dried, obtaining a total amount of 300 g of as-synthesized powder. The as-synthesized powder was divided in for batches with a mass of 50 g each, and it were heated to a different temperature each, ranging from 700 to 1000 °C. The heating procedure was performed in a Naberthem muffle oven model L1 1/11/R6. In this case, the annealing procedure consisted of an increasing temperature ramp of 10K/min from room temperature to the goal temperature which was maintained for 1 hour before cooling down to room temperature. This treatment allows to crystallize the inverse spinel structure of $CoFe_2O_4$ with different crystallite sizes and strains for every batch as a function of the temperature used in the heat treatment (see chapter 4, Figures 4.3 and 4.4). The characterization and properties of these materials were previously discussed, named 'Powder C' in section 4.2.

HEBM experiments with a total duration of 180 seconds were performed to 4 grams of each $CoFe_2O_4$ powder batch, using a high-energy ball milling equipment Pulverizete 7 premium line from Fritsch at a speed of 900 rpm and a ball-to-powder ratio of 40:1. The powders were milled in air atmosphere, using tungsten carbide milling media (balls and vessel) to enhance the impact energy, i.e. accelerate an efficient milling process, due to the larger density of tungsten carbide (14.95 g/cm^3) by comparison with that of steel (7.8 g/cm^3). The characterization and properties of these materials were previously discussed in section 5.2.

Batches used in this experiment will be referred as:

- **Powder A**, for the batch heated to 700 °C and then milled during 180 seconds.
- **Powder B**, for the batch heated to 800 °C and then milled during 180 seconds.
- **Powder C**, for the batch heated to 900 °C and then milled during 180 seconds.
- **Powder D**, for the batch heated to 1000 °C and then milled during 180 seconds.

These as-milled powders were separated in batches of 150 mg each, and heated in a temperature range from 400 to 1000 °C, with 100 °C intervals, using air atmosphere with a Carbolite tubular oven model STF 15/450. The heating procedure consisted of an increasing temperature ramp of 10K/min from room temperature to the goal temperature which was maintained for 1 hour before cooling down to room temperature.

XRD spectra were measured with a Highscore X'pert θ-2θ diffractometer, using Cu-K_{α} radiation source. Mean crystallite size was calculated by applying the Equation 1.2 to the four most intense peaks and averaging the value, as well as the mean average strain that was obtained with the same method using Equation 1.3. These parameters extracted from XRD data are analyzed as a function of heating temperature.

SEM images were collected with a Carl-Zeiss Auriga microscope at a filament voltage of 3 kV, and were employed to obtain morphological information of $CoFe_2O_4$ powder.

A Lakeshore 7400 VSM was employed to measure magnetization M-H curves at room temperature. Parameters extracted from the hysteresis loops include magnetization at maximum applied field of 20 kOe (M_{20kOe}), remanence (M_r), and coercivity (H_c). Energy product, $(BH)_{max}$, has been evaluated, in order to quantify the performance as permanent magnets and to assess the suitability of this methodology.

6.2.2 Structural and compositional analysis

In order to analyze the effect of heating temperature on different as-milled powders, Powder A and Powder D will be studied as the extreme cases. Representative XRD patterns of Powder A and D are shown in Figure 6.7.(a) and (b) respectively. XRD spectra of both as-milled powders were discussed in chapter 5. As-milled Powder A pattern (Figure 6.7.(a)) display an extra peak at 2θ=33.2 ° originated by a small fraction of α-Fe_2O_3, already present in the as-synthesized powder (see Figure 4.9), in addition to $CoFe_2O_4$ spinel phase diffraction peaks. However, $CoFe_2O_4$ phase is exclusively observed in as-milled Powder D. It was previously discussed how an annealing process applied to the powder obtained from the co-precipitation synthesis reaction provides energy to form $CoFe_2O_4$ crystals [1–3] (see section 4). Moreover, in section 6.1 was shown that α-Fe_2O_3 diffraction peaks were observed in $CoFe_2O_4$ milled powder when heated to a temperature in the range from 500 °C to 900 °C, and this peak disappeared when the heating temperature was 1000 °C. In this case, initial Powder A was constituted by a small portion of α-Fe_2O_3 that was observed in the as-milled powder. Interestingly, in Powder A hematite was present in all heated powders with the exception to the sample heated to 1000 °C, where only $CoFe_2O_4$ was observed. The appearance of α-Fe_2O_3 in Powder D, where it was not initially present, in addition to the observation of exclusively $CoFe_2O_4$ in Powder A and D after heating to 1000 °C, points to the fact that α-Fe_2O_3 is a secondary phase formed in the transition to pure stoichiometric $CoFe_2O_4$ [12].

Parameters extracted from XRD spectra, including crystallite size, $<D_V>$, and strain, ε, are analyzed as a function of the post-milling heating temperature. Figure 6.8.(a) displays the evolution of the$<D_V>$, and Figure 6.8.(b), the calculated values ε.

A difference in crystallite size of 6 nm was observed between $<D_V>$ = 15 nm of as-milled Powder A, and $<D_V>$ = 9.1 nm of as-milled Powder D. The lower crystallite size assessed in as-milled Powder D by comparison with that of as-milled Powder A is related with the effectiveness of HEBM process depending on the initial material microstructure. In any case,

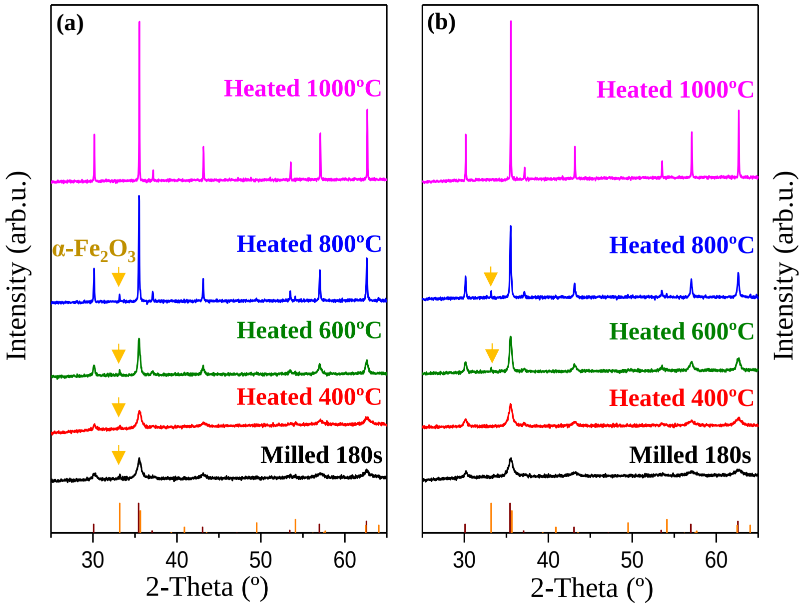

Figure 6.7: XRD spectra of CoFe$_2$O$_4$ powders from (a) Powder A and (b) Powder D. In both cases, from bottom to top are represented: as-milled powder (180 seconds) and after heating at 400, 600, 800 and 1000 °C. Yellow arrows emphasize α-Fe$_2$O$_3$ diffraction peaks.

both batches display an average crystallite size well below the magnetic monodomain critical size of 40 nm [6]. As a general tend, a monotonic increase of $<D_V>$ with increasing the heating temperature is observed. $<D_V>$ values of Powder A are greater than the calculated for Powder D heated to the same temperature. This would be explained as the correlation of a short heating time in addition to the influence of as-milled crystallite size. The difference in $<D_V>$ among both batches was greater when the powders were heated to temperatures above 600 °C, where coalescence began to occurs.

Attending to calculated strain values as a function of heating temperature plot in Figure 6.8.(b), the relaxation of ε induced during milling is observed in heated powders. The decline of ε is more pronounced at moderated heating temperatures, i.e. in a temperature range from 400 °C to 600 °C. A strain value $\varepsilon = 6.7 \cdot 10^{-3}$ assessed in as-milled Powder A, and $\varepsilon = 9 \cdot 10^{-3}$ of Powder D, were equated to $\varepsilon = 6.1 \cdot 10^{-3}$ calculated in both batches after heating to 400 °C. The strain induced during mechanical milling is almost eliminated when the as-milled powder is heated to temperatures above 900 °C, with calculated ε values $0.7 \cdot 10^{-3}$ in both batches after heating to 1000 °C.

As in the previous case, $< D_V >$ increases with increased heating temperature while ε is decreased. Remarkably, it is shown that the microstructure of powder heated after HEBM process depends on parameters such as strain present in the powder before milling. It is observed a higher increase of $< D_V >$ in that powder with lower strain after milling. Interestingly, note that ε values of powders heated to temperatures above 700 °C are similar to that previously calculated in as-synthesized powders prior to milling (see Figure 4.10).

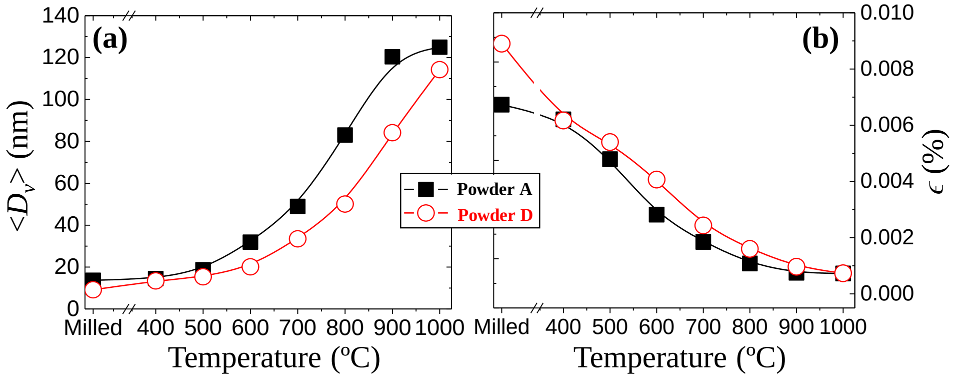

Figure 6.8: Evolution of (a) mean crystallite size (filled symbols), and (b) residual strain (empty circles) with annealing temperature of Powder A (black) and Powder D (red). Lines and guides for the eyes.

6.2.3 Magnetic properties analysis

RT magnetization curves of as-milled $CoFe_2O_4$ powders, and after a post-milling heat treatments to different temperatures are represented in Figure 6.9. The evolution of Powder D hysteresis loop with heating temperature was discussed in the previous section 6.1.4. In brief, the same tendency is observed in the evolution of *M-H* curves of all batches; as-milled samples display rounded hysteresis loops (Figure 6.9.(a)) that becomes more squared after being heated. This is an effective increase of the knee-point of a magnetic material, which is translated in an enhanced energy product as it will be shown in the following. Nevertheless, a two-steps hysteresis loop measured after heating to 1000 °C is characteristic of a magnetic material with an inhomogeneous microstructure consisting of particles with a broad particle size distribution, where particles with sizes below and above the magnetic monodomain critical size coexist.

Interestingly, *M-H* curves of samples heated to 1000 °C, plot in Figure 6.9.(d), are almost identical, confirming that a heat treatment to this temperature is a good procedure to achieve powder homogenization in terms of magnetic properties. Recrystallization and grain growth of $CoFe_2O_4$ particles with heating temperature are the responsible of the increased magnetization at expenses of coercivity, as it was previously discussed in section 6.1.4. Parameters extracted from the *M-H* curves are plot in Figure 6.10, as a function of a post-milling heat treatment in a temperature range from 400 °C to 1000 °C.

At a first glance, Figure 6.10.(a) displays a linear increase of $M_{20\text{kOe}}$ with the heating temperature of all batches as a consequence of the bigger particle size [13, 14]. This is in good agreement with XRD and SEM data previously discussed (see Figure 6.8 and Figure 6.4). Nevertheless, the saturation magnetization of bulk $CoFe_2O_4$ was only achieved when the heating temperature was 1000 °C. All powders heated to the same temperature display quite similar $M_{20\text{kOe}}$, with the exception of Powder D when it was heated in a temperature range from 400 °C to 700 °C. $M_{20\text{kOe}}$ of as-milled powders is quite similar, being $M_{20\text{kOe}} = 57.2$ emu/g the lowest value measured in Powder C and M_{20kOe} = 58.7 emu/g the highest obtained in Powder A. As-milled Powder D posses a M_{20kOe} = 58.6 emu/g which rose up to M_{20kOe} = 63.7 emu/g when it was heated to 400 °C, and M_{20kOe} = 70.3 emu/g for a temperature of 500 °C. Notwithstanding, considering Powder A as the representative among Powders A, B and C (it was the batch with the highest initial M_{20kOe}), this powder display values of M_{20kOe} = 62.8 emu/g and M_{20kOe} = 66.4 emu/g when it was heated to 400 °C and 500 °C respectively. The greatest increase in Powder of M_{20kOe} might be related with the formation of secondary iron oxide phases, such as the observed α-Fe_2O_3 (see Figure 6.7) that crystallizes in this temperature range [4] but its concentration is lower than XRD experiments resolution. If this is the case, the reduced amount of these possible secondary phases in the sample was small, and that explains why only a difference a few emu/g in M_{20kOe} was observed. A heat treatment to a temperature above 700 °C

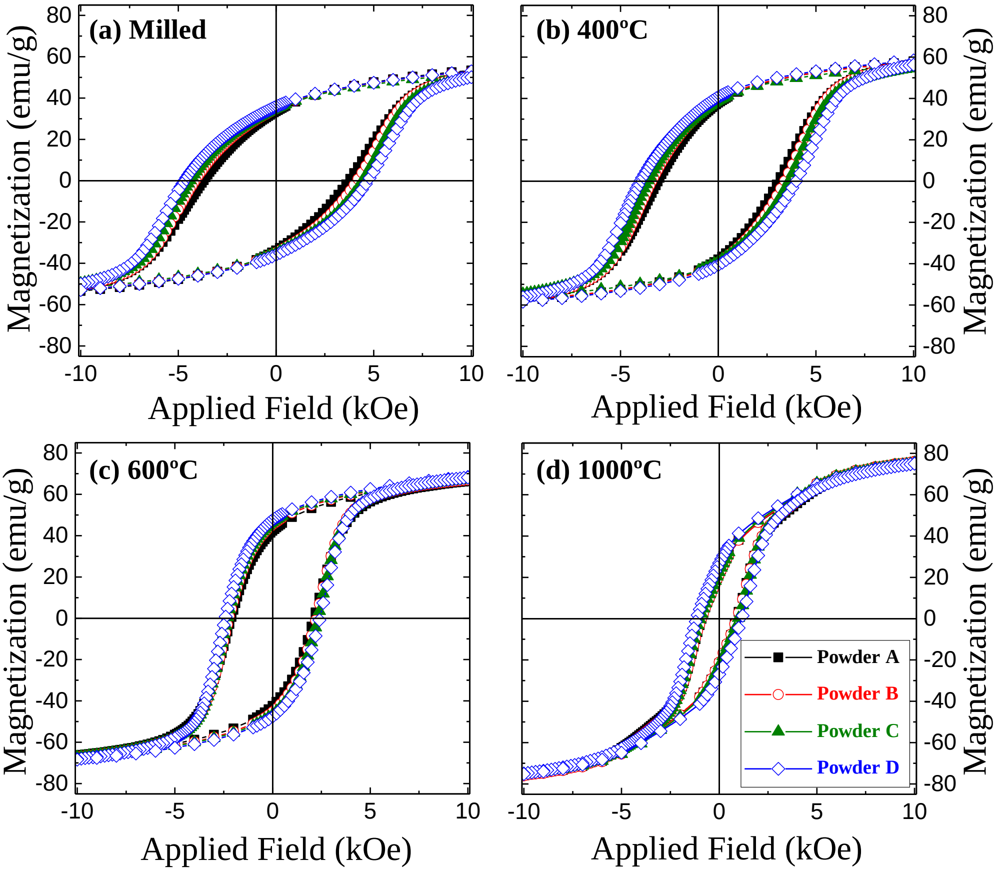

Figure 6.9: *M*-*H* curves of (a) initial $CoFe_2O_4$ powders after 3 minutes milling, and the hysteresis loops of these samples after a heat treatment to (b) 400, (c) 600 and (d) 1000 °C. The curves correspond to powder A (black), powder B (red), powder C (green) and powder D (blue)

provides powders with practically the same $M_{20\mathrm{kOe}}$, regardless of batch provenance.

The evolution of remanence magnetization, M_{r}, with the heating temperature is shown in Figure 6.10.(b) In general, all batches follows the same evolution; M_{r} is increased when the as-milled powders are heated in a temperature range from 400 °C to 700 °C due to recrystallization and grain growth, and this value drops when the heating temperature is above 700 °C. By comparing Figure 6.10.(b) with Figure 6.8.(a) one can see that when the powder (Powder A or Powder D) overtake a size of 40 nm (single-domain critical size) M_{r} starts decreasing. This is associated with the minimization of magnetostatic energy leading to a multidomain magnetic state [10]. Powder A displays the lowest values of remanence and Powder D is the one with the highest M_{r}. These quantitative differences might be due to the existence of α-$\mathrm{Fe_2O_4}$ that decreases M_{r}. Among all the samples, the maximum M_{r} = 47.5 emu/g was measured in Powder D after a heat treatment to 600 °C. As it was observed for $M_{20\mathrm{kOe}}$, Powders A, B and C display similar M_{r} when heated to 1000 °C.

Coercivity, H_{c}, follows a decline with increased temperature. The large coercivity achieved with the HEBM process, is due to the combined result of a reduced mean crystallite size and the induced strain during milling that results in the creation of defects acting as pinning centers during magnetization reversal (see Section 5.2). Heating above 214 °C causes cobalt ferrite recrystallization, and thus the relaxation of strain induced during milling, favoring magnetic domain wall movement that is translated into a diminished H_C. A correlation between H_C with strain and particle size is discussed in detail in Chapter 7

Figure 6.10.(b) shows the evolution of $(BH)_{\mathrm{max}}$ with the annealing temperature. It is observed how energy product rose to a maximum value, which was achieved when the powders were heated in a temperature range fo 600-700 °C independently of the batch provenance. Increased annealing temperatures produced the reduction in energy product, since $(BH)_{\mathrm{max}}$ results from the combination of H_C (which is continuously decreased with increased heating temperatures) and M_{r} that decreases when heating above 700 °C. Powder A display the lowest energy product with, a maximum $(BH)_{\mathrm{max}}$ = 14.0 kJm^{-3} after heating to 600 °C. The highest energy product was measured in Powder D after being heated to 600 °C, with a $(BH)_{\mathrm{max}}$ = 17.8 kJm^{-3} resulting from the combination of M_{r} = 42.5 emu/g and H_C = 2.4 kOe.

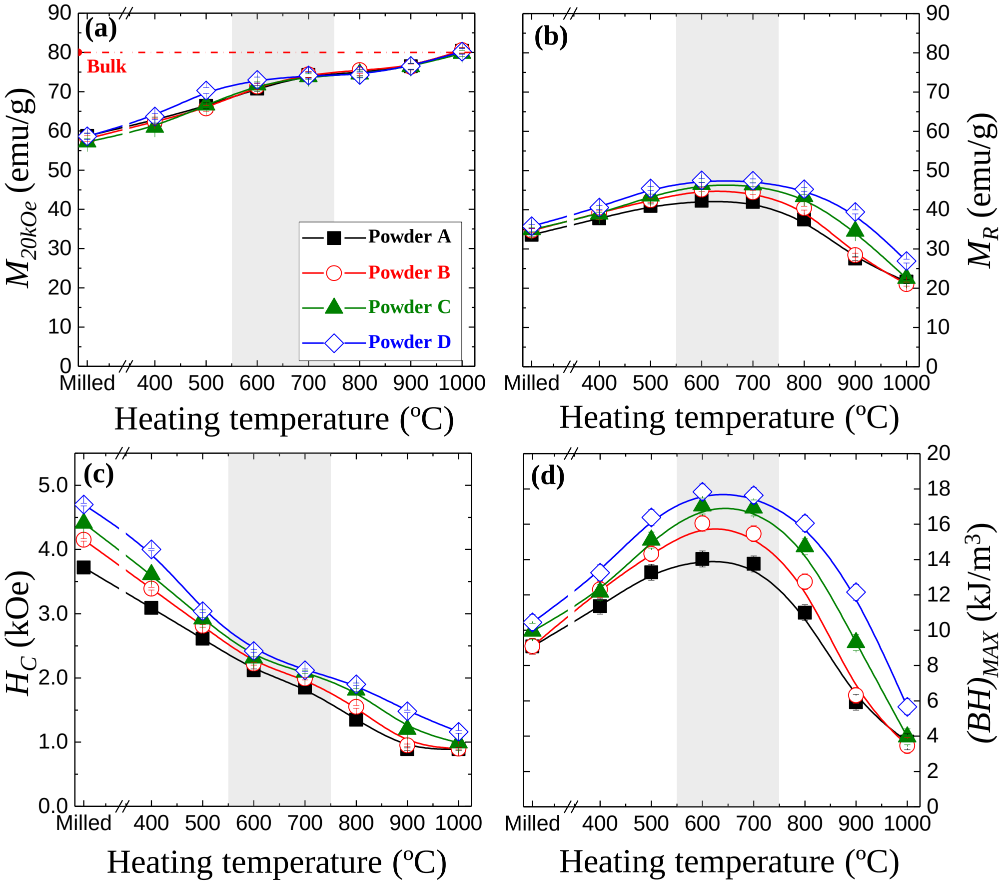

Figure 6.10: Evolution with post-milling heat treatment temperature of (a) saturation magnetization, $M_{20\mathrm{kOe}}$, (b) remanence magnetization, M_r, (c) coercivity , H_c and (d) Energy product, $(BH)_{\max}$, for CoFe$_2$O$_4$ powders synthesized at temperatures of 700, 800, 900 and 1000°C (black, red, green and blue respectively) and milled during 3 minutes.

6.3 Heating wet milled $CoFe_2O_4$

The characterization analysis regarding the behavior of milled cobalt ferrite powder with the temperature of a post-milling heat treatment indicates that, on the one hand, the increased coercivity is related with induced disorder in the crystal lattice, which is rearranged when heated to temperatures above 400 °C. On the other hand, $(BH)_{max}$ increases up until a certain temperature, which seems to be when coalescence among particles start to occur. This is the main cause in the detriment of remanence magnetization, originating a decrease og $(BH)_{max}$.

In order to look for the most favorable conditions to obtain cobalt ferrite powder with enhanced $(BH)_{max}$, $CoFe_2O_4$ powders that were previously milled by the wet milling method are studied as a function of a post-milling heat treatment temperature. The use of surfactant in the HEBM process was shown to be advantageous in the formation of a more homogeneous structure constituted by non-agglomerated nanoparticles, which might be beneficial to enhance energy product since it hinder coalescence. In fact, this section describes how a record $(BH)_{\mathrm{max}}$ value of 18.6 kJ m^{-3} has been obtained for wet milled $CoFe_2O_4$ isotropic powder after a post-milling annealing process.

6.3.1 Experiment description

$CoFe_2O_4$ powder synthesized following a sol-gel route using Fe and Co nitrates. The nitrates were dissolved in 1:2 ratios in deionized water. Citric acid was subsequently added to the solution, which was then constantly stirred at 60 °C for 1 h. The gel formed was dried in a hot air oven for 24 h. The precursor obtained was calcined for 1 h at 400 °C. The resulting powder was subsequently annealed at 900 °C to crystallize the inverse spinel structure of $CoFe_2O_4$.

HEBM of $CoFe_2O_4$ powder with 2wt.% of oleic acid added as surfactant prior to milling (wet milling) was carried out during 3 and 9 minutes. The milling was performed to 4 grams of $CoFe_2O_4$ powder. A rotational speed of 900 rpm and a ball-to-powder ratio of 40:1 were used in the milling experiments. Oleic acid was removed after the milling process by washing the powder with acetone. Finally, a subsequent heat treatment in air at 200 °C allowed for the complete evaporation of any residual organic components.

Post-milling heat treatment to different temperatures, in the temperature range 500-900 °C were performed using air atmosphere in a Carbolite tubular oven model STF 15/450. The heating procedure consisted of an increasing temperature ramp of 10K/min from RT to the goal temperature which was maintained for 3 hour before cooling down to RT.

A Lakeshore 7400 VSM was employed to measure magnetization M-H curves at room temperature. Parameters extracted from the hysteresis loops include magnetization at maximum applied field of 20 kOe (M_{20kOe}), remanence (M_{r}), and coercivity (H_{c}). Energy product, $(BH)_{\mathrm{max}}$, has been evaluated, in order to quantify the performance as permanent magnets and to assess the suitability of this methodology.

6.3.2 Results and discussion

CoFe$_2$O$_4$ powder was milled by the wet milling method during 3 and 9 minutes. In the previous section 5.3 was shown that the use of oleic acid leads to a more homogeneous microstructure and a significantly reduced number of agglomerates than by the dry milling method. Milled powder comprise submicron particles with a well-defined polyhedral shape, due the polar nature of the solvent that eases the creation of a protective layer around the particles during milling. After milling, the powder was washed and and separated in batches of 100 mg that were heated to a different temperature each. Powder milled during 3 minutes present an average crystallite size of 28.9 nm, which is slightly above twice the 13.8 nm size obtained for powder milled during 9 minutes. This difference in crystallite size, due to the different milling times, was previously discussed in section 5.3.

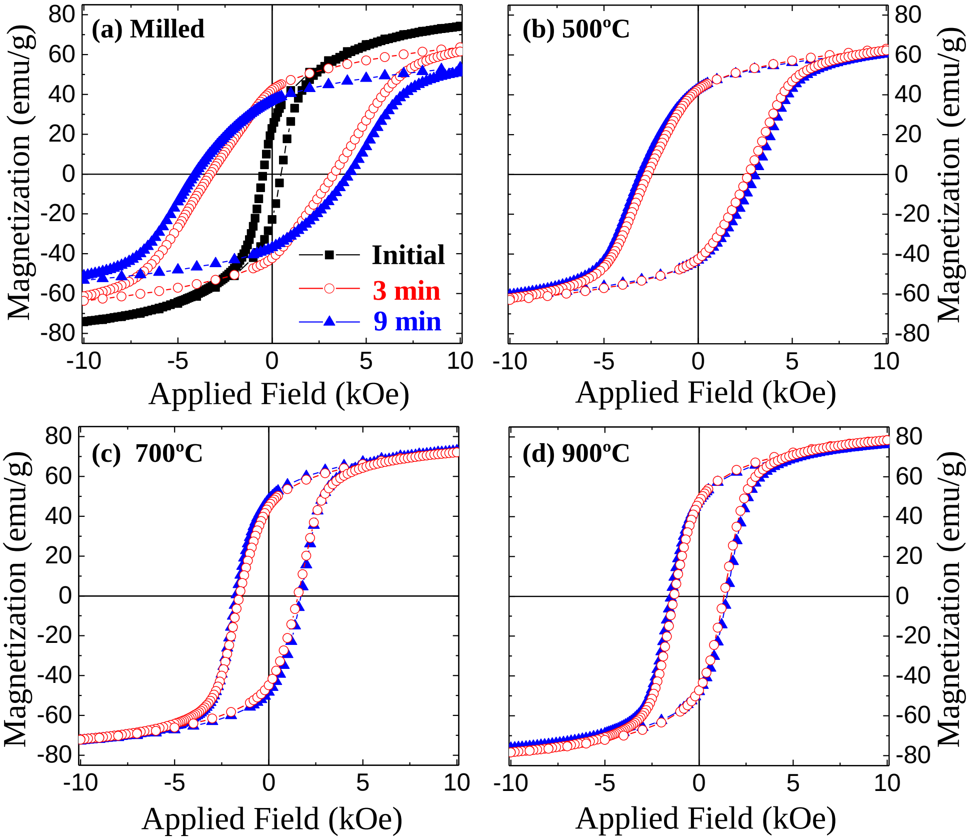

Figure 6.11: *M*-*H* curves of (a) initial CoFe$_2$O$_4$ and after 3 (red) and 9 (blue) minutes of wet milling, and after a post-synthesis heat treatment at (b) 500 °C, (c) 700 °C and (d) 900 °C.

Figure 6.11.(a) shows the effect of HEBM by the wet method during at 3 and 9 min in the characteristic hysteresis loop of the initial as-synthesized material. The magnetization curves after milling are notably wider while magnetization is decreased due to the reduced particle size. Note that magnetization of milled powders are considerably higher than the obtained when HEBM process is performed with the dry method. The evolution of milled powders magnetization curves after a post-milling heat treatment at three representative temperatures, 500, 700, and 900 °C) are plot in Figures 6.11.(c-d). Interestingly, it is appreciated that hysteresis curves of both samples heating to 500 °C are quite similar; magnetization curves seems to follow the same behavior, however considerable quantitative differences between samples are found.

Parameters extracted from these hysteresis loops including saturation and remanence magnetization, coercivity and energy product of both milled powders as a function of heating temperature (500-900 °C) is shown in Figure 6.12. As in the case of dry milled powder, heating the milled up to 750 °C causes the increase of saturation magnetization and remanence magnetization (Figures 6.12.(a-b)). When the heating temperature was above 600 °C, both milled samples displayed similar M_{20kOe}. In case of M_R, same behavior with practically identical values are observed in all the temperature range with the exception of samples heated to 700 and 750 °C. This might be associated with the the formation of a transitory phase like α-Fe_2O_3. The reduced coercivity obtained after heating can be explained as a consequence of recrystallization effect, i.e. relaxation of the strain induced during milling. The strain of the 9 min wet-milled powder is 0.006%, while this value is reduced to 0.002% after heat treatment at 750 °C, thus proving the relaxation effect induced by the post-heating process on the as-milled powders.

The optimum combination in terms of energy product was found in the powder wet milled during 9 minutes after heating to 750 °C, with a calculated $(BH)_{\max} = 18.6$ kJ m^{-3} which stands as the maximum $(BH)_{\max}$ reported to date in literature for isotropic $CoFe_2O_4$ powder, and exceeds the 12.5 kJ m^{-3} reported by Yang et al [15] for pure isotropic $BaFe_{12}O_{19}$ powders. This value results from the combination of $H_c = 1.6$ kOe and and $M_r = 48.8$ emu/g. The isotropic powders produced in this study might be further used in the fabrication of anisotropic magnets by different routes such as magnetic-annealing. [16, 17]

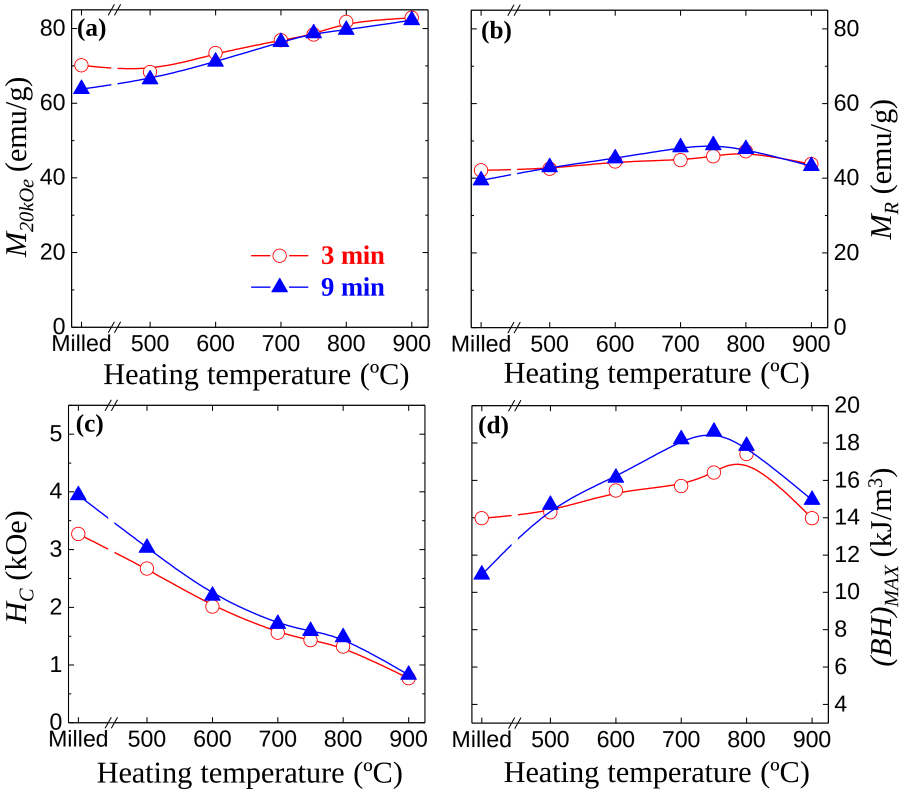

Figure 6.12: Evolution of (a) saturation magnetization, $M_{20\mathrm{kOe}}$, (b) remanence magnetization, M_r, (c) coercivity, H_c, and (d) energy product, $(BH)_\mathrm{max}$, with milling time of powder wet milled for 3 min (black), and 9 minutes (red).

6.4 Conclusions

The evolution of cobalt ferrite powder subjected to a heat treatment after a HEBM process have been analyzed and discussed in this chapter. Unlike experiments presented in Chapter 4 where $CoFe_2O_4$ was crystallized after the synthesis reaction, in this case, the powder is already crystallized but with high level of defects, strain and amorphization imparted through the HEBM process. The appearance of α-Fe_2O_3 diffraction peak when the heating temperature was in the range 500 °C to 900 °C, in addition to its disappearance when the as-milled powder was heated to 1000 °C indicates that hematite is a transitional phase prior to obtain bulk cobalt ferrite, as it has been previously reported [12].

Microstructure of cobalt ferrite is highly influenced by this post-milling heat treatment. In general, ε evolves with a linear decline as a function of heating temperature, while $< D_V >$ slightly increases with heating temperature when $T \leq 700$ °C, then a considerable grain growth was observed. Remarkably, it was observed that the more strained $CoFe_2O_4$ the lower increase in crystallite size after the heat treatment. These modifications in the microstructure entails variations in magnetic properties; the increased coercivity obtained by the HEBM process is as far as the induced disorder in the crystal lattice through the milling is rearranged. This occurs at 'low' temperatures, in the range from 400 to 700. In addition, this enhanced crystallinity while maintaining the average crystallite size of particles below the monodomain crystallite size results in an enhanced energy product with respect to the milled powder. SEM observations revealed that morphology of milled $CoFe_2O_4$ when heated in a temperature range 400 to 800 °C goes from particles with sharp edges to rounded particles, while with higher temperatures enlarged particles with polyhedral shapes, typical of sintered metallic materials, are observed.

In this chapter has been shown how to obtain a combination of an optimum remanence magnetization and a still significant coercivity in $CoFe_2O_4$ powders after HEBM process, obtaining the highest $(BH)_{max}$ reported up to date for a cobalt ferrite. This value was obtained after heating to 750 °C a cobalt ferrite powder that was previously milled with the wet milling method during 9 minutes, resulting in a maximum $(BH)_{\mathrm{max}}$ = 18.6 $\mathrm{kJm^{-3}}$. This energy product value is a 69 % higher than that determined for the as-milled powders, and compares to the state-of-the-art value of 18 $\mathrm{kJm^{-3}}$, reported for Co-ferrite nanoparticles synthesized by thermal decomposition of metal-organic precursors [11], with the difference that the method here described is easily scalable to an industrial level.

It is interesting to note that heating of the as-milled powder to 1000 °C results in practically complete reversibility in microstructural (Figure 4.4) and magnetic properties (Figure 4.12), i.e. obtaining values comparable to those measured in the starting material prior to milling. Powders heated to 800 °C and higher temperatures already display strain values comparable to as-synthesized powders previously discussed (see section 4.2.2). Furthermore, note that ε values of powders heated to temperatures above 700 °C are similar to that previously calculated in as-synthesized powders prior to milling (see Figure 4.10).

References

[1] Francisco Augusto Tourinho, Raymonde Franck, and René Massart *Aqueous ferrofluids based on manganese and cobalt ferrites*. in: *Journal of Materials Science* ***25***,7 (1990), 3249–3254 (cit. on pp. 91, 99)

[2] Yeong Il Kim, Don Kim, and Choong Sub Lee *Synthesis and characterization of $CoFe_2O_4$ magnetic nanoparticles prepared by temperature-controlled coprecipitation method*. in: *Physica B: Condensed Matter* ***337***,1 (2003), 42–51 (cit. on pp. 91, 99)

[3] Debabrata Moitra, Subhenjit Hazra, Barun Kumar Ghosh, RK Jani, MK Patra, Sampat Raj Vadera, and Narendra Nath Ghosh *A facile low temperature method for the synthesis of $CoFe_2O_4$ nanoparticles possessing excellent microwave absorption properties*. in: *RSC Advances* ***5***,63 (2015), 51130–51134 (cit. on pp. 91, 99)

[4] TR Tatarchuk, EV Boyko, IP Yaremiy, BI Rachiy, and SV Fedorchenko *Synthesis, Crystal Chemistry and Antistructure Modelling of $CoFe_2O_4$ Nanoparticles Prepare by Citrat Sol-Gel Method*. in: *Physics and Chemistry of Solid State* ***15***,4 (2014), 792–797 (cit. on pp. 91, 102)

[5] ED Kolb, AJ Caporaso, and RA Laudise *Hydrothermal growth of hematite and magnetite*. in: *Journal of Crystal Growth* ***19***,4 (1973), 242–246 (cit. on p. 91)

[6] CN Chinnasamy, B Jeyadevan, K Shinoda, K Tohji, DJ Djayaprawira, M Takahashi, R Justin Joseyphus, and A Narayanasamy *Unusually high coercivity and critical single-domain size of nearly monodispersed $CoFe_2O_4$ nanoparticles*. in: *Applied physics letters* ***83***,14 (2003), 2862–2864 (cit. on pp. 91, 100)

[7] M Rajendran, RC Pullar, AK Bhattacharya, D Das, SN Chintalapudi, and CK Majumdar *Magnetic properties of nanocrystalline $CoFe_2O_4$ powders prepared at room temperature: variation with crystallite size*. in: *Journal of Magnetism and Magnetic Materials* ***232***,1 (2001), 71–83 (cit. on p. 96)

[8] Kush Rana, Preeti Thakur, Parul Sharma, M Tomar, V Gupta, and Atul Thakur *Improved structural and magnetic properties of cobalt nanoferrites: influence of sintering temperature*. in: *Ceramics International* ***41***,3 (2015), 4492–4497 (cit. on p. 96)

[9] Ekaphan Swatsitang, Sumalin Phokha, Sitchai Hunpratub, Brian Usher, Atipong Bootchanont, Santi Maensiri, and Prinya Chindaprasirt *Characterization and magnetic properties of cobalt ferrite nanoparticles*. in: *Journal of Alloys and Compounds* ***664***, (2016), 792–797 (cit. on p. 96)

[10] M Chithra, CN Anumol, Baidyanath Sahu, and Subasa C Sahoo *Exchange spring like magnetic behavior in cobalt ferrite nanoparticles*. in: *Journal of Magnetism and Magnetic Materials* ***401***, (2016), 1–8 (cit. on pp. 96, 103)

[11] Alberto López-Ortega, Elisabetta Lottini, Cesar de Julian Fernandez, and Claudio Sangregorio *Exploring the magnetic properties of cobalt-ferrite nanoparticles for the development of a rare-earth-free permanent magnet*. in: *Chemistry of Materials* ***27***,11 (2015), 4048–4056 (cit. on pp. 96, 109)

[12] IC Nlebedim, JE Snyder, Anthony John Moses, and David C Jiles *Effect of deviation from stoichiometric composition on structural and magnetic properties of cobalt ferrite, CoxFe3- xO4 (x= 0.2 to 1.0)*. in: *Journal of Applied Physics* ***111***,7 (2012), 07D704 (cit. on pp. 99, 109)

[13] Ekaphan Swatsitang, Sumalin Phokha, Sitchai Hunpratub, Brian Usher, Atipong Bootchanont, Santi Maensiri, and Prinya Chindaprasirt *Characterization and magnetic properties of cobalt ferrite nanoparticles*. in: *Journal of Alloys and Compounds* ***664***, (2016), 792–797 (cit. on p. 101)

[14] A Franco Jr, FC e Silva, and Vivien S Zapf *High temperature magnetic properties of Co1-xMgxFe2O4 nanoparticles prepared by forced hydrolysis method*. in: *Journal of Applied Physics* ***111***,7 (2012), 07B530 (cit. on p. 101)

[15] Haibo Yang, Ting Ye, Ying Lin, Miao Liu, Ge Zhang, and Pan Kang *Giant enhancement of (BH) max in BaFe 12 O 19/Y 3 Fe 5 O 12 nanocomposite powders*. in: *Materials Letters* ***145***, (2015), 19–22 (cit. on p. 107)

[16] YX Zheng, QQ Cao, CL Zhang, HC Xuan, LY Wang, DH Wang, and YW Du *Study of uniaxial magnetism and enhanced magnetostriction in magnetic-annealed polycrystalline* $CoFe_2O_4$. in: *Journal of Applied Physics* ***110***,4 (2011), 043908 (cit. on p. 107)

[17] Atif Muhammad, Reiko Sato-Turtelli, Martin Kriegisch, Roland Grössinger, Frank Kubel, and Thomas Konegger *Large enhancement of magnetostriction due to compaction hydrostatic pressure and magnetic annealing in* $CoFe_2O_4$. in: *Journal of Applied Physics* ***111***,1 (2012), 013918 (cit. on p. 107)

Chapter 7

Modelling $CoFe_2O_4$ thermal behavior

Cobalt ferrite microstructure modifications entails the modification of its magnetic properties. Actually, nanostructuration have been demonstrated to be the key element behind all the enhancements presented in this work. In this section, magnetic measurement at different temperatures are used to characterize cobalt ferrite. Effective anisotropy as well as saturation magnetization are correlated with microstructural data, demonstrating that strain is the main parameter behind the high increase observed in coercivity, and the crystallite size determines the saturation magnetization.

Three different products of cobalt ferrite are proposed as candidates for permanent magnets applitacions, a simply synthesized $CoFe_2O_4$ with optimum magnetic properties, a cobalt ferrite product with high coercivity, or a enhanced $(BH)_{max}$ $CoFe_2O_4$. Furthermore, the temperature dependence of these products magnetic properties are analyzed in order to determine the most suitable industrial applications for this material as permanent magnets.

7.1 Modelling $CoFe_2O_4$ magnetic properties

Temperature dependence studies are required to obtain a better understanding of magnetism and related phenomena. In particular, intrinsic properties such as saturation magnetization or coercivity are temperature dependent. By fitting experimental data to the reported models, for instance to the Bloch's law, it os possible to obtain a estimation of Curie temperature. Furthermore, the Kneller's fits allows the estimation of the superparamagnetic blocking temperature. In both cases, the value of these parameters at $T = 0$ K can be extrapolated. In addition, in this study the LAS approximation is applied to magnetization curves in the high field range, allowing to estimate the effective magnetic anisotropy as well as the saturation magnetization as a function of temperature. Moreover, with this data it is possible to verify the as-known as 'callen-callen' law, which states that magnetic anisotropy is proportional to a power of the magnetic moment, and this dependence have been calculated.

It is important to consider that depending on the $CoFe_2O_4$ preparation conditions, a secondary phase might be present, concretely hematite, which is a ferromagnetic phase at room temperature, but below 260K it displays what is known as the Morin transition, wherein α-Fe_2O_3 behaves as a antiferromagnet. This in important to keep in mind when analyzing the obtained data as a function of temperature. In order to evaluate a batch of pure $CoFe_2O_4$, a high coercive cobalt ferrite obtained by HEBM process after its synthesis by the co-precipitation, with a heat treatment to 1000 °C for cobalt ferrite crystallization method is performed. A more detailed description of the sample preparation can be found in the experimental description.

7.1.1 Experiment description

Using the co-precipitation method, two syntheses were performed in a reaction volume of 3 L each. Powders of both reactions were mixed when dried, obtaining a total amount of 300 g of as-synthesized powder. A batch with a mass of 50 g was prepared and heated to 1000 °C. The characterization and properties of this material were previously discussed, named 'Powder C', in section 4.2. The heating procedure was performed in a Naberthem muffle oven model L1 1/11/R6. In this case, the annealing procedure consisted of an increasing temperature ramp of 10K/min from room temperature to the goal temperature which was maintained for 1 hour before cooling down to room temperature. This treatment allows to crystallize the inverse spinel structure of $CoFe_2O_4$ (see chapter 4.

HEBM experiment with a total duration of 180 seconds was performed to 4 grams of the aforementioned $CoFe_2O_4$ powder, using a high-energy ball milling equipment Pulverizete 7 premium line from Fritsch at a speed of 900 rpm and a ball-to-powder ratio of 40:1. The powder was milled in air atmosphere, using tungsten carbide milling media (balls and vessel) to enhance the impact energy, i.e. accelerate an efficient milling process, due to the larger density of tungsten carbide (14.95 g/cm^3) by comparison with that of steel (7.8 g/cm^3). The characterization and properties of this materials were previously discussed in section 5.1. This material will be referenced as 'as-milled' in the following.

EQUIPOÂ¿? VSM was employed to measure magnetization M-H curves with controlled temperature, ranging from 5 K to 400 K. Parameters extracted from the hysteresis loops include magnetization at maximum applied field of 50 kOe ($M_{50\mathrm{kOe}}$), remanence (M_r), and coercivity (H_c). Furthermore, the magnetic anisotropy constant K_1, and saturation magnetization, M_S, were estimated from the *M-H* curves using the LAS approximation described in section 1.

7.1.2 Results and discussion

M-H curves of the sample under test were measured with a maximum magnetic applied field of 50 kOe. A sufficiently intense magnetic field is needed in order to ensure that all irreversible magnetization reversal processes were completed, and the changes in magnetization are only due to coherent rotational processes. All *M-H* curves discussed up to now were measured with a maximum applied field of 20 kOe. Figure 7.1 depict a comparison of *M-H* curves of the sample under study measured RT with a maximum applied field of 50 kOe and 20 kOe. In brief, one can see that both curves are overlapped and that $M_{50kOe} > M_{20kOe}$, indicating that the sample is not fully saturated even at fields above 50 kOe. This will be later confirmed by the LAS approximation. This difference between M_{50kOe} and M_{20kOe} observed in the as-milled powder can be ascribed to the increased number of defects created during processing, which might act as pinning centers during magnetization reversal. Note that this sample posses a high density of defects due to the applied HEBM process (see Section 5.1). Furthermore, it is observed that coherent rotation is the predominant behavior for applied magnetic fields above 20 kOe, and thus both curves are mayor loops even if the sample was not fully saturated.

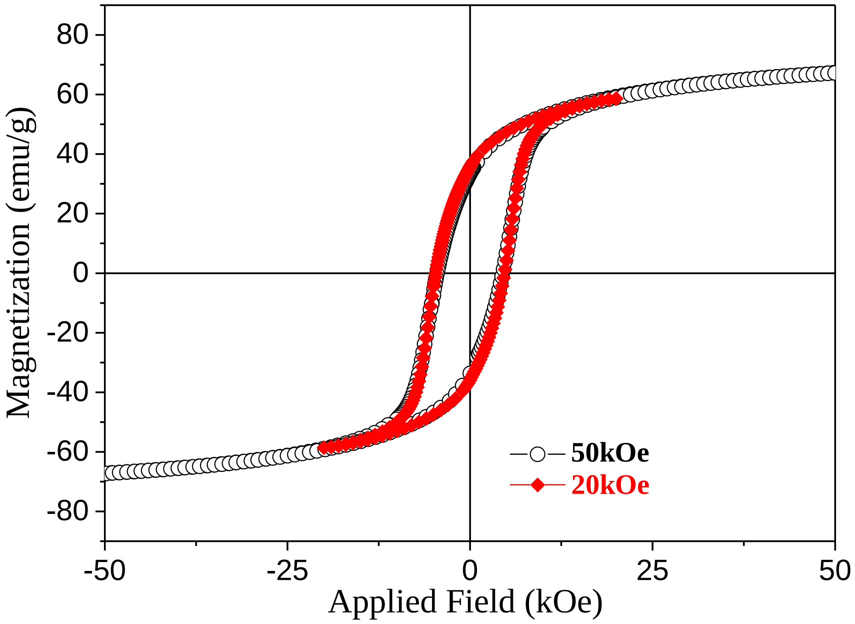

Figure 7.1: *M-H* curves at RT of milled CoFe$_2$O$_4$ measured with an applied field of 50 kOe (black, empty squares) and 20 kOe (red, full diamonds).

Using a maximum applied magnetic field of 50 kOe, magnetization curves of the sample under study were measured at temperatures of 5 K, 150 K, 250 K and 400 K. These curves are displayed in Figure 7.2. In addition, *M-H* curves at 200 K and 300 K were recorded for a posterior analysis. At a first glance, it is observed that increasing temperature results in the narrowing of the magnetization curve, as well as the decrease of both parameters, magnetization saturation and remanence magnetization, as expected for the inverse spinel cobalt ferrite [1, 2].

From these *M-H* curves, the temperature dependence of H_C was directly determined. Moreover, saturation magnetization, M_S, and effective anisotropy constant, K_{eff}, were estimated by the LAS approximation, fitting the hysteresis loop in the high field range where $0.97 \cdot M_{50kOe} \leq M(_H) \leq M_{50kOe}$.

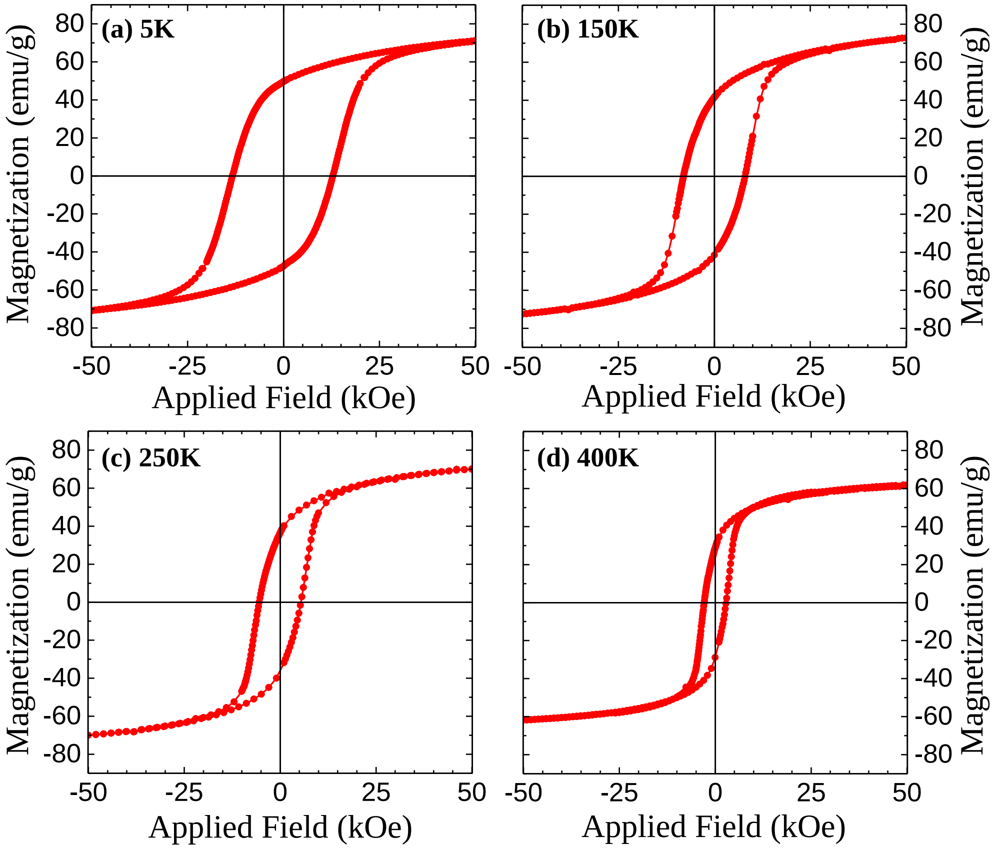

Figure 7.2: *M-H* curves of 180 s HEBM milled CoFe$_2$O$_4$ measured at (a) 5 K, (b) 150 K, (c) 250 K and (d) 400 K.

Figure 7.3 yields the temperature dependence of $M_S(T)$, which exhibits gradual increase as the temperature decreases. The $M_S(T)$ value of this sample is below 80 emu/g of CoFe$_2$O$_4$ bulk saturation magnetization [3] due to the reduced particle size, which is related to surface effects (disordered magnetic moments at the surface) [4–6]. In case of bulk magnetic systems, the thermal behavior of saturation magnetization is related to the presence of low energy collective excitations (spin waves or magnons) following the Bloch's law of the form:

$$M_S(T) = M_S(0)\left[1-\left(\frac{T}{T_C}\right)^{\alpha}\right] \tag{7.1}$$

where $M_S(0)$ is the spontaneous magnetization at absolute zero and T_C the Curie temperature and α is the Bloch constant (α = 3/2). However, deviations from the α = 3/2 law have been observed for sufficiently small nanoparticles. The temperature dependence of M_S for nanoparticles diverges from Bloch's law as the spatial confinement reduces the number of degrees of freedom generating an energy gap in the corresponding spin wave spectrum. The so-called modified Bloch's law consider an α = 2 value for nanoparticles. For example, an effective T^2 law was found for nanosized amorphous iron-carbon particles [7, 8], magnetite-based ferrofluids [9], and CoFe$_2$O$_4$ milled nanoparticles [10]. Assessed values from the fit of M_S calculated by LAS to equation 7.1, using α = 2 are: a saturation magnetization at zero kelvin, $M_S(0)$ = 77.4 ± 0.7 emu/g, and a Curie temperature, T_C = 974.9 ± 49.2 K. The R-squared parameter remains close to 0.956.

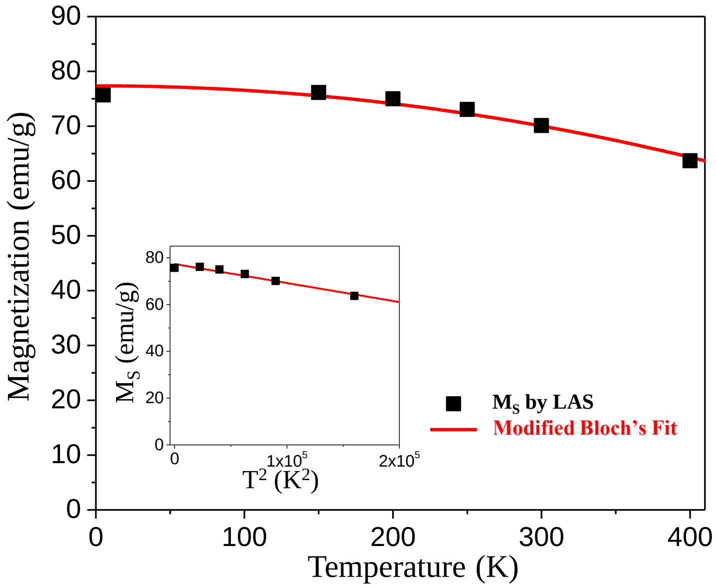

Figure 7.3: Evolution of saturation magnetization, M_S, assessed by the LAS approximation, as a function of temperature. Scatters correspond to calculated values, while the red line is the fit of data using Equation 7.1. Inset: M_S as a function of T^2.

Measured values of H_C from the M-H curves at different temperatures are shown in Figure 7.4. Coercivity is strongly dependent of temperature as expected; it is observed that H_C decreases monotonically with increasing temperature [1, 2]. For single-domain non-interacting nanoparticles, the temperature behavior of H_C can be described by the Kneller's law [11, 12], which must follow the expression of Equation 7.2:

$$H_C(T) = H_{C0}\left[1 - \left(\frac{T}{T_B}\right)^{\frac{1}{2}}\right] \tag{7.2}$$

where H_{C0} is the coercive field as T tends to zero and T_B is the superparamagnetic blocking temperature of the nanoparticles. Nevertheless, the real situation is that the CoFe$_2$O$_4$ nanoparticles might present dipolar interactions, but these are weak by comparison with the anisotropy constant, as it will be later shown. In fact, such assumption has usually been considered to be reasonable in many previous reports [13–16]. In this case the data of H_C between 5 K and 400 K were fitted well to Equation 7.2 with the fitting parameters H_{C0} = 14.8±0.3 kOe and T$_B$ = 633.5±20.1 K. The R-squared parameter of this fit was 0.996, which suggests that the quality of fitting is very good, and indicates that H_C varies linearly with T$^{\frac{1}{2}}$ up to 400 K, as can be observed in the inset of Figure 7.4. This linear increase of H_C with decreasing T$^{\frac{1}{2}}$ is ascribed to the dynamical thermal blocking of spin moments due to intrinsic anisotropy barrier. Calculated values of H_{C0} and T_B are comparable to those previously reported [13]

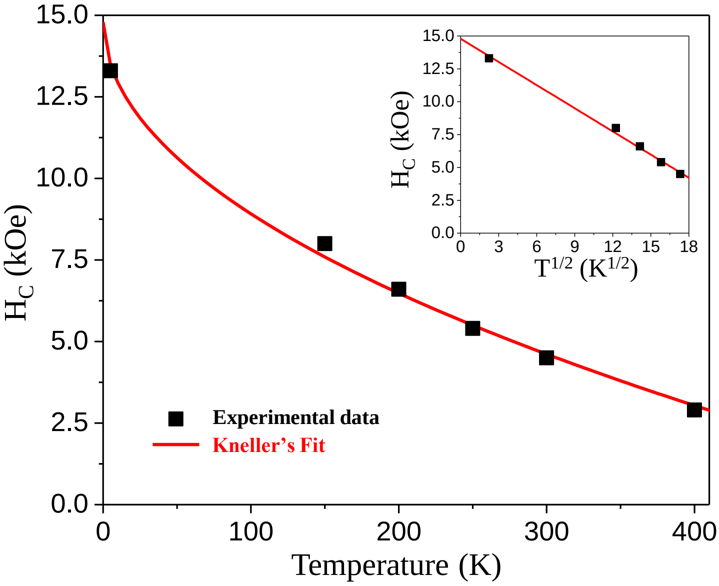

Figure 7.4: Evolution of coercivity, H_C, extrapolated the M-H of Figure 7.2, as a function of temperature. Scatters correspond to calculated values, while the red line is the fit of the data to Equation 7.2. Inset: H_C as a function of $T^{\frac{1}{2}}$.

The effective magnetic anisotropy constant, K_{eff}, calculated through the LAS approximation to the M-H of Figure 7.2, is displayed in Figure 7.5 as a function of temperature. At 5 K, the effective anisotropy constant is estimated as $K_{eff}(T=5)$ = 14.6·10^6 erg/cm^3, which monotonically drops with increased temperature down to $K_{eff}(T=400)$ = 0.9·10^6 erg/cm^3. It is well known that anisotropy of CoFe$_2$O$_4$ follows a T^2 dependence [10, 16, 17] as it is described in equation 7.3, where $K(0)$ is the effective anisotropy constant at absolute zero, and A is a constant. The inset of Figure 7.5 plot the evolution of assessed effective anisotropy values by the LAS approximation in dependence of T^2, where a straight line can be observed.

$$K(T) = K(0) \cdot 10^{(A \cdot T^2)} \tag{7.3}$$

The fit displayed in Figure 7.5 generated an effective anisotropy $K(0)$ = 14.7·10^6 erg/cm^3 with a constant A = -1.3·10^{-6}±xx. Shenker et al. [17] estimated a $K(0)$ = 19.6·10^6 erg/cm^3 for bulk cobalt ferrite. It is expected a higher anisotropy in strained nanoparticles since in terms of magnetoelastic theory, the residual strain may induce additional uniaxial magnetic anisotropy, i.e., stress anisotropy K_S, and this term contributes to the effective anisotropy in addition to magnetocrystalline anisotropy. Therefore, the high level of strain induced through the HEBM results in an increased effective magnetic anisotropy, as it will be shown in following sections. Liu et al. [10] reported the evolution of K_{eff} as a function of milling time, obtained strained cobalt ferrites with ε =10·10^{-3} after 1.5 hours milling, with an anisotropy of K_{eff} = 5.8·10^6 erg/cm^3 , in this case below the values reported in this work. López-Ortega et al. [13] reported K vales for CoFe$_2$O$_4$ comparable to those here obtained.

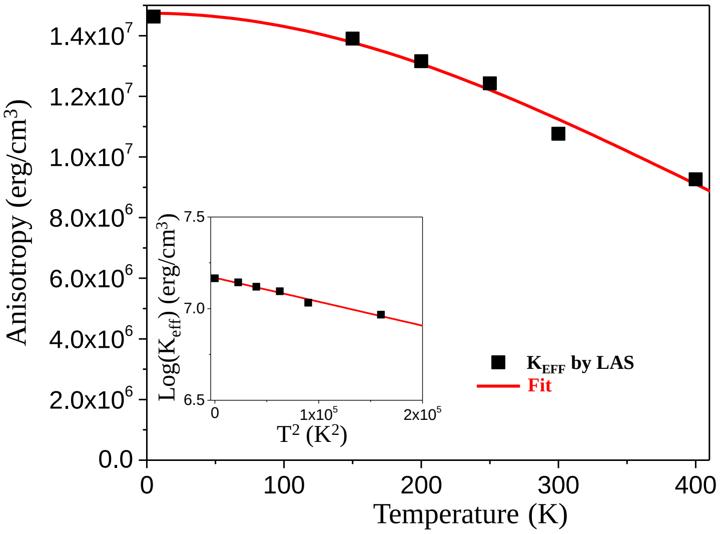

Figure 7.5: Evolution of effective anisotropy, K_{eff}, assessed by the LAS approximation, as a function of temperature. Scatters correspond to calculated values, while the red line is the fit of the data using Equation 7.3. Inset: K_{eff} as a function of T^2.

Up to now have been demonstrated that magnetization, coervity and anisotropy, are temperature dependent parameters. Furthermore, the temperature dependence of anisotropy is directly proportional to nth power of spontaneous magnetization M_S. Both parameters follows Callen-Callen's theory [18] based on the thermodynamic local anisotropy model yields the famous $l(l+1)/2$ power law correlating $K(T)$ and $M_S(T)$ at low temperatures ($T \ll T_C$) as:

$$\frac{K(T)}{K(0)} = \left[\frac{M(T)}{M(0)}\right]^n \tag{7.4}$$

where $K_{eff}(T)$ is anisotropy constant, $M_S(T)$ is the saturation magnetization and $n = l(l+1)/2$ is an exponent depending on the crystal symmetry and degree of correlation between the directions of adjacent spins. Here, l is the order of the spherical harmonic describing the angular dependence of the local anisotropy. According to the theories of Van Vleck [**van1937anisotropy**] and Zener [**zener1954classical**], n was predicted to be 6 and 3 for cubic (multiaxial) and uniaxial anisotropy, respectively, if there is no correlation. In the case of complete correlation, the exponent n was calculated to be 10 for cubic anisotropy and 3 for uniaxial anisotropy.

CoFe$_2$O$_4$ posses a cubic anisotropy, therefore a calculated n in a range 6 to 10 expected. Figure 7.6 represents $Ln(K(T)/K(0))$ versus $Ln(M(T)/M(0))$, and fits with n = 2, 3, 4 and 6. In brief, considering that at 0 K, both logarithms will be 1, it is observed that n = 6 fits well with the low temperature points. However, the last three points diverge considerably. If all the points are considered for the fit, it seems that the slope is in a range $3 \leq n \leq 4$, far away from the expected $6 \leq n \leq 10$. The same behavior was observed by Chatterjee et al. [16] in NiFe$_2$O$_4$ nanoparticles reporting a value of n = 2.6 in the temperature range of 5-280 K. Notwithstanding, they assumed that the anisotropy in NiFe$_2$O$_4$ was uniaxial (not cubic).

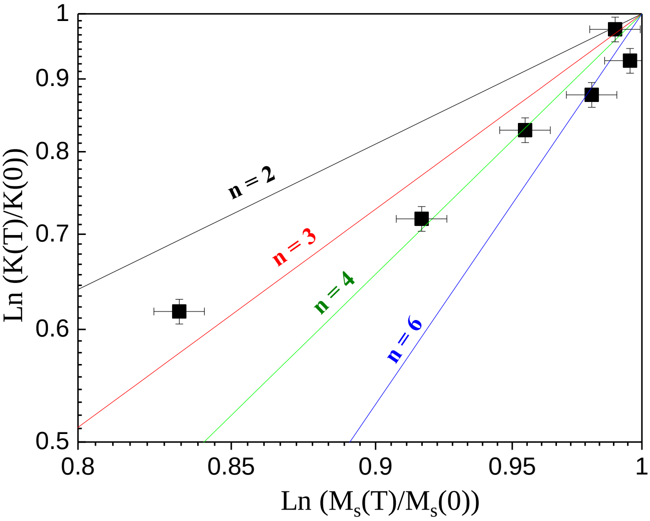

Figure 7.6: *M-H* curves of milled CoFe$_2$O$_4$ measured at (a) 5 K, (b) 150 K, (c) 250 K and (d) 400 K.

7.2 Analysis of $CoFe_2O_4$ magnetic properties enhancement

The possibility to enhance $CoFe_2O_4$ magnetic properties through different processes have been analyzed during this part of the thesis. In general, all these modifications are achieved by the control of the powder microstructure such as particle size, strain and defects mainly. For instance, cobalt ferrite synthesized by the co-precipitation posses a higher coercivity if the as-synthesized powder is crystallized using a heating temperature of 700 °C instead of 1000 °C. This is due to the different crystallite size of $CoFe_2O_4$ particles achieved; while the powder heated to 700 °C is constituted by nanoparticles with sizes around 50 nmm, very close to the 40 nm of critical single domain size and therefore with a magnetization reversal process by coherent rotation, the powder heated to 1000 °C is formed by polycrystalline nanoparticles where magnetization reversal is dominated by domain wall propagation.

On the other hand, HEBM was demonstrated to be an efficient method for rapidly rise H_C of cobalt ferrite up to a 5-fold increase, which is attributed to an increased level of induced strain. Section 5.2 described the comparison of $CoFe_2O_4$ powers with different initial microstructure that were milled by the HEBM technique, using in al cases the same preparation conditions. In this case, the batch with the highest coercivity was that with the highest induced strain after the milling process, since in all case all powders were constituted by particles with crystallites sizes below de monodomain crystallite size.

Finally, the possibility to further control the microstructure of as-synthesized cobalt ferrite by the temperature of post synthesis heating temperature allows to discriminate the effect of strain and size. This section discuss the evolution of a single $CoFe_2O_4$ batch magnetic properties after the different manufacturing processes described in this work, with the aim to analyze the correlation between both, microstructural and magnetic properties.

7.2.1 Experiment description

Using the co-precipitation method, two syntheses were performed in a reaction volume of 3 L each. Powders of both reactions were mixed when dried, obtaining a total amount of 300 g of as-synthesized powder. A batch with a mass of 50 g was prepared and heated to 1000 °C. The characterization and properties of this material was previously discussed, named 'Powder C', in section 4.2.

The heating procedure was performed in a Naberthem muffle oven model L1 1/11/R6. In this case, the annealing procedure consisted of an increasing temperature ramp of 10K/min from room temperature to the goal temperature which was maintained for 1 hour before cooling down to room temperature. This treatment allows to crystallize the inverse spinel structure of $CoFe_2O_4$ (see chapter 4.

HEBM experiment with a total duration of 180 seconds was performed to 4 grams of the aforementioned $CoFe_2O_4$ powder, using a high-energy ball milling equipment Pulverizete 7 premium line from Fritsch at a speed of 900 rpm and a ball-to-powder ratio of 40:1. The powder was milled in air atmosphere, using tungsten carbide milling media (balls and vessel) to enhance the impact energy, i.e. accelerate an efficient milling process, due to the larger density of tungsten carbide (14.95 g/cm^3) by comparison with that of steel (7.8 g/cm^3). The characterization and properties of this materials were previously discussed in section 5.1. This material is referenced as 'as-milled' in the following.

The as-milled powder was separated in batches of 150 mg and heated in a temperature range from 400 to 1000 °C, with 100 °C intervals, using air atmosphere with a Carbolite tubular oven model STF 15/450. The heating procedure consisted in an increasing temperature ramp of 10K/min from room temperature to the goal temperature, which was maintained for 1 hour before cooling down to room temperature. This material is referenced as 'Heated_X' in the following, being X the temperature used in the heat treatment.

ACTUALIZAR!! A Lakeshore 7400 VSM was employed to measure magnetization M-H curves at a controlled temperature, ranging from 5 K to 400 K. Parameters extracted from the hysteresis loops include magnetization at maximum applied field of 50 kOe ($M_{50\mathrm{kOe}}$), remanence (M_r), and coercivity (H_c). Furthermore, using the law of approach to saturation, the magnetic effective anisotropy constant K_{eff}, as well saturation magnetization, M_S, were estimated from the M-H curves as a function of temperature.

7.2.2 Results and discussion

Figure 7.7 depicts the comparison of magnetization curves measured at RT and 5 K of a single CoFe$_2$O$_4$ batch after the different processing steps. As it was discussed in the previous section, it is observed a widening of the M-H curves measured at T = 5 K as a consequence of the minimization of thermally activated reversal processes. Moreover, this widening is accompanied by an enhancement of the remanence to saturation ratio that is translated in a higher squareness of the curves. First, magnetization curves of cobalt ferrite powder crystallized with a post-synthesis heat treatment to 1000 °C, plot in Figure 7.7.(a), display a single loop behavior. This powder is formed by polycrystalline particles with crystallite sizes of hundred nanometers, well above CoFe$_2$O$_4$ critical single domain size. While a double-loop behavior in observed in this sample at RT, the hysteresis loop recorded at 5 K, where thermally driven phenomenas are avoided, seems to be a single loop.

This powder is the best option as starting material in order to obtain highly strained CoFe$_2$O$_4$ particles through a HEBM process. M-H curves recorded in this powder after 180 s milling are plot in Figure 7.7.(b). The increase in coercivity is quantitatively appreciated by comparing these curves with the last discussed, as well as the slight decrease of saturation magnetization. The fact that at T=5 K, the hysteresis loop of the sample prior to milling was close to saturation while after milling it is observed linear increase of magnetization in the area where the curves are closed indicates that rotational processes are important during magnetization reversal. This is translated into a higher value of the effective anisotropy constant.

Heating this powder to temperatures above 400 °C produce the relaxation of the induced strain and grain growth for heating temperature is above 700 °C. Interestingly, M-H curve at RT of the initial material (synthesized with a post-synthesis heat treatment to 1000 °C, plot in Figure 7.7.(a)) and after a post-milling heat treatment to the same temperature (Figure 7.7.(d)) are quite similar, while at T = 5 K the powder processed after milling (Figure 7.7.(d)) display a curve with greater H_C than the initial powder (Figure 7.7.(a))

Figure 7.8 depicts the evolution of microstructural properties such as strain, ε, and crystallite size, <D_V>, as well as estimated values of effective anisotropy, K_{eff}, and saturation magnetization, M_S, both assessed by the application of LAS approximation to the high field range of M-H curves above at 5 and 300 K.

By comparing the $\varepsilon = 0.7{\cdot}10^{-3}$ and $< D_V > = 130.2$ nm of starting material with $\varepsilon = 9{\cdot}10^{-3}$

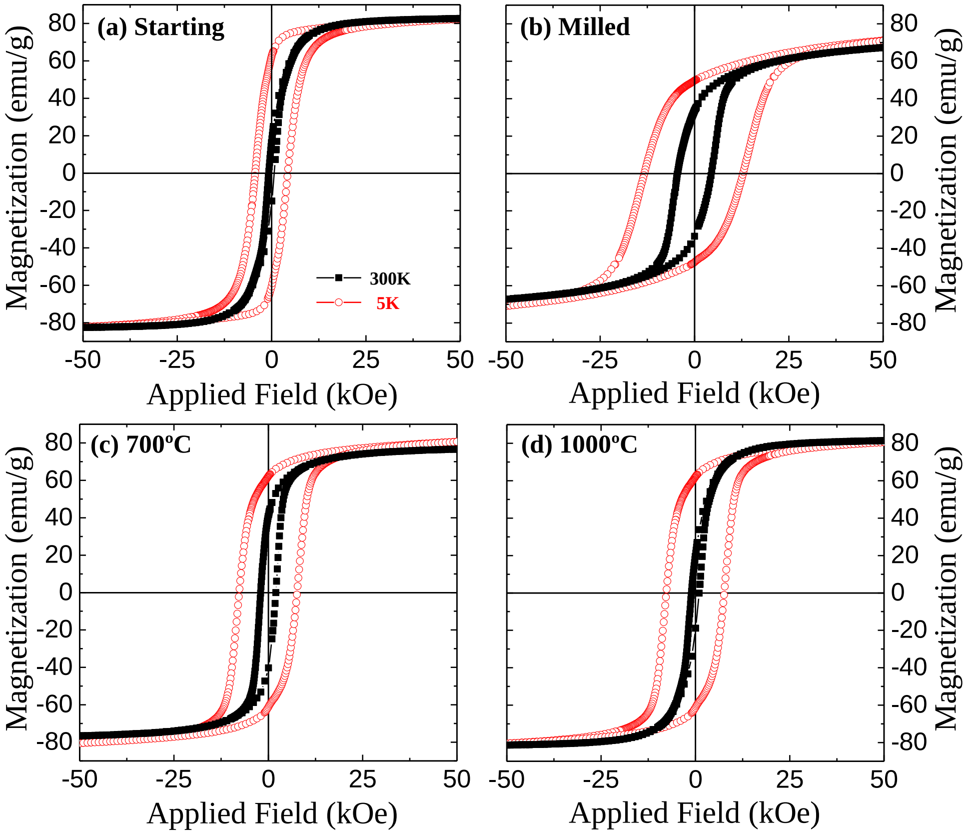

Figure 7.7: *M-H* curves measured at 5 K (black, full squares) and RT (red, open circles) of: (a) initial CoFe$_2$O$_4$ powder synthesized with a post-synthesis heat treatment to 1000 °C, (b) the same powder after a HEBM process during 180 seconds, and after a post-milling heat treatment to (c) 700 °C and (d) 1000 °C.

and $< D_V > = 9.2$ nm calculated in the milled powder (see Figures 7.8.(a-b)), the high efficiency of HEBM process inducing strain and reducing crystallite size of CoFe$_2$O$_4$ powder is clearly seen in addition to a considerable increase of magnetic anisotropy from K = 9.3·10^6 erg/cm^3 of starting powder to K = 14.5·10^6 erg/cm^3 after milling, both estimated from hysteresis loops measured at T = 5 K. At this point the increase in H_C might be ascribed tho the diminished particle size or to the high level of residual strain. The same apply for saturation magnetization, where a decrease after milling, from M_S = 83.6 emu/g to M_S = 74.9 emu/g is observed, and that might be due to amorphization or because of the diminished size of particles, pr even both effects might contribute.

Now, the effect of a heat treatment to the as-milled powder as a function of the heating temperature was studied in the previous section 6.1, concluding that heating to moderate temperatures -i.e. in a temperature range 400 - 700 °C - causes mainly strain release, while at higher temperatures CoFe$_2$O$_4$ crystals size is increased (see Figure 6.3). Interestingly, when the as-milled powder was heated to 400 °C, strain was reduced with respect to the milled powder from $\varepsilon = 9{\cdot}10^{-3}$ to $\varepsilon = 6{\cdot}10^{-3}$, while K_{eff} only decreased $0.8{\cdot}10^6$ erg/cm^3 from $K_{eff} = 14.6{\cdot}10^6$ erg/cm^3 to $K_{eff} = 13.7{\cdot}10^6$ erg/cm^3. This suggest that strain highly influence the effective magnetic anisotropy once the particle size is below the monodomain critical size.

Figure 7.9.(a) plots the K_{eff} calculated versus the level of strain. Note that in that figure there is no discrimination between powders with crystallite sizes above or below the cobalt ferrite monodomain critical size. Interestingly, it is observed that the data fits well to a linear function with a slope of 8.85cot 10^8 erg/cm^3 per strain unit, and an intercept of 8.8 erg/cm^3, that compares well with magnetocrystalline anisotropy constant of bulk CoFe$_2$O$_4$ [13]

Figure 7.9.(b) exhibit estimated M_S values as a function of $< D_V^{-1}$. Once again, it is observed a linear correlation between both parameters, being saturation magnetization value closer to the M_S = 80 emu/g expected for bulk CoFe$_2$O$_4$ with the bigger particle size. The intercept point was calculated to be 84.5 emu/g, and M_S is decreased at a rate of 89.2emu/g nm^{-1}.

In summary, this study have demonstrate that the high coercive cobalt ferrite increased its effective anisotropy due to the contribution of induced strain. Furthermore, the reduction in particle size leads to a diminished remanence magnetization. The optimum magnetic properties

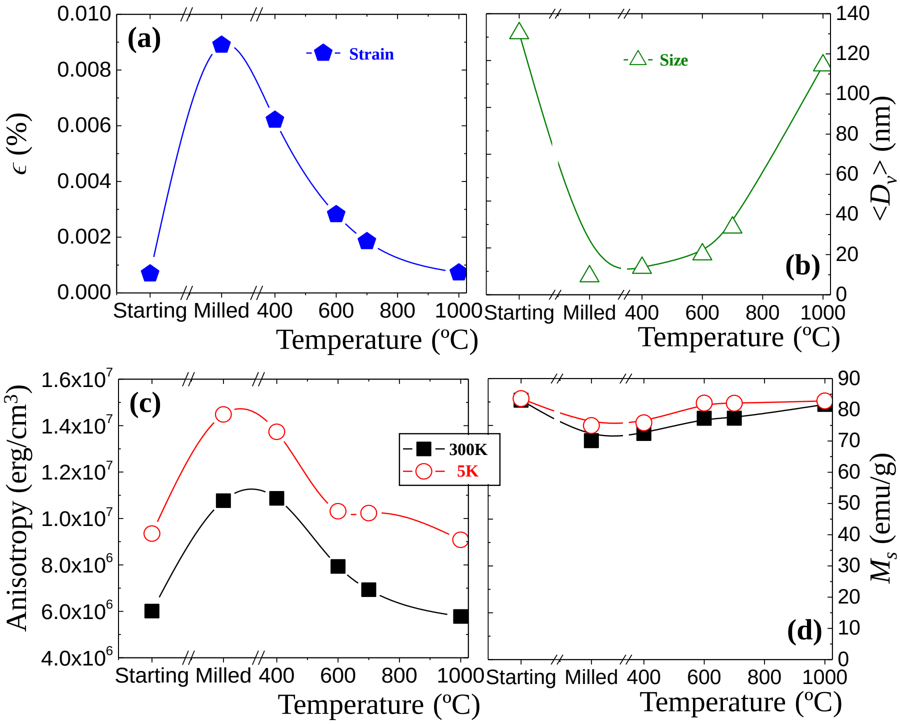

Figure 7.8: *M-H* curves of (a) initial CoFe$_2$O$_4$ and after 3 (red) and 9 (blue) minutes of wet milling, and after a post-synthesis heat treatment at (b) 500 °C, (c) 700 °C and (d) 900 °C.

for the application of cobalt ferrite as permanent magnets are obtained when accomplishing that a) the average crystallite size is below the monodomain critical size, but close to this limit since a reduced particle size means a decreased magnetization, and thus a lower energy product, and b) the highest strained particles leads to the highest anisotropy.

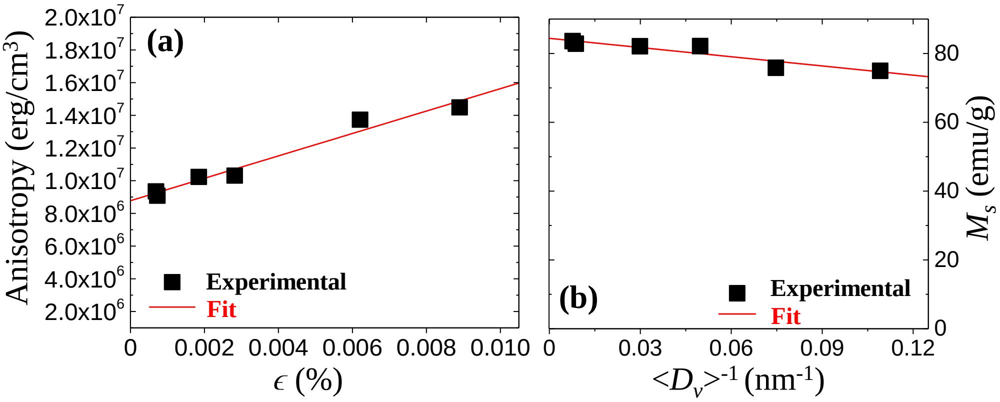

Figure 7.9: *M-H* curves measured at (a) 5 K, (b) 150 K, (c) 250 K and (d) 400 K, of three CoFe$_2$O$_4$ products; a cobalt ferrite synthesized by the co-precipitation method (full squares, black), a high coercive cobalt ferrite (open circles, red) and a cobalt ferrite with enhanced energy product (full triangles, blue).

7.3 Three CoFe$_2$O$_4$ products

The characterization of magnetic properties as a function of operating temperature is not only interesting from a scientific point of view, but also an important issue from a technical point of view since this type of measurements allows to evaluate the potential application of CoFe$_2$O$_4$ as permanent magnets and to decide for which application this type of magnets fit better. As an example, consider that magnets used as the rotor of an electric motor might request a good performance at high temperatures (to avoid demagnetization due to the heat generated by the motor), while for cryogenic applications, or low temperature applications, a material with a good magnetic performance at low temperature is required.

The different manufacturing processes applied to cobalt ferrite power described in this work provide CoFe$_2$O$_4$ powders with different properties enhanced. While for permanents magnets the $(BH)_{max}$, is the figure of merit since it describes the energy stored on it, for some application might be interesting to refuse a high magnetization in favor of high coercivity (and thus lower energy product). Here, three products of cobalt ferrite are proposed for its use as permanent magnets, attending to the complexity of its fabrication process and the enhanced property that the powder display. First, CoFe$_2$O$_4$ powder synthesized by the co-precipitation method with a post-synthesis heat treatment to 700 °C provides energy products up to 10 kJ m^{-3}. Seconds, a high coercive cobalt ferrite achieved in record time of few minutes by using a HEBM process, obtaining CoFe$_2$O$_4$ powder with H_C = 5.1 kOe. Finally, a CoFe$_2$O$_4$ powder with enhanced $(BH)_{max}$ is obtained after a post-milling heat treatment to 600 °C of the high-coercive powders.

In this section, the three products of cobalt ferrite described above are characterized as a function of temperature - Note that milled cobalt ferrite was analyzed in section 7.1-. The most relevant magnetic properties, such as coercivity, magnetization and energy product were inferred from the *M-H* curves measured at different temperatures.

7.3.1 Experiment description

All CoFe$_2$O$_4$ powders analyzed in this section were described previously. The three products here analyzed were obtained as follows:

- Product A is cobalt ferrite powder synthesized by the co-precipitation method and heated to 700 °C. Microstructural and magnetic characterization of this sample was shown in section 4.2.2 named as Powder C heated to 700 °C. This powder is constituted by CoFe$_2$O$_4$ with a crystallite size, $< D_V >$ = 65.1 nm, and ε =1.4$\cdot 10^{-3}$. A small contribution of α-Fe$_2$O$_3$ was observed in the XRD spectra of this sample.

- Product B is cobalt ferrite synthesized by the co-precipitation method, heated to 1000 °C and milled during 180 seconds by HEBM. Microstructural and magnetic characterization of this sample was discussed in section 5.1. This powder is constituted by CoFe$_2$O$_4$ with a crystallite size, $< D_V >$ = 9.2 nm, and $\varepsilon = 8.9 \cdot 10^{-3}$.

- Product C is cobalt ferrite synthesized by the co-precipitation method, heated to 1000 °C, milled during 180 seconds by HEBM and heated after the milling procedure to 600 °C. Microstructural and magnetic characterization of this sample was analyzed in section 6.1. This powder is constituted by CoFe$_2$O$_4$ with a crystallite size, $< D_V >$ = 20.1 nm, and $\varepsilon = 4.1 \cdot 10^{-3}$. A small contribution of α-Fe$_2$O$_3$ was observed in the XRD spectra of this sample.

EQUIPO! was used to perform this characterization. *M-H* curves of the samples were measured in a temperature range from 5 K to 400 K, using a maximum applied field of 50 kOe. Note that in this section, the temperature unit will be changed to Kelvin to refer the temperature at which the data was obtained, while as in previous experiments, the temperature unit used to refer heat treatments is denoted in Celsius degrees.

From this magnetization curves, magnetization at the maximum applied field, M$_{50kOe}$, remanence magnetization, M_R, and coercivity, H_C are obtained. Additionally, energy product, $(BH)_{max}$ was calculated. Anisotropy and saturation magnetization were estimated by the application of LAS approach in the high field range,as it is described in experimental section **??**.

7.3.2 Results and discussion

M-H curves of the three products under study were measured at 5 K, 150 K, 250 K and 400 K, and these magnetization curves are compared in Figure 7.10. Additionally, hysteresis loops at 200 K, 300 K and 350 K were recorded. The magnetic properties at RT of each product were discussed elsewhere (chapters 4 to 6).

As a general tend, the widening of the *M-H* curves with increasing temperature accompanied by a decrease in magnetization is observed. It is worth to mention that hysteresis loops measured at 5 K displayed in Figure 7.10.(a) are single-loops, since Products A and C contains a fraction of hematite, (being this content greater in Product A) that displays a ferromagnetic behavior at low temperature [19–21].

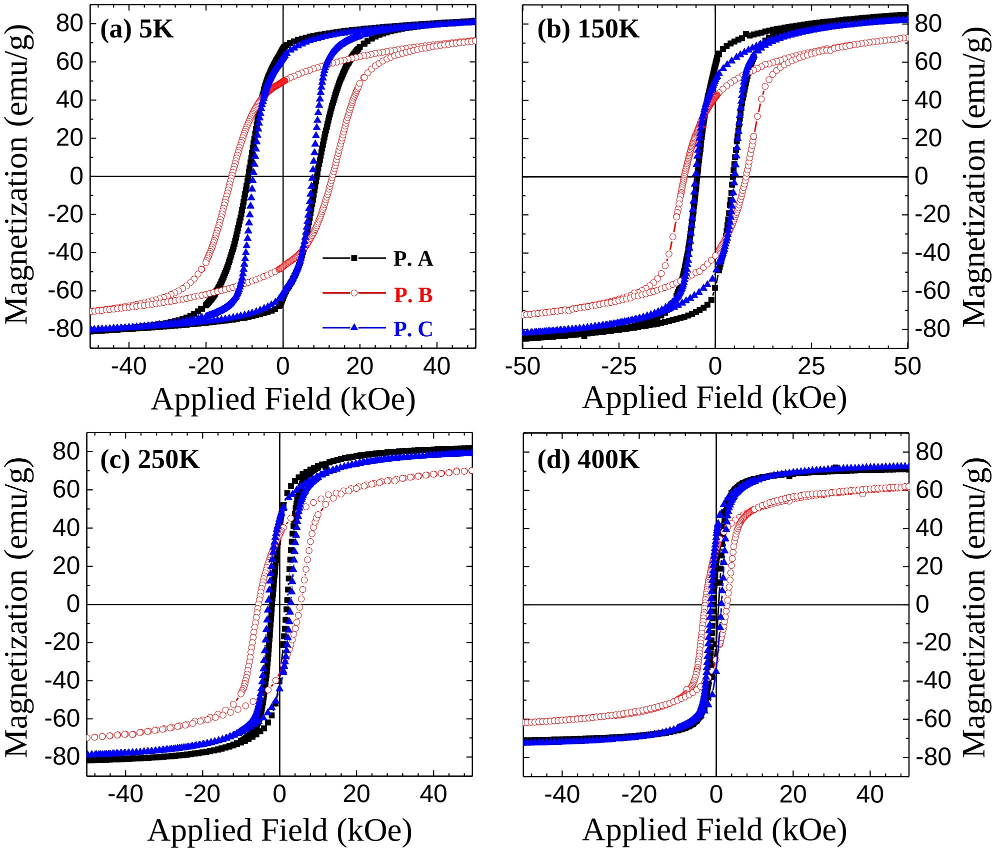

Figure 7.10: *M*-*H* curves measured at (a) 5 K, (b) 150 K, (c) 250 K and (d) 400 K, of three CoFe$_2$O$_4$ products; a cobalt ferrite synthesized by the co-precipitation method (Product A, full squares, black), a high coercive cobalt ferrite (Product B, open circles, red) and a cobalt ferrite with enhanced energy product (Product C, full triangles, blue).

Parameters extracted from magnetization curves as a function of temperature, including coercivity, H_C, remanence magnetization, M_R, magnetization at the maximum applied field, M_{50kOe}, and energy product, $(BH)_{max}$, are depicted in Figure 7.11.

Magnetization at the maximum magnetic applied field, M$_{50kOe}$, is plot in Figure 7.11.(a). Products A and C display a comparable saturation magnetization value at 5 and 400 K while for intermediate temperatures, M$_{50kOe}$ of Product A is slightly above that of Product C. In any case, both products display M$_{50kOe}$ values close to the 80 emu/g expected for bulk cobalt ferrite. On the other hand, M_{50kOe} measured in Product B is well below to that M$_{50kOe}$ value measured in Products A and C, probably because this batch was subjected to a HEBM process and the powder is constituted by particles with a reduced crystallite size. At 5 K, M_{50kOe} = 81.3 emu/g was measured for Product A and M_{50kOe} = 80.6 emu/g for Product C, while in Product B this value was M_{50kOe} = 71.0 emu/g only.

Regarding the temperature dependence of M_R in each product, plot in Figure 7.11.(b), a monotonic increase is observed in all batches, and remarkably, an inflection point in Product A is observed around T = 250 K, where M_R display an increase in this temperature range which is greater than the increase of this parameter observed in Products B or C. This might be ascribed to the Morin transition of hematite, which is a characteristic low-temperature transition T = 263 K (known as Morin temperature, T_M); at temperatures above T_M hematite is a spin-canted antiferromagnet, resulting thus in a lower magnetization per unit of mass, while below T_M it behaves as a ferrimagnet [19–21] and rising the total magnetization per unit of mass.

Coercivity, H_C, shown in Figure 7.11.(c) reveals a monotonic increase of this paremeter with decreasing temperature. The reason for the increasing coercivity with decreasing temperature can be understood by considering the effects of thermal fluctuations of the blocked moment across the anisotropy barrier [15]. Product B is the sample with higher H_C values, as expected since is the sample with the highest strain value and smallest particle size, while Products A and C display a similar H_C. Coercivity follows the Kneller's law was previously discussed in Section 7.1. H_{C0} = 14.8 kOe was obtained by the fitting of Product B experimental data to Equation 7.2. By fitting H_C data of Products A and C, values of H_{C0} = 10.1 kOe and H_{C0} = 8.84 kOe were estimated for Products A and C respectively.

The energy product assessed as a function of temperature for the three cobalt ferrite products under study are plot in Figure 7.11.(d). At RT, Product C is the one with the highest energy product, with a $(BH)_{MAX}$ = 17.9 kJm^{-3}. The lowest $(BH)_{MAX}$ = 10kJ kJm^{-3} was measured in Product A. In all cases, decreasing temperature causes an increase in both, coercivity and magnetization, therefore an increased energy product is expected. However, it is interesting to observe the behavior of Product A; the considerable increase in M_R at temperatures below the Morin transition might be the origin of the energy product increase up to $(BH)_{MAX}$ = 17.9 kJm^{-3} at T = 5 K, being the product with the highest energy product for temperatures below 200 K.

Using the M-H curves shown in Figure 7.10, the LAS approximation was applied in order to estimate the effective anisotropy constant, K_{eff}, as well as saturation magnetization, M_S. Assessed values from curves at RT and 5 K for the different products under study are compared in Figure 7.12.

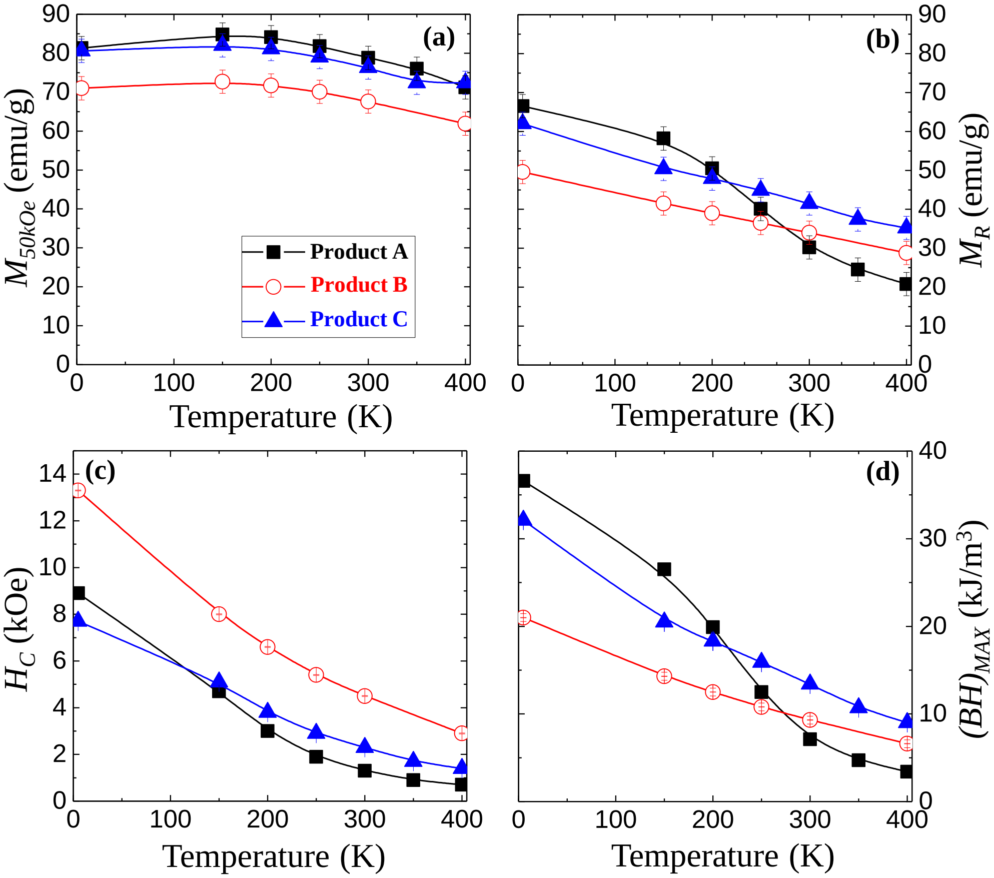

Figure 7.11: Evolution with temperature of (a) M_{50kOe}, (b) M_R, (c) H_C and (d) $(BH)_{MAX}$, of the three CoFe$_2$O$_4$ products; a cobalt ferrite synthesized by the co-precipitation method (full squares, black), a high coercive cobalt ferrite (open circles, red) and a cobalt ferrite with enhanced energy product (full triangles, blue).

The effective magnetic anisotropy of each product as a function of temperature is plot in Figure 7.12.(a). In general, it is observed that K_{eff} is decreased with increasing temperature. This is ascribed to the contribution of thermal activated demagnetization processes is diminished. In section 7.1 was demonstrated that anisotropy is proportional to saturation magnetization to the power by the 'callen-callen' law. However, it is interesting to pay attention to the behavior of K_{eff} when the temperature is in the range 100 - 200 K. While Products A and B display a monotonic decrease of K_{eff} with increasing temperature, Product C displays a $K_{eff}(T=5) < K_{eff}(T=150)$. Moreover, Product A display a considerable greater increase of K_{eff} below 200 K. This is ascribed to the effect of hematite, modifying its magnetic behavior from antiferromagnetic to ferromagnetic hen the temperature is below the Morin transition. The highest K_{eff} is observed in the sample subjected to HEBM process due to the high level of strain that contributes to K_{eff} in addition to magnetocrystalline anisotropy. If this high anisotropic sample is heated, the strain anisotropy is diminished, and even if magnetocrystalline anisotropy is increased due to the better crystallinity of CoFe$_2$O$_4$ particle, the total K_{eff} is decreased with respect the milled sample.

Regarding saturation magnetization, M_S, depicted in Figure 7.12.(b), the same behavior than for effective anisotropy is observed; M_S is reduced with increasing temperature. Products A and C display a very similar saturation magnetization, as it is expected sin both samples were heated to similar temperatures (Product A was heated to 700 °C in order to achieve cobalt ferrite crystallization, and Product C was heated to 600 °C after milling) and both have similar crystallite size. Notwithstanding, Product B posses a lower saturation magnetization of about 10 emu/g in the whole temperature range. By comparing vales saturation magnetization values assessed by LAS with the magnetization measured at the maximum applied field, M_{50kOe}, one can see that while for Products A and C, $M_{50kOe} \approx M_S$, for Product B this difference is slightly higher. This is because of the strain and defects induced during HEBM is translated into a magnetization reversal process by rotation instead of domain wall propagation.

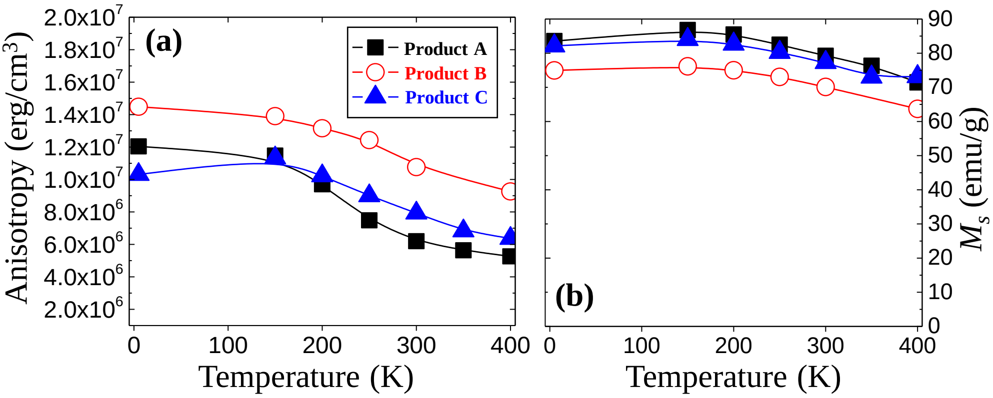

Figure 7.12: Evolution with temperature of (a) effective magnetic anisotropy constant, K_{eff}, and (b) saturation magnetization, M_S , of the three products under study. Both parameters were estimated using the LAS.

7.4 Conclusions

This chapter starts fitting experimental data obtained from magnetization curves measured at different temperatures with the models that described the magnetic behavior of $CoFe_2O_4$ after a HEBM process. The modified Bloch's law was found to fit well to magnetization at the maximum applied field, with Bloch constant of 2 as it is expected for nanostructures. Coercivity was fitted with the Kneller's law, and H_{C0} was estimated to be 14.8 kOe. Moreover, the evolution of the effective magnetic anisotropy as a function of temperature was successfully fitted, and the 'Callen-callen' relation that states the proportional evolution of magnetic anisotropy to a power of magnetization value.

Magnetic properties of cobalt ferrite can be controlled by using the proper manufacturing process. This chapter have analyzed how the different manufacturing processes here described modify the magnetic properties of cobalt ferrite. Once cobalt ferrite particles size are below the monodomain critical size, the effective anisotropy seems to be highly affected by the level of strain. HEBM milling process is revealed to be a efficient method in order to reduce crystallite size and induce strain in $CoFe_2O_4$; the increase of magnetic anisotropy parallel to the induced strain value confirms the considerable contribution of this term in the effective anisotropy value. A linear correlation between the average strain of $CoFe_2O_4$ crystals with the effective anisotropy was found.

Finally, three products of cobalt ferrite are proposed for its implementation in permanent magnets. First, an co-precipitated cobalt ferrite with no more processing than the synthesis reaction and the subsequent heat treatment for cobalt ferrite crystallization. Energy products about 10 kJm^{-3} can be achieve at this level. In addition, it was found that the presence of this material is beneficial in order to increase its magnetization; this material presents a $(BH)_{max}$ = 36.0 kJm^{-3} at 5 K, so it would be a good candidate for cryogenic applications. Second, a high coercive cobalt ferrite obtained by an ultrafast HEBM, with H_C values up to 5.0 kOe at RT and 14.6 kOe at $T = 5$ K. Finally, a cobalt ferrite fulfilling a compromise between magnetization and coercivity, therefore the best candidate to be used as a common permanent magnet. In this case we have a higher coercivity at RT than the first product, and the highest energy product at RT among the three products. Furthermore, the evolution of $(BH)_{max}$ with decreased temperature is better than the first product since the energy product rises at a greater rate.

References

[1] AE Berkowitz and WJ Schuele *Magnetic properties of some ferrite micropowders*. in: *Journal of Applied Physics* ***30***,4 (1959), S134–S135 (cit. on pp. 115, 117)

[2] Y Melikhov, JE Snyder, David C Jiles, AP Ring, JA Paulsen, Chester CH Lo, and Kevin W Dennis *Temperature dependence of magnetic anisotropy in Mn-substituted cobalt ferrite*. in: *Journal of applied physics* ***99***,8 (2006), 08R102 (cit. on pp. 115, 117)

[3] J Ding, PG McCormick, and R Street *Magnetic properties of mechanically alloyed* $CoFe_2O_4$. in: *Solid state communications* ***95***,1 (1995), 31–33 (cit. on p. 116)

[4] Ekaphan Swatsitang, Sumalin Phokha, Sitchai Hunpratub, Brian Usher, Atipong Bootchanont, Santi Maensiri, and Prinya Chindaprasirt *Characterization and magnetic properties of cobalt ferrite nanoparticles*. in: *Journal of Alloys and Compounds* ***664***, (2016), 792–797 (cit. on p. 116)

[5] A Franco Jr, FC e Silva, and Vivien S Zapf *High temperature magnetic properties of Co1-xMgxFe2O4 nanoparticles prepared by forced hydrolysis method*. in: *Journal of Applied Physics* ***111***,7 (2012), 07B530 (cit. on p. 116)

[6] John Michael David Coey *Noncollinear spin arrangement in ultrafine ferrimagnetic crystallites*. in: *Physical Review Letters* ***27***,17 (1971), 1140 (cit. on p. 116)

[7] Peter Vang Hendriksen, Søren Linderoth, and P-A Lindgård *Finite-size modifications of the magnetic properties of clusters*. in: *Physical Review B* ***48***,10 (1993), 7259 (cit. on p. 116)

[8] Søren Linderoth, Ll Balcells, A Labarta, J Tejada, PV Hendriksen, and SA Sethi *Magnetization and Mössbauer studies of ultrafine Fe-C particles*. in: *Journal of magnetism and magnetic materials* ***124***,3 (1993), 269–276 (cit. on p. 116)

[9] C Caizer T^2 *law for magnetite-based ferrofluids*. in: *Journal of Physics: Condensed Matter* ***15***,6 (2003), 765 (cit. on p. 116)

[10] Bing Hai Liu, J Ding, ZL Dong, CB Boothroyd, JH Yin, and JB Yi *Microstructural evolution and its influence on the magnetic properties of* $CoFe_2O_4$ *powders during mechanical milling*. in: *Physical Review B* ***74***,18 (2006), 184427 (cit. on pp. 116, 118)

[11] Yue Zhang, Yong Liu, Chunlong Fei, Zhi Yang, Zhihong Lu, Rui Xiong, Di Yin, and Jing Shi *The temperature dependence of magnetic properties for cobalt ferrite nanoparticles by the hydrothermal method*. in: *Journal of Applied Physics* ***108***,8 (2010), 084312 (cit. on p. 117)

[12] Biplab K Chatterjee, Abhishek Dey, Chandan K Ghosh, and Kalyan K Chattopadhyay *Interplay of bulk and surface on the magnetic properties of low temperature synthesized nanocrystalline cubic Cu 1- x Zn x Fe 2 O 4 (x= 0.00, 0.02, 0.04 and 0.08)*. in: *Journal of Magnetism and Magnetic Materials* ***367***, (2014), 19–32 (cit. on p. 117)

[13] Alberto López-Ortega, Elisabetta Lottini, Cesar de Julian Fernandez, and Claudio Sangregorio *Exploring the magnetic properties of cobalt-ferrite nanoparticles for the development of a rare-earth-free permanent magnet*. in: *Chemistry of Materials* ***27***,11 (2015), 4048–4056 (cit. on pp. 117, 118, 123)

[14] K Maaz, A Mumtaz, SK Hasanain, and MF Bertino *Temperature dependent coercivity and magnetization of nickel ferrite nanoparticles*. in: *Journal of Magnetism and Magnetic Materials* ***322***,15 (2010), 2199–2202 (cit. on p. 117)

[15] K Maaz, M Usman, S Karim, A Mumtaz, SK Hasanain, and MF Bertino *Magnetic response of core-shell cobalt ferrite nanoparticles at low temperature*. in: *Journal of Applied Physics* ***105***,11 (2009), 113917 (cit. on pp. 117, 127)

[16] Biplab K Chatterjee, CK Ghosh, and KK Chattopadhyay *Temperature dependence of magnetization and anisotropy in uniaxial NiFe2O4 nanomagnets: Deviation from the Callen-Callen power law*. in: *Journal of Applied Physics* ***116***,15 (2014), 153904 (cit. on pp. 117–119)

[17] Henry Shenker *Magnetic anisotropy of cobalt ferrite (Co 1.01 Fe 2.00 O 3.62) and nickel cobalt ferrite (Ni 0.72 Fe 0.20 Co 0.08 Fe 2 O 4)*. in: *Physical Review* ***107***,5 (1957), 1246 (cit. on p. 118)

[18] H.B. Callen and E. Callen *The present status of the temperature dependence of magnetocrystalline anisotropy, and the l(l+1)2 power law*. in: *Journal of Physics and Chemistry of Solids* ***27***,8 (1966), 1271–1285 (cit. on p. 119)

[19] Allan H Morrish *Canted antiferromagnetism: hematite* World Scientific, *1995* (cit. on pp. 126, 127)

[20] JDA Piper *DUNLOP, DJ & ÖZDEMIR, Ö. 1997. Rock Magnetism. Fundamentals and Frontiers. Cambridge Studies in Magnetism Series. xxi+ 573 pp. Cambridge, New York, Port Chester, Melbourne, Sydney: Cambridge University Press. ISBN 0 521 32514 5*. in: *Geological Magazine* ***135***,02 (1998), 287–300 (cit. on pp. 126, 127)

[21] Cor B De Boer, Tom AT Mullender, and Mark J Dekkers *Low-temperature behaviour of haematite: susceptibility and magnetization increase on cycling through the Morin transition*. in: *Geophysical Journal International* ***146***,1 (2001), 201–216 (cit. on pp. 126, 127)

Part III

Enhanced permanent magnets manufacturing and innovative magnetic-based applications

Introduction

Last part of this thesis is devoted to export the knowledge acquired during the realization of this research out from the lab. In particular, nanostructured cobalt ferrite powder was demonstrated to be a potential candidate for RE-free permanent magnets thanks to its good magnetic performance; a high both, magnetization and coercivity, among ferrites that is comparable to low grade RE bonded magnets.

At the end of the day, after long time of scientific research, it is expected to translate all the knowledge generated during this activity to the market with a new product or an enhanced one. That is also the main interest of this scientific work; to develope an enhanced ferrite material to fabricate permanent magnets.

Section 8 explores the fabrication process of Co-ferrite permanent magnets, using different techniques in order to validate the most suitable procedure. Since the magnetic performance is directly influenced by the morphology, it is important preserve, or not to modify it too much to keep the enhancement in magnetic properties. Hence, the most suitable fabrication route need to be found. In this chapter is shown that the conventional SPS method employed for ceramics is not a suitable process to fabricate cobalt ferrite permanent magnets because the enhancement of magnetic properties achieved previously is vanished once compacted. It is found that polymerization is the best option to manufacture cobalt ferrite with high coercivity or enhanced energy product because it allows to provide mechanical stability to the formed piece while the microstructure is almost unaltered. Finally, the usability of these magnets is demonstrated through a proof of concept consisting on the implementation of a fully operative stepper motor with cobalt ferrite magnets installed in the rotor.

This part ends up with chapter 9, where the attention is mainly focused on applications comprising both, magnetic sensors and permanent magnets: from this combination arise a diverse number of new applications thanks to the new generation of magnetic sensors based on the magnetoresistance phenomena. It is worth to mention that these implementation of these sensors is leading to a technological revolution; while in the last decade the state-of-the art for magnetic field measuring was mainly based in inductive sensors that requires the movement of one part (the magnetic source or the magnetic sensor) because its operating principle is based on the measurement of an electrical current generated by an alternating magnetic fields. This new generation of magnetoresistive sensors improve Hall effect sensors with a higher sensitivity and lower power consumption, and the are nowadays implemented in, for instance, all smartphones as a compass to support GPS navigation. This devices have been recently commercially available for normal user, and there are some interesting examples of applications with this technology like non-contact joysticks, contactless switches or as cars detectors in parkings by measuring how the vehicle chasis disturbates the Earth's magnetic field. Here, a discussion of the technique known as 'Magnetovision' and its potential application when introducing in the equation permanent magnets that generates a known magnetic field is done. In particular, it is described the use of these sensors as a part of a recycling process, specifically in the automatic detection of permanent magnets enclosed inside electronics devices such as a hard disks or a smartphone, allowing then to recover the magnet in an automatic process with no need of human intervention. Moreover, since this type of sensors allows to determine not only a one-dimensional intensity, but the full magnetic vector, it is described how to implement an identification systems where the traditional binary state bit is substituted by a multistate but.

Chapter 8

$CoFe_2O_4$ permanent magnets

The manufacturing of cobalt ferrite magnets is studied in this section. Several processes are applied in order to find the optimum fabrication routine for this type of permanent magnets; spark plasma sintering, cold-compaction and polymerization. Finally, these magnets are implemented in a stepper motor in order to demonstrate its functionality.

Figure 8.1: Ferrite based permanent magnets with different shapes.

8.1 Techniques for permanent magnet manufacturing

Many different processes are implemented in permanent magnets fabrication industry, depending on multiple factors such as the operability of the materials during its manufacture or the physical properties of the final piece such as the shape. An interesting highlight of ferrites against rare-earth permanent magnets is that for the latter, a protective layer is needed in order to avoid the oxidation of the magnetic phase, while for ferrites this production step can be avoided because these materials are already oxidized. This is important not only in the production cost, but in the possible applications of these type of magnets, i.e: in highly oxidative environments.

A typical ceramic manufacturing process applied to ferrites starts with the refinement of the initial powder, for instance being subjected to a heat treatment for tuning the microstructure, or to a ball milling process in order to reduce particle size. Once the powder posses the desired characteristics, next step is the forming of the piece. There are multiple existing methods for this process, generally by the application of a compaction force in one or multiple directions. With this process, the powder acquires the shape of the piece (because of the mold), however its mechanical stability is fragile and thats why the next step is a heat treatment to cause the piece densification, usually via 'liquid phase sintering'. Notwithstanding, in some cases this type of densification is not recommended since its involves a considerable modification of the magnetic particles microstructure, and thus its magnetic properties. For this situations, a plausible option is to fabricate a polymerized magnet that requires low temperatures to achieve a sufficient mechanical resistance. Sometimes, at one point of the magnet manufacturing process, a magnetic field is applied in order to align the magnetic particles to form an anisotropic magnet. This can be done during the compaction, or during the sintering stage. Finally, the last step for the permanent magnet manufacturing is the magnetization. The magnetic piece is subjected to an external magnetic field that magnetizes the magnet. This is usually accomplished with electromagnets that generates brief pulses with a strong intensity of magnetic field, but there are other techniques such as the known as 'roll-on' which consist in rolls attached with permanent magnets (with high intensity of it magnetic field) that allows to impart unique magnetic patterns in polymerized magnets.

In this work, two fabrication processes were employed: Spark Plasma Sintering (SPS) and the cold-compaction method. While SPS is a technique that combines both steps, forming and sintering, the cold-compaction method is a two-steps procedure but additionally, it is possible to manufacture polymerized magnets, which is the alternative if high temperature treatments needs to be avoided after the forming step. The techniques employed to fabricate the magnets studied in this thesis are described in the following.

8.1.1 Spark Plasma Sintering

SPS is a well known method used for the preparation of ceramics based on nanoparticles with enhanced piezoelectric, [1] thermoelectric, [2] optical [3] or biomedical [4] properties. SPS is also used for sintering of Carbon Nanotubes [5] used in development of field electron emission electrodes.While this technique is commonly named as 'spark plasma sintering', the term is misleading since neither a spark nor a plasma is present in the process. [6]

The SPS process is based on the electrical spark discharge phenomenon: a high energy and low voltage spark pulse current momentarily generates spark plasma at high localized temperatures, from several to ten thousand celsius degrees between the particles resulting in optimum thermal and electrolytic diffusion. The powder materials are stacked between the die and punch on the sintering stage in the chamber and held between the electrodes. Under pressure and pulse energized, the temperature quickly rises to temperatures in the order of 1000 °C, resulting in the production of a high quality sintered compact in only a few minutes.[SPS-BOOK] The SPS might be operated in current-assisted mode or current insulated mode. In both cases, a pulsed DC current that generates heat internally in the compacted piece due to Joule heating, by contrast to the conventional hot pressing methods where the heat is provided by external heating elements. In the current assisted mode, this current flows through the graphite die, as well as the powder being compacted, while in the curren-insulated mode the current flows around the die (see Figure 8.2)

The fact that heat is generated internally has been found to play a dominant role in the densification of powder compacts allowing to achieve near theoretical density at lower sintering temperature compared to conventional sintering techniques [7]. Moreover, this technique allows to perform high heating or cooling rate (up to 1000 K/min), therefore the sintering process generally is very fast (within a few minutes). So that, this technique has the potential of densifying powders with nanosize or nanostructured particles while avoiding coalescence that accompanies standard densification routes.

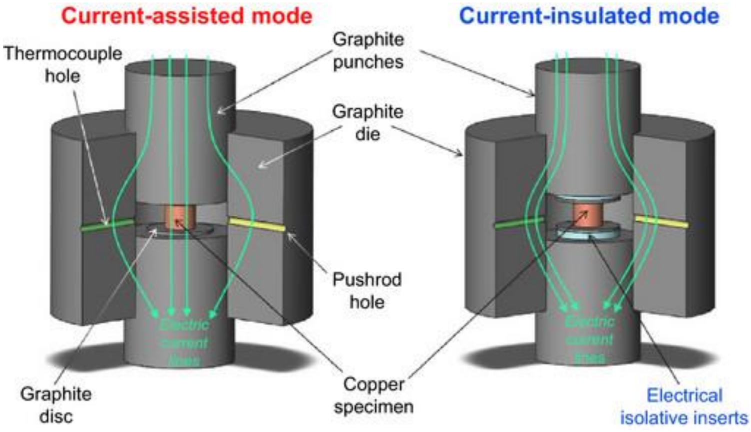

Figure 8.2: Scheme of a SPS process in (a) current-assisted mode and (b) in current insulated mode.

8.1.2 Cold-compaction

The most common method used in powder metallurgy for pieces forming is the cold-compaction method, also known as uniaxial pressing, since it is suitable for high-volume production of simple shapes permanent magnets such as refractories, tiles, electronic ceramics, etc. The uniformity of compaction is not very high. This procedure consist on the compaction of the powder into a rigid die by applying pressure in a single axial direction through a rigid punch or piston using a mechanical or hydraulic press. The negative point of this compaction method is that it limits the shape to only cross-sections shapes of the formed piece that can be pushed out of the die cavity. Regarding the force application step there are different variations; while sometimes a high compaction force is applied during seconds to hours, and some others procedures consist on continuously hammer the powder. The compaction force might be applied in one direction (uniaxial or transverse pressing) or from many different directions (isostatic pressing).

In this work, all magnets manufactured by this method where compacted with an axial force. The equipment used for this purpose is shown in Figure 8.3. The procedure followed to manufacture a magnet consisted on, first, place the magnetic powder in the mold's cavity, followed by the application of a uniaxial compaction force using two punches. An electromagnet can be placed as shown in Figure 8.3 in order to apply a magnetic field just before applying the compaction force. The goal of this step is to physically orient the magnetic particles with this applied magnetic field to latter fix these particles position with the compaction force. In the setup shown in Figure 8.3, the aligning applied magnetic field is parallel to the direction of compaction force.

Figure 8.3: Hidraulic press applying pressure to the powder to form a magnet. At the same moment, a magnetic field is being applied to the powder under compaction too.

8.1.3 Post compaction heat treatment

Once the magnetic piece is formed after the compaction process, it is fragile and can be pulverized if hit. Because of this fact, a heat treatment is performed to transform the compacted pieces into fused, solid ceramic pieces. This process is also known as sintering, and it usually consists on three stages. In the first stage, the compressed material is heated at a low temperature to slowly drive off any moisture or other contaminants that may have become entrapped during the pressing process. In the second stage, the temperature is raised to about 70-90% of the melting point of the metal alloy and held there for a period of several hours or several days to allow the small particles to fuse together. Finally, the material is cooled down slowly in controlled, step-by-step temperature increments. During sintering, the magnets can shrink about 15-20% linearly its initial dimensions. Completed magnets have a rough surface and only approximate dimensions. They also exhibit no external magnetic field because the temperatures used are above the curie temperature of the magnetic material. The sintered material then undergoes a second controlled heating and cooling process known as annealing. This process removes any residual stresses within the material and strengthens it.

8.1.4 Polymerization

The polymerization technique consists in the addition of a small fraction of powdered polymer, usually below a 5% in weight, to the magnetic starting powder prior compaction, and this polymer is later activated - by different ways such as UV-light of heat - to form a polymer chain lattice hence providing mechanical stability to the formed piece. So that, the polymerization technique is very useful when the sintering stage wants to be avoided, however this technique is not suitable to obtain dense pieces. The polymer used to fabricate these magnets was polyamide based commercially known as 'PA11', with a grain size distribution in the range of 40 to 50 microns. In the experiments presented below, the amount of polymer added to the magnetic material was a 2% in weight, which was previously check not to influence in the magnetic properties of the starting material (i.e. magnetization curves of the material with and without polymer are identical).

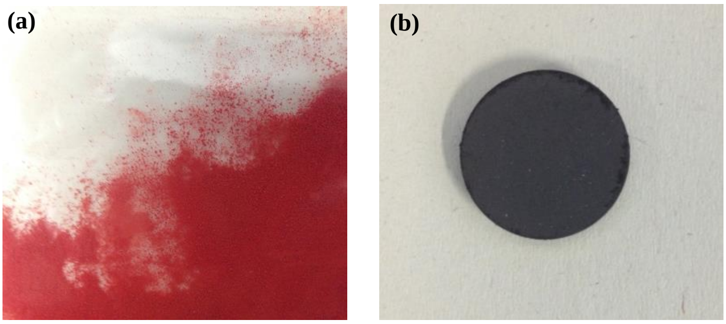

Figure 8.4: Figure (a) displays the polyamide-11 powder used in polymerization experiments. Figure (b) shows a polymerized magnet obtained using this polymer.

8.2 CoFe$_2$O$_4$ products compacted by SPS

After analyzing the results of experiments discussed in part **??**.. show that a heat treatment to cobalt ferrite can be used as a tool for controlling the particles microstructure. In particular, one conclusion of chapter**??** experiment where high coercive cobalt ferrite was subjected to a post-milling heat treatment was that high coercivity is linearly decreased with increased temperature but energy product increased if heating temperatures is below 700Âº the enhancement, however for higher temperatures both magnetic properties (H$_C$ and BH_{MAX}) will decrease. In all cases these modifications of magnetic properties are due to microstructural modifications (relaxation of strain and recrystallization). The preservation of an adequate microstructure is an important challenge regarding magnets fabrication since it left the mechanical stability of the final piece in a predicament. Spark plasma sintering minimizes grain growth and allows the use of lower temperatures than conventional methods, and thus it is therefore a potential candidate to be used in CoFe$_2$O$_4$ permanent magnets fabrication.

As the SPS technique allows the combination of pressure application with a heat treatment, it is used to manufacture three cobalt ferrite magnets of a different product each.

In this section, cobalt ferrite magnets fabricated by the SPS method are studied as a first approach for CoFe$_2$O$_4$ permanent magnet manufacturing. The three cobalt ferrite products proposed in part **??** (as synthesized, high-coercive and with an enhanced $(BH)_{max}$) were compacted forming magnets by using the SPS. The magnets manufacturing using the SPS method shown in this work were performed by Prof. Mogens Christensen research group at Aarhus University in Denmark.

8.2.1 Experimental details

Three cobalt ferrite products, synthesized and processed as described in part II, were manufactured by the SPS technique previously described. These products are described below:

- Product A is cobalt ferrite powder synthesized by the co-precipitation method and heated to 700 °C. Microstructural and magnetic characterization of this sample was shown in section 4.2.2 named as Powder C heated to 700 °C. This powder is constituted by CoFe$_2$O$_4$ with a crystallite size, $< D_V >$ = 65.1 nm, and ε =$1.4 \cdot 10^{-3}$. A small contribution of α-Fe$_2$O$_3$ was observed in the XRD spectra of this sample.

- Product B is cobalt ferrite synthesized by the co-precipitation method, heated to 1000 °C and milled during 180 seconds by HEBM. Microstructural and magnetic characterization of this sample was discussed in section 5.1. This powder is constituted by CoFe$_2$O$_4$ with a crystallite size, $< D_V >$ = 9.2 nm, and $\varepsilon = 8.9 \cdot 10^{-3}$.

- Product C is cobalt ferrite synthesized by the co-precipitation method, heated to 1000 °C, milled during 180 seconds by HEBM and heated after the milling procedure to 600 °C. Microstructural and magnetic characterization of this sample was analyzed in section 6.1. This powder is constituted by CoFe$_2$O$_4$ with a crystallite size, $< D_V >$ = 20.1 nm, and $\varepsilon = 4.1 \cdot 10^{-3}$. A small contribution of α-Fe$_2$O$_3$ was observed in the XRD spectra of this sample.

A mass of 1 grams on each batch was used. The SPS procedure consisted on, first, the placement of cobalt ferrite powder inside the mold cavity with the graphite die, and then the temperature is raised to 750Â°C and held during 2 minutes while applying a compaction pressure of 80 MPa. A Lakeshore 7400 VSM was employed to measure magnetization *M*-*H* curves at RT. Parameters extracted from the hysteresis loops include magnetization at maximum applied field of 20 kOe, ($M_{20\mathrm{kOe}}$), remanence magnetization (M_r), and coercivity (H_c).

8.2.2 Results and Discussion

The last step of the manufacturing process of a ceramic permanent magnet is a heat treatment to cause the particles sintering. However, intrinsic magnetic properties of Co-ferrite are altered due to these particles microstructure modification, hence this heat treatment has to be somehow avoided because the improvement on magnetic properties obtained is extincted. In this sense, the SPS technique is choosen for this experiment magnets preparation because one of the main advantages of that it takes only a few minutes for the whole process, including he application of a compaction force and a high temperatures (up to 1000 ° C) simultaneously.

Figure 8.5 plots the comparison the starting powder hysteresis loop with the one obtained from the manufactured magnet. At a first glance, the most striking is the observed decrease in coercivity in all cases. This might be ascribed to the high heating temperature that modifies the microstructure by increasing particle size. Chapter 6 analyzes the effect of heating temperature in milled cobalt ferrite powders, showing that when the heating temperature is in a range from 400 to 600 there is a strain relaxation and recrystallization of particles, and at higher temperature it is mainly observed $CoFe_2O_4$ grain growth.

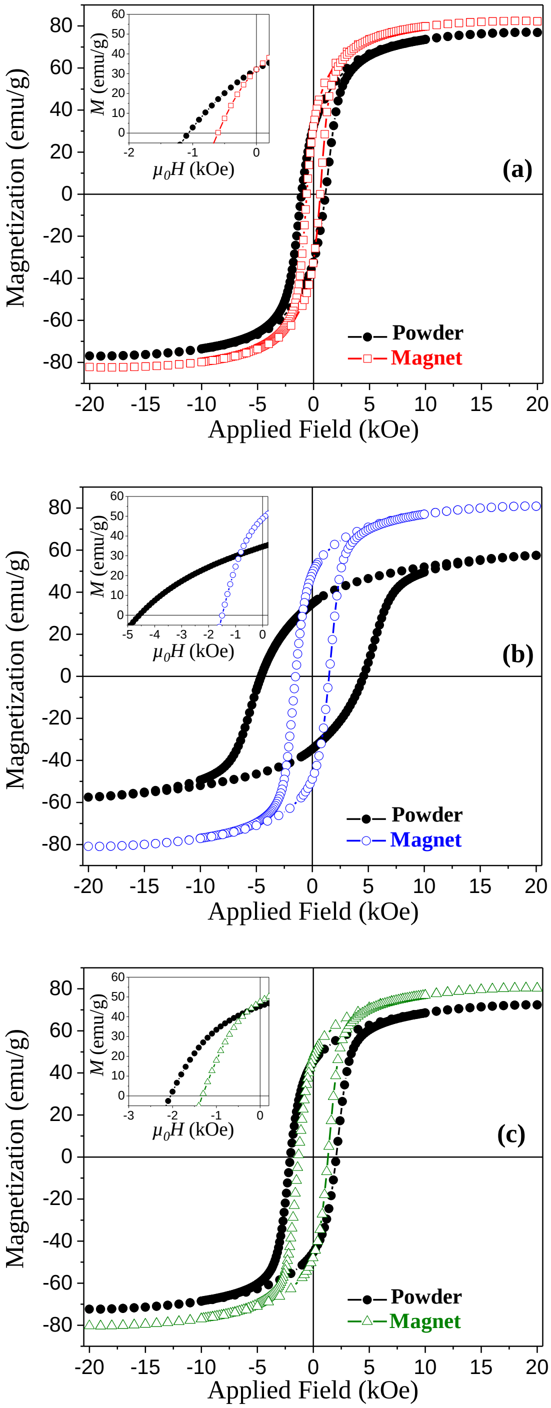

Figure 8.5: M-H curves at RT of milled $CoFe_2O_4$ measured with an applied field of 50 kOe (black, empty squares) and 20 kOe (red, full diamonds).

8.3 Polymerized CoFe$_2$O$_4$ magnets by cold-compaction

Unlike other magnetic materials that needs to be sintered, in the case of cobalt ferrite, sintering diminish the magnetic properties enhancement, as it was demonstrated with magnets fabricated by SPS. The polymerization technique is very useful when sintering needs to be avoided; a temperature of 250Â°C during 1 hour is sufficient to activate the polymer providing mechanical stability to the piece. Furthermore, the magnetic properties are not decreased since the temperature is not high enough to cause microstructural modifications in cobalt ferrite particles.

In this scenario, the only free parameter that might influence cobalt ferrite microstructure is the pressure used during the cold-compaction process. To shed some light, a systematic study regarding the influence of the pressure applied during compaction on the final magnetic properties of cobalt ferrite magnets manufactured by the cold-compaction method is performed.

8.3.1 Experimental details

The tools for compacting magnetic powders were designed and fabricated at IMA S.L. The design always was done considering the actual state-of-the-art for that purpose in an industrial environment Image 2.(a) shows the final designed mechanism for compaction process, with punches made out of tempered steel to achieve high compaction forces. The mold material is non-magnetic in view of the avoidance of powder agglomeration if magnetized.

This structure is assembled on an automatic hydraulic mechanical press. The mechanical structure is formed by two plates placed in two linear bushings, which restrict the movement to a single degree of freedom. Two punches are attached to the plate, and the compaction is done inside a mold which is placed in between the punches. This mold has the shape of the final magnet, and an important solution implemented has been to design the mold with a conical shape in the edges to allow the extraction of the magnet without damaging it. As can be seen on Image 3. This design also allows the use different coils during compaction process, intended to align the material. In all fabricated magnets, the magnetic applied field was in the direction of compaction force.

All magnets have cylindrical shape with a diameter of 14 mm. The height is dependent on the mass of the magnet and the manufacturing process, i.e. post-compaction heat treatment.

Three cobalt ferrite products, synthesized and processed as described in part II, were manufactured by the SPS technique previously described. These products are described below:

- Product A is cobalt ferrite powder synthesized by the co-precipitation method and heated to 700 °C. Microstructural and magnetic characterization of this sample was shown in section 4.2.2 named as Powder C heated to 700 °C. This powder is constituted by CoFe$_2$O$_4$ with a crystallite size, $< D_V >$ = 65.1 nm, and ε =1.4$\cdot 10^{-3}$. A small contribution of α-Fe$_2$O$_3$ was observed in the XRD spectra of this sample.

- Product B is cobalt ferrite powder synthesized by the co-precipitation method and heated to 700 °C. Microstructural and magnetic characterization of this sample was shown in section 4.2.2 named as Powder C heated to 700 °C. This powder is constituted by CoFe$_2$O$_4$ with a crystallite size, $< D_V >$ = xxx nm, and ε =yyy$\cdot 10^{-3}$.

- Product C is cobalt ferrite synthesized by the co-precipitation method, heated to 1000 °C and milled during 180 seconds by HEBM. Microstructural and magnetic characterization of this sample was discussed in section 5.1. This powder is constituted by CoFe$_2$O$_4$ with a crystallite size, $< D_V >$ = 9.2 nm, and $\varepsilon = 8.9 \cdot 10^{-3}$.

A mass of 1 grams on each batch was used. The SPS procedure consisted on, first, the placement of cobalt ferrite powder inside the mold cavity with the graphite die, and then the temperature is raised to 750Â°C and held during 2 minutes while applying a compaction pressure of 80 MPa. A Lakeshore 7400 VSM was employed to measure magnetization M-H curves at RT. Parameters extracted from the hysteresis loops include magnetization at maximum applied field of 20 kOe, ($M_{20\mathrm{kOe}}$), remanence magnetization (M_r), and coercivity (H_c).

CoFe$_2$O$_4$ powder was compacted in magnets using different compaction pressures. In order to avoid post-compaction microstructural modifications, and to increase the mechanical stability of the magnetic piece for its ulterior characterization, the magnets were polymerized using a 2% of PA11. Note that magnetic properties of the starting material after the addition of the polymer did not vary significantly.

The starting powder was compacted into pieces of 5 mm in diameter, using an hydraulyc press to apply a pressure of 200 Kg/cm^2 and 500 Kg/cm^2

8.3.2 Results and discussion

It is expected that through the polymerization process, the microstructure will not be excessively modified, specifically avoiding grain growth due to the lower temperatures used in the post-compaction procedure to provide mechanical resistance to the formed pieces. Here, the magnetization curves measured on the fabricated magnets are compared with that of its constituent free powder. Hysteresis loops are plot in figure 8.6, where one can clearly see that, in contrast to that magnets manufactured by the SPS method, these ones did not display a decrease of its magnetic performance. This is because the maximum temperature in the manufacturing process is not higher than 250 ° C and so not enough to produce recrystallization and grain growth (see chapter 6) to significantly modify cobalt ferrite microstructure. The fact that magnetization curve of Product C free powder is similar to the fabricated magnet, with H_C = 4.9 kOe and 4.8 kOe, and M_R = 34.6 emu/g and 34.0 emu/g respectively confirms this.

Because of the only free parameter is the pressure applied during the compaction, its influence on the final magnet magnetic properties was study using powders A and B. These powders were compacted at a pressure of 200, 400 and 600 kg/cm^{2}g. The evolution of coercivity, H_C and remanence magnetization, M_R for both series are plot in Figure 8.7. At a first glance it is seen that for both powders, these parameters follows the same tendency with increased pressure. In particular, H_C is linearly increased with compaction pressure, in case of Powder A from 1.3 kOe to 2.2 kOe and in Powder B from 1.1 kOe to 2.0 kOe. This might be explained as the effect of pressure on CoFe$_2$O$_4$ particles that is somehow decreasing the powder particle size and inducing strain. Furthermore, the relative increase of coercivity per unit of pressure is almost identical. However this is not the case in M_R evolution with pressure; while the initial powders possessed 29.4 and 31.6Â§ emu/g respectively, after applying 600 kg/cm^2 this value rose up to 39.9 and 45.3 for Powder A and B respectively.

The increase in coercivity is goberned by the particle size if this is above of the critical domain size. Powder A is a cobalt ferrite synthesized with a heat treatment of 700 °C with nanosized particle size but poor crystallinity, and Powder B is cobalt ferrite synthesized with a heat treatment of 1000 °C with big ($\geq$ 1 μ) polycrystalline particles (see Figure 4.4). It is unclear the origin of the increased coercivity, since in case of Powder B might be due to the decrease of particle size and for Powder A might be due to strain induction through the compaction process. On the other hand, saturation magnetization is related to dipolar interactions inside the magnet and the crystallinity level of the particles. The first can be discard because of the similarity of the magnetization curve of both, the magnet and its constituent free powder (that in saturation state can be considered as a single domain), but the second is consistent with the higher M_R of Powder B by comparison with that of Powder A.

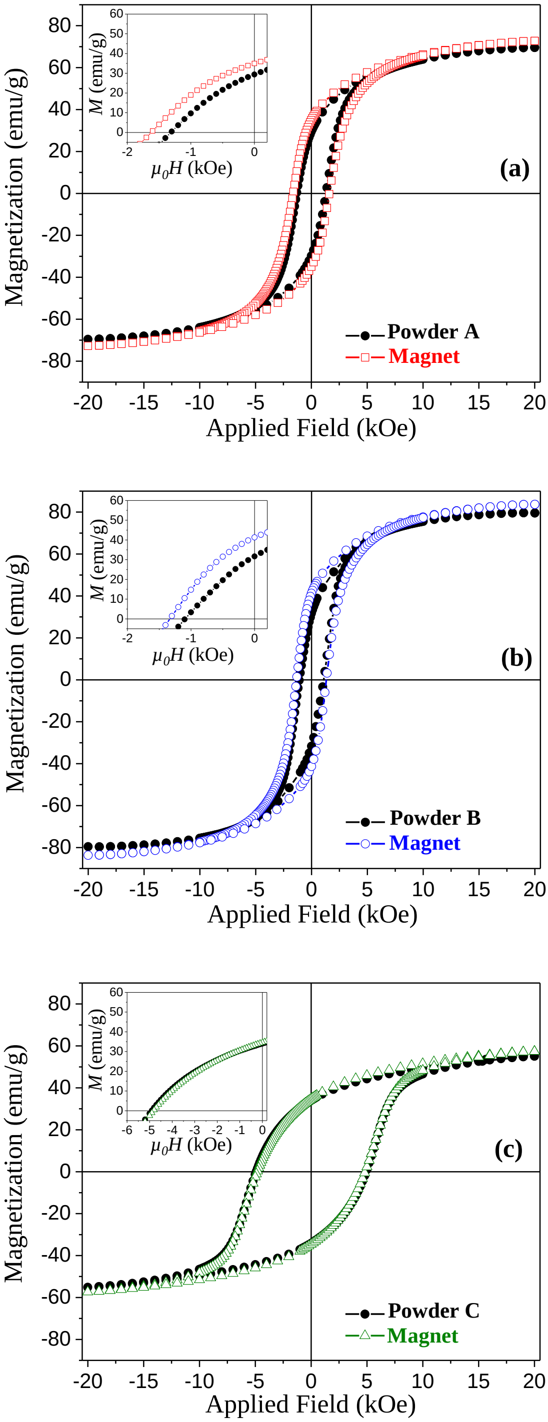

Figure 8.6: M-H curves at RT of free CoFe$_2$O$_4$ powder and its polymerized magnet of (a) Powder A, (b) Powder B and (c) Powder C.

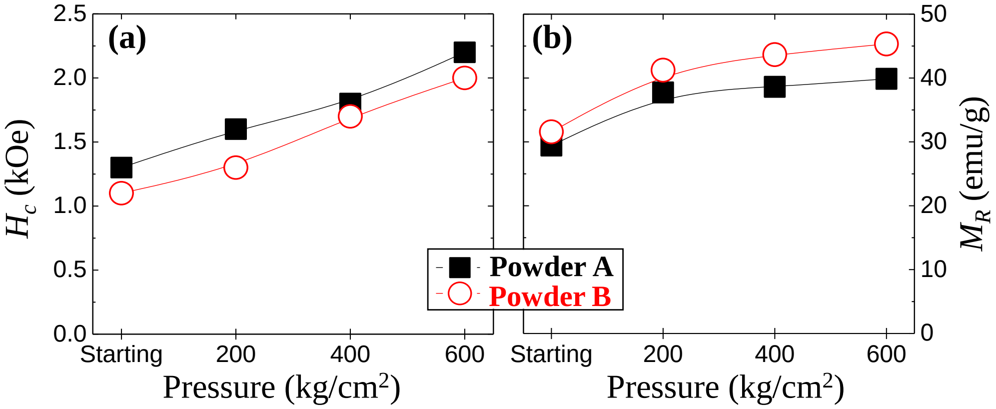

Figure 8.7: Evolution with applied pressure during compaction of (a) coercivity, and (b) remanence magnetization of Powder A (black squares) and Powder B (red circles)

8.3.3 Conlusions

The aim of this particular experiment was to manufacture a permanent magnet in such a way that the enhancement achieved in the starting free powder magnetic properties were not deteriorated later when manufacturing the permanent magnets. This was achieved through the polymerization method in combination with a cold compaction technique. Obtained results indicates that coercivity is not only maintained in case of high coercive starting powder, but exceeding in some cases the value of the starting powder. Unfortunately it was not possible to perform a detailed XRD study of these samples that might shed some light regarding particle size, induced strain and particles alignment. Nevertheless, this is something to take into consideration for future works

8.4 A proof of concept: stepper motor

This experiment was performed with the goal to demonstrate the applicability of the $CoFe_2O_4$ magnets fabricated as described in previous section. This complete task was jointly performed with Jose Luis Fernández Cunnado. Considering the size and shape of the fabricated magnets as a limiting factor (a new mold is needed if the magnet shape or dimensions wants to be modified), it was decided to fabricate a stepper motor as the proof of concept application. In particular, a stepper motor is a brushless type DC motor where the rotor contains a toothed disk with alternating poles on each tooth, and the stator is usually formed by two or four pairs of electromagnets, with a geometrical distribution that allows to rotate the rotor when the electromagnets are excited with a determined sequence. So that, the operating principle is as simple as to attract a magnet with another one (in this case an electromagnet). Interestingly, in this type of motors the direction of rotation as well as the speed can be easily controlled trough the sequence and frequency of pulses applied to activate the electromagnets.

To understand the operating principle it is important to point out the most relevant parts that implement the stepper motor. Figure 8.8 shows a transversal schematic view of a stepper motor; the inner part (rotor) is formed by six magnets numbered from 1 to 6, all placed with the same pole pointing out, and the outer part (stator) contains 4 pairs of electromagnets, denoted from A to D. The coils marked with prime symbols are the pairs. The electromagnets are excited in the particular sequence A-B-C-D or D-C-B-A depending on the desired sense of rotation. Situation represented in Figure 8.8 correspond to that case in which the pair B is the activated electromagnet, and because of this the magnets 6 and 3 are attracted to face them. The rest of electromagnets pairs are disabled or generating a magnetic field with the same sign that the magnets, so they are repelled. If in the next steps, the pair A is activated, electromagnet A will attract the magnet 1 until face it, as same as electromagnet A' will do with the magnet 4. This means that the rotor will rotate with an anticlockwise sense. On the other hand, activating the C-C' pair, same description as before applies but with magnets 5 and 2, therefore rotating in a clockwise sense.

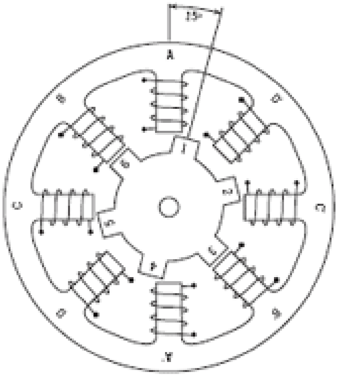

Figure 8.8: Schematic transverse view of a stepper motor. The inner part is the rotor containing six numbered magnets, while the outer part correspond to the stator with four pairs of electromagnets, labeled from A to D.

An additional benefit of considering a stepper motors is the fact that these devices are easy to disassemble, allowing the original rotor substitution by a new one containing our fabricated magnets. Thank to this we can avoid to manufacture a stator as well as the electromagnets coils. Our home-made rotor was fabricated with a 3D printer using white ABS plastic, and contains 6 polymerized magnets of cobalt ferrite with cylindrical shape of 5 mm in diameter and mass of 300 milligrams approximately, including a 2% in weight of polymer. The powder was compacted at a pressure of 400kg/cm^2 which was held during 30 seconds. No magnetic field was applied during the compaction, and after it a heat treatment to 250Â°C for 1 hour was applied to activate the polymer and provide mechanical stability to the magnets. The magnets were axially magnetized (in the direction of cylinder c-axis) using the VSM electromagnet with an applied field of 2 Tesla, and glued to the 3D-printed rotor. This specific configuration of magnets in the rotor and electromagnets in the stator provides a stepper motor capable of 15 degree full steps and 7.5 degree half steps.

Figure 8.9 shows a picture of the final assembly of the stepper motor. This device was presented in the NANOPYME workshop celebrated at IMDEA Nanoscience in September 2015. The demo included an Arduino based driver for the stepper motor that was controlled through a Labview program from a PC. The user was allowed to select the number of steps, speed and sense of rotation. The motor was operated in full step mode.

Since the main objective in this experiment was to demonstrate the applications of cobalt ferrite magnets, a systematic characterization of the stepper motor properties were not performed. Furthermore, it is well known that the efficiency of these type of electrical machines strongly depends on the geometrical design. For instance, the torque might be considerable increased by using a single-piece rotor with the number of teeth necessary for the optimum operation according to the used stators. This kind of studies can be considered as a future work, since the good performance of cobalt ferrite make it a potential candidate in many applications.

Figure 8.9: Image of the stepper motor while in operation. This stepper was modified with a home-made 3d-printed rotor containing 6 polymerized cobalt ferrite magnets.

8.5 Conclusions

Cobalt ferrite PMs were manufactured by the SPS method and cold-compaction with polymerization.

Permanent magnets fabricated with the SPS method show a comparable hysteresis loop independently of the magnetic performance of the starting powder. Furthermore, all these magnetization curves display low coercivity and high saturation magnetization, pointing to the fact that the temperature is probably modifying the microstructure, increasing particle size and overpassing the critical magnetic monodomain size, even if it was applied for a short time (below 5 minutes). On the other hand, by adding just a 2%wt. of polymer to the starting powder and with the cold-compaction method, it is possible to obtain cobalt ferrite magnets where the magnetic performance is preserved. This is because the polymer provide mechanical stability to the piece when melted, and this occurs at low temperatures that do not affect cobalt ferrite microstructure.

References

[1] Jing-Feng Li, Ke Wang, Bo-Ping Zhang, and Li-Min Zhang *Ferroelectric and Piezoelectric Properties of Fine-Grained Na0. 5K0. 5NbO3 Lead-Free Piezoelectric Ceramics Prepared by Spark Plasma Sintering*. in: *Journal of the American Ceramic Society* ***89***,2 (2006), 706–709 (cit. on p. 138)

[2] Heng Wang, Jing-Feng Li, Ce-Wen Nan, Min Zhou, Weishu Liu, Bo-Ping Zhang, and Takuji Kita *High-performance* $Ag_{0.8}Pb_{18+x}SbTe_{20}$ *thermoelectric bulk materials fabricated by mechanical alloying and spark plasma sintering*. in: *Applied physics letters* ***88***,9 (2006), 092104 (cit. on p. 138)

[3] Byung-Nam Kim, Keijiro Hiraga, Koji Morita, and Hidehiro Yoshida *Spark plasma sintering of transparent alumina*. in: *Scripta Materialia* ***57***,7 (2007), 607–610 (cit. on p. 138)

[4] YW Gu, NH Loh, KA Khor, SB Tor, and P Cheang *Spark plasma sintering of hydroxyapatite powders*. in: *Biomaterials* ***23***,1 (2002), 37–43 (cit. on p. 138)

[5] Pejman Hojati-Talemi, Aravindaraj G Kannan, and George P Simon *Fusion of carbon nanotubes for fabrication of field emission cathodes*. in: *Carbon* ***50***,2 (2012), 356–361 (cit. on p. 138)

[6] Dustin M Hulbert, André Anders, Dina V Dudina, Joakim Andersson, Dongtao Jiang, Cosan Unuvar, Umberto Anselmi-Tamburini, Enrique J Lavernia, and Amiya K Mukherjee *The absence of plasma in 'spark plasma sintering'*. in: *Journal of Applied Physics* ***104***,3 (2008), 033305 (cit. on p. 138)

[7] K Sairam, JK Sonber, TSR Ch Murthy, C Subramanian, RK Fotedar, P Nanekar, and RC Hubli *Influence of spark plasma sintering parameters on densification and mechanical properties of boron carbide*. in: *International Journal of Refractory Metals and Hard Materials* ***42***, (2014), 185–192 (cit. on p. 138)

Chapter 9

Innovative magnetic-based applications

This chapter describes two applications developed during my thesis work and that might not be possible without nanoscience. Both make use of a new type of magnetic sensors comercialized as three-dimensional magnetometers. First, it is described the two type of sensors used for this work. Then, it will be described how it is possible to implement one of these sensors in a CNC device programmed to obtain magnetic field distributions images of static elements. Finally, examples of applications for this device are shown.

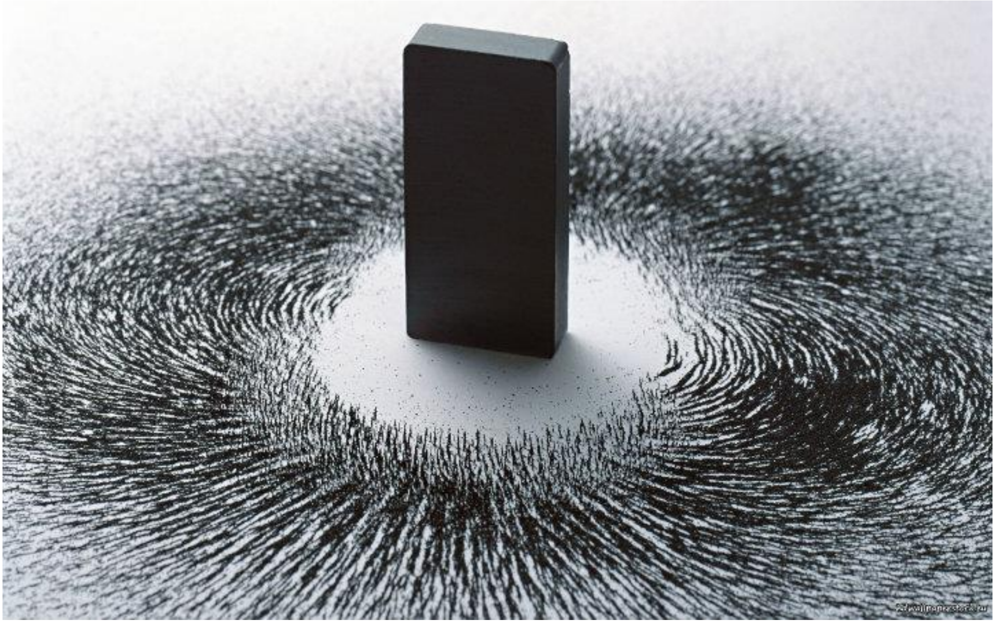

Figure 9.1: Visualization of the magnetic field generated by a permanent magnet using ferrite powder

9.1 Magnetovision

Magnetovision [1] is the name given to a technique for imaging the magnetic field distribution over a sample of ferromagnetic materials. The name magnetovision comes from the analogy technique for the observation of thermal distributions known as thermovision. This technique consist in the use of one or multiple magnetic sensors that are moved above a ferromagnetic surface, measuring the magnetic intensity field value at different positions to finally compose a magnetic map representing the magnetic field intensity measured at every position.

There are many type of magnetic field sensors, and different properties are found on each one. An option might be pick-up coils that can be easily fabricated just by winding up a cable, but this type of sensors are only useful for AC measurements. Hall-effect sensors allows the measurement of DC and AC magnetic fields, and additionally it provides a high full-scale range. Magnetoresistive sensors presents higher sensitivity than hall effect sensors, but with a lower full-scale range. In general, most studies found on literature refers to a magnetic sensor as a device to measure a single component of the magnetic field.

A diverse number of applications based on magnetovision have been proposed. This imaging techniques can be mainly applied in two different ways. In the first, it is known the position of a magnetic source, and the magnetic maps are commonly used to study magnetism of samples, for instance in the determination of the demagnetizing factor of a magnet with a particular shape [2]. Magnetovision was initially applied to the investigation of steel sheets [3–5], making use of the inverse magnetostriction effect (Villari effect) that allows for the visual determination in a non-destructive way of mechanical properties, especially in fatigue tests. These materials generate a magnetic field whose intensity is dependent on the stress state of the piece. During these tests, microfractures on the piece under study might appear as differences on its generated magnetic field.

A great advance was achieved by Hu et al [6] by the implementation of a magnetovision system with an increased number of sensors (64), as well as to the use of 3-axis magnetometers instead of unidimensional sensors, proposing this application to perform a wireless endoscopy with a pill containing a magnet. An array of sensors disposed in the sides the cube allows to track, in real-time, the position and orientation of the magnet. The key in this type of applications is to combine magnetovision with the control over the generated magnetic field; the position of a magnetic source that is previously characterized can be inferred through the measurements of its generated magnetic field in various spatial position. Nevertheless, when working with this type of applications it is important to consider the processing time, since the calculation algorithms are usually based in the errors minimization of the calculated position from each sensor measurements, and this might requires long time computation.

It has been proposed the use of an array of sensors to accelerate the measuring process. Cano et al [7] described the implementation of a 16-channel magnetoresistive array, each of them able to measure the normal B_Z component. Moreover, the equipment necessary to operate the sensor is complex since extra circuitry is needed, such as signal amplifiers, analog to digital converters, power source and data acquisition cards among others, and so, an increased number of sensors involves the multiplication of this set of devices. In 1988, Tumanski et al. [2] already reported on the possibility of applying permalloy magnetoresistive sensors for magnetic imaging purposes. in 2012, Freescale launch to market MAG3110, a sensor IC that is controlled with only 3 wires.

This integrated circuit from Freescale is a digital 3-axis magnetometer able to measure magnetic fields with a sensitivity of 0.1 μT and a SNR of 0.4 μT rms. This sensor is based on the magnetoresistance phenomena to measure the magnetic field, and it outputs B_X, B_Y and B_Z in a low full-scale range of ± 1 mT with high sensitivity of 100 nT. The operation curve of the sensor presents a lineal output for input magnetic fields in a range of ± 1 mT. It is important to notice that at this order of magnitude (microtesla), the magnetic field from the earth is present and might interference the measurements if the strength of the magnetic field to measure is in the range of the Earth's magnetic field (60 μT). This problem can be easily solved since the device allows to correct the offset, however one important handicap of this technology is referred to the possibility of saturation of the soft magnetic layer of the sensor when a high magnetic field is applied (i.e. both layers magnetization are reversed) or with high frequency magnetic fields, resulting in an overflow reading even when the magnetic field is removed. Nevertheless, there is a reset procedure for this type of situations.

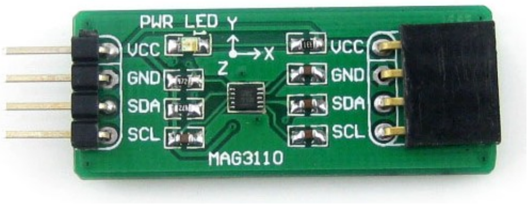

Figure 9.2: Image of a PCB containing the sensor MAG3110. This circuits is directly connected to the microcontroller using a I2C communication protocol.

The integrated circuit of MAG3110 is packaged in a 10-pin DFN chip. In this work, an ATMEGA1280 from an Arduino Mega is used to control the sensor with the computer. The input voltage of the sensor is 3.3V that is sourced by the Arduino Mega Board. Necessary operations to control the sensor are programmed in the microcontroller following the fabricant instructions. It is possible to use on-chip filters to reduce the noise paying the price of longer measuring times. The microcontroller is communicated with the sensor using I2C protocol, where the master (microcontroller) identifies a device (the sensor) by its address. This address is predefined by the sensor fabricant, meaning that it is not possible to implement an array with this sensors because of the impossibility to control each individual sensor. In a close future, more IC's of this type will appear with the possibility of address configuration by the user or with other communications protocol faster than I2C such as SPI. Regarding timing, two parameters have to be considered. First, the sampling time of the sensor, and second the time consumed in communications with the PC.

Thanks to the advances in the field of nanoscience and microelectronics, the sensor MAG3110 is commercially available at prices below 2 €. The estimated cost of a magnetovision device including electronics and mechanical parts (a CNC machine) is below 150 €, with the latter being the most expensive. Therefore this advance makes more affordable these type of devices for its use with research purpose or in industrial applications. In the following sections, different applications based in this sensor performance are described.

9.2 The Magnetic Field Scanner

The Magnetic Field Scanner (MFS in the following) here described, is a CNC device able to place a MAG3110 sensor in different spatial positions, with respect to the device under test, providing a map of the magnetic field intensities generated or modified by the device under test, for instance a permanent magnet, a DC current or a metallic sheet. The mechanical structure of the device was built using an aluminum frame designed for a 3D-printer model "PRUSA". These pieces are quite easy to obtain at a reasonable price (75€), and allows the implementation of a three degrees of freedom CNC. A MAG3110 is implemented as the magnetic sensor, being placed in the extruder position (the extruder is not implemented, only the X-axis carriage with the sensor). A transmission belt is used to implement the X and Y axis that move the sensor and the bed respectively. In this case, the resolution for the minimum step size is 10 μm. For the Z axis, the step size is even lower than 10 μm because the transmission is done with two M8 threated rods directly connected to a stepper motor each. This device is very similar to that previously reported [1, 7] but with all benefits of using an on-chip circuitry, therefore doing the task less complex.

Figure 9.3 shows an image of the device connected to the computer that operates it. The operating volume is the yellow marked bed where the hard disk is deposited (it will be used in an experiment later), The bed can be moved along the Y axis. The X axis consist in a carriage that contains the sensor (see the red part in Figure 9.3). The Z axis is implemented with two stepper motors that control the height of the X-axis carriage. The device is through an Arduino Mega with a RAMPS v1.4 (the whole kit cots 41 €) connected to a PC via USB. The firmware was programmed in the microcontroller and developed based on a G-Code-type self-designed protocol with elemental instructions such as the move of one axis to a particular position or to obtain a measure.

A Graphical-User-Interface (GUI) was developed with LabView to accomplish three important tasks for the system operation. First, it is the connection between the user and the device, so it has to clearly plot the obtained data, as well as to allow the control of the device in real-time remotely from a computer. Second, this GUI is the tool for the user to design an experiment, translating the experiment conditions to the G-Code instructions that later will be sequentially executed during the running of the experiments. Third, it has to manage the device during the execution of an experiments, with the elemental instructions provided through the file previously generated with the G-Code instructions. With this software, the user is able to design the experiment with the spatial conditions where three-dimensional magnetic measurements have te be done. For instance, it can be selected a constant Z value to obtain an XY image or several images can be saved with different Z values. Regarding the measurement process, it is possible to calculate the average of a defined number of readings in a determined position, in addition to the possibility of setting the internal filters of the sensor for noise minimization. Regarding the calibration process, the first step of every experiment is to place the probe in a determined position and get a reference measure. Ideally, a magnetic source that generates a well known magnetic field is placed in that position. However, if this magnetic source is very intense (for instance a NdFeB permanent) it might affect the measurements of experiments, and if it is used a weak magnetic source, or even none, it is important to consider that the MFS can be easily move by the user, and the Earth's magnetic field will influence the reference measurement in dependence of the orientation of the device with the Earth's magnetic poles.

The MFS was conceive as a device to perform a proof-of-concept. The experience of this work suggest that the MFS might be enhanced with the implementation of additional sensors in order to provides information of the physical location of the object under test. Another interesting improvement might be the design of a tip with the sensor at the end, and the implementation of two more degrees of freedom. These two improvement might allow to measure objects with special shapes, such a as sphere. An additional improvements might be the implementation of a control in the machine with the support of an SD card containing the code to run a particular experiment. However, all these improvements are based on the functionality given to the device; this is, the task that it has to perform.

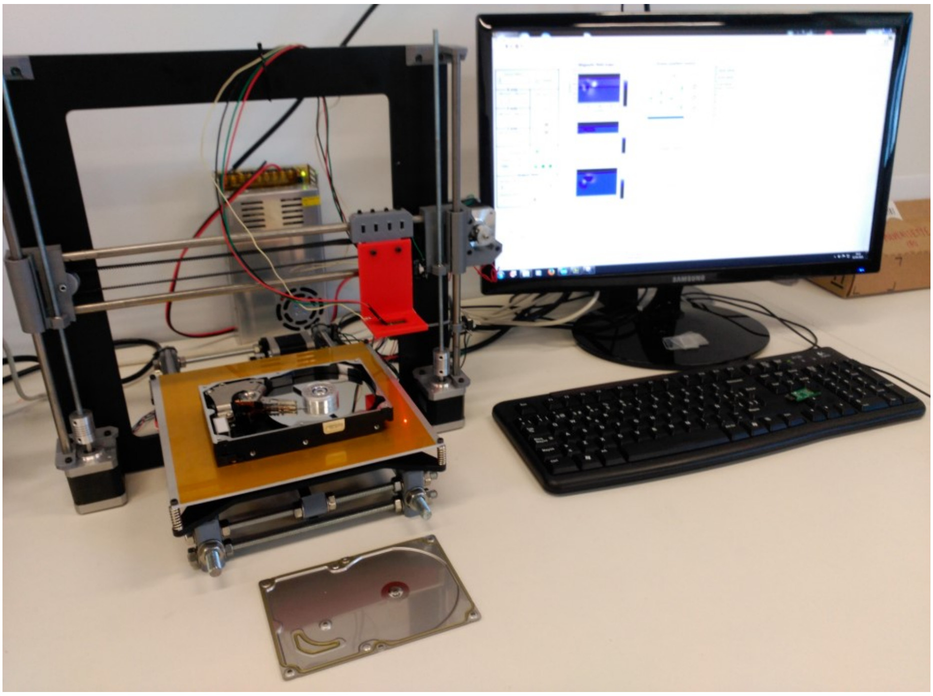

Figure 9.3: Picture of the magnetic field scanner, with a hard disk in the operating area, and the computer that controls the device.

9.3 Example Of Application 1: Magnets Detection

Nowadays technology is increasing the consumption of permanent magnets which are composed by critical elements such as rare-earth. For instance, the magnets of a hard disk are made out of Nd_2Fe_14B. At the moment, there is no automatic procedure for the recovery of these items, mainly due to the difficulty found on its extraction from the hard disk; the magnets might be placed in any corner of the device depending on the fabricator design, and thus it is necessary a manual procedure to initially locate the position of the magnets inside the device, involving the opening of the device for its visual inspection. As this task requires the human intervention, it is a slow procedure and because of this the only feasible industrial method to recover the RE-elements consist in the complete destruction of the device to later use a technique that decomposes it (i.e. hydrogen decrepitation) to its constituent elements, including the rare-earths, for its ulterior recovery to be re-introduced in the market as raw materials.

The MFS described in section 9.2 is a device that might be implemented, for instance, as a part of a process oriented to a fully automatic procedure for the recovery of permanent magnets inside of extended used electronic devices such as loudspeakers, smartphones and specially, hard-disk devices which contain a pair of rare-earth magnets each. These two magnets are the main magnetic field source that the device contains, and are located inside an iron yoke being one on top of the other, with alternated magnetic poles facing each other (this is, the north pole of one magnet faces the south pole of the other).

By using the MFS, it is imaged the magnetic field distribution map generated by the permanent magnets of a hard disk, in an XY-plane at a certain distance, Z, from the hard disk surface is measured with the MFS, for Z values of 0.5, 10.5 and 20.5mm. Figure 9.4 shows the B_Z component of the magnetic field distribution generated by the two RE-based permanent magnets of a hard disk that was scanned (with the cover) at different Z heights. The distribution of elements inside the hard disk can be observed on Figure 9.4.(a) (the cover was removed to allow the observation). The target magnets are in the top left corner inside the iron yoke.

At a first glance it is easily identified the magnets position since the intensity of B_Z is considerably higher in that zone of the map (see Figure 9.4.(b-d)). Each color (blue-red) of the magnetic map corresponds to one sign of the magnetic field. It can be observed that there are two red and blue regions on top of another two blue and red regions respectively. This is because the magnet is radially magnetized; a half of the piece is a north pole and the other half is a south pole. In addition, the magnets faces opposite poles and therefore, the dispersion of magnetic field when moving away from the surface causes that the region originated from the top magnet (which is closer to the sensor) will the smaller in size than the one generated by the bottom magnet. It is important to note that the magnetic field strength at a determined point is inversely proportional to the distance from the sensor to the magnetic source that generates it. The measured XY-plane might present some misalignment respect to the magnets plane. This might be the explanation of asymmetries found in regions with similar intensities but different signs.

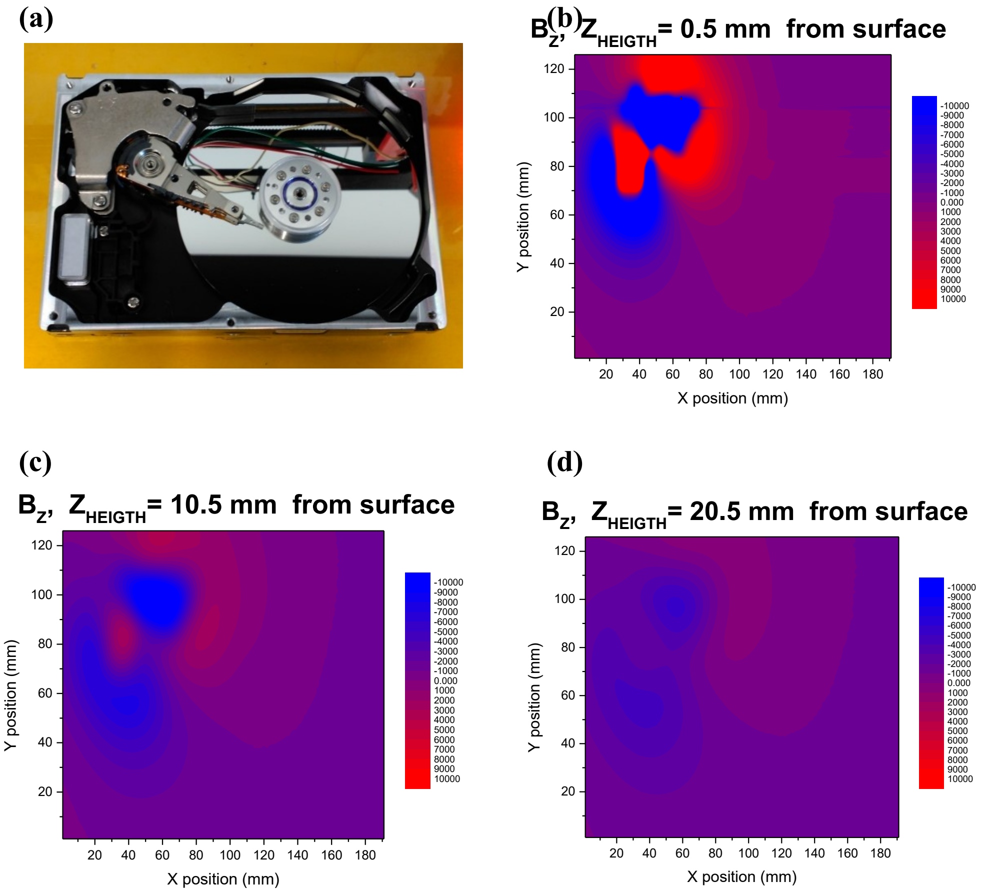

Figure 9.4: The magnetic field generated by the magnets inside a hard-disk (a) was measured, with the hard-disk closed, collecting the magnetic field map of the B$_Z$ component at (b) Z = 0.5 mm (c) Z = 10.5 mm and (d) Z = 20.5 mm.

With a careful analysis of the collected data, it is possible to discriminate other elements of the hard disk such as the screws and the hard disk motor. This is related with the different magnetic susceptibility of each material used in the hard disk: the cover (mu-metal), the screws (steel), and for the rotor of the motor that spins the disk, hence these elements modify the magnetic field generated by the RE magnets. However, the differences in the magnetic field around these elements are quite small, but measurable anyway. Using this possibility, it is possible to implement an algorithm for the localization of the magnets in the device from the magnetic measurements, as well as to determine the position of other elements.

9.4 Example Of Application 2: Study of Magnetic Field Domain Configuration

An interesting application of the MFS device concerns the study of materials magnetic domain configuration and how these materials interact between them (for instance the magnetic field interaction of two magnets). This type of experiments are very useful, for instance, in the determination of the demagnetizing factor of a magnet with a particular shape [2] or in non-destructive fatigue tests [3–5]. The main goal of this experiment is not to perform a quantitative analysis but to explore the limits of the MFS device when performing this task.

In this experiment, the magnetic field generated by a ferrite bonded magnet with special motives imprinted in the magnetic field domain configuration is mapped. These type of magnets are extensively used in the aesthetics market, specifically to draw predefined patterns when painting nails. The paint contains magnetic particles that, when the magnet is approached, trends to agglomerate in the regions where the magnetic field intensity is higher. The same principle is employed to fabricate the 'magnetic field visualizers cards, but in this case, the magnetic particles are included in between two transparent plastics; the magnetic field generated by the ferrite bonded magnet on its surface is shown in Figure 9.5.(a) by using one of this visualizer card. The magnet is magnetized with five concentric circles, being apparently a single point the one located in the inner part.

Next step was to map the magnetic field generated by the magnet using the MFS device described in section 9.2. First, an XY-plane map was taken above the magnet at a constant $Z =$ 3.2 mm. The three magnetic field components were measured in an XY area of 42.6 x 30 mm with a grid of 0.1 mm side. The collected B_Z map is plot in Figure 9.5.(b). No correction is done in the collected data, so that the magnetic map includes an offset corresponding to the Earth's magnetic field B_Z component. By comparing absolute values of the measured magnetic field with the Earth's magnetic field (60 μT) can be concluded that this offset is not relevant against the magnet signal. In this representation, blue color correspond to a vector pointing to the magnet surface (north pole), the red color represents positive magnetic field intensity pointing out from the magnet (south pole), and green means that the magnetic field at this point is null.

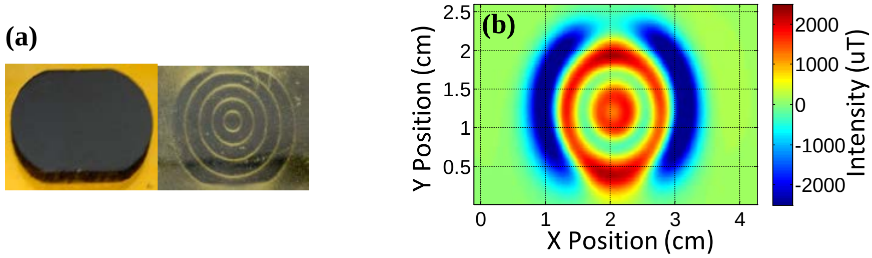

Figure 9.5: Image of (a) the ferrite bonded magnet (left) and the magnetic field configuration observed with a magnetic field visualizer card, and (b) the B_Z component of the ferrite bonded magnet generated magnetic field measured with the MFS device.

At a first glance, a green background is seen where one can identify two red circles corresponding to positive values of B_Z, and one blue circle (the outer one) corresponding to negative B_Z intensities. Moreover there is a green circle in between the two reds. By comparison of maps of Figures 9.5.(a) and (b), what attracts the attention is that two circles are not observed in Figure 9.5.(b), which might be due to the high distance between the sensor and the magnet's surface. The dispersion of the magnetic field generated by the magnet can be evaluated with the MFS device by measuring an XZ-plane map. The measured B_Z intensities recorded at different heights from the magnet's surface are plot in Figure 9.6.(a), while the full magnetic map obtained from a scan at a constant Y = 1.2 mm, in an area $3 \leq Z \leq 5$ mm and $0 \leq X \leq 4.3$ mm is represented in Figure 9.6.(b). This data provides useful information to understand the absence of the two north poles missed in Figure 9.5.(b).

Focusing the attention in Figure 9.6.(a), it is observed 5 pairs of peaks coming from a circle each. Almost all the peaks are saturated in exception to the first and third circle (considering the first circle the inner one). Increasing the Z height in 1 mm results in the increment of B_Z measured above the first circle region, and the decrease of intensity in the rest of the pairs. For $Z \geq 5.5$ mm, all peaks decrease its intensity and for $Z \geq 13$ mm the measured B_Z signals are null. This can be intuitively observed in the XZ-map plot in Figure 9.6.(b). Furthermore, looking at this figure one can understand why two circles are missed in the XY-map of Figure 9.5.(b); the height Z = 3.2 mm used in this experiment do not allow to visualize the magnetic field generated by the first and third circles. After this analysis the magnetic domain configuration of the magnets can be understood and the magnetization state of each circle is now identified. This magnet is magnetized with concentric circles that alternate its magnetic polarity; the inner circle is a north pole, the next a south pole...etc and this sequence ends with the fifth circle that is a north pole. Interestingly, it is observed that the highest B_Z intensities are found in the inner circles for positives B_Z values but in the outer circles for negative B_Z.

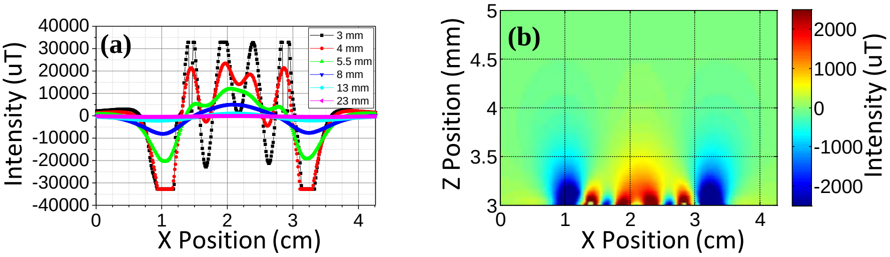

Figure 9.6: Image of (a) the polymericed ferrite magnet and (b) circles, (c) scrape-like and (d) diamons magnetic motives imprinted.

With this experiment, the utility in magnetic field configuration study of the MFS device based on a magnetoresistive sensor is demonstrated. In addition to the low complexity of the device, it is possibly to obtain 3D magnetic maps in a reasonable time. A relevant difference between the magnetic field visualizer card employed to obtain the image of and the MFS map is that, while the first device is only sensitive to the magnetic field intensity, the MFS sensor also provides the sign of the magnetic field, and thus being possible to determine if the circle is a north pole or a south pole.

9.5 Example Of Application 3: Magnetic Codification

Having in mind the results of experiments previously discussed, in this section it is propose an application combining the magnetovision technique, with the possibility TO imprinting a particular magnetic domain configuration with permanent magnets. The idea behind this application is to use the magnetic field generated by a set of magnets to codify metallic boxes; a card containing permanent magnets is the identification element which is attached to metallic box in such a way that, from the other side of the box, the magnetic reader is able to read the magnetic map generated by the identification element, and thus assign a code to the box. This application would be an alternative to, for instance, the traditional optical code-writting method, and can be applied to classify metallic boxes, or in general, containers made out of high magnetic permeability materials.

In order to proof te feasibility of this idea, the possibility of identifying a magnetic tag inside a metallic box is discussed. First, a card containing permanent magnets is fabricated with a 3D-printer. This plastic card, with a size of 50x80 mm contains a matrix of 3x5 gaps to introduce the magnets (Figure 9.7.(a)). These magnets have rectangular shape with 5x6 mm size and they are magnetized axially (i.e. north pole in the top face and south in the bottom), and were placed randomly in the card. Three states are assigned to each gap of the card; 1) there is no magnet, 2) there is a magnet with north face, and 3) there is a magnet with south face. Figure 9.7 contains the B_Z values recorded in with constant Y = 22, 55 and 38 mm. Simply by the visual inspection can be known if at a determined position there is a magnet because of the high B_Z component value observed in that localization, as well as to determine the position how it is placed (top or bottom, south or north). Moreover, this method is susceptible to introduce intensity codification; for instance one state every 10μT increment in the B component intensity.

The characteristic magnetic field generated by this card is measured and compared with the magnetic field map obtained with that same card inside a metallic box. The Z height from the sensor to the card surface used in this experiment is high, Z = 20 mm, due to fact that the high magnetization of the magnets can saturate the sensor. The image studied at 20 mm above the card surface is compared with the data obtained when Z was 1 mm above the box containing the card. Scanned maps of the identification card containing the permanent magnets are shown in Figures 9.7.(c-d). It is noteworthy the drastic decrease of B_Z intensity when the card is inside of the box, even if the distance from the sensor to the card surface is reduced since the magnetic flux lines generated by the magnets will go trough the metal of the metallic box (and it will get attached). On the other hand, and depending on the magnetic susceptibility of the metallic material is important to be considered since the obtained image will vary or remain similar to as it was when measured without the box. However, it is clearly observed the increased magnetic field intensity above the magnets. It is important to note the relevance of magnets distribution, as it is observed with the three magnets located in the central row. The one in the left is placed with the north pole facing up, and the others two with the south pole.

With this experiment, it is demonstrated the possibility to implement magnetic tags for metallic containers based in the use of permanent magnets. This application display a very important advantages; the possibility of use 3D-magnetic readings multiplies exponentially the number of combinations that can be obtained with one magnet, that is analogue to one bit. Furthermore, this tag is inside the metallic box, and in consequence it is not exposed to environmental conditions. For instance, one can think in a container used for maritime transport.

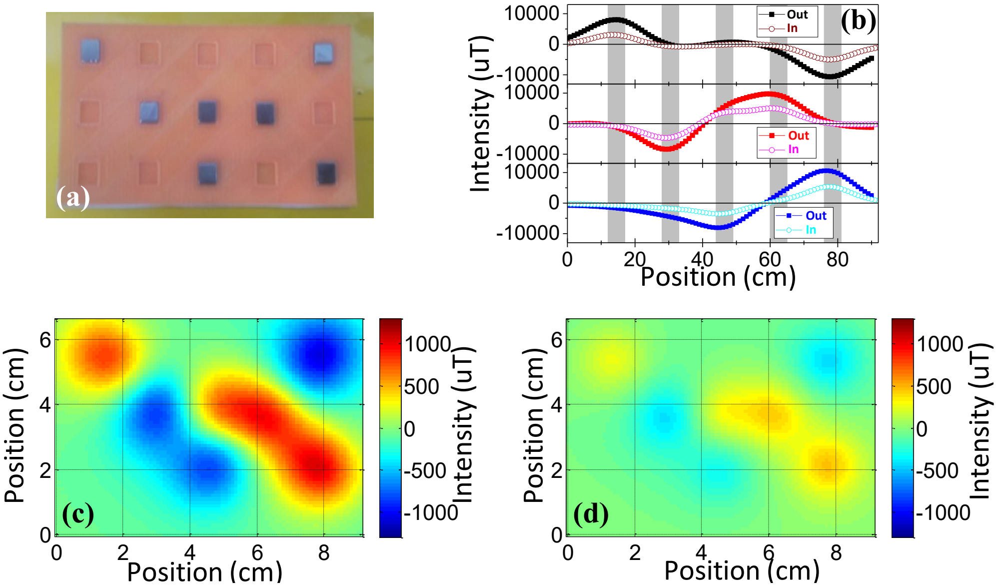

Figure 9.7: Image of (a) the card containing the magnets. Figure (b) is the B_Z vales measured at Y = 22 , 38 and 55 mm. Magnetic map on Figure (c) represents B_Z with the card aoutside the box at a Z = 20mm. Figure (d) is the magnetic map measured for B_Z when the card is inside the box at a Z = 1mm aboce the box surface.

9.6 Conclusions

Magnetovision is an important area emerging in recent times due to advances on magnetic sensors manufacturing. In this chapter, the implementation of a MAG3110 sensor in a preliminary device, in order to image the magnetic field generated by a ferromagnetic element have been described. The novelty of this device is the use of a sensor with on-chip circuitry, reducing the complexity of the system: a sensor placed in a three degrees of freedom CNC, all this controlled with an Arduino as a bridge between a PC and the fabricated instrument is sufficient to perform the task. The MFS is goberned through a computer, but it can be modified to work independently.

The possibility of detecting the permanent magnets of electronic devices at the end of their lifetime has been demonstrated in this section. A relevant case is a hard disk because of the value of its magnets, and a very common device in our actual live such as smartphone, that contains at least two magnets. Both elements are analyzed demonstrating the feasibility of the implementation of these devices as elements to identify the presence of permanent magnets on electronic devices. Additionally, it might be used not for the future extraction of the permanent magnet, but for quality control processes.

Furthermore, from a scientific point of view it is possible to use the MFS device to study magnetic configurations. The magnetic field domain configuration of ferrite polymerized magnets magnetized with special motives imprinted are measured and discussed. Noteworthy, this device allows to study how magnetization of different regions of a permanent magnet interact with each other, or even to study how different magnets interact between them.

Finally, an application combining the magnetovision technique with the codification of elements, for its posterior classification, making use of permanent magnets is described. A proof on concept is performed to demonstrate that it is possible to identify an element, located inside a metallic box, that generates a magnetic field previously known. Moreover, due to the 3D character of the obtained measurements, it is possible to obtain a considerably high number of possible combinations.

References

[1] Sławomir Tumaski and Marek Stabrowski *Magnetovision system: new method of investigating steel sheets*. in: *Journal of magnetism and magnetic materials* ***160***, (1996), 165–166 (cit. on pp. 154, 156)

[2] Sławomir Tumański *The application of permalloy magnetoresistive sensors for nondestructive testing of electrical steel sheets*. in: *Journal of magnetism and magnetic materials* ***75***,3 (1988), 266–272 (cit. on pp. 154, 160)

[3] Slawomir Tumanski and Marek Stabrowski *The magnetovision method as a tool to investigate the quality of electrical steel*. in: *Measurement Science and Technology* ***9***,3 (1998), 488 (cit. on pp. 154, 160)

[4] Jerzy Kaleta, Slawomir Tumański, and Jacek Żebracki *Magnetoresistors as a tool for investigating the mechanical properties of ferromagnetic materials*. in: *Journal of magnetism and magnetic materials* ***160***, (1996), 199–200 (cit. on pp. 154, 160)

[5] Klaus Szielasko, Albert Kloster, Gerd Dobmann, H Scheel, and B Hillemeier *High-speed, high-resolution magnetic flux leakage inspection of large flat surfaces*. in: *European Conference on Nondestructive Testing* 2006 (cit. on pp. 154, 160)

[6] Chao Hu, Mao Li, Shuang Song, Rui Zhang, Max Q-H Meng, et al. *A cubic 3-axis magnetic sensor array for wirelessly tracking magnet position and orientation*. in: *IEEE Sensors Journal* ***10***,5 (2010), 903–913 (cit. on p. 154)

[7] ME Cano, JC Martínez, J Bernal-Alvarado, M Sosa, and T Córdova *16-channel magnetoresistive scanner for magnetic surface imaging*. in: *Review of scientific instruments* ***76***,8 (2005), 086106 (cit. on pp. 154, 156)

Coclusiones

Esta tesis es un trabajo científico-tecnológico experimental donde se han combinado tareas de caracterización (microestructrural y magnética), procesado de muestras (mediante procesos físicos), y desarrollo de nueva tecnología (prototipado).

Para los estudios microestructurales se han combinado técnicas de difracción (XRD), microscopía (TEM) y para la caracterización magnética se han utilizado técnicas vectoriales de magnetometría (v-MOKE y v-VSM) a temperatura ambiente y SQUID en el caso de las medidas a baja temperatura.

Se han estudiado sistemas modelo con anisotropía bien definida impuesta por la cristalografía (películas delgadas epitaxiales de magnetita $Fe_3O_4(001)$) ó por la forma (nanohilos de aleación de FeCo crecidos en membranas porosas de alúmina) así como sistemas isótropos de polvo de ferrita refinada mediante procesos combinados térmicos y de molienda.

Se ha desarrollado una nueva metodología para potenciar las propiedades magnéticas de polvo de ferrita combinando molienda ultra-rápida (en condiciones secas y húmedas) y tratamientos térmicos. A su vez, dentro del desarrollo tecnológico hay que reseñar:

a) La nueva metodología para refinar/controlar la microestructura del polvo isótropo de ferrita con el fin de potenciar sus propiedades magnéticas.

b) El desarrollo de nuevas aplicaciones de nanomagnetismo usando los sistemas estudiados.

Cuatro aportaciones científicas merecen ser destacadas:

1. Determinación de los efectos de anisotropía, forma y dimensionalidad en materiales magnéticos.

2. Determinación y control de la relación entre la microestructura y las propiedades magnéticas de sistemas en polvo (ferrita de Co) isótropos, tratados y refinados mediante diferentes procesos.

3. Desarrollo de tecnología eficiente para controlar y aumentar la calidad magnética (coercitividad y producto BH) de polvos isotrópico de material magnético libre de tierras raras.

4. Desarrollo y prototipado de nuevas aplicaciones haciendo uso de los imanes permanentes libres de tierras raras desarrollados.

   Además, hay que destacar tres aportaciones tecnológicas :

5. El uso de la magnetometría vectorial para determinar los procesos microscópicos de la inversión de imanación en los sistemas modelo.

6. El desarrollo de una metodología eficiente (ultra-rápida y con requerimientos de temperaturas moderadas), reproducible y escalable para refinar/controlar la microestructura de polvo de ferrita.

7. Diseño y prototipado de nuevas aplicaciones de nanomagnetismo

Por lo tanto, este trabajo aporta resultados relevantes en el área del Nanomagnetismo, en general al campo de los imanes permanentes y en particular para el desarrollo de imanes permanentes libres de tierras raras. Además, el diseño y creación de prototipos de nuevas aplicaciones tecnológicas basadas en los adelantos científicos mencionados y, en general, en nanomagnetismo, abre nuevas vías para el desarrollo de nuevos dispositivos con aplicaciones potenciales

Coclusions

This thesis is an experimental scientific-technological work where characterization tasks (microstructural and magnetic), processing of samples (through physical processes), and development of new technology (prototyping) have been combined. For the microstructural studies, diffraction techniques (XRD), microscopy (TEM) have been combined, and for magnetic characterization vectorial magnetometry measurements (by using v-MOKE and v-VSM) have been carried out at room temperature and SQUID measurements at low temperature. We have studied model systems with well-defined anisotropy imposed by crystallography (thin epitaxial films of Fe_3O_4 (001) magnetite) or by the shape (FeCo alloy nanowires grown in porous alumina membranes) as well as isotropic systems of refined ferrite powder by combined thermal and grinding processes. A new methodology has been developed to enhance the magnetic properties of ferrite powder by combining ultra-fast milling (in wet and dry conditions) and thermal treatments. At the same time, within the technological development, highlight:

a) The new methodology to refine / control the microstructure of isotropic ferrite powder in order to enhance its magnetic properties.

b) The development of new applications of nanomagnetism using the systems studied.

Four scientific contributions deserve to be highlighted:

1. Determination of the effects of anisotropy, shape and dimensionality on magnetic materials.
2. Determination and control of the relationship between the microstructure and the magnetic properties of isotropic powder systems (Co ferrite), treated and refined by different processes.
3. Development of efficient technology to control and increase the magnetic quality (coercivity and $(BH)_{\mathrm{max}}$) of isotropic powders of rare earth-free magnetic material.
4. Development and prototyping of new applications making use of permanent magnets free of developed rare earths.

   In addition, there are three technological contributions:

5. The use of vector magnetometry to get a microscopic understanding on the magnetization reversal processes in model systems.
6. The development of an efficient methodology (ultra-fast and with moderate temperature requirements), reproducible and scalable to refine/control the microstructure of ferrite powder.
7. Design and prototyping of new applications based on nanomagnetism.

Therefore, this work brings relevant results in the area of Nanomagnetism, in general to the field of permanent magnets and in particular for the development of permanent magnets free of rare earths. In addition, the design and prototyping of new technological applications based on the aforementioned scientific advances and, in general, in nanomagnetism open new routes for developing novel devices with potential applications.

Related to this thesis

[1] Matylda N Guzik, Karol M Golasiński, **Pedrosa, F Javier**, Petra Jenuš, Alberto Bollero, Bjørn C Hauback, and Stefano Deledda *Influence of ultra-short cryomilling on the microstructural and magnetic properties of cobalt ferrite*. in: *Journal of Alloys and Compounds* (2017)

[2] **Pedrosa, FJ**, J Rial, KM Golasinski, MN Guzik, A Quesada, JF Fernández, S Deledda, J Camarero, and A Bollero *Towards high performance CoFe2O4 isotropic nanocrystalline powder for permanent magnet applications*. in: *Applied Physics Letters* ***109***,22 (2016), 223105

[3] **Pedrosa, FJ**, J Rial, KM Golasinski, M Rodríguez-Osorio, G Salas, D Granados, J Camarero, and A Bollero *Tunable nanocrystalline CoFe 2 O 4 isotropic powders obtained by co-precipitation and ultrafast ball milling for permanent magnet applications*. in: *RSC Advances* ***6***,90 (2016), 87282–87287

[4] **Pedrosa, FJ**, J Rial, KM Golasinski, J Camarero, and A Bollero *CoFe 2 O 4 isotropic powders for permanent magnet applications*. in: *EUROCON 2015-International Conference on Computer as a Tool (EUROCON), IEEE* IEEE 2015, 1–2

[5] Matteo Monti, Mikel Sanz, Mohamed Oujja, Esther Rebollar, Marta Castillejo, **Pedrosa, Francisco J**, Alberto Bollero, Julio Camarero, Jose Luis F Cunado, Norbert M Nemes, et al. *Room temperature in-plane< 100> magnetic easy axis for Fe3O4/SrTiO3 (001): Nb grown by infrared pulsed laser deposition*. in: *Journal of Applied Physics* ***114***,22 (2013), 223902

[6] Mikel Sanz, Mohamed Oujja, Esther Rebollar, José F Marco, Juan de la Figuera, Matteo Monti, Alberto Bollero, Julio Camarero, **Pedrosa, Francisco J**, Mar García-Hernández, et al. *Stoichiometric magnetite grown by infrared nanosecond pulsed laser deposition*. in: *Applied Surface Science* ***282***, (2013), 642–651

[7] M Oujja, M Sanz, E Rebollar, JF Marco, J de la Figuera, M Monti, A Bollero, J Camarero, **Pedrosa, FJ**, M Garcia-Hernandez, et al. *Structural and magnetic characterization of magnetite deposits prepared by infrared pulsed laser deposition*. in: *Lasers and Electro-Optics Europe (CLEO EUROPE/IQEC), 2013 Conference on and International Quantum Electronics Conference* IEEE 2013, 1–1

Other publications

[1] F Cuñado J Luis, **Pedrosa, FJ**, F Ajejas, P Perna, R Miranda, and J Camarero *Direct observation of temperature-driven magnetic symmetry transitions by vectorial resolved MOKE magnetometry*. in: *Journal of physics. Condensed matter: an Institute of Physics journal* ***29***,40 (2017), 405805

[2] E Céspedes, G Rodriguez-Rodriguez, C Navío, MR Osorio, R Guerrero, **Pedrosa, FJ**, FJ Mompeán, M García-Hernández, JF Fernández, A Quesada, et al. *Inter-grain effects on the magnetism of M-type strontium ferrite*. in: *Journal of Alloys and Compounds* ***692***, (2017), 280–287

[3] Nathan Jackson, **Pedrosa, Francisco Javier**, Alberto Bollero, Alan Mathewson, and Oskar Z Olszewski *Integration of Thick-Film Permanent Magnets for MEMS Applications*. in: *Journal of Microelectromechanical Systems* ***25***,4 (2016), 716–724

[4] Adrian Quesada, Cecilia Granados-Miralles, Alberto López-Ortega, Sergey Erokhin, Elisabetta Lottini, **Pedrosa, Javier**, Alberto Bollero, Ana M Aragón, Fernando Rubio-Marcos, Marian Stingaciu, et al. *Energy Product Enhancement in Imperfectly Exchange-Coupled Nanocomposite Magnets*. in: *Advanced Electronic Materials* ***2***,4 (2016)

[5] A Bollero, **Pedrosa, FJ**, J Cuñado, J Camarero, M Seifert, V Neu, V Baltz, D Serantes, O Chubykalo-Fesenko, R Del Real, et al. *Extraordinary exchange-bias effects in coupled SmCo 5 (perpendicular)/CoFeB (in-plane) bilayers*. in: *Magnetics Conference (INTERMAG), 2015 IEEE* IEEE 2015, 1–1

[6] Jose Luis F Cuñado, **Pedrosa, Javier**, Fernando Ajejas, Alberto Bollero, Paolo Perna, Francisco J Teran, Rodolfo Miranda, and Julio Camarero *Note: Vectorial-magneto optical Kerr effect technique combined with variable temperature and full angular range all in a single setup*. in: *Review of Scientific Instruments* ***86***,4 (2015), 046109

[7] E Jiménez, N Mikuszeit, JLF Cuñado, P Perna, **Pedrosa, J**, D Maccariello, C Rodrigo, MA Niño, A Bollero, J Camarero, et al. *Vectorial Kerr magnetometer for simultaneous and quantitative measurements of the in-plane magnetization components*. in: *Review of Scientific Instruments* ***85***,5 (2014), 053904